POLITECNICO DI MILANO

Facoltà di Ingegneria Industriale

Corso di Laurea Magistrale in
Ingegneria Energetica

CFD STUDY OF FLUID DYNAMICS OF EJECTOR AND DUCTS IN GALVANIZING PLANT

Relatore: Prof. Matteo Carmelo Romano

Co-relatore: Ing. Francesco Dentalla
Ing. Giorgio Besagni

Tesi di Laurea di:

Luca Gino Capitanio

Matricola 784307

Anno Accademico 2012 – 2013

This work is dedicated to

My Mother

My Father

My Brother

My Sister

In memory of

My grandparents
My friend Stefano

"I nostri sogni e desideri cambiano il mondo."

Aknowledgements

Se oggi posso scrivere queste parole è solo grazie al sostegno della mia famiglia, che mi ha incoraggiato nei momenti di difficoltà, mi ha spronato ad andare avanti e a cercare il meglio in ogni situazione, mi ha insegnato l'umiltà e la bellezza del sorriso. Una dedica particolare va a mia sorella, che pur vivendo lontano mi è sempre stata vicina, i suoi consigli e le sue "tirate d'orecchie" mi hanno permesso di affrontare questo cammino più serenamente.

Ringrazio DCHP e il mio tutor Francesco per l'opportunità concessami, per la gentilezza, la disponibilità, e per avermi mostrato che la passione è fondamentale per affrontare le difficoltà e a raggiungere i propri obiettivi.

Ringrazio il mio relatore, il Professor Matteo Carmelo Romano, e il mio co-relatore Ing. Giorgio Besagni, per l'importantissimo supporto che mi è stato offerto, ma anche per la loro disponibilità e la loro gentilezza, per il tempo dedicatomi nonostante i numerosi impegni accademici.

Ringrazio la mia squadra di pallanuoto, con cui ho trascorso momenti indimenticabili in questi ultimi anni, che mi ha insegnato che non si deve mai mollare.

Ringrazio tutti gli amici ed i colleghi di lavoro, che sono stati capaci di strapparmi un sorriso nei giorni di tristezza e che mi hanno insegnato che la vita va vissuta intensamente, senza negarsi nulla.

Grazie a tutti voi.

Abstract

Blast Furnace Gas (BFG) represents a key in the reduction of greenhouse emissions and operational cost of a steel production plant. In the last decades equipment manufacturers have adapted their combustion systems design to allow the switch to this low energy content fuel (LHV ≈ 800 kcal/Nm^3) in the processes downstream the blast furnace, for instance continuous reheating furnaces. In the last years a further improvement of efficiency optimisation technologies focused on the finishing production lines (galvanizing lines), usually fuelled with traditional sources. The switch to BFG revealed to be problematic in these units mainly for two reasons: the combustion process sustainability is compromised by the presence of a big amount of inert of reaction (nitrogen above all) in the stream, and the fumes volume ratio is significantly increased as a consequence of the poor energy content of the BFG, with respect to the traditional source. Hence it is required an improvement of the combustion techniques combined with a verification of the suitability of the existing frame with the new volume rates. The pressure drop analysis of a galvanization plant fumes duct, whose combustion system was switched to BFG feed (oxygen and LPG are added to enhance LHV and stabilize the flame), is the first objective of this thesis work. The investigated condition refers to the highest fumes volume rate admissible, corresponding to air and BFG as reactants. The zinc pot is heated by pure convection, and a negative pressure value is required inside the furnace, in order to avoid the fumes exit through the not airtight junctions. On the other hand an excessive negative pressure would cause the dilution of gases with the cold air drawn from the external environment, causing a heat loss. Hence the second objective of this work is to determine the localized pressure drop, obtained through a damper, which assures the correct furnace operation. The dissertation is organized as follows: in the first chapter the key aspects and problems of the BFG employment, with respect to the traditional sources, and the galvanization plant are presented. In the second chapter the two main topics concerning the plant are highlighted: the ejector, which assures the fumes suction, and square ducts. The literary review presents their working principles and the state of art of their numerical modelling. The third chapter offers a brief description of the CFD fundamentals and the Q^3 approach, a helpful instrument through which the quality of results is guaranteed. The fourth chapter contains the geometric modelling, the grid generation and the solver settings for each domain that constitute the plant. This process is usually named “Pre-processing”. In the following chapter results are reported and discussed with the help of fluid flow contours, visualizations and charts for each domain. This is called “Post-processing”. In the last chapter significant results are reported and commented, and future investigations are briefly explained.

Keywords: BFG, fumes duct, industrial stack, subsonic ejector, square sectioned duct, RANS turbulence models, pressure drops in channels, 3D modelling.

Italian Abstract

Il recupero del gas d'altoforno (Blast Furnace Gas) rappresenta una soluzione chiave per la riduzione dell'impatto ambientale e dei costi d'esercizio di un'acciaieria. Per poter utilizzare questo combustibile a basso potere calorifico (LHV ≈ 800 kcal/Nm^3), negli ultimi decenni i produttori di forni per i processi di riscaldamento ad alta temperatura hanno adeguato i propri sistemi di combustione. Negli ultimi anni la ricerca di un'ulteriore ottimizzazione economica ha posto l'attenzione sui processi di finitura, alimentati a combustibile tradizionale. Gli aspetti chiave della loro conversione al BFG sono due: la auto-sostenibilità della combustione alle minori temperature d'esercizio e gli spazi disponibili per lo smaltimento fumi. Il primo è legato alla elevata presenza di inerti nel gas (prevalentemente azoto), che rendono la fiamma instabile e ne abbassano la temperatura massima. Il secondo aspetto è una conseguenza del minore potere calorifico. Fissato l'input termico del processo, un combustibile povero richiede una maggior portata volumetrica rispetto a quello tradizionale, quindi è necessaria una verifica di compatibilità con la struttura esistente. In questa tesi è proposto lo studio CFD delle perdite di carico nei condotti fumi e nel camino-eiettore di un impianto di galvanizzazione, il cui sistema di combustione è stato convertito da tradizionale a BFG Nel caso in analisi, in cui aria e BFG sono i soli reagenti, la portata volumetrica di gas è la massima ammissibile dall'impianto. Il riscaldamento della vasca contenente lo zinco fuso avviene per sola convezione, e il forno opera in leggera depressione, per evitare la fuoriuscita di gas nocivi dalle giunzioni non a tenuta. Un eccessivo rientro d'aria dall'ambiente esterno tuttavia diluirebbe fortemente i gas combusti, aumentando i consumi per fornire lo stesso input termico al processo. A fronte di ciò il secondo obiettivo della tesi consiste nel calcolo della perdita di carico concentrata, ottenuta mediante l'abbassamento di uno smorzatore, che garantisca le adeguate condizioni di pressione in camera di combustione. A tal fine questo lavoro viene strutturato come segue. Nel primo capitolo sono introdotti gli aspetti chiave e le problematiche derivanti dall'uso del BFG come combustibile, oltre ad una panoramica generale dell'impianto in analisi. Nel secondo capitolo sono evidenziati i due componenti chiave dell'impianto: l'eiettore, che fornisce la forza motrice ai fumi dal forno al camino, e i condotti a sezione quadra. L'analisi letteraria proposta mette in luce e i principi di funzionamento e gli aspetti cruciali della loro modellazione numerica, oltre allo stato dell'arte. Il terzo capitolo offre una breve introduzione alla CFD e al Q^3, l'approccio utilizzato per fornire qualità alla presente indagine. Il pre-processing, che include la modellazione 3D, la generazione di una griglia spaziale e la messa a punto del solutore per ogni parte d'impianto, occupa tutto il quarto capitolo, mentre nel successivo sono riportati i risultati e i commenti per ogni sezione analizzata, con l'ausilio di visualizzazioni e grafici. In conclusione sono riportati i risultati e gli sviluppi futuri possibili di questo lavoro.

Italian keywords: gas d'altoforno, camino industriale, eiettori subsonici, condotti a sezione quadra, modelli di turbolenza RANS, perdite di carico, modellazione 3D.

Contents

List of Figures

List of tables

Introduction

The growing attention to environment and the introduction of regulations for sustainable industry development drive the manufacturers around the word to undertake research for new technologies, which still permit to do business. In this sense companies of several sectors are trying to save money improving or adapting the existing technologies to the new requirements, obtaining economic advantages at the same time. What happened in the past to refineries is an example: specific chemical processes were introduced to extract useful fuels from waste materials. Thus positive results were reached both for the environment and the oil company.
The achievement of efficiency needs to be supported with a continuous research through modern instruments. According to this, CFD reveals its big potentiality in those fields where laboratory experimental activity becomes expensive, and the time required for results is limited. In this work CFD is introduced as a comfortable tool for the analysis of the fluid dynamics of a plant.
In the first chapter are explained the reasons that lead to the realization of this work, starting from the definition of the blast furnace gas (BFG). A brief description of the plant in question is proposed in the last section. Chapter 2 contains a literary review about the main topics concerning with the plant: ejectors and square ducts. In chapter 3 the fundamentals of CFD are presented. Everything concerning with modelling, meshing and solver set up for each domain is included in chapter 4, while results and comments are proposed in chapter 5. The last chapter is dedicated to conclusions and remarks.

Chapter 1 **Blast Furnace Gas**

1.1 Driving forces

The concerns about energy sustainable politics and environmentally friendly approaches, mainly related to greenhouse gases reduction, have been the driving forces to promote, during the last decade, an impressive amount of efficiency optimization technologies. As a significant part of this development, the replacement of "conventional" fossil fuels (i.e. Natural Gas, Light Diesel Oil…) with "alternative" fuels, generally byproducts of other processes (i.e. biomass pyrolysis or gasification), has been applied in several industrial sectors, with a major highlight in the steel industry.

1.2 The steel industry-"auxiliary fuel availability"

Steel production plants, the so called steel mills, are usually arranged as "integrated" plants where a sequence of processes is accomplished, starting from the mineral ores, passing through melting processes and metallurgical chemistry, till the production of semi-finished products. Probably the most well known and established "step" of this transformation is represented by the blast furnace (BF): a vertical shaft where mineral ores are charged and molten in continuous, in order to produce iron thanks to the heat released and the carburizing phenomena of a coke combustion reaction.

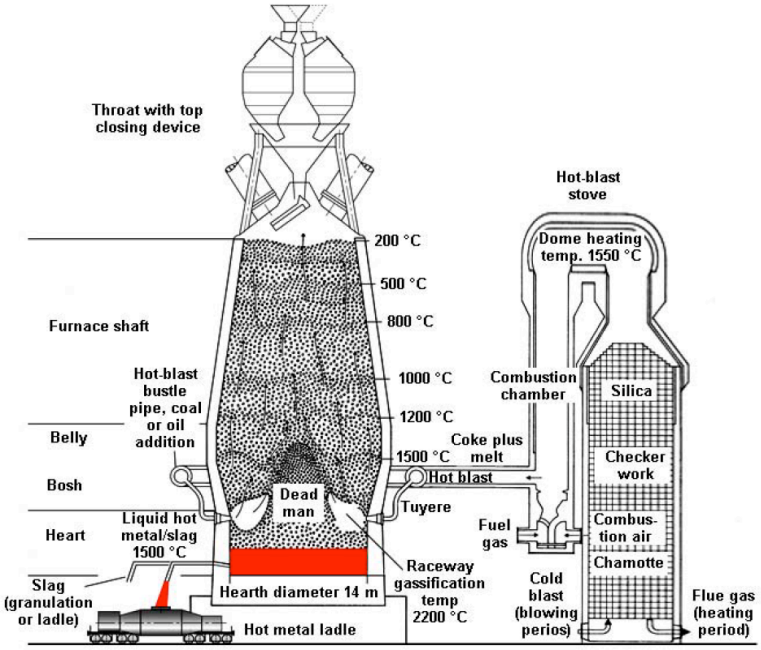

Figure 1-1 Scheme of a blast furnace. Modified from [1]

The chemistry of this furnace is determined by the generation of a reducing atmosphere during the combustion phase (under-stoichiometric reaction conditions). As consequence, the fumes released contain a large amount of CO (i.e. 22-26%) and H2 (i.e. 1-4%) that traditionally were burnt in atmospheric torches to avoid pollution, with an evident loss of energy. This large amount of fumes that was considered as an effluent to be treated to avoid pollution or other risks (because of the H2 presence), has now become one of the primary source of energy (so called BFG, Blast Furnace Gas) for some heating processes "downstream" the BF, for instance continuous reheating furnaces.

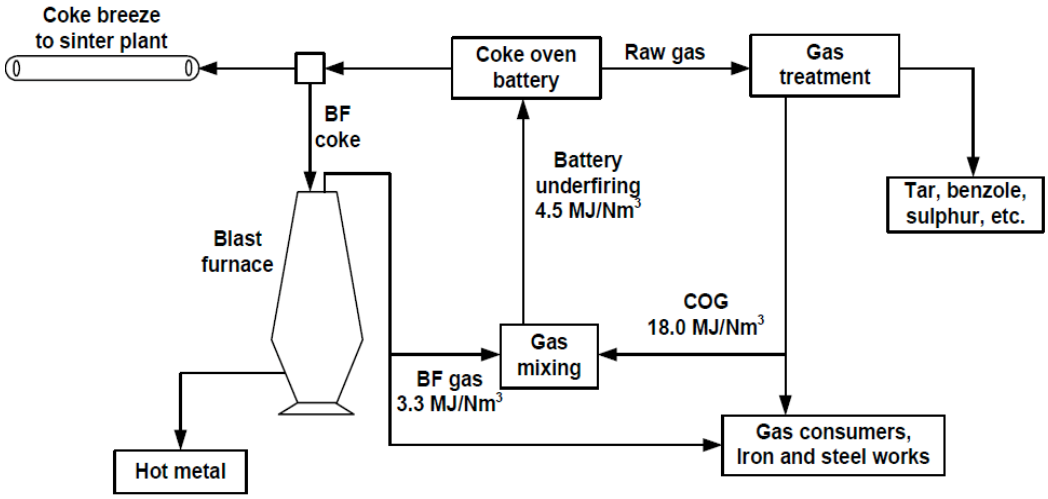

Figure 1-2 Flow sheet of typical gas utilization in integrated sinter, coke and hot metal production. Modified from [2]

In this furnaces steel bars or slabs are reheated and hold at high temperature according a predefined heating curve, in order to release mechanical stresses generated during the previous forming process (transition from liquid to solid phases). Because these furnaces are operated at an extremely high temperature (i.e. 1100-1300°C) in continuous, the major OEMs (Original Equipment Manufacturers) has adapted their design to allow replacing "standard fuels" with BFG, leading an important cuts on operational costs. Although on theoretical base the energy content into the fumes stream could be enough to fully replace the conventional fuels, the extremely poor Heating Value (LHV) of this type of fuel do not allow to design burners that may burn this combustible properly and steadily. For this reason a minimum amount of "conventional" fuel, i.e. NG or LPG, is added to the BFG stream in order to elevate the combustible mixture LHV till an average value of not less than 1.500-2.000 kcal/Nm^3.

1.3 The steel industry – "combustion enhancement availability"

Over the years, in order to improve the thermal efficiency of Blast Furnace, pure Oxygen injection solutions have been developed by Oxygen makers, aimed at minimizing coke consumption, while increasing melt rate and iron temperature at spout. Due to the high consumption of Oxygen requested in continuous by the BF, inside the steel mills there are usually on-site production plants that are able to fulfill the average requirement of pure Oxygen, but that are commonly sized with some "spare extra capacity" to cover peaks of demands or to make O2 available for other applications inside the plant (i.e. oxy-cutting of slabs).

The major properties of oxy-fuel combustion are connected to the increased reaction kinetics, that allow for instance to rise the flame temperature, improving heat release by radiative phenomena, or to stabilize combustion conditions or poor quality fuels (i.e. BFG but also Heavy Fuel Oil). This additional availability become for DCHP the base

for the development of a new combustion technology, subject of the activities hereinafter described.

1.4 Customer requirements

The Customer operates in continuous three blast furnaces in one of its facilities, therefore has a large availability of BFG. All the reheating furnaces that have been installed during the past few years, in fact, were designed by different OEMs to be suitable for firing a mixture of BFG and LPG (LHV mixture approx. 2.200 kcal/Nm^3). The Customer requirement was to find the way to adopt the same fuel in all the finishing production lines (mainly coils and pipe galvanizing lines) that already existed and fired with LPG. This type of gaseous fuel, in fact, is quite expensive because it has to be delivered by truck and stored in liquid form in storage tank: the location of the steel mill is too far from a NG distribution pipeline, where to be connected in order to receive gas at cheaper cost.
The difficulties of the task DCHP had to face were mainly the following:

1. Develop a burner suitable to fire a variable fuel composition, with minimum LPG enrichment (contractual goal was to operate the retrofitted furnaces with LHV fuel mix as low as 1.000 kcal/ Nm^3);
2. Evaluate the possibility to adopt such kind of fuel in an existing furnace facility, built to fire LPG, and therefore with much lower volumetric flow rate of combustion products generated;

1.5 "Combustion changes" related to the fuel switch

While planning the retrofitting/upgrading of any existing "system" or "process", it is compulsory to start from a deep understanding of the current operating conditions. This is the best way to try to forecast at least the main issues to be faced and solved. In order to simplify the understanding of the following dissertation also for non-combustion experts, the Customer's management, DCHP have introduced a specific parameter that should help in understanding the conclusion of proper analysis: the concept of "Energy Density (EnD)".

1.6 The concept of Energy Density

Combustion phenomena consist of chemical reactions between an oxidant molecule (Oxygen, present in air or pure) and the fuel molecules, which contain various amount of Carbon and Hydrogen atoms, according their composition (i.e. CH_4, C_2H_6, CO, H_2, C_8H_{12}, …), to produce mainly CO_2 and H_2O vapor (in case of complete combustion). Hence the amount of energy available in a fuel is basically related to the amount of "useful" molecules (i.e. CO, CH_4, H_2) present inside the reference measurement unit (i.e. one cubic meter of gas). For example, Natural Gas (NG) is normally considered having a LHV of near 8.200 kcal/Nm^3, because it is mostly composed by Methane (CH_4, LHV 9.000 kcal/ Nm^3) "diluted" by the presence of some inert of reaction (i.e.

N_2), that slightly limit the effective concentration of "useful molecules" capable to release energy when burnt.
In order to perform its complete combustion it is requested an amount of oxygen in a ratio of

approx. 2 Nm^3 O_2 per 1 Nm^3 NG

In order to provide the required amount of oxidant reactant commonly the so-called air-fuel combustion technologies are making available

approx. 10 Nm^3 AIR per 1 Nm^3 NG

Therefore roughly 79% of the total air fed is Nitrogen, molecules "inert" of reaction. These inert compounds, present in both combustive air and fuel in much lower percentage, not only are useless for the reaction accomplishment, where fuels molecules are transformed and release their energy, but also play additional roles:

1. *Microscopic phenomena*: they dilute the "useful" molecules present in both reactants making slower their reaction, because it takes longer "contact-time" for the mixed fluids to contact the right molecule (i.e. O_2 and CH_4);
   Macroscopic effect: combustion process (flame) becomes less and less stable with the increase of the inert percentage;

2. *Microscopic phenomena*: they absorb part of the energy released during combustion (sensible heat), diluting the energy released;
   Macroscopic effect: flame temperature decreases with the increase of the percentage of inert, affecting heat transfer capability via radiation;

3. In processes accomplished at high temperature (i.e. steel reheating furnaces) fumes are released at high temperature, hence a reduction of their maximum temperature is obtained through the presence of heat recuperators. The subsequent sensible heat present in flue gases represents a "net loss" of energy, and obviously the larger the amount of fumes, due to the presence of inert compounds, implies higher thermal losses.

Therefore the "quality" of the combustion process can be judged, when comparing several alternatives, introducing the "Energy Density "(EnD), a comparison parameter that is defined as:

$$\mathbf{EnD} = \frac{\textbf{Calorific value of fuel (kcal in 1 Nm}^3\textbf{ of fuel)}}{\sum \textbf{Volumes of reactants (1 Nm}^3\textbf{ of fuel and the stoichiometric comustive stream Nm}^3\textbf{)}}$$

Example

A 2500 kW heating process installation can be fed with three possible types of fuel:
Fuel type 1: Natural Gas (NG)
Combustive stream: Air (O_2 content: 21%)
EnD parameter: **745 kcal/Nm^3** of combustion product
Heat lost from process with fumes @ 700°C: **535.000 kcal/h**
Fuel type 2: Low LHV gas @ 2.500 kcal/Nm3
Combustive stream: Air (O_2 content: 21%)
EnD parameter: **617 kcal/ Nm^3** of combustion product
Heat lost from process with fumes @ 700°C: **592.000 kcal/h**
Fuel type 3: Low LHV gas @ 1.000 kcal/Nm3
Combustive stream: Air (O_2 content: 21%)
EnD parameter: **450 kcal/ Nm^3** of combustion product
Heat lost from process with fumes @ 700°C: **810.000 kcal/h**

As the fuel calorific power decreases, diluting its composition of "useful" compounds, we can observe:

- Decrease of the EnD parameter (we can forecast for instance decreasing of the flame temperature);
- Increase of the heat lost in fumes (decreasing of the process thermal efficiency);

A solution to partially balance the performance reduction of a combustion system that burns a poor quality fuel (Low LHV), with respect to a traditional combustible, could be the addition of a part of "regular quality fuel" into the fuel stream.
The above mentioned is for instance the solution currently adopted at the plant, where LPG to BFG is added in steel reheating furnaces. Vice versa, a similar effect can be obtained acting on the "concentration" of the useful molecules in the reactants. The decrease of the inert species percentage in the combustive stream, adding pure Oxygen to partially replace the Air-Nitrogen rich, is the other possibility for LHV recovery. This second solution can offer results comparable to the previous case, but normally the cost for Oxygen is far lower than the one for gaseous fuels, as NG or LPG for instance. The following chart should be useful to understand better the concepts previously mentioned (we considered simply the comparison between "regular NG" and "Low LHV @ 2.500 kcal/Nm^3).
Values on the coordinate axis represent the LPG percentage in the LHV feed stream:

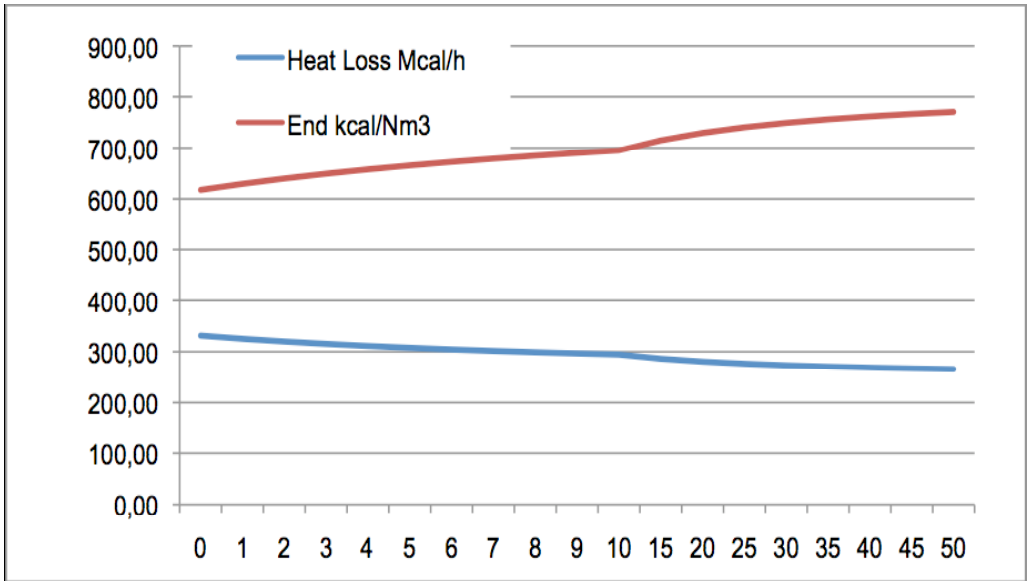

Figure 1-3 Heat Loss [Mcal/h] and EnD [kcal/Nm^3] variations with the LPG [%] content in the LHV fuel. Courtesy of DCHP

In the next graph the coordinate axis values indicate the percentage of pure Oxygen injected into the combustive stream to increase the concentration of "useful molecules":

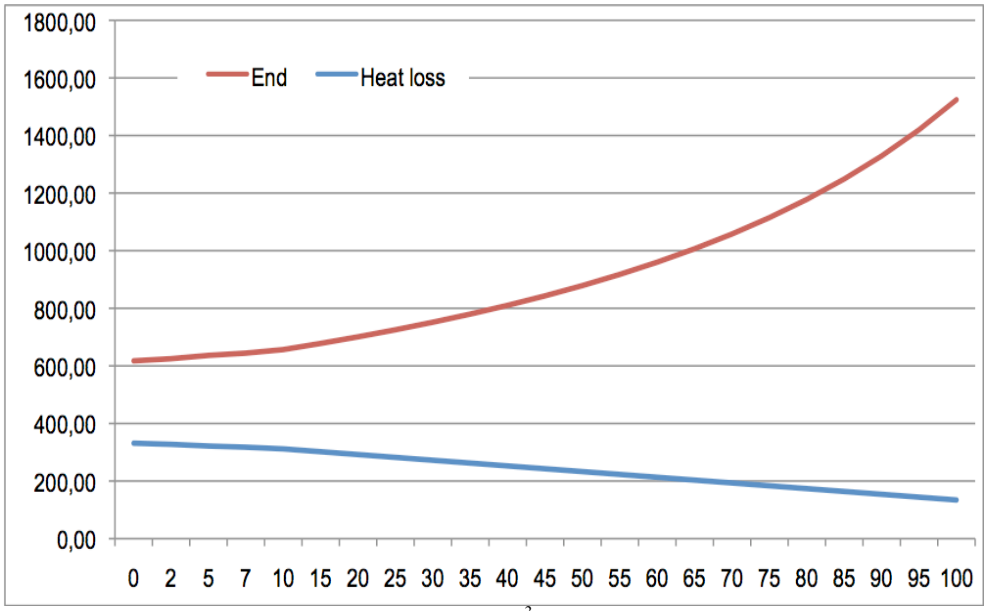

Figure 1-4 Heat Loss [Mcal/h] and EnD [kcal/Nm^3] variations with the pure O_2 [%] content in the LHV combustive stream. Courtesy of DCHP

It is of immediate comprehension that each solution or their combination is useful to improve the performance and quality of a combustion process, where the use of Low

LHV fuel is planned. Moreover, the lower is the value of the LHV of the main fuel to be adopted, the more is needed the implementation of a "corrective" solution.

1.7 The bottlenecks of a "straight conversion" from High LHV to Low LHV fuel

The observation of the current operating conditions of the furnaces, according to the considerations done at the previous section, highlighted the management of the following issues in the accomplishment of the retrofitting project design:

1. The need to maximize the EnD parameter, according the following principles:

    a. In order to minimize operation cost, O_2 has to be preferred to LPG usage;
    b. O_2 availability is limited by the "extra spare capacity" of the on-site plant, while LPG usage has no restriction;
    c. The combustion system has to be designed as a flexible unit, meaning that it can be needed to manage the fuel mixture or air-oxygen mixture in different ways, according to the process phase (initial dry out, furnace preheating, holding phase for temporary stop of production, working phase, working phase in absence of BFG for accidental stop of compression unit…);

2. The respect of the maximum volume capability for furnace, flue ducts and dampers, according to:

    a. Forecasted variation of flue gases flow rate, due to the change of fuel;
    b. Potential variability of the total flow rate in the abovementioned "phases", or flexibility requirements of the system.

In order to meet all previously listed consideration, several simulation of furnace operations have been performed to validate the "oxygen design", to figure some possible results of the retrofitting activities.
Basing on these estimations, DCHP could show a range of forecasted operating conditions, each one having different composition of fuel/combustive mixtures, most of all having different flow rates (assumed at same temperature because the process conditions are not modified).
In order to validate the feasibility of the planning furnace revamping activities it is considered necessary to accomplish of a deeper and fully detailed analysis of the pressure drops along the flue ducts and stack, for the worst case estimated (highest flow rate).

1.8 Galvanizing plant

According to the customer requirement, the pipe galvanizing line has to be converted from gasoline to BFG power source. Starting from the burners and the furnace

chamber, the whole facility is retrofitted to integrate the new equipments with the existing frame.

Figure 1-5 Original burners. Courtesy of DCHP

Figure 1-6 Retrofitted zinc pot and pre-heater exit. Courtesy of DCHP

Figure 1-7 Ejector-stack. Courtesy of DCHP

The longitudinal section of the plant is reported in the next page. The burners chamber is on the left. A refractory wall with distribution holes guarantees almost pure convective heat transfer between hot gas and zinc pot without any direct flame impingement. This solution avoids the excessive thermal stresses of the pot in case of non-uniform irradiation, which could lead to fatigue cracks and wreckages. The ejector-stack is visible on the right. Primary flow consists of air blown from a fan, while sucked flow consists of exhaust gas. Data relative to static pressures, mass flows and temperatures are known for a mean operation condition. The central building is the pipe pre-heater, where heat from fumes is transferred through the metallic roof to the rolling pipes in the top chamber. Square ducts made of refractory bricks connect each mentioned section. Furnace walls are not perfect airtight, hence cold air drawn from external environment dilutes hot exhaust gas, reducing its mean temperature. Required a fixed thermal input at the zinc pot, this implies more fuel consumption. On the over hand in case of positive pressure the fume stream would flow outside from joints, polluting the external environment. Therefore the on design operation condition considers a low negative pressure in the combustion chamber, which allows a slight thermal loss but at the same time preserves workers health. A movable damper, located in the connection duct before the pre-heater, creates a localized pressure drop which mitigates the suction force upstream in the furnace chamber, assuring just a slight air entrance from breaches. In this way thermal losses from cold air heating are minimized, the ejector working point is fixed and the system operation is controlled through a single device.

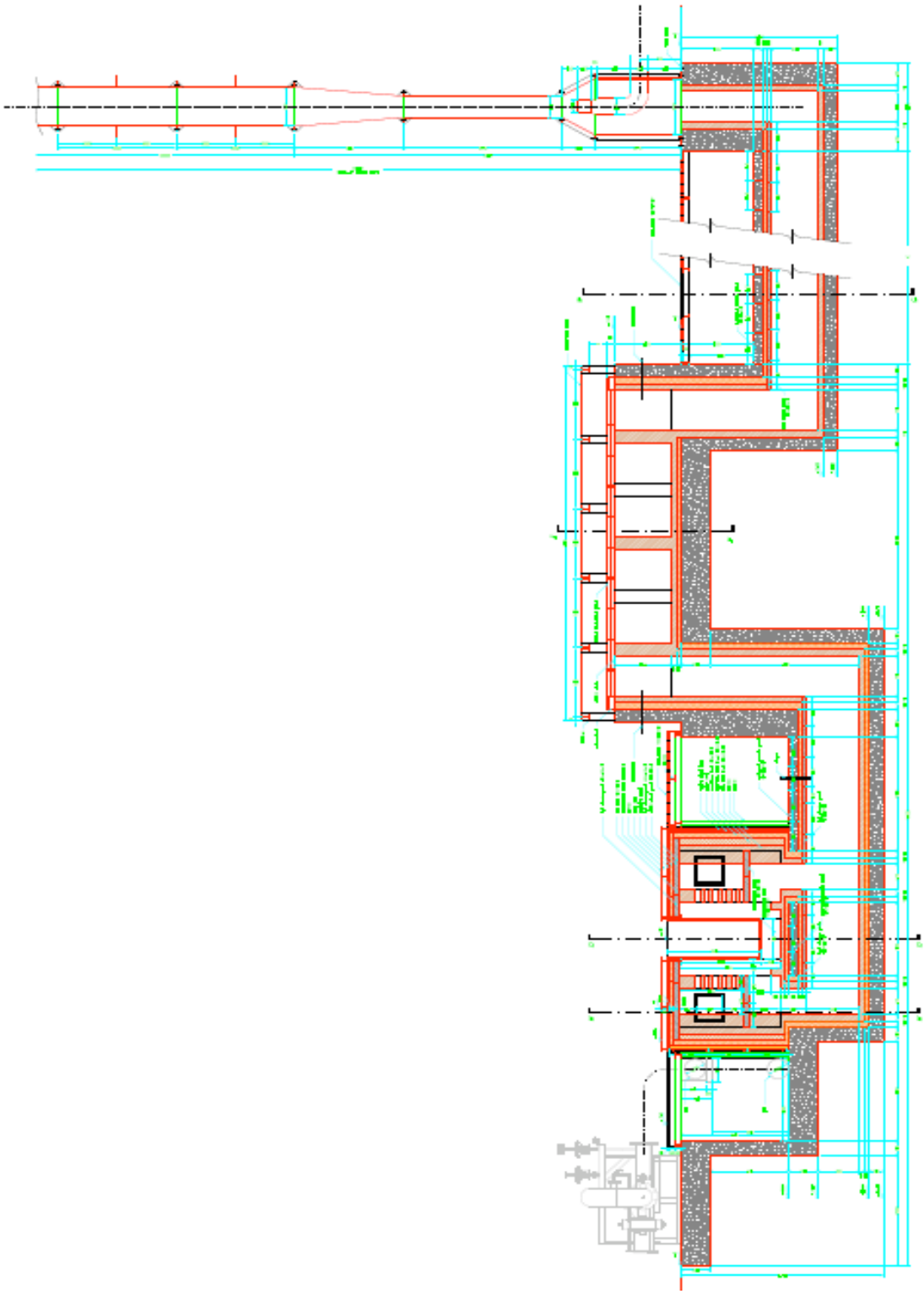

Figure 1-8 Galvanizing plant: longitudinal section

Chapter 2 **Literature Review**

The topics concerning with this plant analysis are mainly two: square sectioned ducts and subsonic ejector.
Hereinafter a review of scientific articles and publications concerned with this devices is proposed. The understanding of characteristics, operation modalities, significant parameters and CFD modelling state-of-art is essential for the purpose of this study.

2.1 Ejectors

Ejectors exploit Venturi-effect to draw fumes from the furnace chamber to stack inlet, overcoming the pressure drops along the ducts.

2.1.1 Working principles

Ejectors generally allow the mixing and/or the recompression of two fluid streams.
They can be classified in three categories, depending on their functions:

- Compressor
- Fluid transport device
- Vacuum pump.

A primary or motive stream, which has the highest total energy, is accelerated through a nozzle, converting part of its pressure energy into kinetic energy. By entrainment-induced effect, due to low pressure, a secondary (or entrained) flow is drawn through the suction chamber into a mixing chamber where mechanical, thermal energy and species transfer occur. The resulting pressure at the end of the mixing chamber will lie between the two inlet streams pressures. In the subsonic diffuser the flow is decelerated and re-compressed. Ejector designs are classified as critical and non-critical. In the first case the fluid velocity in the primary nozzle throat is sonic, in the second case it is subsonic.

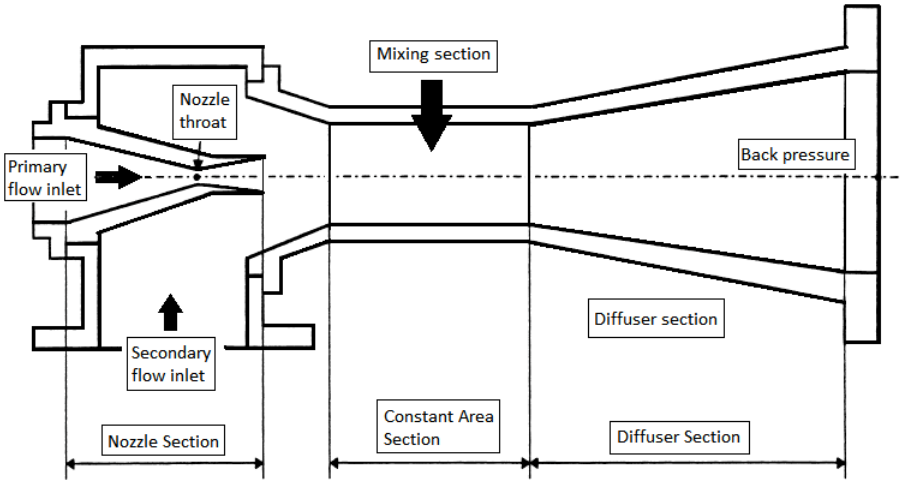

Figure 2-1 Schematic of two phase ejector, modified from [19]

According to fluid phases, ejector can be classified in two ways:

- *One Phase ejector*: streams phases are the same;
- *Two Phases ejector*: streams phases are different [3];

According to nozzle design, ejectors can be classified in two categories:

- *Subsonic* if nozzle is converged;
- *Supersonic* if nozzle is converged-divergent;

According to nozzle exit plane (NXP) position, ejector can be classified in two ways:

- *Constant-Pressure mixing ejector (CPM)* if exit plane is located within the suction chamber, where the mixing of the streams occurs under constant pressure;
- *Constant-Area mixing ejector (CAM)* if exit plane exit is located within constant-area section, where the mixing occurs;

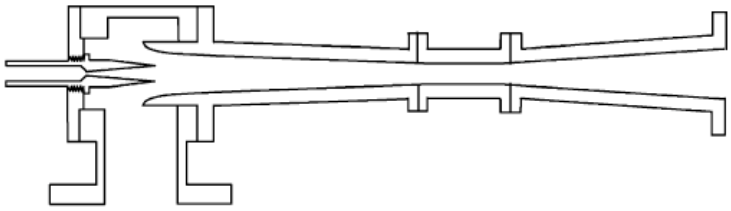

(a) "Constant-Pressure Mixing" Ejector

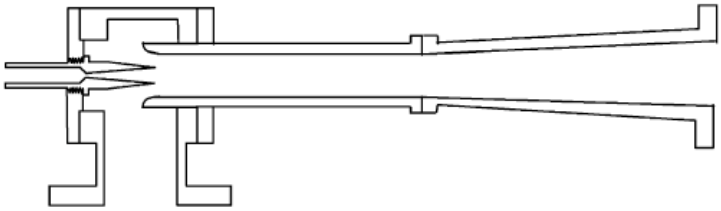

(b) "Constant-Area Mixing" Ejector

Figure 2-2 Schematic view of an ejector: nozzle exit position; taken from [17]

Both this configurations have been tested experimentally over the years. It was found that constant-pressure mixing ejector had a better performance than the constant-area one.

2.1.1.1 Subsonic Ejectors

Primary flow at nozzle exit can be faster or slower than speed sound at certain thermodynamic conditions, depending on nozzle design.
In a subsonic ejector the motive flow in the convergent nozzle can be either subsonic or sonic, depending on pressure ratio critical value:

$$v_{cr} = (p_s / p_p)_{cr} = [2/(\gamma+1)]^{\gamma/(\gamma+1)}$$

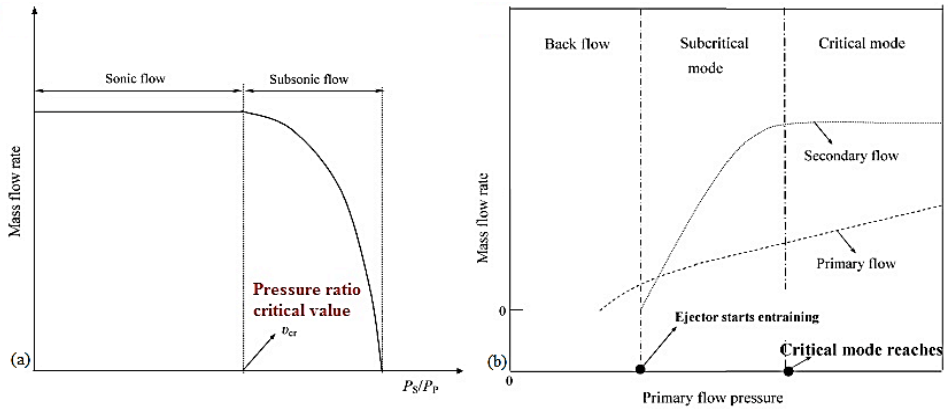

Figure 2-3 Operation modes of subsonic ejector; taken from [10]

Ejector performance can be divided into three operational modes, according to both streams conditions:

I. Back Flow: Flow have reverse motion from exit to the suction chamber, secondary flow does not exist;
II. Subcritical Mode: Secondary mass flow rate depends on primary flow rate and operating conditions: $p_{p,0} < p_{s,0}/v_{cr}$;
III. Critical Mode: primary flow is chocked, while secondary flow rate is nearly costant: $p_{p,0} \geq p_{s,0}/v_{cr}$;

2.1.1.2 Supersonic Ejectors

In supersonic ejectors the primary stream expands and accelerates through the primary nozzle and fans out with supersonic speed, causing low pressure in suction chamber and in the first mixing chamber part.
There are three possible flow regimes that affect this device. In the first, both primary and secondary flows are subsonic. In the second, primary flow is supersonic and the secondary is subsonic. The third possibility is that both streams are supersonic. In the last case, the interactions between motive fluid and ejector walls generate a series of oblique/normal shock waves, called “shock train” or “diamond waves”, which have a great impact on ejector performance [4]. A shear layer between motive and sucked stream develops, due to large velocity difference, and the secondary flow is drawn into mixing chamber.

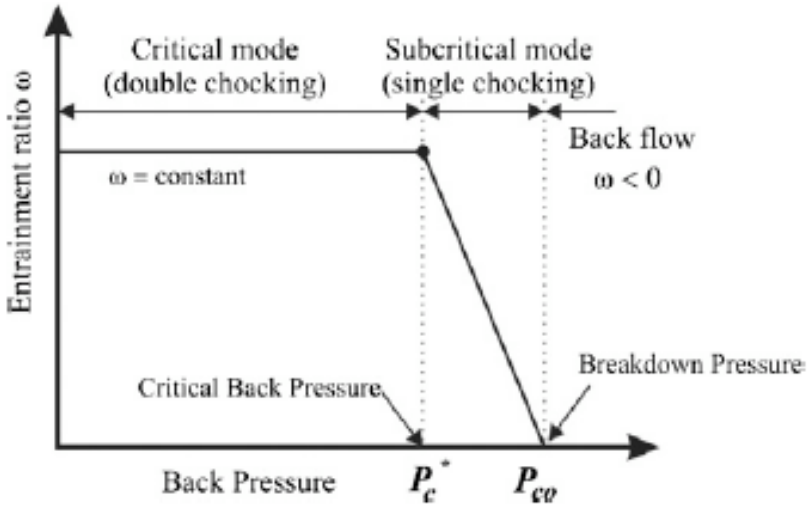

Figure 2-4 Supersonic Ejector operation regimes

In Figure 2-4 the three operational modes, corresponding to flow regime, for are shown. Entrainment ratio, defined as $\lambda = \dot{m}_{\sec} / \dot{m}_{pr}$, is on y axis, the diffuser pressure P_c (or exit pressure) is on x axis. Both this parameters are used to describe ejector's performance, thanks to their sensibility to operating conditions [5].

In the range of exit pressures below the critical value ejector operates in critical mode, where it entrains a fixed amount of secondary fluid, and λ remains constant. Motive flow expands after nozzle exit, introducing a series of oblique shocks that are reflected by walls and fill all the sections in the mixing chamber. Secondary flow is accelerated in the converging duct between wall and primary expanding flow, eventually chocking. Downstream fluid flow encounters a transverse shock, which creates a compression effect. Its position is related to back pressure: decreasing exit pressure it moves toward diffuser, if increased it moves backward to constant area section. This operating condition is also known as "double chocking". Experimental data and flow visualizations have shown that only a small amount of secondary flow is gradually mixed with the primary fluid upstream the effective area.

Most part of the mixing process start when secondary flow chokes, in a mixing chamber section defined "effective area" by Munday and Bagster [6].

If exit pressure is increased higher than critical value, transverse shock in diffuser moves upstream and interferes in the mixing process. Secondary flow is no longer choked, and the entrainment ratio decreases almost linearly [15].

If P_c is increased again, flow will travel in reverse direction and fill secondary chamber. In this condition ejector stop to work.

2.1.2 Supersonic Ejectors Applications

2.1.2.1 Vacuum pump

A typical example of vacuum pump usage can be found in oil refinery plants where ejector systems, made of a number of ejector stages in series with condensers, permit to achieve the severe low pressures required for vacuum distillation.

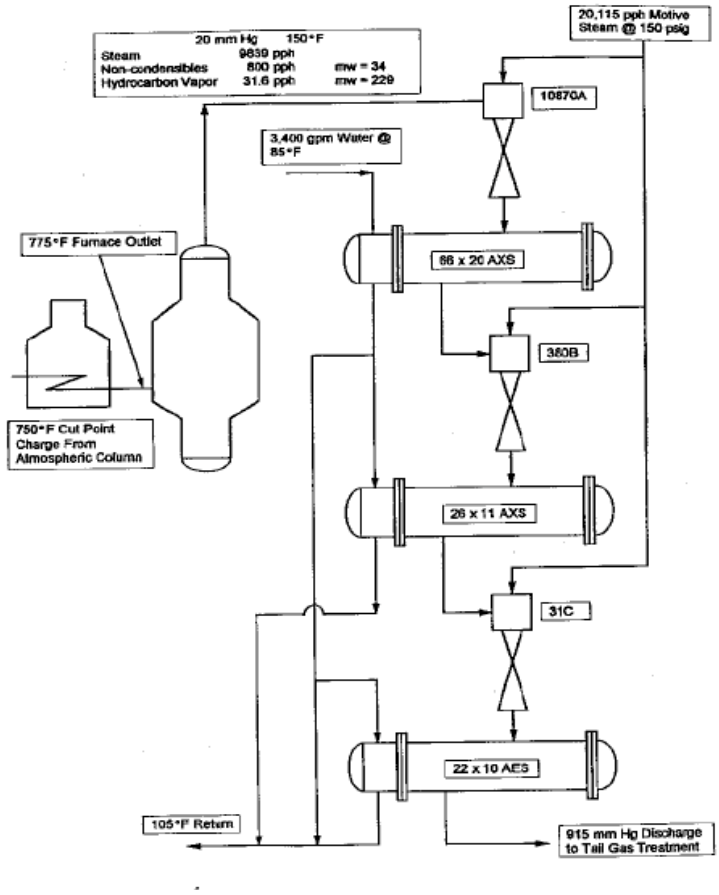

Figure 2-5 Ejectors system for vacuum column in oil refinery

In Figure 2-5 a three-stage condensing ejectors is shown. Intercondensers are used to reduce steam content in the secondary streams, reducing steam partial pressure and the load for the following stage. This configuration is designed to achieve low absolute pressures (from 6.5 to 14 Pa) with minimum operating costs. Combination of non-condensing with multiple stage condensing ejectors give the lowest absolute vacuum level possible with this kind of systems, reaching pressure magnitude of 0.1 Pa.
Single stage steam ejectors, which are the simplest and most economical solution for vacuum purposes, can be also be utilized as recompression boosters, mostly used to

increase efficiency of heaters, dryers or evaporators. Thermocompressors are designed to raise entrained steam to higher pressure and temperature levels.

2.1.2.2 Aerospace area

Since the introduction of jet and rocket propulsion in the last 40's, aerospace engineers have had the necessity to test engines performances at high altitudes conditions but in ground-based facilities. Venturi effect has been used again to obtain low pressure chambers where test propulsion systems:

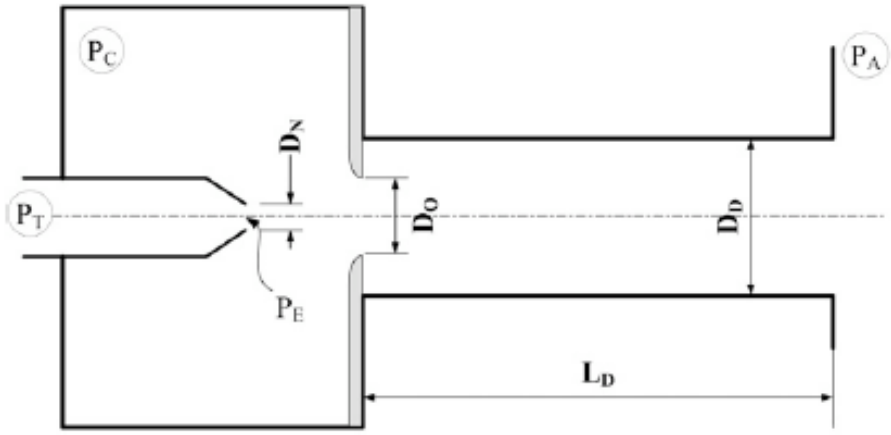

Figure 2-6 High Altitude Testing (HAT) chamber, taken from [7]

In the figure above a High Altitude Testing (HAT) chamber is shown. A jet or rocket engine is located in the cylindrical duct at left side, while exhaust fumes are discharged in the right duct. The momentum of fumes is used to lower pressure in the chamber, creating vacuum at a certain level. This device can work in two different modes: starting diffuser starting and unstarting mode. In the first condition backflow from ambient condition environment is avoided by a complex series of shocks, due to interaction between exhaust plume and chamber walls. In the second condition the shock train do not fill the entire duct section, hence backflow reduces low pressure level.
Matsuo et al. [7] tested the effect of introduction of a simple backflow-reduction device, which reduces exhaust back flow into the test chamber, on global ejector performance.

2.1.2.3 Jet Refrigeration

Since its invention in early '900 by Sir Charles Parsons, ejector was mainly used for refrigeration purpose. During 1930s this device had great success for building conditioning, because of its simplicity and cheapness.

Its development stopped with the diffusion of mechanical compressors and vapour-compression refrigeration systems.
With the increased attention to environmental problems and energy recovery of the last decades, ejectors technology has been rediscovered for refrigeration and conditioning purposes, due to its relative simplicity and low cost, compared to the traditional absorption cooling cycle.
Recent and exhaustive reviews of ejector refrigeration technologies can be found in the works of Chen et al. (2012) [8], Gonzales Bravo et al. (2011) [9] and Aphornratana et al. (2003) [17].
Ejector can couple refrigeration with low-grade waste thermal energy from industrial processes [10, 11, 12] or with renewable energy sources, like solar thermal [13] and geothermal [14], reducing fossil fuels consumption and carbon-dioxide emissions.
Solar cooling is of great interest, since the cooling load can be directly correlated to the intensity of solar radiation. A good review of the several technologies to produce cooling by transformation of solar heat can be found in the works of Sarbu et al. [15], Abdulateef et al.[16], Aphornratana et al. [17] and D.S. Kim [18].

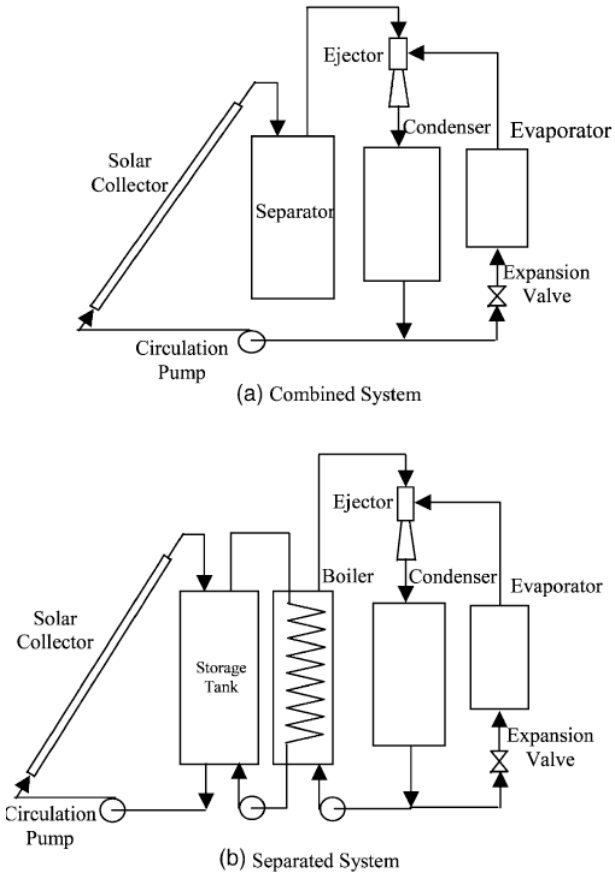

Figure 2-7 Schematic of solar jet refrigeration system. (a) combined system; (b) separated system; taken from [15]

Figure 2-8 shows the two simplest possible plant configurations.
The first, called **single stage ejector refrigeration (a)**, has only one operational fluid. Despite its simplicity, it is difficult to keep it running at optimum state, because the working conditions vary with the solar light intensity. Ejector performance indeed is strictly related to environmental factors such as cooling water temperature, air temperature and solar radiation. Furthermore a single fluid is not desirable, because leaks can cause severe damages.
The second solution, called **multi-stage ejector refrigeration (b),** consists of two sub-systems: a solar system and a refrigeration system. In the first part water with anti-corrosion addictives collects and stores heat in a storage tank. Through an intermediate cycle heat is transferred to the boiler of the refrigeration cycle, where ejector assures the driving force for the recirculation. This solution has more advantages: boiler and evaporator pressures can be better controlled, in order to keep ejector performance around optimum values, and the system is more stable to climate variations, thanks to a heat storage tank. Several refrigerants commonly used in mechanical vapour compression cycles can improve the performance of the cycle, as investigated by Da-Wen Sun [19].
The main disadvantage is still a moderate global efficiency of this technology: COP lie in a range between 0.1 and 0.6, depending mainly on operating temperatures, working fluids and ejector geometry [16,20].

2.1.2.4 MCFC and SOFC power plants

Supersonic ejectors are used for gas streams recirculation in High Temperature Fuel Cells (HTFC): SOFC [21,22,23,24] and MCFC [25,26]. Thanks to the absence of valves, rotor or moving parts, lubrication necessity and their robustness, they guarantee long life operation at high temperatures, and they are safer than traditional blowers.

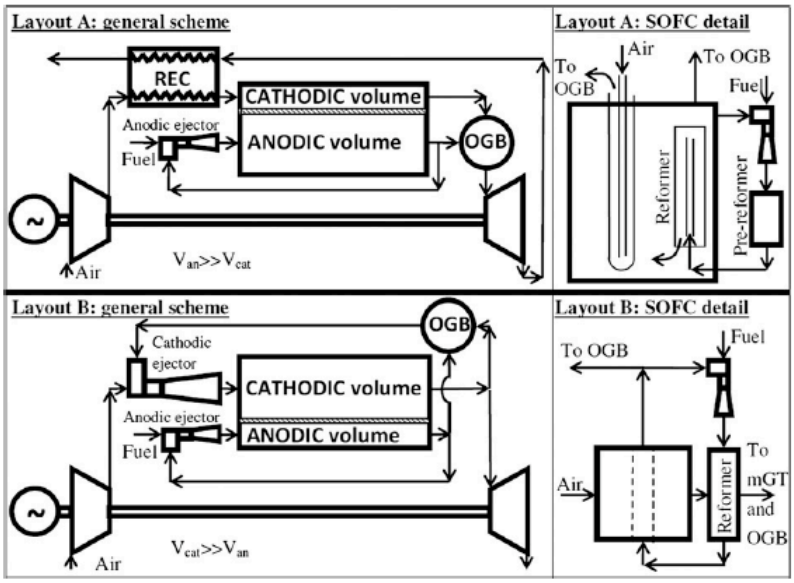

Figure 2-8 Layout of anode and catode recirculation in SOFC [27]

In Figure 2-9 is shown the hybrid technology solution, where a SOFC is coupled with a conventional gas turbine. In layout A the ejector is used for **anodic recirculation** [28]: fuel is the high pressure flow, while anodic-carbon dioxide rich-exhaust is the low pressure entrained flow. The mixed flow is sent into the reformer.
According to Marsano [21], anodic recirculation has several important functions:

I. Guarantee a part of the necessary heat for reforming reaction;
II. Maintain the right steam to carbon ratio (STCR), to avoid the deposition of solid carbon and anode poisoning;
III. Raise the mixed stream to the cell operating pressure required;

In layout B ejector is used both **anodic and cathodic recirculation**. This solution avoid the need of the expensive heat exchanger for burner exhaust heat recovery.

2.1.3 Subsonic Ejector

Converging ejector has limited use to PEMFC [29].

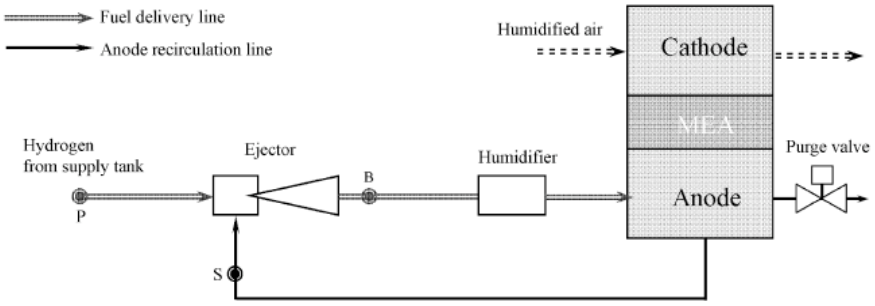

Figure 2-9 PEMFC studied in [30]

Hydrogen, stored at high pressure, acts as primary stream to entrain tail gas from anode and to raise it up to the mixture pressure level required by the cell [30]. Fuel recirculation improves the fuel usage efficiency, at the same time it regulates the water content in the stream. Liquid water, indeed, represents a serious problem in a fuel cell stack [31]. Since it is more viscous than vapour, its non-uniform existence in a fuel cell stack leads to non-uniform gas distribution. This problem is self-defeating, that means once condensation occurs, less gas is fed to the cell, then less water is removed and the problem escalates. This reason leads to the adoption of a convergent instead of a convergent-divergent nozzle.
This type of ejector was analyzed in the work of Zhu [30]. A hybrid fuel delivery configuration with two supply and two recirculation lines is of practical interest [32, 33].

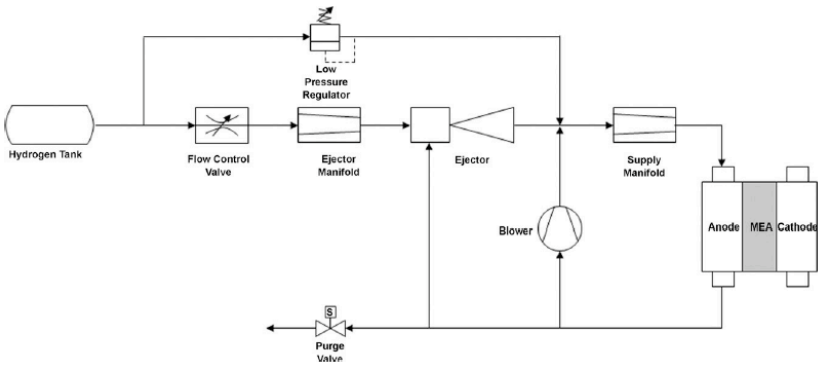

Figure 2-10 Hybrid fuel delivery system

2.1.4 Supersonic ejectors: Thermodynamic Modelling

Since the birth of the first steam jet refrigeration systems, it was necessary to develop models for supersonic ejector's performance prediction. Keenan and Neumann [34] were the first who established a one-dimensional model with continuity, momentum and energy conservation, considering constant area mixing chambers and excluding the diffuser section. In their following work they introduced two feasible hypothesis to obtain a reasonable solution for the momentum conservation equation during the

mixing process [35]. The first **was constant pressure** mixing model, where null pressure gradient along mixing section was considered, while the second assumed **constant area**. These two models relied on one-dimensional approach, based on isentropic relations and some gas dynamic equations and steady state conditions.
Munday and Bagster [6] later supposed that the mixing process between two fluids only occurred after certain mixing length, in a section where the secondary flow chocked, introducing in the constant pressure model the "effective area" concept. This model did not consider friction or heat loss.
In the work of Eames et al. [36] irreversibilities associated with primary nozzle, mixing chamber and diffuser, and friction losses through isentropic efficiencies were included, while normal shock wave was taken to occur at the end of mixing chamber.
In the last years several progresses have been made in the ejector thermodynamic modelling, with the aim to predict better its performance. A Quasi-1-D mathematical model, where ejector flow is one-dimensional with variable section area, was developed in the work of Cheng et al. [37]. An experimental jet refrigeration prototype was built up in order to investigate the effect of stream inlet temperatures, geometry parameters and back pressure on cycle performance. Mathematical model prediction capacity was then tested in order to verify ground-hypothesis validity.

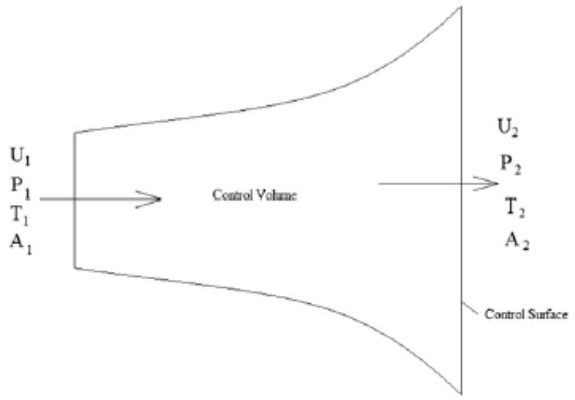

Figure 2-11 Mixing chamber control volume [37]

A lot of 1-D thermodynamic models to evaluate ejectors performance for refrigeration cycles can be found in literature [38, 39, 40], where different hypothesis about fluid behaviour, geometry and device operating conditions lead to results that are compared to experimental data, in order to verify prediction ability.
The work of Wang et al. [41] is an interesting review of mathematical modelling applied to supersonic ejectors for refrigeration purpose. Models are categorized into three groups: thermodynamic, empirical/semi-empirical and dynamic. Differing from the first, which provides a general description of flow behaviour, the last is aimed to represent correctly the local physics along the device. This leads to better shock phenomenon and its generation mechanism, interactions between fluid and boundary walls and recompression understanding, giving better ejector hydrodynamics' knowledge.

2.1.5 Supersonic ejectors: CFD studies

Computational fluid dynamics is the reasonable-cost way to implement dynamic modelling. Nowadays CFD has become a comfortable tool for performance prediction and devices design improvement, being less time and money-expensive than experimental approach. However, relying fluid dynamics on turbulence models, which contain constants and modelled terms built up on several specific cases, it is necessary to verify all results with real data from laboratory tests.
A lot of validation works have been performed in the last decade [42, 43, 44, 45, 46, 47, 48].
In the work of Aphornratana et al. [43] CFD is used as a tool to validate results with experimental values, and to predict performance of a steam ejector used in refrigeration applications.

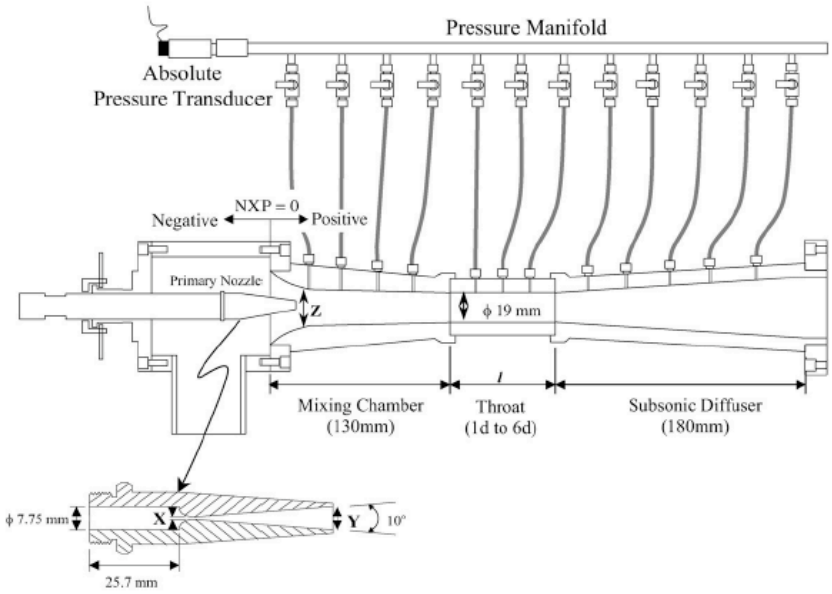

Figure 2-12 Schematic of experimental ejector [43]

The experimental ejector is shown in Figure 2-12. To investigate the effect of geometry on device performance, three different mixing chambers with different inlet diameters, three different throat-diameter nozzles with the same area ratio and 4 different throat-length parts were changed during test. Along the wall static pressure was measured through pipes linked to a pressure manifold. A 2-D structured grid made of 43000 quadrilateral elements was created for simulation. Water vapour was treated as compressible ideal gas, pressure boundary conditions were set at inlets and outlet.
Realizable k-ε turbulence model revealed an efficient tool to predict the entrainment ratio and the critical back pressure, although at some points values were quite different from experimental data. This could be due to the turbulence model, which don't represent perfectly fluid flow phenomena that govern ejectors, and to the ideal gas hypothesis.

In the work of Sharifi et al. [44] a thermal vapour compressor for desalination system was studied. Ejector performance experimental measurements were recorded from a real industrial desalination unit, and were compared to CFD results to investigate agreement with results. A 2-D axisymmetric and a 3-D numerical models were undertaken to see which better represents internal flow pattern, the governing partial differential equations were implicitly solved using the transient density-based method, vapour was considered as ideal gas. Authors knew that this last assumption might produce some deviations from experimental values. Again Realizable k-ε model was selected as turbulent model to predict flow properties in the axisymmetric co-flowing streams. Comparison of velocity field, Mach number, temperature and pressure distributions along the axis centreline showed a slight difference between 2-D and 3-D models, so an axisymmetric domain could be used to study flow pattern inside the device. This last approach results were in a reasonable agreement with the real operating performance curve, confirming CFD as a powerful instrument to predict ejectors performance.
Bartosiewicz et al. [46] tried to understand the CFD ability in the reproduction of axial pressure oscillations in a supersonic ejector. The experimental installation had a capillary tube located on ejector axis as static pressure probe. Air was used as working fluid, and a 2-D axisymmetric grid was generated for computational simulation. Standard wall functions were used as near wall region treatment. The first investigation focused on pressure field and reflection phenomenon in the case of null secondary flow, in order to verify the agreement level between CFD and experimental data. Results plot showed poor prediction capacity of all turbulence models (RSM, k-ω and k-ε), especially in the region just of the nozzle, where there is even a phase opposition with experimental data for the shock reflections.

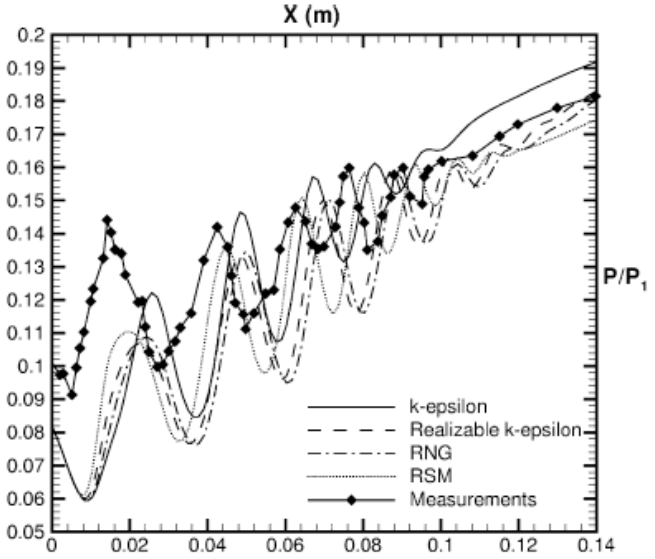

Figure 2-13Normalized axial pressure values for different models

The probe insertion in the numerical model changed flow topology, making shock reflections become annular. Numerical results had better agreement in this case, showing a similar reflection trend but still different values. RNG k-ε and SST k-ω were better suited to predict shock phase and pressure recovery.
The second investigation aimed to compare non-mixing length and secondary inlet pressure for a fixed mass flow rate in the device. In the laboratory experiment laser tomography helped to visualize flow behaviour in the mixing duct, while a scalar user defined function acted as numerical tracer in numerical field. A good prediction of results was achieved with RSM and k-omega SST, although this last gave better prediction of the characteristic length. In the second part of his work the authors applied the former models to study the flow field at different ejector operating condition, trying to identify the causes of a poor performance.
In a more recent validation work Bartosiewicz et al. [49] compared classical k-ε model to the k-ω SST, which is supposed to contain a more detailed physical description of the turbulence, in the ejector entrainment ratio prediction. Starting from on-design condition, where entrainment ratio is constant, he demonstrated that discrepancies between the two models depended on the primary pressure value. In this region similar predictions were obtained. In the off-design condition, the motive pressure reduction lead to significant results difference, and SST over-predicted entrainment ratio. Standard k-ε generally showed good agreement with experimental data for both on-design and critical point. Furthermore the authors noticed that even though the predicted entrainment rate could be in agreement with real data, the prediction of local flow feature such as Mach number and velocity field varied a lot with the chosen turbulence model.

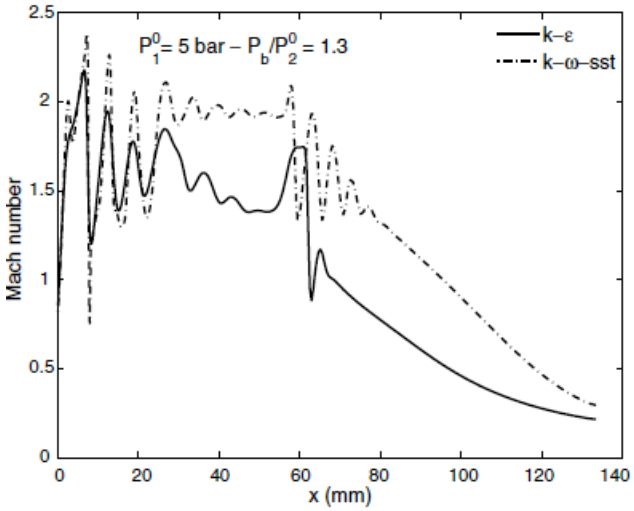

Figure 2-14 Centerline Mach number for the same Entrainment Rate

In the second part of the work [50] the authors investigated the relationship between ejector global operation prediction and local flow pattern, since global measurements are not enough to assess a given turbulence model.
The idea was to check whether models were in agreement with the location of the critical cross section, where secondary flow chocked, for different back-pressure values. In Figure 2-15, case A represents Mach number field at critical point condition. Sonic lines are far from wall boundaries at critical point for both model (SST and k-ε); this means single chocked flow and the highest entrainment ratio. Decreasing discharger pressure, chocking condition location varies a lot with turbulence model: if k-ε gives a certain sonic line, SST even predicts a double critical section. Mach number plot varies with primary pressure, showing the complexity of fluid phenomena inside the mixing chamber.

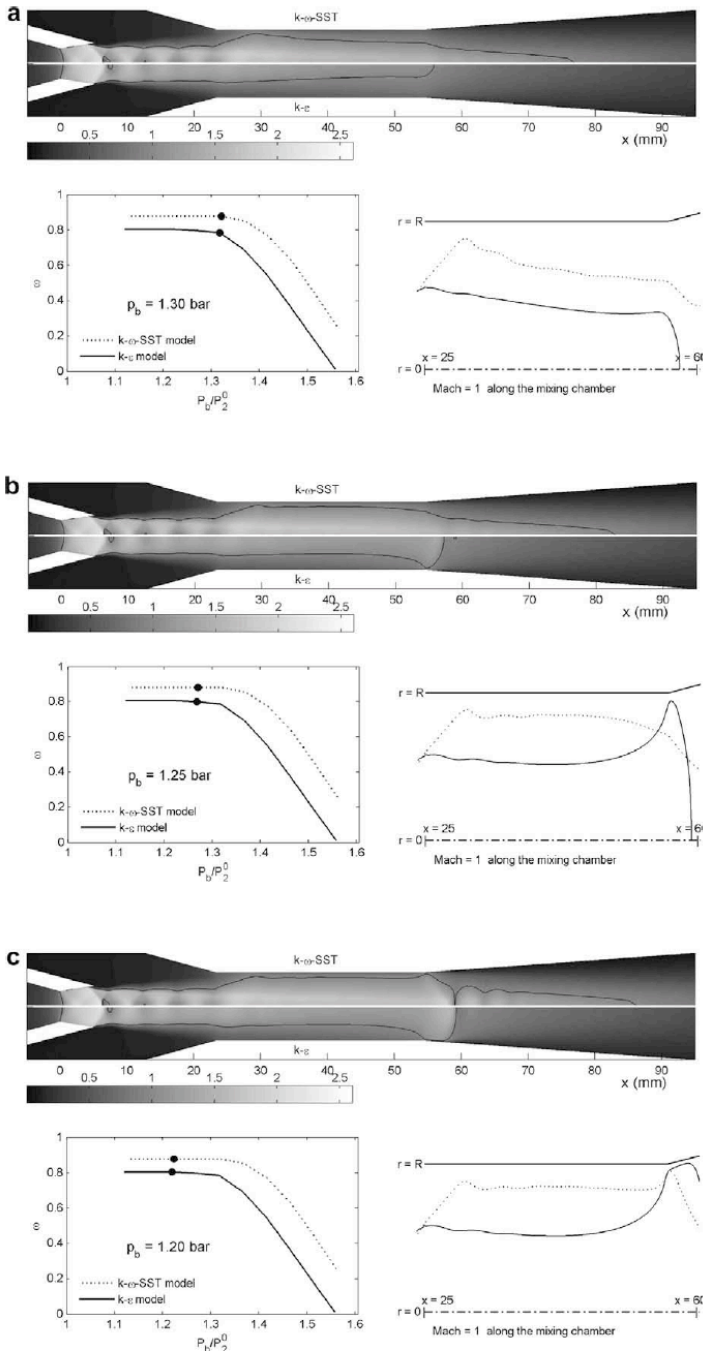

Figure 2-15 Mach number field, sonic line location in the mixing chamber for fixed motive pressure

Results confirmed that performance validation based on the entrainment rate do not imply correct flow field assessment.

Once results are validated, CFD can be employed to investigate flow phenomena when operating conditions and geometry are varied with respect to the original. This is the issue of the second part of Aphornratana et al. [51] work, where the effect of operating conditions and ejector geometry variations on the Mach field and the static pressure pattern were analyzed, focusing on the movement of normal shock along the mixing duct. The effect of downstream pressure on shocking position is shown in the next figure:

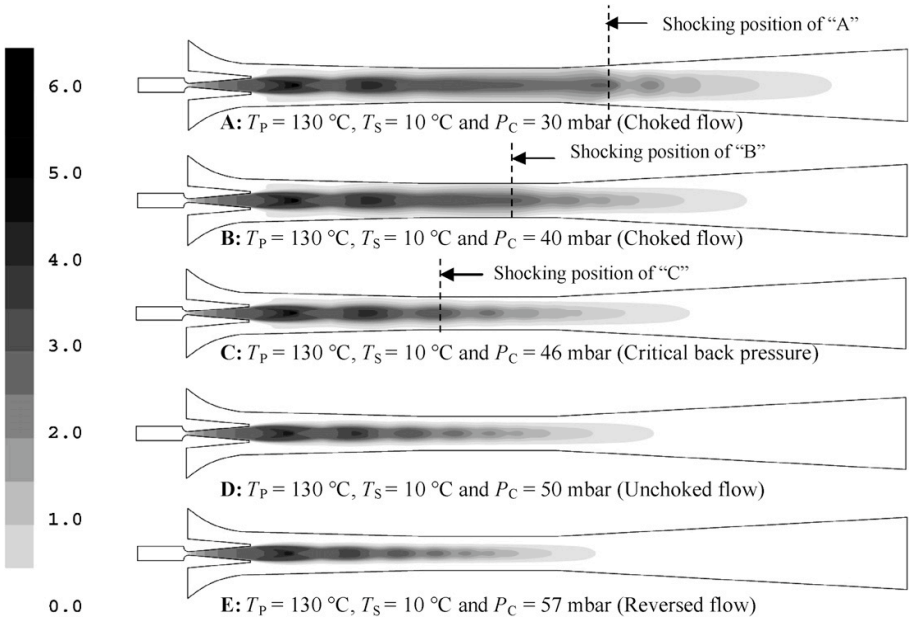

Figure 2-16 Effect of downstream on Mach number contours

This image helps to understand why entrainment ratio drops with back-pressure increase and what is the effect on the mixing process. Similar plots were obtained varying fluid inlet temperatures and geometries of primary nozzle, mixing chamber and ejector's throat section and length, leading to the following conclusions:

- Two series of oblique shocks are present: the first immediately after primary nozzle exit, the second at the beginning of the diffuser, while Keenan theory predicted a single normal shock;
- The effective area where entrained and motive fluid start mixing exists, but is quite difficult to locate the exact position in the mixing chamber;
- A longer constant area section brings to a better mixing process between streams. The induced oblique shocks at diffuser inlet move toward the exit and become more flattened, since less pressure recovery is required.

As seen in the last paper, shock waves characteristics directly affect the ejector performance. Several optical techniques like laser tomography [52,53] and tracers have been exploited to visualize shock structures and mixing process. Zhu and Jiang [54] employed a Schlieren flow visualization technique, using nitrogen as operating fluid, in the investigation of shock wave structures effect on global performance. The obtained pictures, based on diffraction methods, reflect the flow density gradient along the mixing chamber and permit to see clearly shock wave and diamond wave structures, which are typical of the expanding primary flow. Primary and secondary pressures were gradually varied during the experience, with ambient discharger pressure. Fixing slightly decreasing the primary pressure while enhancing the secondary one, it was shown that shock train waves didn't reach mixing chamber walls in the sub-critical mode. In critical mode, on the other hand, shock expansion waves were strong enough to separate the boundary layer and were reflected by walls, obstructing chamber sections. It was discovered that the first shock wavelength decreased with the increasing secondary flow pressure. Since mixing process is related to shock wavelength, shorter one means better mixing and more uniform stream, enhancing the entrainment rate. Four turbulence models were tested on a half part of 3-D domain; working fluid was considered as a compressible ideal gas. It was found that RNG k-ε model gave the most accurate results in terms of first shock wavelength, shocks pattern and mass flow rate through the device.

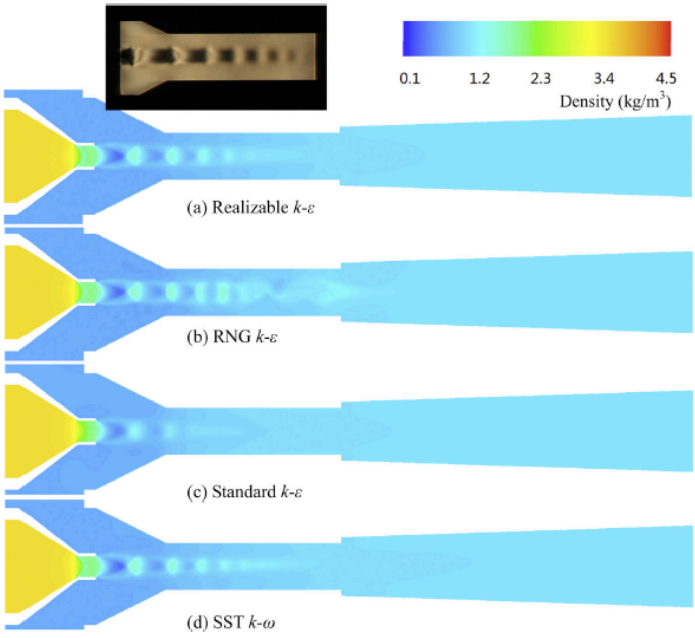

Figure 2-17 CFD-obtained shock train compared to visualization; primary and secondary pressures are fixed [22]

Particle Image Velocimetry (PIV), a non-intrusive laser optical technique, was adopted in the work of Karwachi et al. [55] to obtain velocity field in an air-air fed ejector.

This method can provide more quantitative information about flow field than the Schlieren technique. Mach number distribution was compared to numerical results of 6 different models: k-ε (Realizable, Standard and RNG), k-ω (Standard and SST) and Reynolds Stress Model. It was noticed that differences between static pressure and velocity fields for 3-D and 2-D geometries were negligible, so the latter could be used for further investigations. The best consistency between numerical results and laser visualizations was obtained for the k-ε standard model.

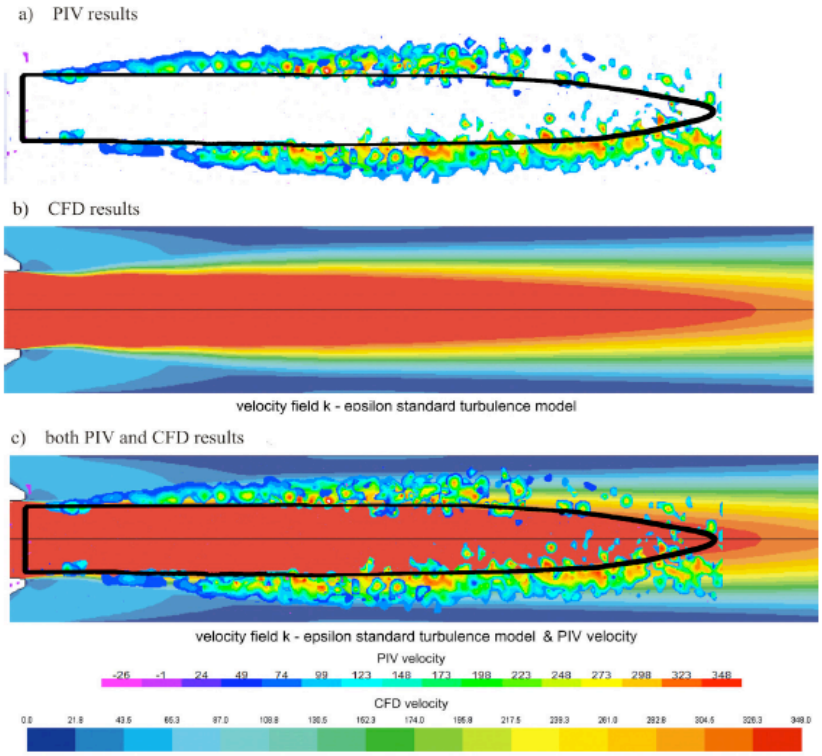

Figure 2-18 Velocity distribution in the mixing chamber: PIV result vs CFD

The abovementioned works generally considered CFD a quite reliable tool to obtain general results with enough accuracy. Other authors pointed out the inaccuracy of predictions due to lack of specific case models in the numerical code.
Sobieski [56] operated a comparison between Standard k-ε model and experimental data obtained on the guidelines of theoretical works. Particularly he investigated the relationship between the pressure loss coefficient and the relative total pressure drop in the diffuser, and the primary stream Mach number. The author stated that the discrepancies in the numerical results were due to:

- Lack of dissipative phenomena typical of ejector included in turbulence model;

- Absence of unsteady phenomena at nozzle exit, like irregular bifurcations or stable Hopf bifurcations;
- Absence of swirls in the boundary area between primary and secondary stream;

The general difficulty in ejector design is the lack of reliable models for the ejectors.
Long et al. [57] evaluated the effects of different nozzle structures on the performance of a steam ejector through numerical technique. Previously the validation process with the experience of Sriveerakul et al. [43] indicated Realizable k-ε as the model with the best agreement. Then it was used to analyze in detail the flow field during the mixing process. A streamwise and a spanwise vortex were defined in order to clarify the energy distribution process and mechanical dissipation along the device. It was discovered that the first kind of vortex structures contributed to the deformation and the rupture of the second structures; this last are broken down with increasing downstream distance until the flow field get well mixed. Each nozzle generates an initial pattern of vortices of different kind, consequently the result of mixing and the entrainment rate depend on geometry. The cross-shaped nozzle indeed can be considered as an extraordinary way of generating strong streamwise vortices, interacting with spanwise vortices they enhance mixing process between co-flowing streams.
In the paper of Aidoun et al. [58] CFD was applied to a R-142b fed ejector to investigated differences with 1-D thermodynamic model predictions. The entrainment ratio was analyzed for different back-pressures with the same model. It was found out that numerical tool was able to predict separation reverse flow condition where 1-D model expected correct operation. This was mainly due to mixing layer separation phenomenon, which caused energy loss in the stream and an adverse pressure gradient at secondary inlet. Prediction performance of the three turbulence models, Standard k-ε, RNG and SST k-ω, increased with back-pressure decrease, moving to on design condition.
Allouche et al. [59] investigated numerically the influence of primary pressure and back-pressure on ejector operation mode through Mach number and velocity field visualization, before confirming results with an experimental solar-driven jet refrigeration system. In a lot of other works CFD was used to investigate flow field details [60, 61, 62, 63, 64], always being supported by experimental data to validate results.

2.1.6 Subsonic ejectors: CFD studies

As shown in the previous section, the biggest amount of the research efforts was concentrated on supersonic ejectors, because of their utility in the industrial environment. Subsonic ejectors have fewer applications, for example in multiple-fluid-mixer devices for agricultural purposes, but the total absence of scientific articles regarding this topic show the general lack of interest toward this type of devices.
To the author's knowledge, the thesis of Besagni [65] is the only thermodynamic-CFD integrated analysis about subsonic ejectors available in literature. The author performed a CFD validation of several turbulence models using experimental data, found in literature, as benchmark. Hence, he developed an approach that integrates both numerical fluid flow investigation and thermodynamic 1-D through efficiency

functions, which account of flow field effects on ejector efficiency. A 2D symmetric half-domain was employed for calculations, air was assumed as compressible ideal-gas working fluid.

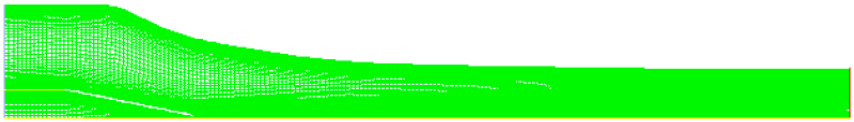

Figure 2-19 Mesh used for calculations in [65]

Temperature, primary and secondary mass flow rates and the outlet total pressure variations on velocity and thermal field distribution were investigated for several turbulence models.
The comparison between experimental data and CFD results showed k-ω SST as the most indicated turbulence model to investigate ejector's fluid flow characteristics and global performance for both subsonic and supersonic cases.

2.1.7 Present analysis

As explained in previous section, the only dissertation found in literature about subsonic ejector refers to a 2D domain, while much more comparisons for 3D domains are available, although the ejectors in question are supersonic. In almost all the cases it was demonstrated that k-ε and k-ω give the best prediction of global performance indicators, even though they lack of accuracy in the flow field representation. Hence these models will be employed in the present investigation.

2.2 Rectangular Ducts

2.2.1 Experimental and CFD approach

Rectangular and square-sectioned ducts are frequently used in a wide range of industrial applications. Examples of such are gas turbine cooling systems, exhaust installations, gaseous fuel supplies, air conditioning pipes, heat exchangers, nuclear reactors.
The study of fluid flow dynamics in such ducts has consequently been an important topic. Transverse motion and three-dimensional effects can be found even in fully developed streams. Two kind of Prandtl's secondary motions can occur: the first, which is pressure driven, is typical of curved passages, where centrifugal forces deviate flow from the streamwise direction. It will be discussed in the next section. The secondary motion of second kind is turbulence-driven, and results from Reynolds stresses anisotropy, in the presence of wall boundary. This phenomenon is visible in corners region of non-circular section ducts.

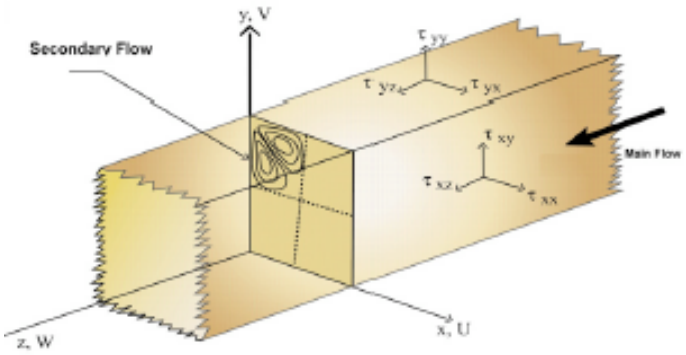

Figure 2-20 Secondary flow in fully developed turbulent stream [66]

Thanks to secondary motion, fluid transportation occurs from the central part of the section to the corners, then from the corner to the adjacent wall and finally back to the central line of the section, almost parallel to the angle bisector; in a square section 8 vortexes - 2 contra-rotating for each corner- are generated. This mechanism improves heat and mass exchange with the axial flow, which is distorted, and the volumetric flow rate diminishes.

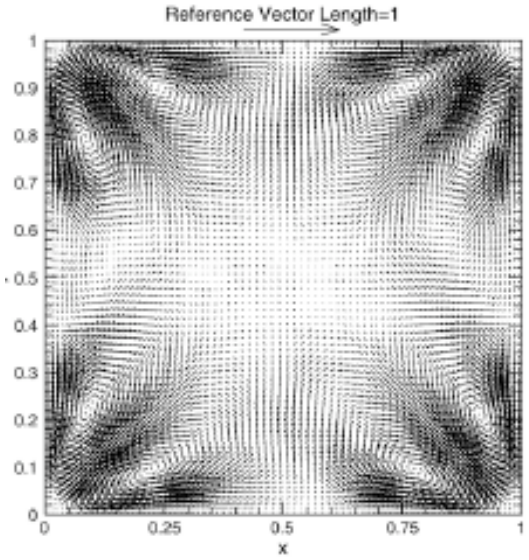

Figure 2-21 Secondary flow in a square duct [67]

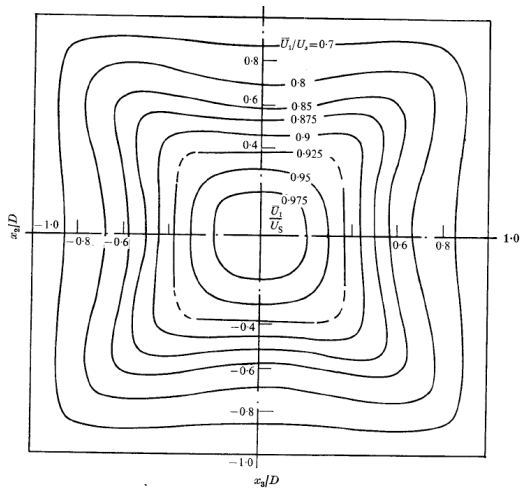

Figure 2-22: Axial velocity contour for fully developed turbulent flow [74]

Secondary flow magnitude varies in the range 1-5% of the bulk mean velocity, depending on Reynolds number, in straight ducts with non-circular section, and has relevant effect both on wall shear stress and heat transfer. The velocity distribution of secondary motion has different pattern, depending on the geometric form of section, and causes a variation of the axial velocity, as shown in Figure 3-3.

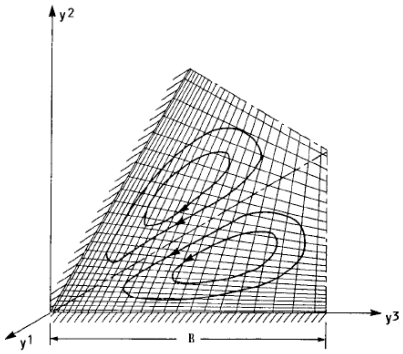

Figure 2-23 Flow configuration for equilateral triangular duct [72]

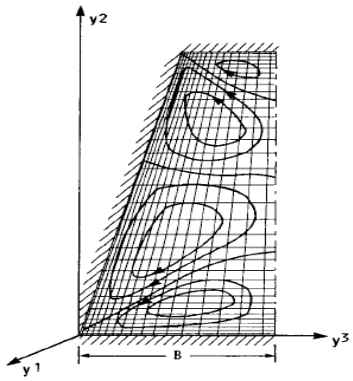

Figure 2-24 Flow configuration trapezoidal duct [72]

Starting from Nikuradse [68], who presented a qualitative description of turbulence driven secondary motions using flow visualization techniques, experimental and numerical studies have been conducted on flows in non-circular ducts [69, 70, 71, 72, 73].
Melling and Whitelaw [74] took measurements of axial, secondary velocity components and turbulence intensity in developing and fully developed regions of a straight rectangular duct, by the use of a laser-Doppler anemomether. Once obtained velocity, turbulence and Reynolds stress contours for several sections, they compare results to previous experiences found in literature.
In the work of Nakayama [71] the algebraic stress model developed by Launder and Ying for the secondary flow of the second kind was employed to investigate fully developed turbulent flow in different shape-section ducts.
In the article of Demuren [72] two different simplified forms of the Reynolds stresses transport equations found in literature were tested to predict fluid flow properties, among them turbulent stresses, in ducts of complex cross sections. Results were then compared with experimental data. It was discovered that Naot and Rodi, simpler version Demuren and Rodi, performed better quantitative agreement with measured secondary flow data, while the latter unpredicted secondary flow magnitude.

Hirota et al. [75] conducted an experimental study on the response of turbulent flow in a rectangular duct to a variation of wall roughness on its short sides. The distributions of primary and secondary velocities, turbulence intensity and turbulent shear stresses have been measured in seven stations located after the boundary change; they were compared to the data recorded in the smooth part upstream and in a section downstream, where fully developed condition occurred.
Since secondary motions are due to Reynolds stress anisotropy, the choice of the adequate turbulent model in numerical simulations is crucial to obtain correct results. k-ε and k-ω closure models rely on the Boussinesq hypothesis, which states a linear relationship between Reynolds stress and mean strain rate tensors. Reynolds stress isotropy is then assumed, that means the normal components of Reyolds tensor are equal. These models are not able to predict secondary flow, generated by anisotropy. By the way, they are able to give qualitative indications about mean flow field, are relatively simple and, the most important quality, they require much less computational resources than Reynolds Stress Model, which is based on 6 partial differential transport equations, one for each term of stress tensor. Anyway, isotropic models were modified in order to take account of rotational fluids and stream reattachment [76,77].
Many authors focused on non-linear eddy viscosity models, where the linear relationship between turbulent stresses and mean strain is replaced with a non-linear function, dependent on mean strain vorticity fields or other turbulent variables. Nisizima [78] applied the formerly proposed anisotropic k-ε model to a fully developed turbulent flow in a square-duct. Comparison of velocity components, turbulent kinetic energy and turbulent stresses show generally quite good agreement with both experimental data and other investigations using second order models, although results were influenced by the use of damping functions for wall treatment. The author stated that further improvements had to be added to the model, in order to overcome the still rather limited capacity in the handling of turbulence.

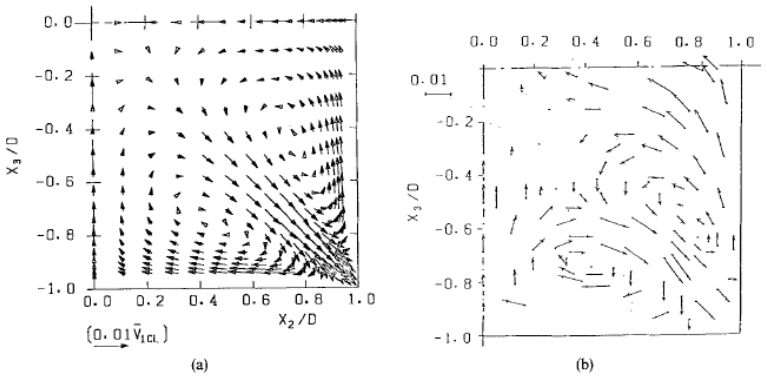

Figure 2-25 Comparison of secondary velocity field for similar Re: a) non-linear k-eps; b) Melling and Whitelaw experience [78]

Speziale [79] formulated a nonlinear k-ε model capable of predicting accurately the normal Reynolds stresses in turbulent channel more accuarately than the linear model.

Furthermore, he showed his model was able to predict turbulent secondary flow in square ducts and generally in noncircular ducts.
Rubinstein and Barton [80] generated a nonlinear eddy viscosity through a renormalization process applied to the equation for the generic turbulent stress component. This led to a model where Reynolds stresses are quadratic functions of the mean velocity gradient and is valid both for high and low Reynolds number, without any need of damping wall functions. A lot of other nonlinear formulations adapted to investigate specific problems can be found in literature [81, 82, 83, 84, 85]. A good review of this model can be found in the work of Gatski and Jongen [86].
Reynolds Stress Model (RSM) remains the most complete tool among RANS (Reynolds Averaged Navier-Stokes) to investigate turbulent stress distributions for every problem, since it solves one transport equation for each tensor component. The main disadvantages are the high computational cost to obtain solution and the stability of the numerical method during the iterative process. The algebraic formulation of this method tries to reduce the computational request simplifying some terms in the transport equations. In a thesis work [87] an explicit algebraic Reynolds stress model, where turbulent stresses are explicitly related to the mean flow field, was implemented.
A comparison between nonlinear two-equations method and RSM is found in several articles. In Rivas et al. paper [66] both models were used to investigate motion and convection problem in a square duct with walls at different temperature. Coefficient of friction and Nusselt number were found for different Reynolds number, and related to experimental data. Both quantity distributions agreed well with correlations in literature and laboratory test results.
Rivas et al. [88] presented the results of a numerical investigation of fully developed turbulent flow in a square duct by RSM model, included in Fluent package, and two versions of a non linear eddy viscosity model (NLEVM), named respectively High and Low Reynolds, both compiled in Fortran language. These last differ in the distinct form of the damping functions in the transport equation for the turbulent dissipation rate ε. Melling and Whitelaw work was used as benchmark. The following images show results qualitative comparison:

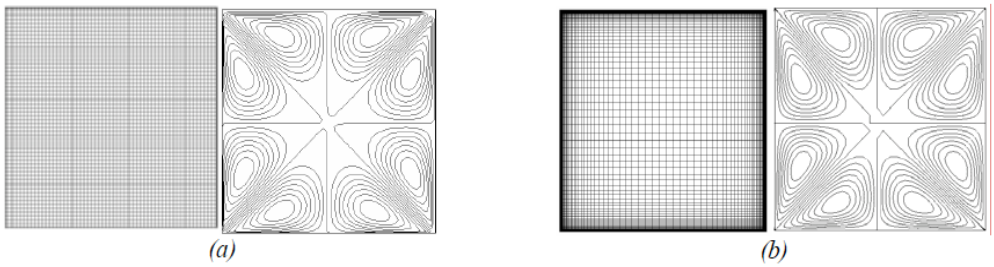

Figure 2-26 Secondary flow streamlines: a) High Reynolds; b) Low Reynolds model [86]

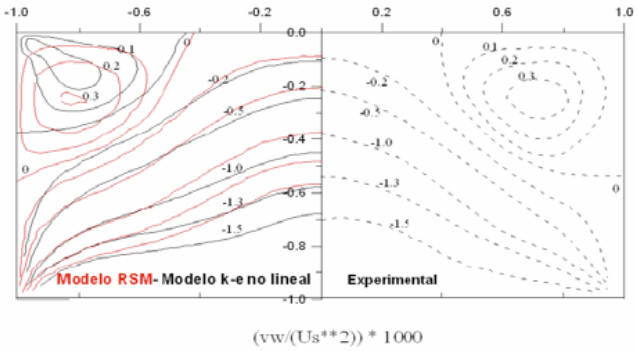

Figure 2-27 Reynolds shear stress contours comparison [86]

It was found out that NLEVM were able to give acceptable predictions of axial mean velocity and secondary fluid flow with a reduction of computational effort of about 30%. RSM resulted to be more accurate, although required more memory usage.

2.3 Square-sectioned ducts with bends

Curved square–sectioned ducts have been studied intensively during the years, because of their use plenty of industrial applications. Fluid flow in such devices is characterized by both first and second kind of Prandtl secondary motion. As explained in the previous section, the motion of second kind is related to the velocity fluctuations typical of turbulent regime in presence of streamwise corners. On the other hand motion of the first kind is generated by the pressure gradient that arises in the curved duct to compensate the inertia forces. It leads to a first order perturbation of the main flow properties that is quite simple to record, since its magnitude is 10-40% of bulk streawise velocity. This phenomenon occurs both in circular and noncircular ducts. A qualitative description is given in the right icon of Figure 3-9.

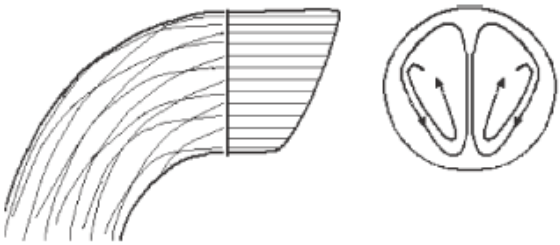

Figure 2-28 Secondary motion at exit of bend [92]

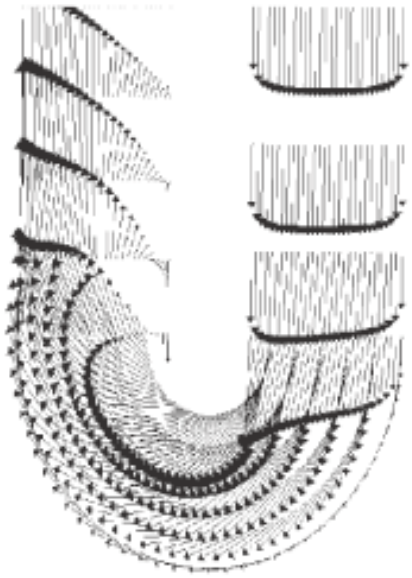

Figure 2-29 Velocity vectors on mid-plane of a U-bend duct of square cross-section [92]

In Figure 3-10 a computed velocity distribution is shown for a sharp 180° bend. The imbalance of centrifugal force between axial fluid, which has higher momentum, and near wall fluid, which has lower momentum, generates a radial pressure gradient in the bend. This forces the axial fluid to move toward the outer wall and the fluid near the wall to move inward, along the inside wall of the duct. In Figure 3-9 this secondary motion can be distinguished clearly.
The pressure gradient generated along the bend influences fluid flow both upstream, at a distance of about two or three hydraulic diameters before the curvature, and downstream, at a distance up to ten diameters. In this direction, thanks to low momentum, the convex zone fluid separates from the inner wall and overturns; several diameters are needed before complete flow stabilization occurs. This stream distortion causes a high-pressure drop and a stream asymmetric distribution, both undesired in most of the applications.
Experimental investigations of mean fluid flow characteristics [89], turbulent intensities and turbulent stresses [90] in a 2-D duct with a 180°-bend were carried out by Jung-Chul Shin.
Tsai's thesis work [91] is concerned with the study of turbulent boundary layer in the corner region of a 60° curved duct. The development of vortex structures in the convex region of the bend, due to secondary motion, was examined through velocity and static pressure measurements along the convex wall at three different stations. Results were useful for the validation of the numerical model built up to solve the partially parabolic equations that governs the flow in the curved duct.
Modi and Jayanti [92] tested the reduction of pressure drop through the introduction of one or two guide vanes in a single sharp 90° bend ore in the U-bend configuration, in order to prevent flow separation and transverse motion. Numerical simulations

with standard k-ε model and wall functions were conducted to determine the loss coefficient for each setting. It was found out that this solution increased skin friction losses, which were compensated by pressure-loss reduction only for low bend curvatures. For the two vanes - high curvature – U type configuration the loss coefficient increased dramatically. In the same work the influence on pressure loss coefficient of an upstream 90° sharp bend was investigated for three different configurations: U-type, Z-type and P-type. In the first and the second all the bends lied on the same plane, in the last the duct developed out of the plane. Several distances between the bends were tested, as the introduction of one or two guide vanes.

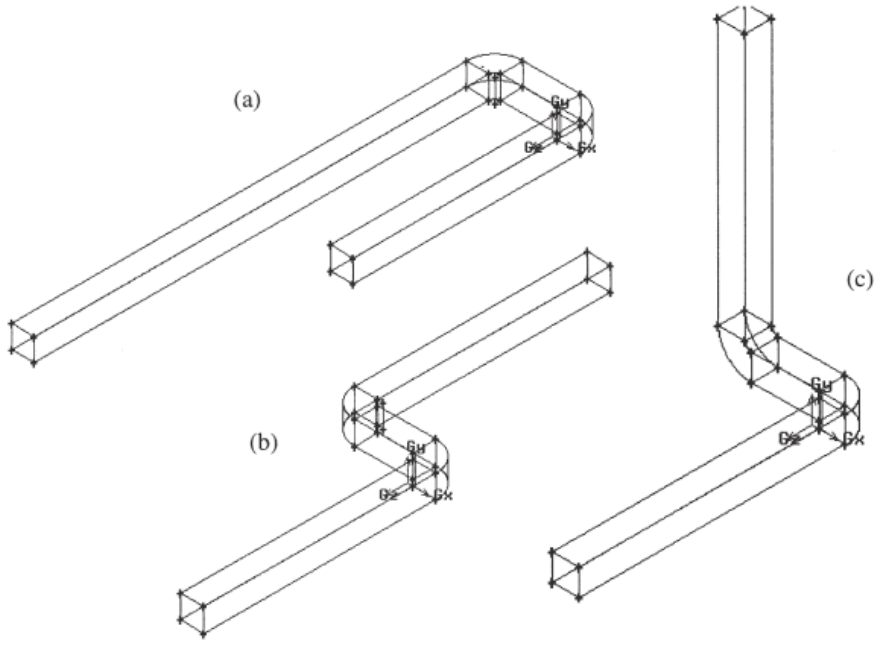

Figure 2-30 a) U-Type; b) Z-type; c) P-type configurations for the study of the influence of upstream bend on flow [92]

For the U-type duct it was found out that for a short span between the bends the loss coefficient was lower than with a longer duct, which allowed the fluid to reach the fully developed condition. Guide vanes gave a healthy contribution in terms of loss reduction. For the Z-type bend a short intermediate duct had worst effects than a longer one, since flow stratification occurs. Guide vanes are necessary to increase system performance. In the P-type the first bend do not affect particularly the pressure drop, both with short or long separation distance. The introduction of vanes is recommended for flow control.
This work has big relevance, since it shows qualitatively to the CFD beginner user what kind of motion and fluid behaviour expect in the first attempt to simulate this kind of problem, although a turbulence model not suitable to square ducts was used.
Yakinthos et al. [93] investigated which among three low-Reynolds-number turbulence models was the most adequate to represent the complex flow development in rectangular duct with a 90° sharp bend.
The adopted models were:

- Launder et Sharma (1974) Linear Eddy Viscosity Model (LEVM);
- Craft et al. (1996) model, based on the cubic constitutional expression for the Reynolds stresses (NLEVM);
- Craft et Launder low Reynolds number Reynolds Stress Model (RSM);

The acceptation "low-Reynolds" is referred to the model capacity of resolving the differential equations to the wall boundary layer, avoiding the necessity of a proper wall treatment. This implied a finer mesh resolution in the near wall region, where 10 points had y+ < 0.1 for the finest grid, in order to compute the derivatives appearing in the RSM without sudden divergence.

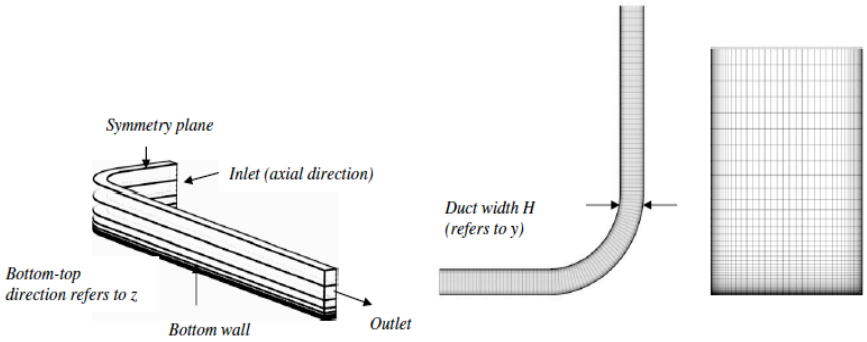

Figure 2-31 Topology of the grid and two cross-sections [93]

Several velocity-profile measurement stations were set along the axial coordinate, according to ERCOFTAC site experiences provided for comparison.

Incompressible Navier Stokes solver was used, and several stability-tricks were adopted for the reduction of the unstable behaviour on NLEVM and RSM. In the following table are shown with their level of success.

	NLEVM	RSM
Preliminary iterations using the LEVM	Good level of success	N/A The solver started with initial values for the Reynolds stresses based on the inlet values
Treatment of the source terms (based on their sign) in the turbulence energy and dissipation rate discretized equations	Good level of success	Applicable only for the turbulence dissipation rate discretized equation. Good level of success
Use of pseudoviscosities	Not used	Unsuccessful
Treatment of the source terms (based on their sign) in the discretized Reynolds-stress equations (only for the normal stress components)	Not applicable	Good level of success
Clipping of turbulence dissipation rate	Not used	Good level of success
Clipping of the negative values of the normal stress during an iteration	Not applicable	Good level of success
Clipping of the A and A_2 parameters during an iteration ($0 < A < 1$, $0 < A_2 < 8/3$)	Not applicable	Good level of success
Clipping of the turbulent Reynolds number $R_t = \max(0, R_t)$	Not used	Good level of success
Use of low values for the under-relaxation factors (the Reynolds-stress discretized equations)	Not used	Good level of success, very slow convergence

Table 2-1 Stability measures for NLEVM, RSM and level of success [93]

Velocity fields obtained from numerical results revealed that all the free models were able to predict the local acceleration of the axial velocity close to the convex wall. The nonlinear model gave better prediction of velocity components in the transversal plane, especially in the core region, while RSM predicted the vortex pair near the convex region with lower accuracy. Generally both models gave acceptable results in the convex part, but lower quality near the concave wall. The authors pointed out that all the three models could produce acceptable results, each one at different accuracy level. RSM could be considered the most appreciable, compared to empirical data, but its computational cost and time required for simulation were really high. On the other hand NLEVM produced good predictions of Reynolds stresses and velocity field in a short time. The linear model could be useful for a first indicative description of fluid flow, surprisingly predicting quite accurate normal and shear stresses in the concave wall region.

Speziale et al. [94] implemented a nonlinear k-l type model developed in a previous work (1987) to represent the turbulence in straight and curved square-sectioned ducts. This model relies on the two classic transport equation for turbulent kinetic energy k and turbulent dissipation ε, and the generic component of Reynolds stress tensor is expressed as a quadratic function of the turbulent length scale l.

This last parameter can be acquired by empirical data or be linked to turbulent quantities k and ε.

For straight ducts the secondary motion, induced by turbulence, consist of 8 counter-rotating vortices.

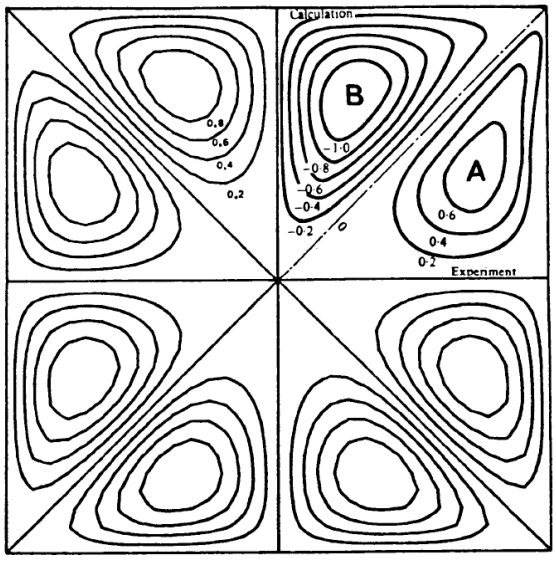

Figure 2-32 Comparison of Secondary Flow Streamlines obtained with Speziale k-l nonlinear model with A) Gessner & Jones experiment; B) Nukiyama et al. calculation for a straight duct [94]

In Figure 3-13 the comparison of secondary flow streamlines with literature results is shown. Curve A was plotted for Re = 150000, curve B for Re = 83000. The distorted

axial velocity profile and Reynolds shear stresses were in good agreement with Melling and Whitelaw work [74].
For curved and helicoidal ducts the secondary flow is characterized by the interaction between centrifugal force and the force induced by the normal Reynolds stresses. The fully developed flow is then characterized by a double vortex structure, which is representative of a flow field dominated by centrifugal effects.

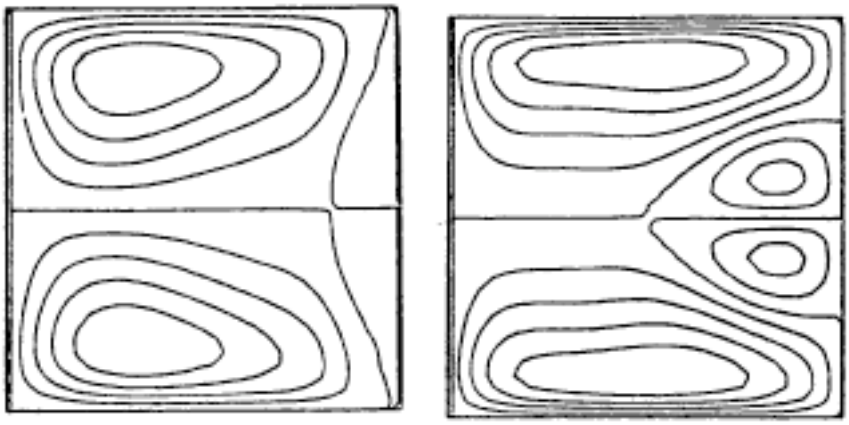

Figure 2-33 Secondary flow in square ducts with different curvature radius.
On the left, big radius (Cr = 125). On the right, little radius (Cr = 15.63); [94]

Authors demonstrated that nonlinear k-l and k-ε models could be a useful alternative to a second order closure model for those applications where savings in computational expense are a high priority.

2.4 Present investigation

Realizable k-ε is known for its general validity for internal fluid flows, and is based on the Boussinesq hypothesis, hence it is not able to represent correctly turbulent normal stresses anisotropy. On the other hand, RSM formulation includes 6 transport equations for the independent components of Reynolds stress tensor, plus one transport equation for turbulent dissipation rate. Thus, it can represent accurately the anisotropy of normal stresses. The main downside is the far higher computational expense than the two-equation models. In the solver code the under-relaxation factors are significant for the convergence of the numerical scheme. Starting from low values, they can be gradually increased to accelerate the convergence. Realizable k-ε is usually stable during iterations, hence a small factors decrease is initially enough to address the solution to the correct course. On the other hand, RSM is extremely sensitive of under-relaxation values. High values lead immediately to numerical instability phenomena in a few cells, spreading rapidly in the neighbouring cells and eventually causing the solution divergence.

In Fluent it is noticeable as sudden increase of the turbulent viscosity ratio to unreasonable level. The comparison of this two models will be performed in the pre-heater section, in order to see if the bigger resources required for RSM will be justified by results improvements, with respect to Realizable.

Chapter 3 CFD Approach

This chapter contains a brief introduction to CFD fundamentals, including turbulence models and boundary conditions. The Q^3 protocol is presented as a tool to give a logic order to this dissertation.

3.1 The CFD method

3.1.1 Overview of CFD models

Computational fluid dynamics is based on the resolution of the Navier-Stokes partial differential equations. Dealing with a turbulent flow field the mass, momentum, total energy and generic scalar variable balance equations are coupled with a proper turbulence treatment.
Three different approaches to the numerical treatment of the turbulence have been developed:

- *Direct Numerical Simulation (DNS):* It resolves the set of partial differential equations on a space and a time mesh fine enough to capture the smallest turbulent scales and the fastest fluctuations. It requires an excessive calculation effort, its application is restricted only to low Reynolds streams in little domains yet;

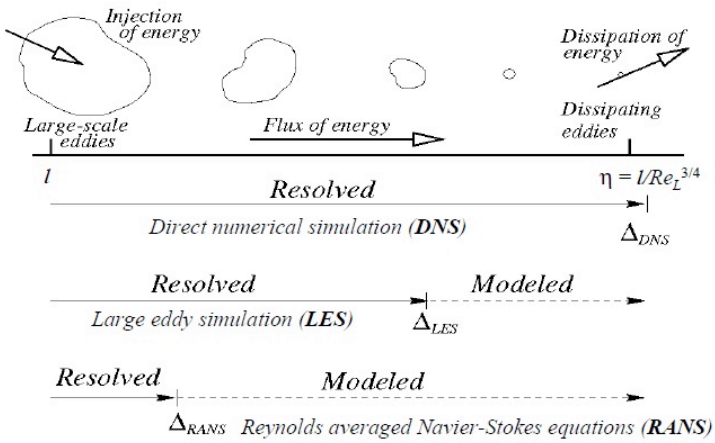

Figure 3-1 Resolved and modelled scales for the three approaches

- *Large Eddy Simulation (LES):* It uses a spatial filtering operation on the unsteady Navier-Stokes equations to separate the larger and the smallest eddies. Filtered equations of balance are solved, while the smallest or sub-grid-scales are modelled.

- *Reynolds Averaged Navier-Stokes (RANS*): The Navier-Stokes partial differential equations time-averaging process produces second-moment velocity fluctuations, known as turbulent stresses or Reynolds stresses:

$$\tau_{ij} = -\rho_{ij} * \overline{u_i' u_j'}$$

Turbulent models are defined to predict these stresses, and are classified on the basis of the number of additional equations that need be solved along with the RANS flow equations. Among them, several models are based on the *Boussinesq hypothesis*, which states that Reynolds stresses might be proportional to mean rate of deformation through a scalar, called eddy viscosity:

$$\tau_{ij} = -\rho_{ij} * \overline{u_i' u_j'} = \mu_t \left(\frac{\partial U_i}{\partial x_j} + \frac{\partial U_j}{\partial x_i} \right) + \frac{2}{3} \rho k \delta_{ij}$$

3.1.2 K-ε model

The general k-ε model has two transport equations, one for the turbulent kinetic energy k and one for the viscous dissipation rate ε, based on their developers' best understanding of the relevant processes causing changes to this variables. The eddy viscosity can be specified as:

$$\mu_t = \rho C_\mu \frac{k^2}{\varepsilon},$$

where C_μ is a dimensionless constant that varies with the model version.
For **standard k-ε model** the transport equations are:

Turbulent kinetic energy k

$$\frac{\partial(\rho k)}{\partial t} + div(\rho k \tilde{\mathbf{U}}) = div\left[\frac{\mu_t}{\sigma_k} grad(k) \right] + 2\mu_t S_{ij} \cdot S_{ij} - \rho\varepsilon$$

Viscous dissipation ε

$$\frac{\partial(\rho \varepsilon)}{\partial t} + div(\rho \varepsilon \tilde{\mathbf{U}}) = div\left[\frac{\mu_t}{\sigma_\varepsilon} grad(k) \right] + C_{1\varepsilon} \frac{\varepsilon}{k} 2\mu_t S_{ij} \cdot S_{ij} - C_{2\varepsilon} \rho \frac{\varepsilon^2}{k}$$

The first equation is a simplified form of the complete turbulent kinetic energy transport equation, while second is an approximate expression, developed copying the form of the first. Indeed, the original transport equation for ε contains many unknown and unmeasurable terms. $C_{1\varepsilon}$, $C_{2\varepsilon}$, σ_k and σ_ε are constants descended from data fitting for a wide range of industrial cases.
Other versions of the k-ε model**,** named respectively **Renormalization Group (RNG) and Realizable**, were introduced to obtain better predictions in certain classes of fluid flows, where the original method usually failed. In detail, the standard model predicted excessive turbulent shear stress values in presence of adverse pressure gradients, leading to suppression of separation on curved walls. Lack of accuracy was verified in jet turbulent flows.
The form of the previous transport equations was slightly modified in the following models; constants values were changed or substituted by functions, which included empirical relations. For a more complete description of the equations Malalasekera [95] is suggested. The standard version has been the most appreciated model for general applications because of its robustness and computational cheapness; furthermore it collected a lot of experiences during the past years. On the other hand, it gives weak predictions in presence of adverse pressure gradients, where separation occurs, in complex or swirling flows with strong streamline and with significant body force fields. RNG enhances accuracy for rapid strain and low-Reynolds flows, while Realizable have improved performance with rotating system and round-jet anomaly.

3.1.3 K-ω models

The rate of dissipation of turbulent kinetic energy ε is not the only possible way to define eddy viscosity. In the k-ω model, first proposed by Wilcox, a turbulence frequency $\omega = \varepsilon/k$ is used to define the eddy viscosity $\mu_t = \rho * k/\omega$. The Reynolds stresses are computed as usual in two-equation models with the Boussinesq expression.
The transport equations for k and ω for turbulent flows at high Reynolds number are:

$$\frac{\partial(\rho k)}{\partial t} + div(\rho k\tilde{\mathbf{U}}) = div\left[\left(\frac{\mu_t}{\sigma_k} + \mu\right) grad(k)\right] + P_k - \beta^* \rho k\omega$$

$$P_k = \left(2\mu_t S_{ij} \cdot S_{ij} - \frac{2}{3}\rho k \frac{\partial U_i}{\partial x_j}\delta_{ij}\right)$$

is the rate of production of turbulent kinetic energy;

$$\frac{\partial(\rho\omega)}{\partial t} + div(\rho\omega\tilde{\mathbf{U}}) = div\left[\left(\frac{\mu_t}{\sigma_\omega} + \mu\right) grad(\omega)\right] + \gamma_1\left(2\rho S_{ij} \cdot S_{ij} - \frac{2}{3}\rho\omega \frac{\partial U_i}{\partial x_j}\delta_{ij}\right) - \beta_1 \rho\omega^2$$

The model constants are $\sigma_k, \sigma_\omega, \mu_t, \gamma_1, \beta_1$.

This model initially attracted because in low-Reynolds number applications, where wall functions based on the log-law are inaccurate and can't be applied for the wall treatment, it did not require damping functions.
Menter SST k-ω is an hybrid version that combines the advantages of the k-ε, which is less sensitive to the values in the free stream, and the k-ω presented before, which revealed to be satisfactory for boundary layers with adverse pressure gradients.
The ε transport equation in the Wilcox version was transformed into a ω-equation by substituting $\omega = \varepsilon/k$, while the k-equation remained the same:

$$\frac{\partial(\rho\omega)}{\partial t} + div(\rho\omega\tilde{\mathbf{U}}) = div\left[\left(\frac{\mu_t}{\sigma_{\omega,1}} + \mu\right) grad(\omega)\right] + \gamma_2\left(2\rho S_{ij}\cdot S_{ij} - \frac{2}{3}\rho\omega\frac{\partial U_i}{\partial x_j}\delta_{ij}\right) - \beta_2\rho\omega^2 + 2\frac{\rho}{\sigma_{\omega,2}}\frac{\partial k}{\partial x_k\omega}\frac{\partial\omega}{\partial x_k}$$

where $2\frac{\rho}{\sigma_{\omega,2}}\frac{\partial k}{\partial x_k\omega}\frac{\partial\omega}{\partial x_k}$ is the cross-diffusion term, which arises during the substitution.

Both models are suited for external aerodynamics, since offer good prediction of boundary layers with adverse pressure gradients, free shear layers, separating flows and vortexes. For general purposes they have similar strengths and weaknesses as the k-ε model, since both assume the turbulent stresses isotropy hypothesis. Thus, they are incapable of capturing the relationship between turbulent energy production and turbulent stresses caused by the anisotropy of the normal stresses.

3.1.4 Reynolds Stress Model (RSM)

The Reynolds Stress equation Model (RSM), called also second order model, provides for the former methods drawbacks through six exact partial differential transport equations, one for each independent turbulent stress, and a extra equation for the scalar dissipation rate ε.
The exact equation for the (kinematic) Reynolds stress R_{ij} takes the form:

$$\frac{\partial R_{ij}}{\partial t} + C_{ij} = P_{ij} + D_{ij} - \varepsilon_{ij} + \Pi_{ij} + \Omega_{ij} \quad \text{where } R_{ij} = \overline{u_i' u_j'}$$

The following three terms are retained in their exact form:

$$C_{ij} = \frac{\partial\left(\rho U_k \overline{u_i' u_j'}\right)}{\partial x_k} = div\left(\rho\mathbf{U}\overline{u_i' u_j'}\right) \qquad \text{Convective term;}$$

$$P_{ij} = -\left(\frac{\partial U_{ij}}{\partial x_m} + R_{jm}\frac{\partial U_i}{\partial x_m}\right) \qquad \text{Production term;}$$

$$\Omega_{ij} = -2\omega_k\left(\overline{u_j' u_m'} e_{ikm} + \overline{u_i' u_m'} e_{jkm}\right) \qquad \text{Rotational term;}$$

While the remaining terms need to be modelled. Many re-elaborate versions can be found in literature, the following equations are used in some commercial CFD codes [95].
The diffusion term D_{ij} is assumed to be proportional to gradients of Reynolds stresses:

$$D_{ij} = \frac{\partial}{\partial x_k}\left(\frac{\nu_t}{\sigma_k}\frac{\partial R_{ij}}{\partial x_m}\right) = div\left(\frac{\nu_t}{\sigma_k} grad(R_{ij})\right)$$

where $\nu_t = C_\mu \frac{k^2}{\varepsilon}$ and C_μ, σ_k are constants;

The dissipation rate ε_{ij} is modelled with the assumption of isotropy of the smallest dissipative eddies, and acts only on the normal turbulent stresses (δ_{ij} is Kronecker delta):

$$\varepsilon_{ij} = \frac{2}{3}\varepsilon\delta_{ij}$$

The pressure-strain interaction Π_{ij} is the most complex term to be modelled. It describes the mechanism of turbulent eddies anisotropy reduction by the interactions between turbulent fluctuations and mean flow strain. Thus, energy is redistributed among the normal stresses, at the expense of turbulent shear stresses.

$$\Pi_{ij} = -C_1\frac{\varepsilon}{k}\left(R_{ij} - \frac{2}{3}k\delta_{ij}\right) - C_2\left(P_{ij} - \frac{2}{3}P\delta_{ij}\right)$$

where C_1, C_2 are constants.
In vicinity of solid walls the damping of the turbulent fluctuations introduces more anisotropic structures, hence it is required an additional correction part that modifies the former equation.
The transport equation for the kinetic turbulent energy dissipation rate is in the form:

$$\frac{\partial(\rho\varepsilon)}{\partial t} + div(\rho\varepsilon\tilde{\mathbf{U}}) = div\left[\frac{\nu_t}{\sigma_\varepsilon} grad(\varepsilon)\right] + C_{1\varepsilon}\frac{\varepsilon}{k}2\nu_t S_{ij}\cdot S_{ij} - C_{2\varepsilon}\frac{\varepsilon^2}{k}$$

with $C_{1\varepsilon}, C_{2\varepsilon}$ are constants.
RSM model has the potential to describe all the components of the Reynolds stresses tensor without any case-adjustment. It is required in all that kind of problems where anisotropy of normal turbulent stresses is expected, since it may give more accurate results. However, the high computational cost and the numerical instabilities that affect the iteration process discourage its employment when is not strictly necessary.

Nonlinear eddy viscosity are improved two-equation models take account of turbulent stresses anisotropy. Progressively developed along the years, they are expected to replace RSM in the future, thanks to their simplicity and less CPU cost [96,97].

3.1.5 Wall Boundary Modeling

3.1.5.1 Overview

Turbulent flows are significantly affected by the presence of walls. No-slip condition causes the progressive reduction of the Reynolds number moving from the free stream to the wall boundary. In the region very close to the wall viscous forces prevail on inertia forces. Thus, the viscous damping reduces the tangential velocity fluctuations, while kinematic blocking reduces the normal fluctuations.
It is clear that the turbulence model nee to take account of the different distribution of velocity and turbulent quantity in the boundary layer. Defined a non-dimensional wall distance y^+ and a friction velocity u_τ:

$$y+ = \rho u_\tau y/\mu \qquad u_\tau = \sqrt{\frac{\tau}{\rho}}$$

the relationship between the logarithm of the first distance and the normalized velocity is shown:

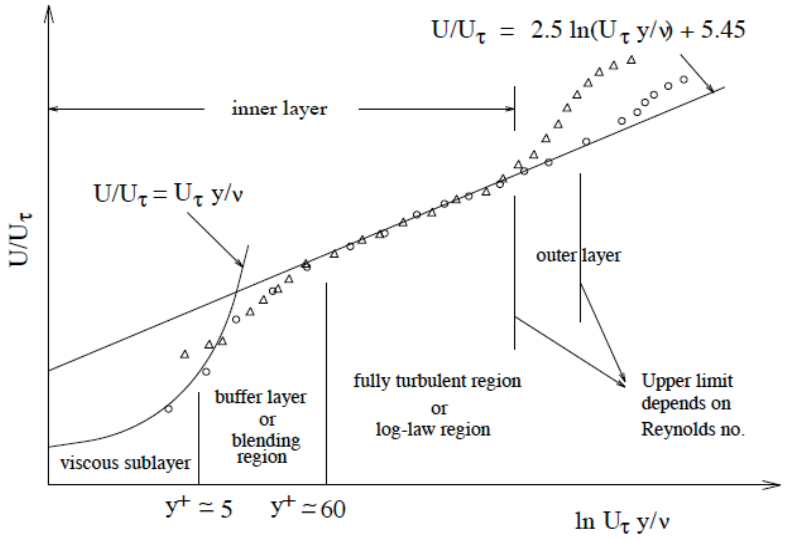

Figure 3-2 Near-Wall Region classification [98]

In Figure 4-1 is shown the three layers division of wall region. Its correct reproduction is extremely important for an accurate numerical solution, being walls the main source of turbulence and mean vorticity. In the viscous sublayer the flow is almost laminar

and viscosity plays a dominant role in the momentum, heat and mass transfer. In outer layer, called fully turbulent layer, turbulence plays a major role and inertial forces are dominant. In the buffer layer, situated between viscous sublayer and fully turbulent layer, both molecular viscosity and turbulence are equally important.
Two different approaches can be adopted to represent the different layers. The first relies on **Wall Functions**, which are semi-empirical functions introduced in the model to bridge the viscosity region and the fully-turbulent region, without resolving the viscous sublayer. In the **Near-Wall approach**, on the over hand, the turbulence model is modified to resolve all the layers down to the wall.

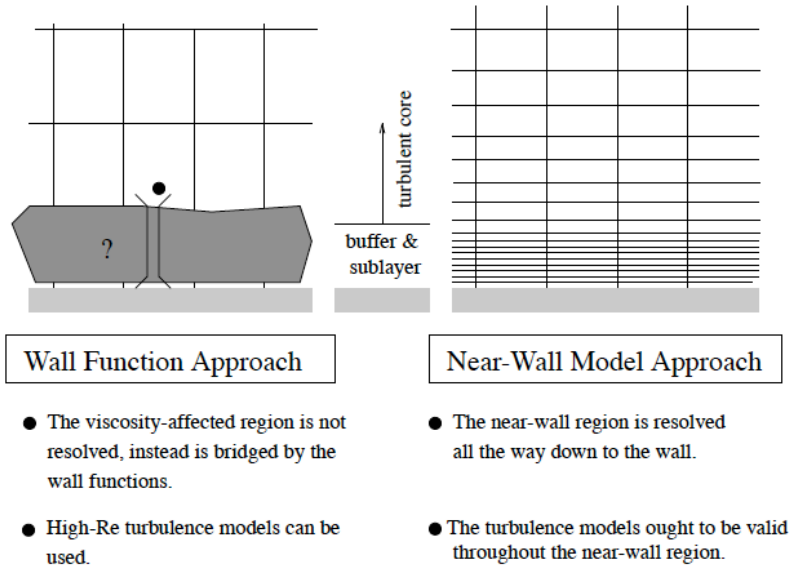

Figure 3-3 Near-Wall treatment in ANSYS FLUENT

The chosen approach has important consequences on the mesh grid dimension: if the first requires a certain resolution near the wall, the second requires a much higher refinement level, severely increasing the computational cost.
FLUENT offers several wall-treatment modalities options, each one with its y^+ of validity. The three most common for industrial usage are:

- **Standard Wall Functions**: This was the industrial standard until some years ago. The main drawback is the numerical results deteriorations if applied out of its proper range of use, which depends on the Reynolds number, typical value are $30< y^+<300$. Values below 30 will result in unbounded errors in shear stress and heat transfer predictions.
  The law-of-the-wall is used to yield the mean velocity distribution in the shear layer.

- **Scalable Wall Functions**: This approach produces consistent results for grids of arbitrary refinement, since it avoids the numerical deterioration of

standard wall functions for low y^+ values. Scalable wall functions activate the local usage of the log law in regions where the y+ is sufficiently small, in conjunction with the standard wall function approach in coarser y+ regions. The log-law validity is extended through the introduction in the algorithm of a limiter function, where y^*_{limit}= 11.225. If $y^* < y^*_{limit}$, the algorithm will choose 11.225 as y*.

- **Enhanced Wall Treatment**: It combines the two-layer model with the enhanced wall functions. In the two-layer model the domain is subdivided in a viscosity-dominant and a fully-turbulent region; ε and μ_t are specified in the near-wall cells. This approach is valid when $y^+ \approx 1$ at the first cell in direction perpendicular to the wall. However, in the most common industrial problem it is difficult to obtain this value for all the wall boundaries in the domain, because it would mean an excessive memory usage. Hence enhanced wall treatment is used. It blends the separate models of the two layers approach by the use of a damping function, in order to have a smoother transition between the two regions. This is useful whenever the first near-wall node is placed in the buffer-layer region, where neither the low-Reynolds approach for viscous sublayer nor wall functions for the turbulent layer are valid.

The right choice of the wall treatment has great impact on simulation quality, especially if pressure drop, wall shear stress, heat or mass exchanges at the wall are investigated.
Some models are available in two versions: high-Reynolds and low-Reynolds models. The first needs wall functions to resolve boundary layer, the second is a modified formulation which allows the integration of the differential equations straight to the wall.

3.1.5.2 Wall Roughness

Wall roughness affects drag (resistance), heat and mass transfer on the wall. A equivalent sand-grain roughness k is introduced in the numerical code to take account of its effects, as shown in figure 4-3:

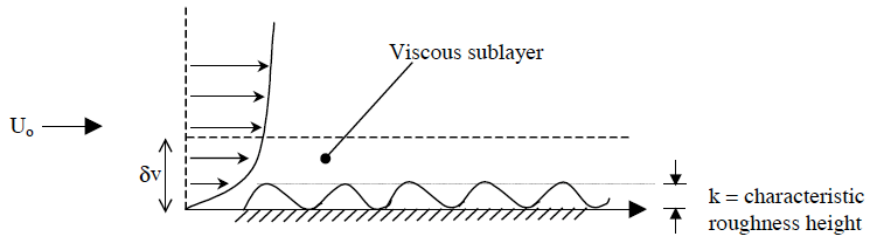

Figure 3-4 Effect of wall roughness on boundary layer

The law-of-the-wall was demonstrated to have the same slope as in the smooth boundaries, but the intercept was different. Thus, a modified law-of-the-wall is introduced in the numerical code to evaluate the shear stress at the wall and other wall functions for the mean temperature and turbulent quantities.
According to the sand grain element height, the whole roughness regime is divided into three different sub-regimes. Each one corresponds to a certain empirical formula that describes the intercept term.
In FLUENT the equivalent sand-grain roughness K_S^+ has a blockage effect, since the wall is ideally lifted up to 50% of the height of the roughness elements: $y^+ = y^+ + \frac{K_S^+}{2}$. It is important to highlight that wall roughness is set as boundary condition, while y^+ is related to mesh generation. Hence, mesh and roughness do not have direct relationship. The numerical solver simply shifts up or down the law of the wall, according to the calculated y^+.

3.1.5.3 Density calculation

In the hypothesis of incompressible ideal gas, the solver computes the density as:

$$\rho = \frac{p_{op}}{\frac{R}{MM} * T}$$

where $\mathbf{p_{op}}$ is the operating pressure, **R** the universal gas constant and **MM** the gas molecular weight.
In this form the density does not depend on the pressure field, but only on temperature by calculating the ideal gas equation. This is the reason of the density equation presence among the balance equations even if the fluid flow is set as incompressible.

3.2 The Q^3 Approach

Colombo et al. [99] discussed the importance of a methodological approach to insure quality in the CFD analysis.
The Q^3 (or Q-cube) approach relies on three specific dimensions:

- *User knowledge*
- *Software reliability*
- *Process control*

The first dimension is related to the personal training and university education that keep the user up-to-date of CFD evolution. Software developers have to guarantee the second dimension to obtain quality. The last dimension is related to user skills, so the introduction of guidelines would be required to avoid systematic errors. A protocol was developed as analysis process control tool, thus limiting the introduction of errors or uncertainties.

It is useful for the common user who has to face with numerical simulation for the first time and has to achieve quality assurance requirements.
The protocol is structured on 4 main points, which corresponds to the phases of a CFD cycle process:

1. *Cycle phase 1 – Problem analysis*. Here the main goals of the project and the engineering problem are described;

2. *Cycle phase 2 - Conceptual model setting: results and approach.* In this section the specific goals of the CFD project are defined; existing documentation, benchmarks for validation procedure and literature review about similar problems are here exposed. Assumption and hypothesis to simplify the problem and build the mathematical model are discussed;

3. *Cycle phase 3 – Model building and solving: deployment*. The geometrical approach and the meshing process are here described. All the settings of the numerical model are then discussed: numerical code, dimensional approach, type of solver, boundary conditions, material properties, turbulence models, and all the necessary specifications to set up the computational simulation. This phase also is identified as "pre-processing";

4. *Cycle phase 4 – Problem evaluation: assessment and review*. Calculation validation and verification are performed in this section. Results are shown for each configuration tested. Strategies for accuracy improvement, approach review and future development are discussed;

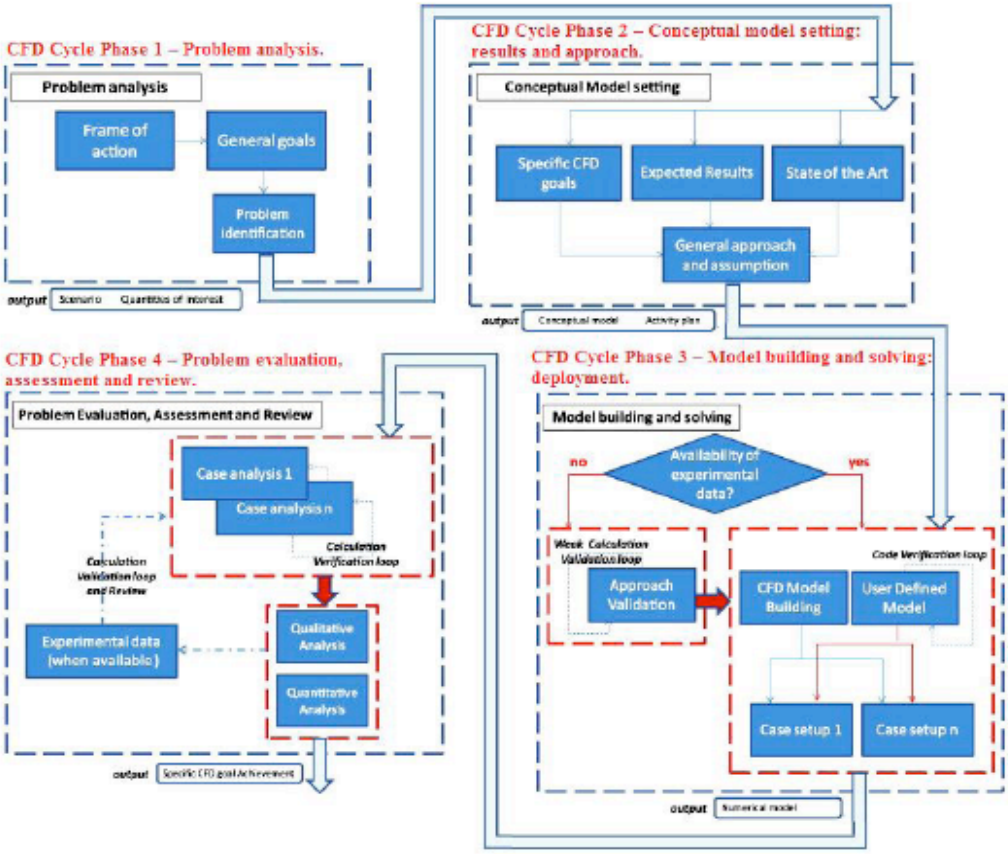

Figure 3-5 Protocol scheme for CFD analysis. Taken from [100]

In this work the protocol scheme presented above is generally followed in order to guarantee an appreciable quality analysis.

3.3 Pre-processing

Pre-processing involves mainly three activities: geometry creation, mesh generation and solver set up. The first is aimed to the faithful reproduction of the real domain, the second to the computational grid generation. This last process requires particular care, because simulation results strictly depend on mesh accuracy, which in turn depends on the kind of grid chosen for calculations.
Three types of grids are mostly used: structured, unstructured and hybrid. The structured are made of quadrilateral (2D) or hexahedral (3D) elements, repeated regularly. Their main advantage is memory saving, compared to unstructured mesh, thanks to the implicit storage of the cell connections.
The unstructured consist of arbitrarily shaped elements, which do not have any regularity among them. Such type of meshes is generally represented by triangles (2D)

and tetrahedrons (3D), which main advantage is the ability to resolve finely around very complex geometric topologies. Hybrid grid is the solution that combines both the above-mentioned elements. During the numerical analysis cycle is not uncommon the necessity of repeating several times the meshing operation, in order to obtain a desired solution. The Multi-Block grid generator is a comfortable choice whenever the domain is composed of simple shapes. In this modality the mesh generator creates arrays of same elements, starting from a face of the solid and moving to the opposite side. This process is repeated for each sweepable shape identified by software. The resulting mesh is structured, and consists only of hexahedral element.
Generally elements in central regions have high orthogonal quality and low skewness, while near-wall zones are more problematic, since inflactions are used to capture boundary layer. Very high aspect ratios are obtained when inflation layer height is really small, compared to the transverse cell dimension. High skewed cells are also generated at intersections of different blocks, especially when, in the sweep process, the target surface of the former part do not coincide with the start surface of the next body. Elements with aspect ratio higher than 100 and skewness up to 0.9 are to be avoided, because they are detrimental for the convergence of the numerical solution. Among all the Reynolds Stress Model is particularly sensible to cell quality.

3.4 Convergence controls

Several criteria can be applied to define the convergence of a solution:

- **Residuals errors** reached acceptable values (usually between 1E-04 and 1E-05);
- **Monitored quantities of interest** have reached a steady state solution, no variations occur with further iterations;
- **The domain imbalances** are less than 1%;

Their usefulness depends on the type of problem. In the analysis of ejector stack, for example, the static pressure at inlet openings still varies even if residual of all quantities are below 5E-04. In other problems continuity equation residual can barely reach 1E-03, but other criteria are fully satisfied.
Residuals criterion can be misleading in all the cases initialized very close or very distant to the solution, where it does not mean physical convergence is reached.

The convergence of solution is generally obtained if the following criteria are satisfied:

- Residual errors are all in the order of 1E-04;
- Area-weighed-averaged static pressure at primary and secondary flow inlet reached stable value;
- Net mass flow rate outlet-inlets is below 1E-07 kg/s;

3.5 Grid independence

Grid independence (or grid convergence) study is necessary to evaluate if the solution, obtained through a turbulence model, is independent of the mesh resolution. It is necessary to verify it for each domain, only in this way the usage of a certain grid for calculations is justified.
The proceeding to assure grid independence consists mainly of 3 steps:

- *Step 1:* Meet the convergence criteria cited in the previous section, for a chosen turbulence model;

- *Step 2:* Refine the grid. The ideal procedure would claims a 1,5 times refinement, actually it is difficult to respect it dealing with industrial problems with high number of elements. Then repeat calculations, meeting the former convergence criteria. Now the monitored values of step 1 and step 2 are compared. If their difference is within the user-defined tolerance, a coarse grid is enough to confirm the independence. Guidelines usually suggest a discrepancy around 1% as acceptable.

- *Step 3:* Refine the grid again and repeat calculations as in step 2. Then compare the monitored quantities with step 2. If their difference is in the acceptable range, the objective is reached. Else, repeat again step 3.

Chapter 4 **Pre – Processing**

The Q^3 approach is hereinafter applied to develop the current analysis. Objectives of the work are defined, and all the aspects concerning with the simulation set-up are exposed.

CFD phase cycle 1: Problem Analysis

4.1.1. Frame of action and general purposes

The subject of the CFD analysis is the galvanizing furnace gas discharge system, whose furnace has been retrofitted to burn BFG.
Given a fixed thermal input for the maintenance of the galvanisation process, the reduction of fuel LHV leads to a several-times growth of fumes volumetric flow rate, with respect to the traditional source. Hence, it is necessary to verify if ducts and furnace maximum capabilities, according to the original project, are compatible with the new feeding. A subsonic ejector, located just below the stack, provides the suction force for the fumes along the ducts. Its operational settings, in terms of primary and secondary flow condition, are known for the case under investigation.

4.1.2. Problem identification

The fumes duct of an industrial galvanizing plant is here analyzed with the help of computational fluid dynamics. A quantitative and qualitative study of the fluid flow and of the physical quantities of interest will help to understand critical aspects. This work will be useful whenever future improvements to plant parts will be asked.

4.2. CFD phase cycle 2: Conceptual Model Setting. Results and Approach

4.2.1. Specific goals of the CFD analysis

The first objective of this work is to determine the static pressure value at the fumes duct inlet, which corresponds to the furnace chamber exit opening, with the help of CFD. Fixed the ejector working point, the magnitude of that (negative) pressure would be too high for the correct operation of the plant. The big air intake from not perfect tightness of the furnace would dilute exhaust gas too much, resulting in big thermal losses. A damper is lowered in the duct downstream the furnace to create a localized pressure drop. In this way pressure magnitude is reduced upstream to the correct operation condition, allowing a slight amount of air intake.
The second objective of this work is the evaluation of the damper lowering level.

4.2.2. State-of-the-art of CFD in the field

Chapter 2 and 3 contain a brief literature review about ejectors and square ducts, the two main topics faced in this plant analysis. Significant was the work of Besagni [], who performed a CFD validation of a subsonic ejector with experimental data found on literature, in his attempt to create an integrated numerical-thermodynamic model.

4.2.3. Guidelines

DCHP tutor professional experience is the main source for the judgment of assumptions and working hypothesis. It is important to notice that a complete set of operation data is available only at the ejector-stack inlets. Validation is not possible for the other examined parts of the plant, since no manifolds are installed and pressures along the ducts are unknown. Thermocouples are present in the furnace chamber and at pre-heater inlet and exit. Hence the correctness of simulation results has been evaluated with the help of the DCHP tutor professional experience.
Guidelines suggest procedures to assure quality in the CFD process analysis. For example, ERCOFTAC guideline includes best practice advices on how to carry out quality CFD calculations and how to interpret and deploy CFD results with trust. Another valid source is the United States Nuclear Regulatory Commission (U.S. NRC) document [101], available online for free. This contains a copy of the ERCOFTAC section about uncertainties and error sources in CFD simulations, best practice guidelines about grid requirements, numerical schemes, convergence control, wall treatment, boundary conditions and every aspect that characterizes the simulation.
Hence, the guidelines contained in this section have been followed to perform a valid investigation of the fluid flow in the fumes duct.

4.2.4. Expected results

Fluid flow in each section will be visualized through velocity contours and vector plots, highlighting recirculation and flow reattachment phenomena. Contours representations are even useful in the comparison of different turbulence models.

4.2.5. General approach: main assumption and working hypothesis

All the plant parts are modelled as 3D geometries. The working fluids involved in this study are exhaust gas, coming from furnace burners, and ambient air, blown by the ejector into the stack section. Both are treated as ideal incompressible gas to reach the continuity equation convergence within an acceptable number of iterations, since fluid compressibility hypothesis increases it of several times. Furthermore, no chemical reactions exist between the different species in the gas streams.
This case of analysis is relative to the highest volume flow rate discharged, where BFG, air and a low LPG addiction (for flame stabilization and LHV enhancement) are the reactants.

4.2.6. Domain approach

The complete geometrical domain is divided into three main blocks, in order to simplify the analysis and, at the same time, to manage the computational resources in the best way possible. The original idea behind this operation was to have velocity profile uniformity along the cut-off sections, but this hypothesis was discovered not being respected during the study. Preliminary calculations (not reported in this dissertation) were run on a part and subsequently on the two sub-parts, divided in a section correspondent to recirculation phenomenon. In this way it was tested the effect of the choice of the cut off section on the pressure drop, giving a uniform velocity profile as inlet. Eventually it was confirmed that the discrepancy of the total pressure drop along the two parts was only in the range of a few percent with respect to the complete device values.
In the ejector-stack block, the first part explored, air coming from a fan is the primary flow accelerated through a nozzle. This creates a suction force for fumes, called secondary flow, which come from the furnace chamber. Subsequently a pressure adjustment to a stable value occurs in the mixing section. In the stack fumes are lifted up and discharged in the atmosphere.
The second part includes both the dryer, where fumes flow supplies heat for the steel pipes pre-heating, and the connection duct to the ejector-stack section. In the first chamber the maze-path disposition of the walls assures the necessary heat exchange between the gas stream and the steel roof. The refractory bricks let assume the connecting duct adiabatic, although a well insulation do not exclude a little heat exchange through walls.
The connection duct between the furnace ground opening and the pre-heater chamber is the third and last part explored. Like the former duct, the inner side is made of fire bricks, the outer side with insulation bricks and concrete. It lies entirely underground, while the upper side of the aforementioned connection duct is a floor area. A manually controlled damper, moved through a mechanical system by an operator, can be lowered or lifted up in the middle of the straight part of the duct to guarantee the right operation condition upstream in the furnace.

4.2.7. Pre-processing: General remarks

All the geometries and meshes were developed by Ansys ® Workbench ™: DesignModeler ™ for domain modelling, Meshing ™ for grid generation.
Ansys User Guide provides a lot of suggestions and examples through several tutorials for each tool. Furthermore the U.S. NRC guidelines [101] and CFD forums on the web [102, 103, 104, 105, 106] have been extremely useful to develop the necessary skills required for this study.

4.2.8. Activities and plan

A schematic plan that portrays the phases of this work is presented hereinafter.

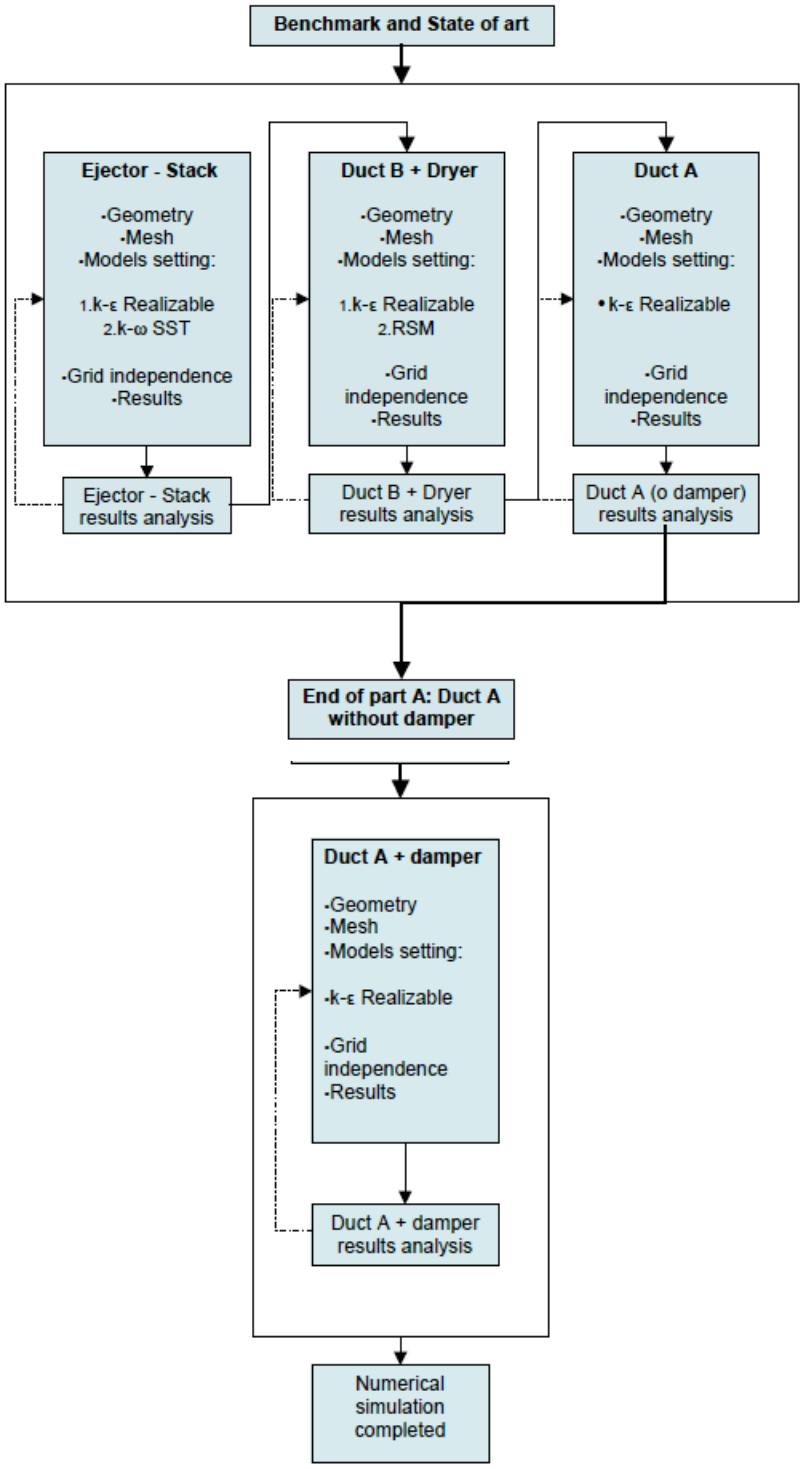

Figure 4-1 Schematic plan of work

4.3. CFD phase cycle 3: Model building and solving

4.3.1. Ejector-stack

The ejector-stack is the first part explored.

4.3.1.1. Domain Overview and Geometry Definition

A transverse section of the ejector-stack is reported in Section 5-1. The height of the whole domain is 26520 mm, while the ejector's length is 6520 mm, measured from fumes inlet to the diffuser section end. Stack is defined as the long half-cylinder after the diffuser. Its diameter is 700 mm.

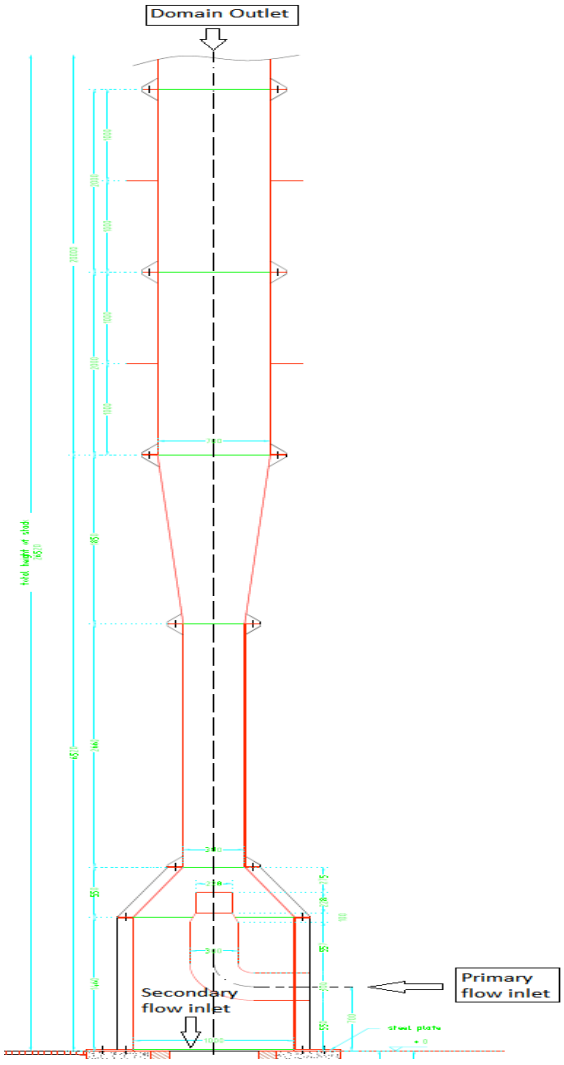

Section 4-1 Ejector-stack transverse section. Courtesy of DCHP

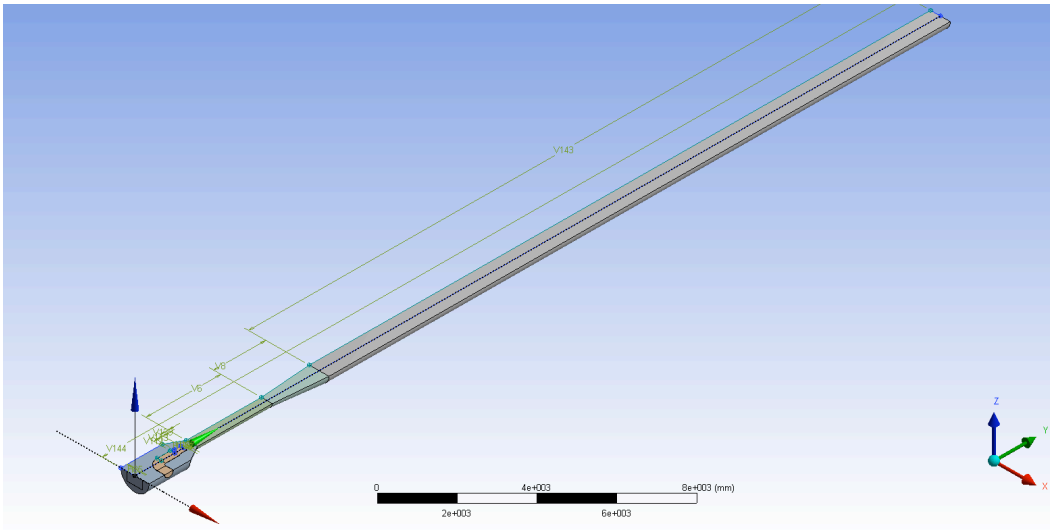

Figure 4-2 Global layout of the ejector-stack. Only half of the whole domain has been modelled, thanks to symmetry

A 3D domain is chosen to take account of the effects of the curved pipe, which disturbs the fumes flow rising from the square-section opening at the ejector base. Thanks to the symmetry of the problem, only half of the whole domain is represented.

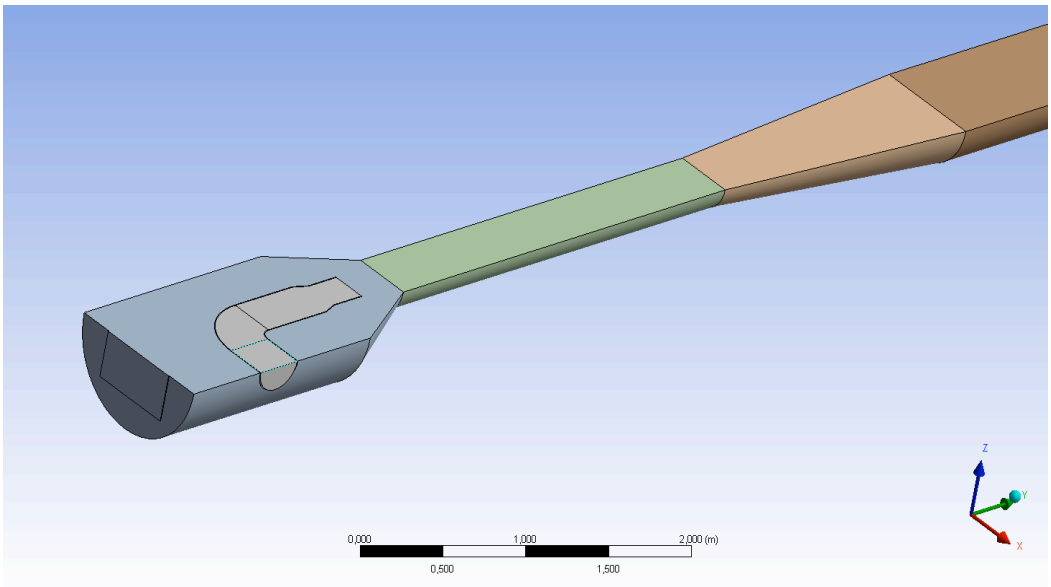

Figure 4-3 Ejector layout

In the figure above the components of the ejector-stack are presented: in grey is the primary flow pipe, the light blue part is the suction chamber, the rectangle at its left is the secondary flow inlet. The light green straight duct in the centre of the picture is the mixing section, on the right the diffuser. The duct on the right is the stack.

The mixing section diameter is 380 mm. Primary flow pipe thickness is 5 mm, the nozzle exit diameter is 228 mm. For further measurements check Figure 5-1.

4.3.1.2. Mesh generation

A hybrid computational grid was used for spatial discretization of the domain. All except the suction chamber are sweepable parts. It means that the program starts from a defined face and extrudes the whole grid moving along the body toward a target face. The suction chamber has a particular no-sweepable shape, hence only tetrahedrons are used to obtain an accurate mesh.

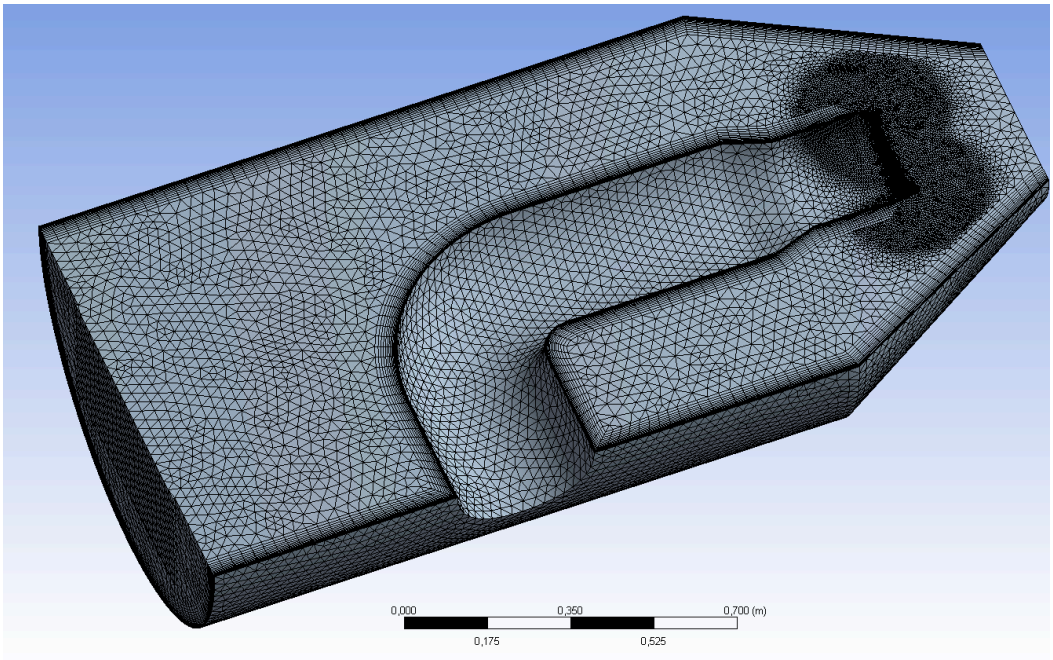

Figure 4-4 Suction chamber layout

A cell refinement is introduced at primary nozzle exit, where stream expands and encounters the exhaust flow.

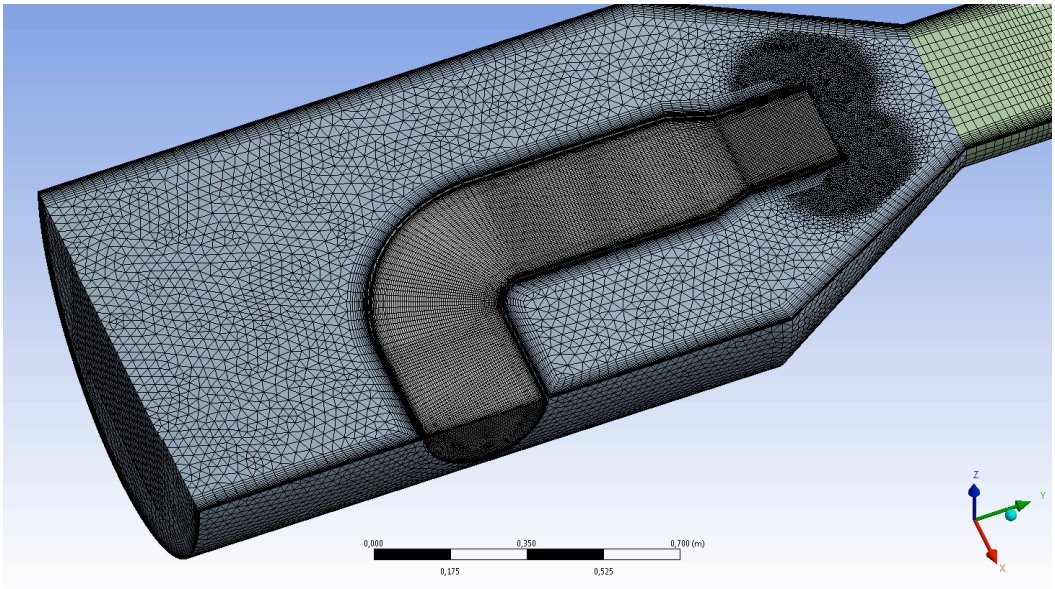

Figure 4-5 Layout of suction chamber and primary flow pipe. Tetrahedrons are used for the first part, hexahedrons for the second part

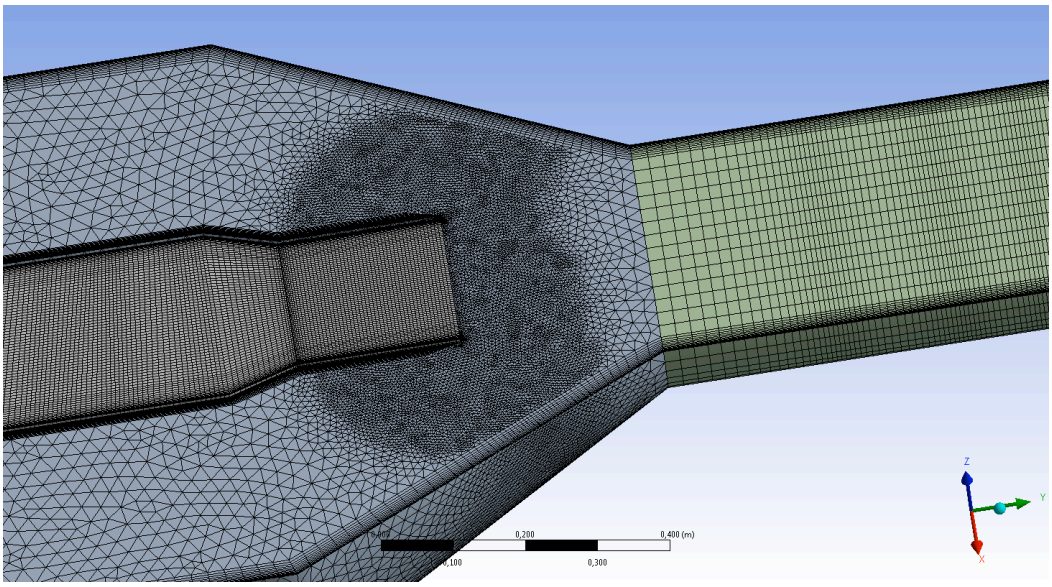

Figure 4-6 Detail view: grid refinement at nozzle exit

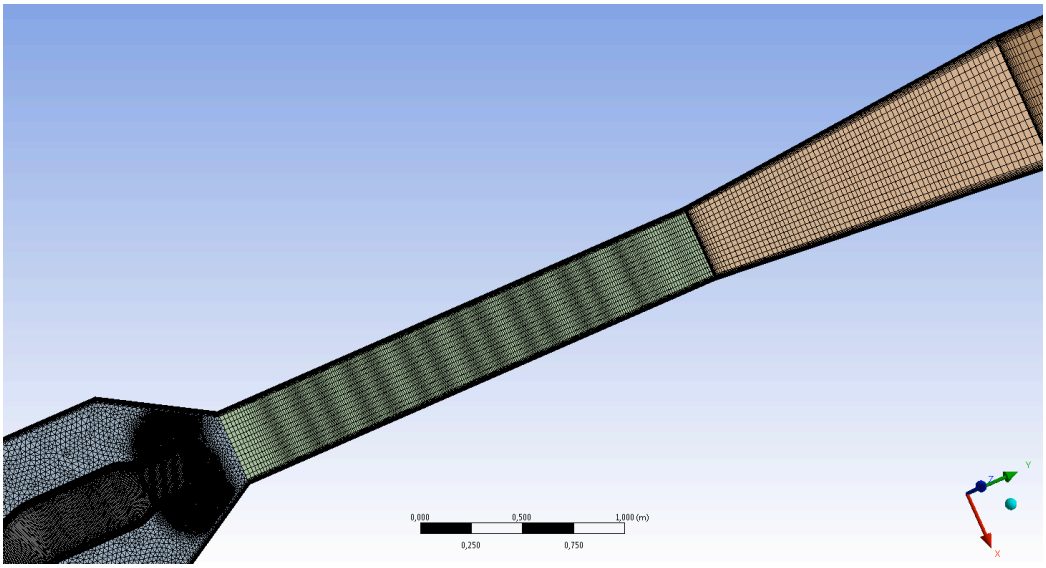

Figure 4-7 Element size variation between suction chamber, mixing section and diffuser.

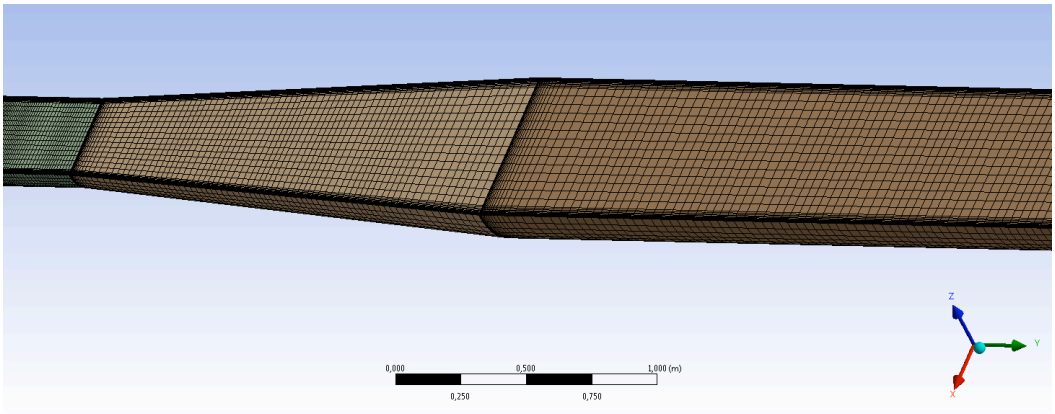

Figure 4-8 Mesh transition between mixing section, diffuser and stack

Hybrid formulation allows the coexistence of both hexahedral and tetrahedral elements in the same part. This gives an optimized mesh both near walls and near the centreline at the same time. Inflation layers are added in the wall regions to resolve properly the boundary layers. The “First layer thickness option” is chosen, that allows to set the first cell row height and the growth rate of the successive rows.

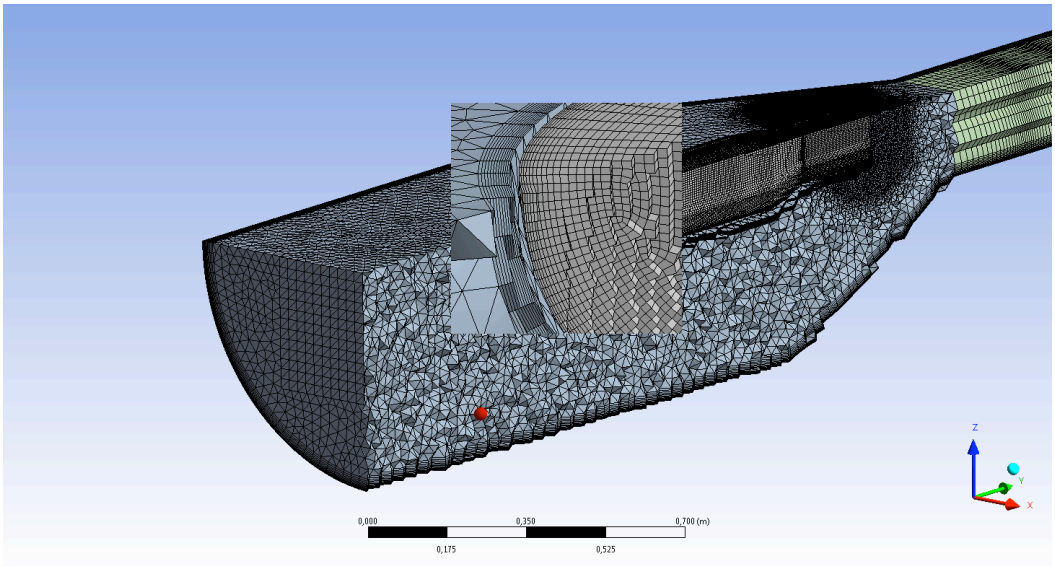

Figure 4-9 Longitudinal section. Details of inflation layers in suction chamber and primary flow pipe

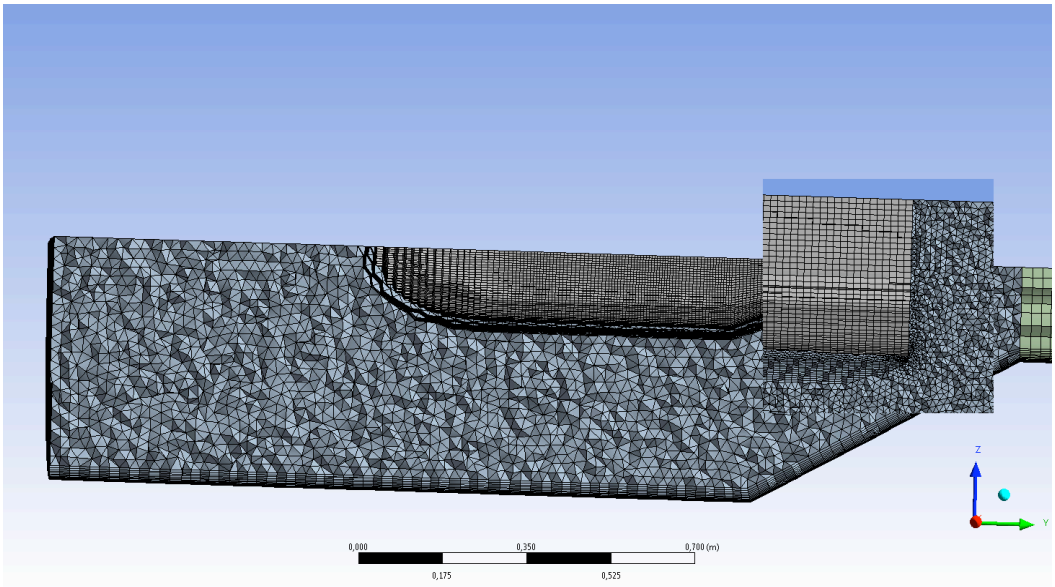

Figure 4-10 Suction chamber section. Details of mesh refinement at primary nozzle exit

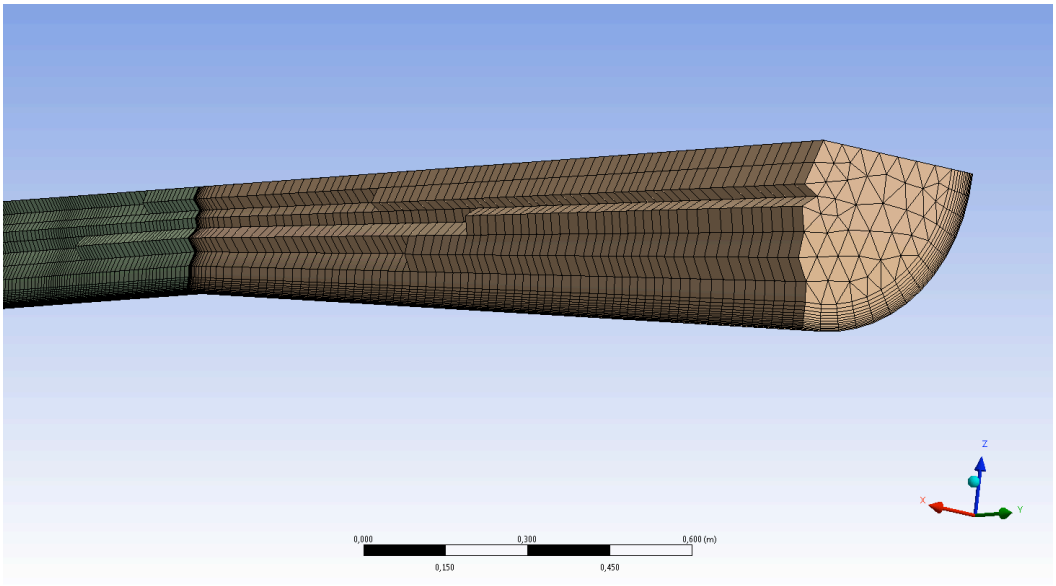

Figure 4-11 Diffuser section. Hexa elements are used for boundaries, tetra elements for the core of the domain

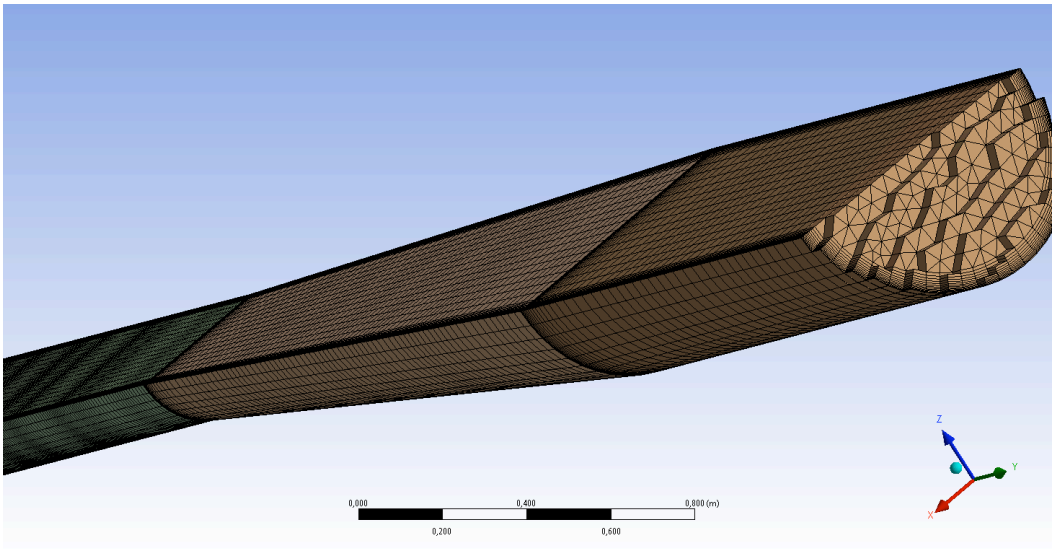

Figure 4-12 Stack transversal section. Details of the hexahedral elements utilized for the inflations, and the tetraherdal elements for the central region

Elements of different size were used: smaller in the critical parts like the mixing chamber or the primary flow pipe, bigger in the stack, where fumes flow is almost fully developed.

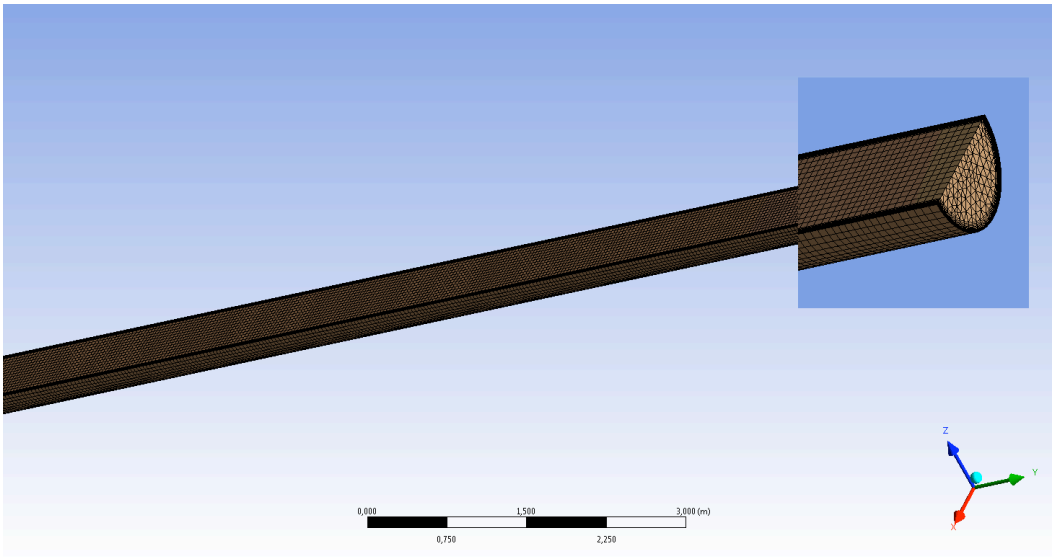

Figure 4-13 Stack layout, with magnified window detail of the exit

Generally all the parts are modelled accounting of two criteria: number of cells and elements quality. This second aspect is extremely important during the calculation session, since high skewed cells have catastrophic impact on the solution convergence. Skewness is defined as the element deviation from the equi-angle shape, and is defined as:

$$equiangle\_skew = \max\left[\frac{\vartheta_{\max} - \vartheta_e}{180 - \vartheta_e}; \frac{\vartheta_e - \vartheta_{\min}}{\vartheta_e}\right]$$

where θ_{max}, θ_{min} are respectively the largest and the smallest angles in a cell, θ_e is the angle of the equiangular correspondent cell. For hexahedral and tetrahedral cells it should not exceed 0.85-0.9.

4.3.1.3. Model setting

In this section the general settings of the model are presented.

4.3.1.3.1. Solver

An Intel® Quadcore™ i5-3330S CPU @ 2.70 GHz is used to run the commercial software FLUENT 14.5. The Finite Volume Method is used to convert the partial differential equations of balance for mass, momentum, energy, species and the general scalar quantities into algebraic form. The resulting equations system is solved numerically [107].

Solver	Dimension	Time	Velocity formulation	Gradient option	Velocity-pressure coupling
Pressure-based	3D	Steady	Absolute	Least Squares Cell Based	SIMPLE

Table 4-1 Solver settings

Pressure-based solver is chosen because the streams are considered as incompressible ideal gases.

4.3.1.3.2. Turbulence approach

For ejector-stack the performance of two *turbulence models* is evaluated*:*

- Realizable k-ε;
- SST k-ω;

Near-Wall treatment: Scalable Wall Functions is an obligated choice for Realizable k-ε. The inlet velocity value of the two streams is one order of magnitude different, so different inflation layers would be required. On the other hand, changes in adjacent boundary layers can lead to high skewed cells, which decrease the global mesh quality. Thus, the author opted for a fixed inflation method for all the components of the domain, and a wall treatment that covers a wide range of y^+ values.
For SST k-ω a proper enhanced wall treatment formulation is the only choice for the boundary layer resolution. Fluent User Guide assures that approach is compatible with values of y^+ up to 30, because it is able to jump to wall functions.

4.3.1.3.3. Physical properties

Working fluids are *exhaust gas and air*, which are blended in the ejector's mixing section. Their physical properties are reported in the next table:

	ρ [kg/m^3]	Cp [J/kg/K]	k [W/m/K]	μ [kg/m/s]	MM [kg/kmol]
Flue gas	Incompressible ideal gas	1186.37	0.0242	3.263 e-05	27.68
Air	Incompressible ideal gas	1006.43	0.0242	1.789 e-05	28.97

Table 4-2 Working fluid properties

4.3.1.3.4. Boundary conditions

- *Boundary conditions at domain openings are:*

  - Primary flow inlet: mass flow rate, inlet temperature;
  - Secondary flow inlet: mass flow rate, inlet temperature;
  - Stack exit: outlet pressure;

	Mass flow rate [kg/s]	T [K]	Static Pressure [Pa]
Primary inlet (air)	1.252*	313	----
Secondary inlet (fumes)	0.592	573	----
Outlet	----	----	0

Table 4-3 Boundary conditions at domain openings

The reported mass flow rates are obtained from the volumetric flow rate measurements. Their accuracy is in the range of 10%. Temperature data have an accuracy of 1°C.

- *Boundary conditions at the walls are:*

  - No slip;
  - Fixed wall roughness;
  - Adiabatic walls;

	Roughness height [mm]	Roughness constant
Walls	0.2	0.5

Table 4-4 Wall boundary conditions - roughness

Stack and ejector walls are entirely steel made. Roughness height value is taken from online database [108].

- *Boundary condition at the symmetry planes:*

  - symmetry;

- *Turbulence and hydraulic diameter:*

* Thanks to the symmetry only one half of the whole domain has been modelled, thus the inlet mass flow rates will be one half of the real values.

Stream turbulence intensity and hydraulic diameter are chosen as boundary conditions both for inlets and outlet. Since no measurements are available, totally random turbulence intensity values are supposed.

	Stream turbulence intensity [%]	Hydraulic diameter [mm]
Primary inlet	2	300
Secondary inlet	3	573.9
Outlet (backflow quantities)	3	49

Table 4-5 Boundary conditions for turbulence

4.3.1.4. Numerical Settings

Numerical settings are reported in this section.

4.3.1.4.1. Numerical Strategy

Initialisation: Hybrid initialization is chosen, due to the presence of multiple inlets.

Discretization schemes: U.S. NRC guide suggests to begin the simulation using a low order scheme, because it goes straight near the solution. However this kind of scheme is subject to high numerical diffusion, so it is necessary to switch to a second order after a certain number of iterations (Table 5-6).

	Equation of balance	Numerical Method
Preliminary flow field	Pressure	Standard
	Momentum	First Order Upwind
	Turbulence parameters	First Order Upwind
	Energy	First Order Upwind
Final results	Pressure	Second Order Upwind
	Momentum	Second Order Upwind
	Turbulence parameters	Second Order Upwind
	Energy	Second Order Upwind

Table 4-6 Numerical settings

Under-relaxation factors: It is suggested to start the simulation with under-relaxation factors reduced to at least one half of the default values, in order to stabilize the numerical scheme. Once monitored quantities are flattened, these parameters can be increased (Table 5-7).

	Equation of balance	Under-relaxation factor
Preliminary flow field	Pressure	0.3
	Density	0.5
	Body Forces	0.5
	Momentum	0.5
	Turbulent Kinetic Energy	0.6
	Turbulent Dissipation Rate	0.6
	Turbulent Viscosity	0.7
	Energy	0.8
Final results	Pressure	0.3
	Density	0.7
	Body Forces	0.7
	Momentum	0.8
	Turbulent Kinetic Energy	0.9
	Turbulent Dissipation Rate	0.9
	Turbulent Viscosity	1
	Energy	1

Table 4-7 Solution Controls

4.3.1.5. Convergence controls

The convergence of solution is obtained if the following criteria are satisfied:

- Residual errors are all at least in the range of 1E-04;
- Area-weighed-averaged static pressure at primary and secondary flow inlet reached stable value;
- Net mass flow rate outlet-inlets is below 1E-07 kg/s;

4.3.2. Duct B + Dryer

In this section the dryer (or pre-heater) and its connection duct to the ejector-stack are examined. The first part is essentially a big heat exchanger, where fumes are forced through a maze path, while the second is a square sectioned duct with multiple 90° bends.
It is named "Duct B" to discern it from Duct A, which connects the dryer with the furnace bottom.

4.3.2.1. Domain Overview and Geometry Definition

The transverse sections of the dryer and duct B are shown in Section 6-1 and Section 6-2. In the first picture two chambers can be distinguished: the upper, through which tubes roll, and the lower, where exhaust gas flows. The metallic roof consists of 2 layers of carbon steel slabs, between which cold air is pumped and heated. In the upper chamber the rolling tubes are heated by hot air jet impingement. In Figure 6-3 is shown a longitudinal section of the pre-heater. The maze path created by the walls increases the residence time of the gas stream, allowing the adequate heat transfer between fluid and roof.

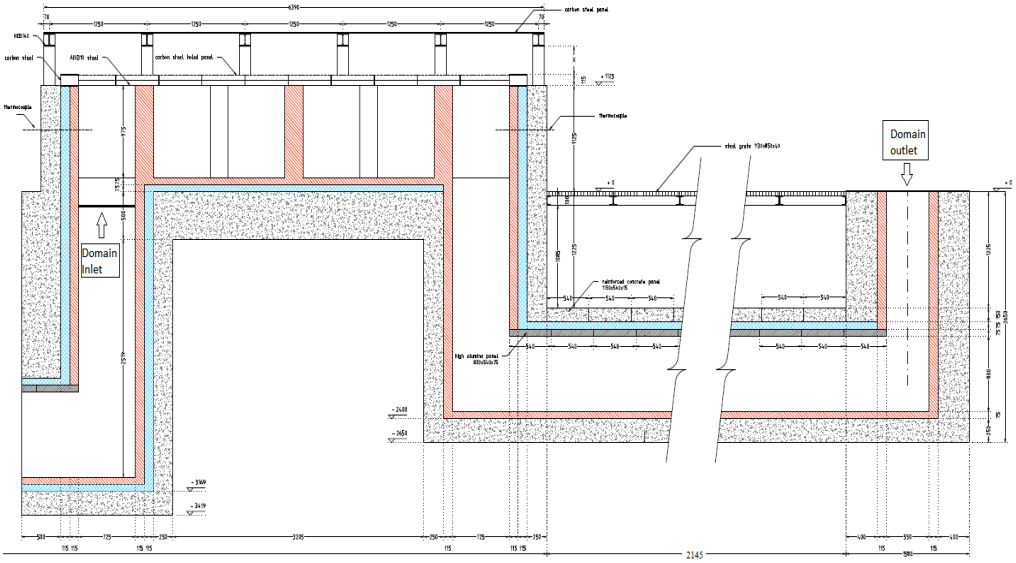

Section 4-2 Dryer + Duct B transverse section. Courtesy of DCHP

The whole part is symmetric with respect to the longitudinal coordinate, therefore only one half is modelled.

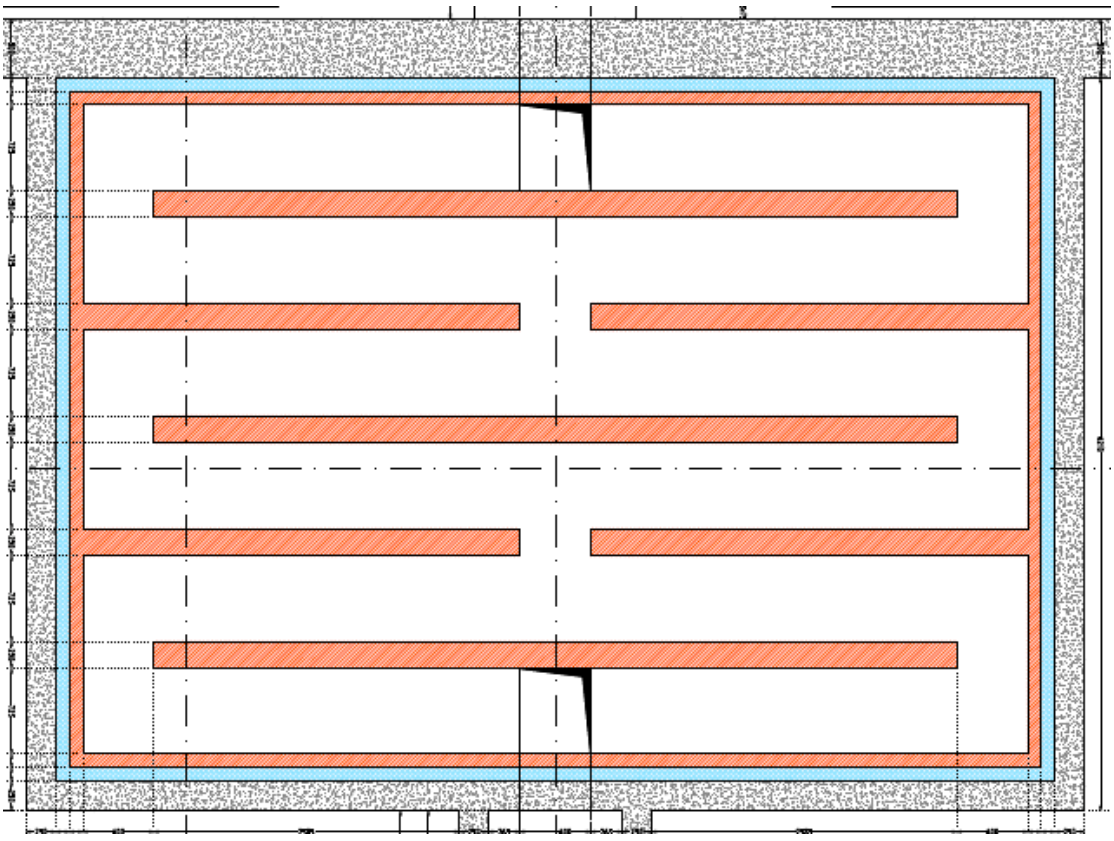

Section 4-3 Top view-section of the pre-heater. Two openings can be distinguished in the upper and in the lower part of the picture. Courtesy of DCHP

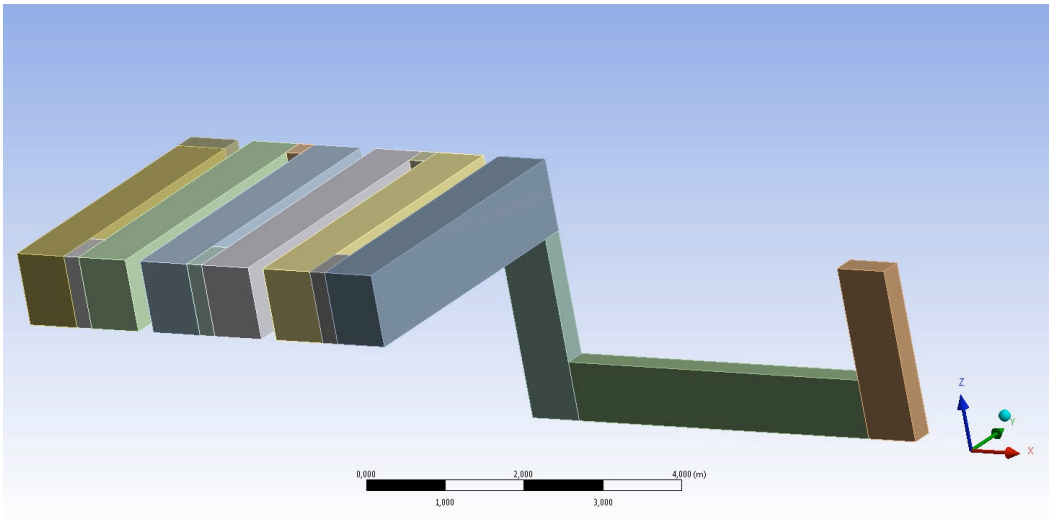

Figure 4-14 Global layout. Dryer and duct B

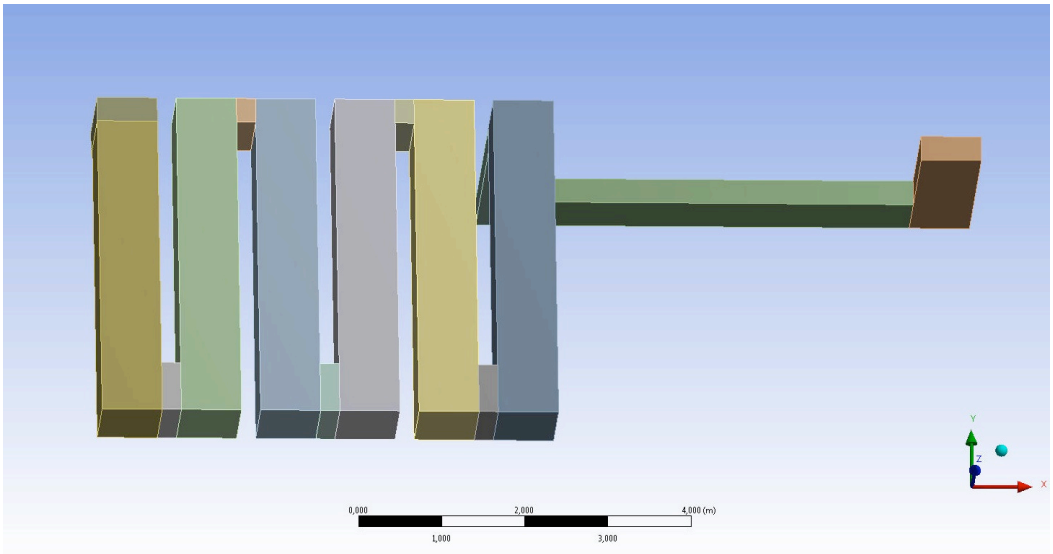

Figure 4-15 Dryer and duct B. Top view

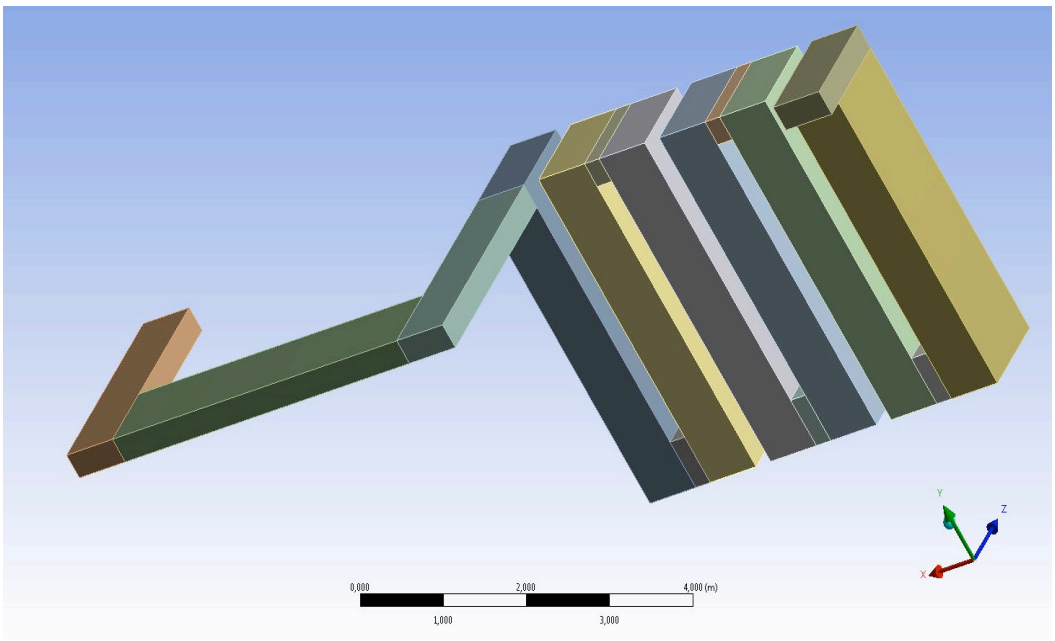

Figure 4-16 Dryer and duct B. Bottom view

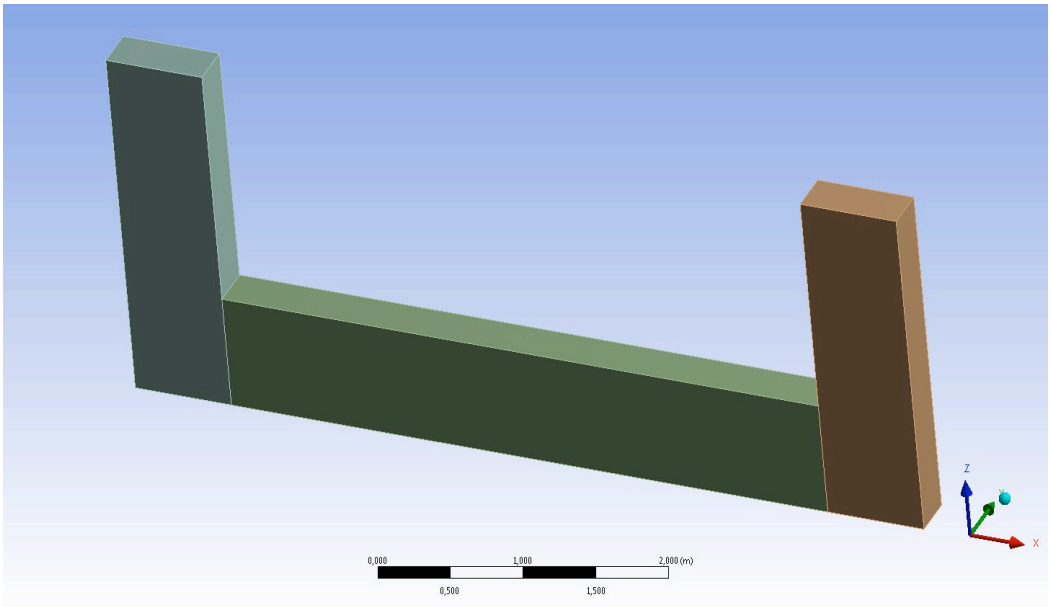

Figure 4-17 Duct B layout

4.3.2.2. Mesh generation

The Multi-Block grid generator is employed, thanks to the relative simplicity of domain, which can be sub-divided in several rectangles. The mesh quality is globally high. Particular care needs the choice of the inflation parameters.

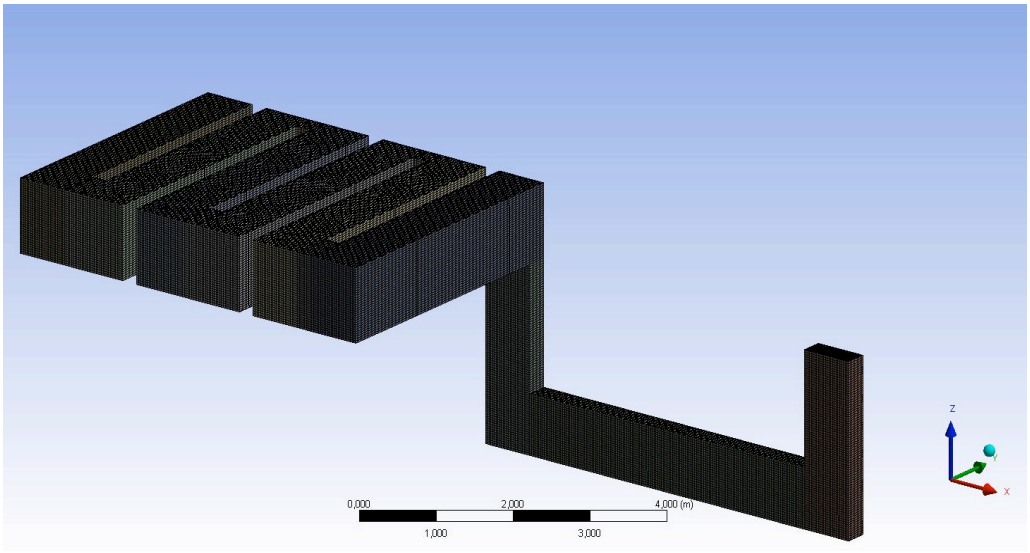

Figure 4-18 Global mesh layout

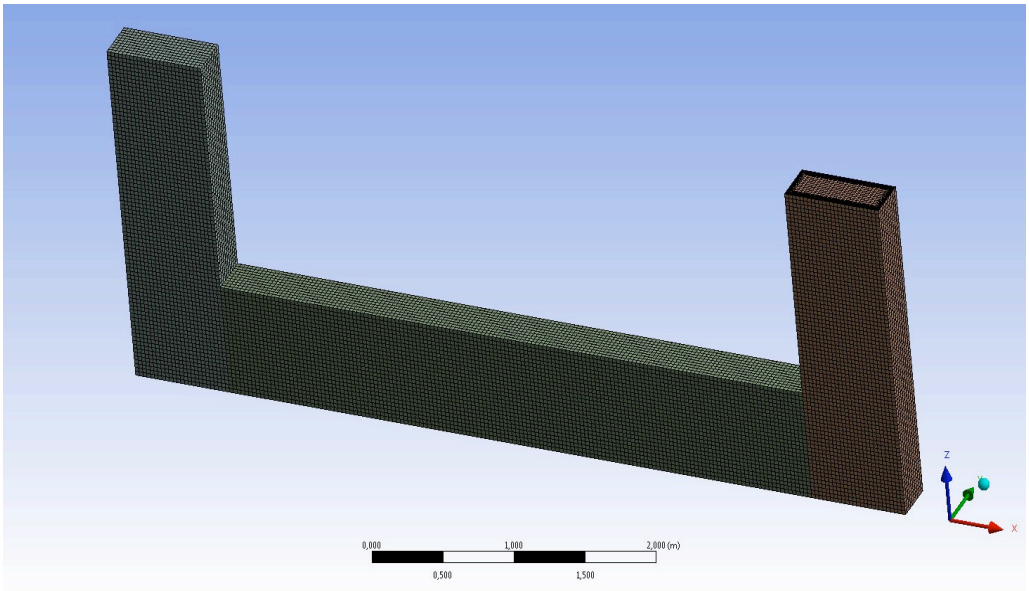

Figure 4-19 View of duct B

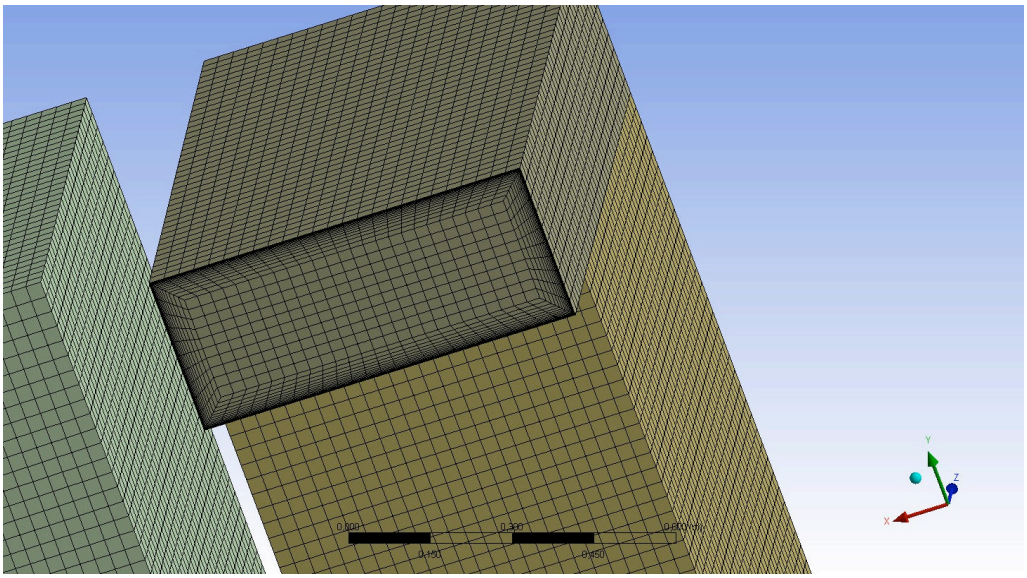

Figure 4-20 View of mesh and inflations at domain inlet

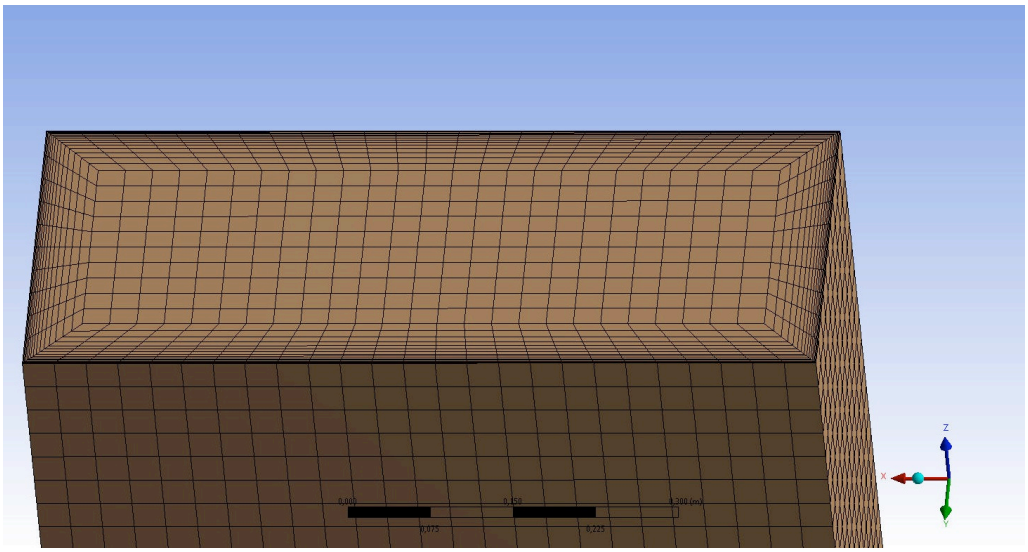

Figure 4-21 View of mesh and inflations at domain outlet

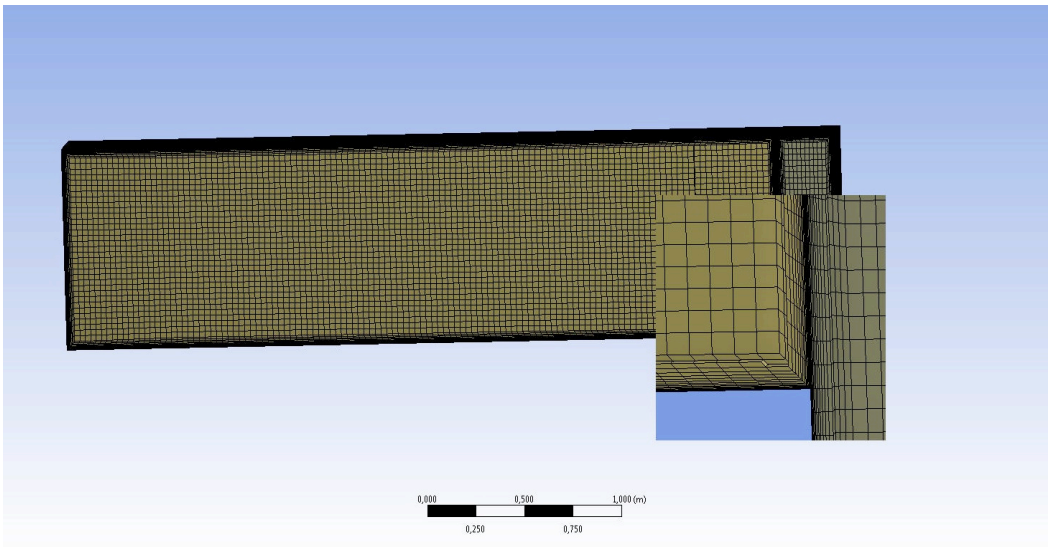

Figure 4-22 Dryer transverse section. Detail of inflations

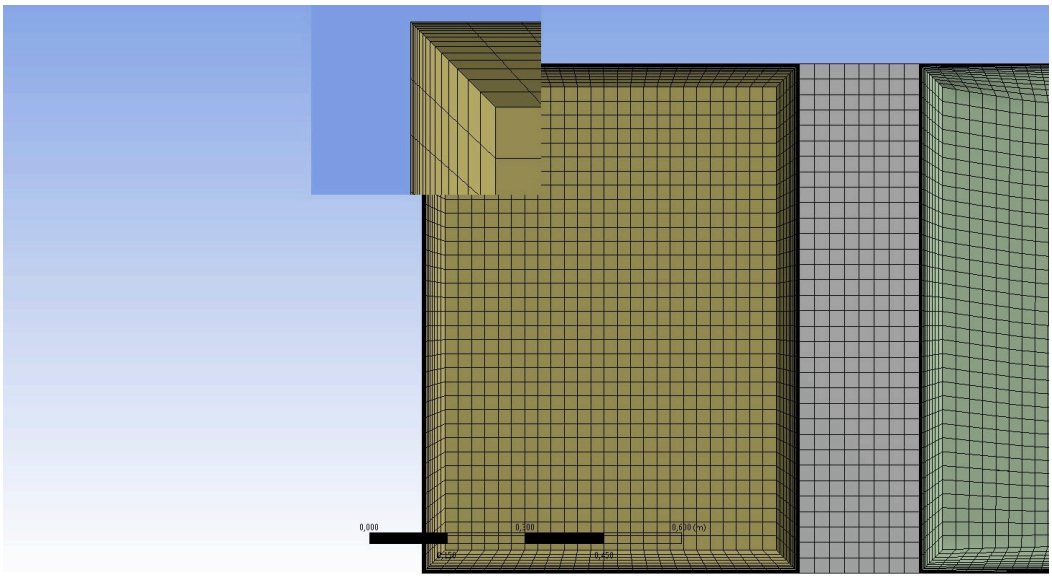

Figure 4-23 Dryer longitudinal section. Detail of inflations in the corner

4.3.2.3. Model Settings

In this section the general settings of the model are presented.

4.3.2.3.1. Solver

The solver general settings are reported in the following table:

Solver	Dimension	Time	Velocity formulation	Gradient option	Velocity-pressure coupling
Pressure-based	3D	Steady	Absolute	Least Squares Cell Based	SIMPLE

Table 4-8 Solver settings

4.3.2.3.2. Turbulence approach

The performance of two turbulence models is evaluated for the domain in question:

- k-ε Realizable;
- Reynolds Stress Model (RSM);

The aim of the comparison of the above mentioned models is to see what model can give better predictions, according to the computational resources required.

Near-Wall treatment: Enhanced Wall Treatment has been chosen. Fluent User Guide assures that this model offer a valid blended formulation in the case $y^+_{max}>11$.

4.3.2.3.3. Physical properties

Furnace exhaust gas is the working fluid. Its properties are:

	ρ [kg/m^3]	Cp [J/kg/K]	k [W/m/K]	μ [kg/m/s]	MM [kg/kmol]	T[K]
Flue gas	Incompressible ideal gas	1186.37	0.0242	3.263 e-05	27.68	723

Table 4-9 Working fluid properties

The adiabatic wall hypothesis is assumed. Since no heat flux is set as boundary condition, and the real distribution of temperature inside the domain is unknown, temperature is considered constant on first approximation. For this reason, a mean value between inlet and outlet is calculated.

6.1.1.1. Boundary conditions

- *Boundary conditions at domain openings are:*

  - Domain inlet: mass flow rate;
  - Domain outlet: outlet static pressure;

	Mass flow rate [kg/s]	Static Pressure case 1 [Pa]	Static Pressure case 2 [Pa]
Domain inlet	0.592	----	----
Domain outlet	----	-550.3	-478.3

Table 4-10 Boundary conditions at domain openings

The static pressure values reported in the table above were determined in the ejector-stack analysis. Case 1 refers to the result found through k-ε Realizable, while case 2 refers to the k-ω SST simulation.

- *Boundary conditions at the walls are:*

  - No-slip;
  - Adiabatic walls;

Domain walls are assumed as adiabatic. This statement is valid, on first approximation, for two reasons:

  - Walls are made of fire-bricks, which guarantee a high degree of insulation;
  - Duct B has an external cover made of concrete, ¾ of which are underground;

- *Boundary condition at the symmetry planes:*

  - Symmetry;

- *Turbulence and hydraulic diameter:*

Stream turbulence intensity and hydraulic diameter are chosen as boundary conditions for inlet and outlet. For this last opening properties are referred to backflow. As suggested in the Fluent User Guide, the 7% of the hydraulic diameter and near-unity values of turbulence intensity are set for the outlet.
Random turbulence intensity values are supposed, because no experimental data are available.

	Stream turbulence intensity [%]	Hydraulic diameter [mm]
Inlet	2	656.6
Outlet (backflow quantities)	3	50

Table 4-11 Boundary conditions for turbulence

4.3.2.4. Numerical Settings

Numerical settings are reported in this section.

4.3.2.4.1. Numerical Strategy

Initialisation: Hybrid initialisation was chosen.

Discretization scheme: A first order upwind scheme is used initially, then it is switched to second order upwind to limit the numerical diffusion.

	Equation of balance	Numerical Method
Preliminary flow field	Pressure	Standard
	Momentum	First Order Upwind
	Turbulence parameters	First Order Upwind
	Energy	First Order Upwind
Final results	Pressure	Second Order Upwind
	Momentum	Second Order Upwind
	Turbulence parameters	Second Order Upwind
	Energy	Second Order Upwind

Table 4-12 Numerical scheme settings

Under-relaxation factors: It is important to keep really small factors whenever RSM is employed for the stability of the numerical scheme.

	Equation of balance	Realizable k-ε	RSM
Preliminary flow field	Pressure	0.3	0.2
	Density	0.5	0.3
	Body Forces	0.5	0.3
	Momentum	0.5	0.3
	Turbulent Kinetic Energy	0.6	0.2
	Turbulent Dissipation Rate	0.6	0.2
	Turbulent Viscosity	0.7	0.2
	Energy	0.8	0.4
	Reynolds Stresses	------	0.1

Final results	Pressure	0.3	0.3
	Density	0.7	0.5
	Body Forces	0.7	0.5
	Momentum	0.8	0.5
	Turbulent Kinetic Energy	0.9	0.4
	Turbulent Dissipation Rate	0.9	0.4
	Turbulent Viscosity	1	0.4
	Energy	1	0.6
	Reynolds Stresses	------	0.1

Table 4-13 Solution controls

As result, RSM will require much more time to converge to solution than Realizable k-ε, since every balance equations output (for each step of the iterative process) is reduced of the corresponding factor before being introduced in the next step.

4.3.2.5. Convergence controls

Solution reached convergence if the following criteria are all satisfied:

- Residuals magnitude is at least in the range of 1E-04, continuity equation residual is in the range of 1E-03;
- Area-weighed-averaged static pressure at domain inlet reached stable value;
- Net mass flow rate outlet-inlets at least is in the range 1E-07 kg/s;

4.3.3. Duct A

In this section the duct A, which connects the furnace bottom with the dryer, is examined.

4.3.3.1. Domain Overview and Geometry Definition

The longitudinal section of the duct A is shown:

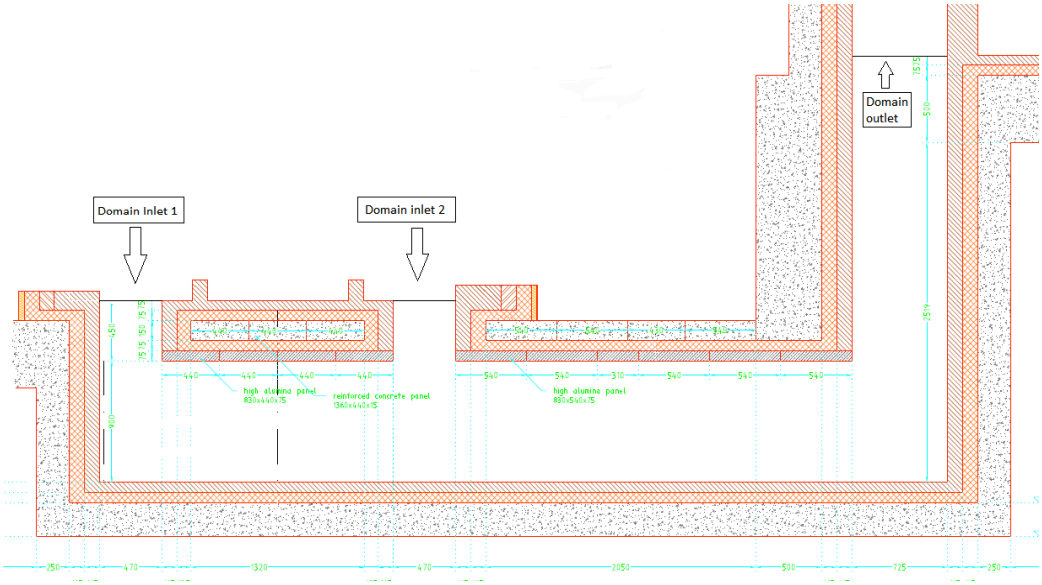

Section 4-4 Longitudinal section of duct A. Courtesy of DCHP

The geometry consists of two small square-sectioned inlets, which descend directly from the furnace bottom, and a square sectioned duct with a 90° straight elbow. It is noticeable the symmetry with respect to the longitudinal coordinate, hence only one half of the whole part is modelled.

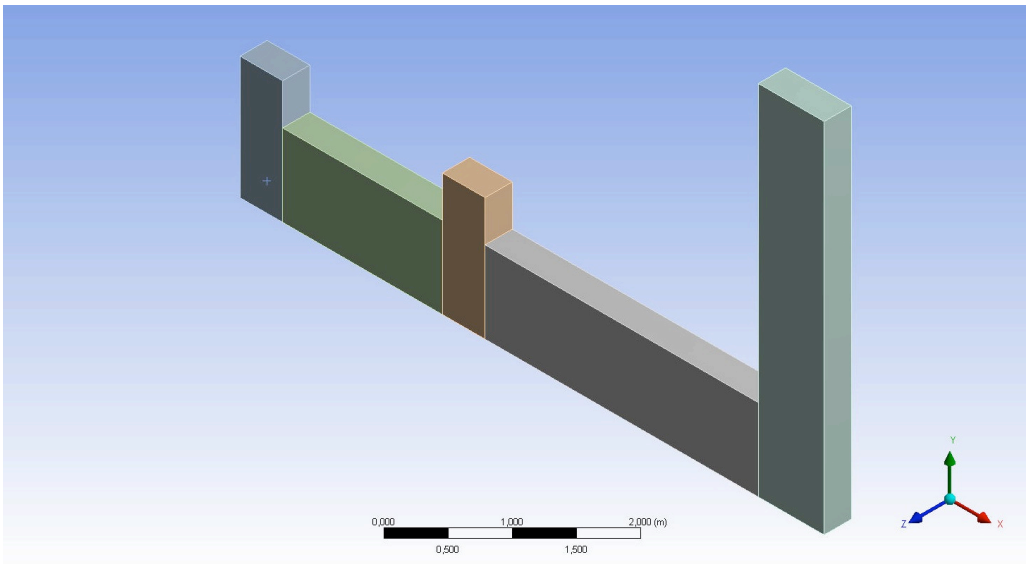

Figure 4-24 Duct A layout

4.3.3.2. Mesh generation

Duct A is breakable into parallelepipeds of different sizes, therefore it is possible to employ multi-block technique for grid generation. The resulting arrays of hexahedral elements constitute a high quality mesh.

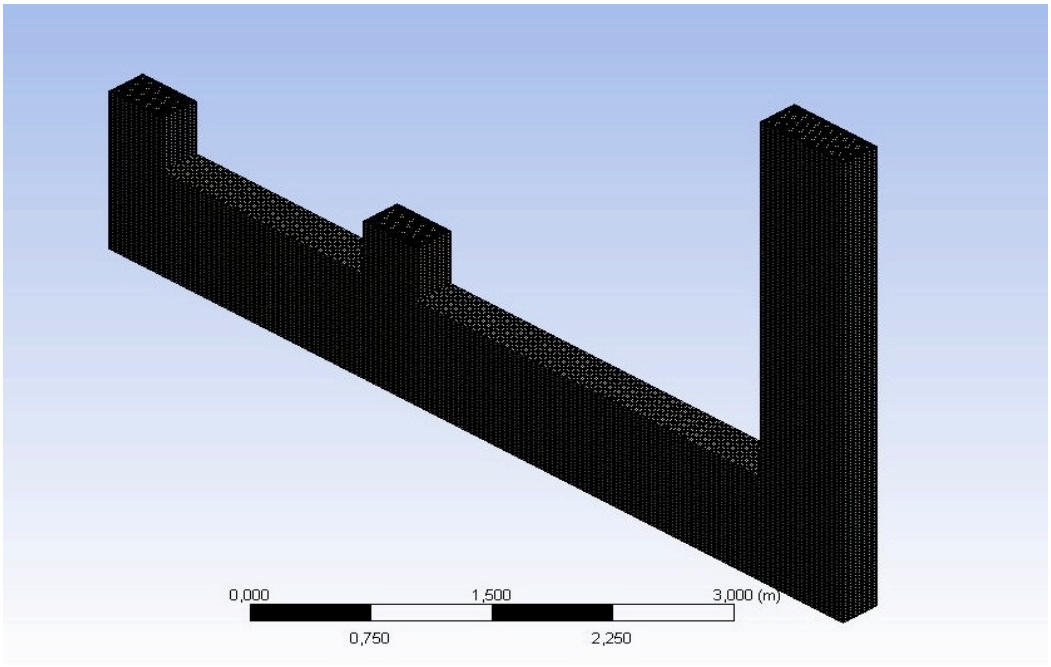

Figure 4-25 Duct A grid. Global view

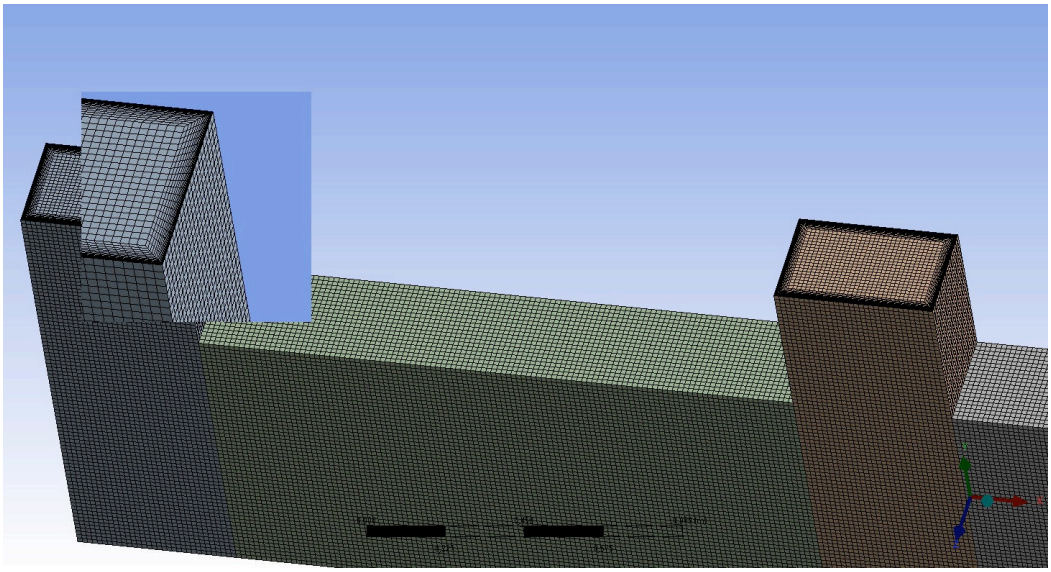

Figure 4-26 Duct A grid. Detail of inflations

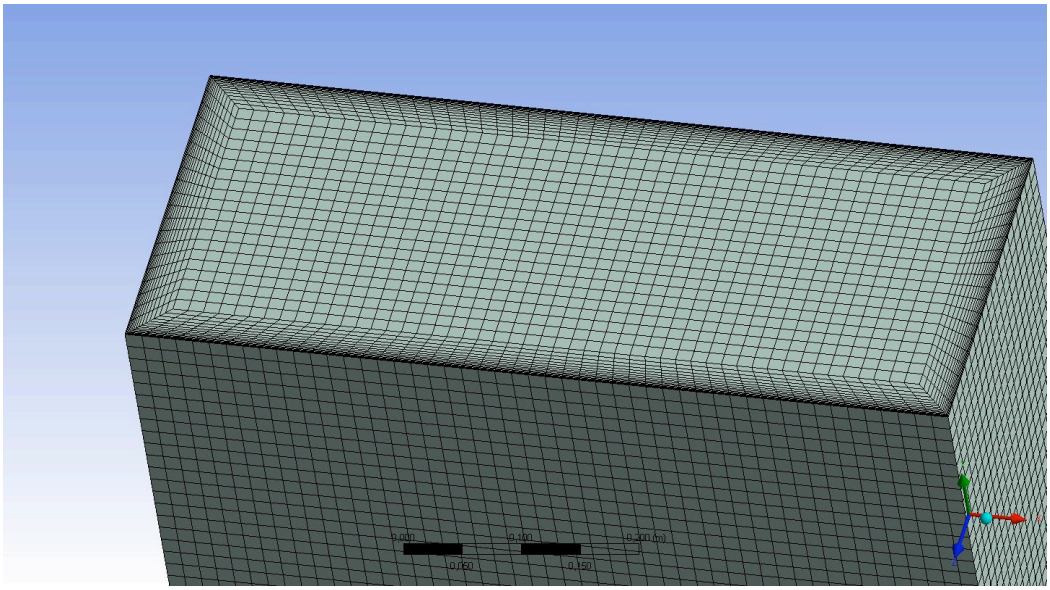

Figure 4-27 Duct A grid. Domain exit

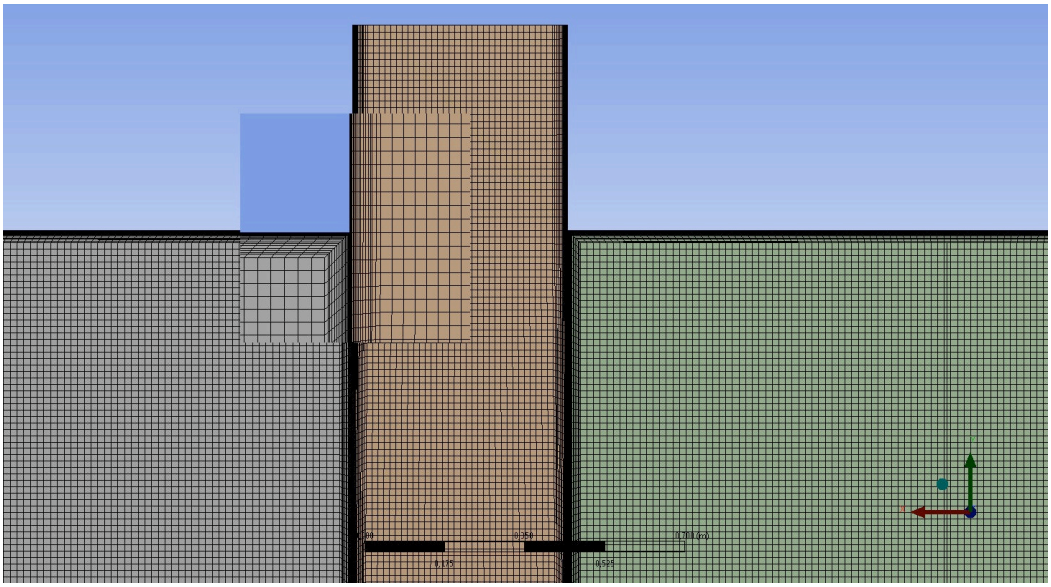

Figure 4-28 Duct A grid. Longitudinal section. Detail of the inflations on each side of the parallelepipeds

4.3.3.3. Model settings

In this section the general settings of the model are presented.

4.3.3.3.1. Solver

The solver general settings are reported in the following table:

Solver	Dimension	Time	Velocity formulation	Gradient option	Pressure-velocity coupling
Pressure-based	3D	Steady	Absolute	Least Squares Cell Based	SIMPLE

Table 4-14 Solver settings for duct A

4.3.3.3.2. Turbulence approach

The turbulence model chosen to represent the fluid flow in the duct is:

- k-ε Realizable;

The reason the choice, even though the domain is a square sectioned duct, is that in the duct B + dryer part RSM gave a static pressure at domain inlet comparable with the Realizable, although velocity field were totally different. Hence the less computational expensive model is used.

Near-Wall treatment: Enhanced Wall Treatment has been chosen. The first inflation layer thickness of 1 mm gives values of $y^+ < 5$ everywhere, which is the appropriate range for the correct resolution of the viscous boundary layer.

4.3.3.3.3. Physical properties

Working fluid is the same furnace exhaust gas considered in the previous chapters. Its physical properties do not vary, with exception of the fluid temperature, which is a mean value between the inlet and the outlet temperatures.

	ρ [kg/m^3]	Cp [J/kg/K]	k [W/m/K]	μ [kg/m/s]	MM [kg/kmol]	T [K]
Flue gas	Incompressible ideal gas	1186.37	0.0242	3.263 e-05	27.68	948

Table 4-15 Working fluid properties

The working fluid is a mixture of carbon dioxide, water vapour and nitrogen, which do not to react each other. Its temperature is assumed fixed along the duct on first approximation, because of the adiabatic walls hypothesis and the unknown fluid temperature profile in the domain.

4.3.3.3.4. Boundary conditions

- *Boundary conditions at domain openings are:*

    - Domain inlet 1: mass flow rate;
    - Domain inlet 2: mass flow rate;
    - Domain outlet: outlet static pressure;

	Domain inlet 1	Domain inlet 2	Domain outlet
Mass flow rate [kg/s]	0.296	0.296	------
Static Pressure Case 1 [Pa]	------	------	-494.
Static Pressure Case 2 [Pa]	------	------	-422

Table 4-16 Boundary conditions at domain openings

- *Boundary conditions at the walls are:*

    - No-slip;
    - Adiabatic walls;

Here the hypothesis of adiabatic walls is assumed reasonable because:

    - The duct lies completely underground. It is internally made of fire bricks, which give good thermal insulation, while the external cover is made of concrete.
    - This study is a primary calculation. Further improvements beyond this assumption could be investigated in future.

- *Boundary condition at the symmetry planes:*

    - Symmetry;

- *Turbulence and hydraulic diameter:*

Stream turbulence intensity and hydraulic diameter have been chosen as boundary conditions for the two inlets and the outlet. Random turbulence intensity values are specified, since no experimental data are available.

	Stream turbulence intensity [%]	Hydraulic diameter [mm]
Inlet 1	1	527.1
Inlet 2	1	527.1
Outlet (backflow quantities)	2	46

Table 4-17 Boundary conditions for turbulence

4.3.3.4. Numerical Settings

Numerical settings are reported in this section.

4.3.3.4.1. Numerical Strategy

Initialisation: Hybrid initialisation is chosen.

Discretization scheme: A first order upwind scheme is adopted for the first few hundred iterative steps. Then it is switched to second order upwind, to limit the numerical diffusion problem typical of the first order.

	Equation of balance	Numerical Method
Preliminary flow field	Pressure	Standard
	Momentum	First Order Upwind
	Turbulence parameters	First Order Upwind
	Energy	First Order Upwind
Final results	Pressure	Second Order Upwind
	Momentum	Second Order Upwind
	Turbulence parameters	Second Order Upwind
	Energy	Second Order Upwind

Table 4-18 Numerical scheme settings

Under-relaxation factors: Realizable is considerably stable, hence it requires only a slight factors reduction in the preliminary iterations.

Turbulence model	Equation of balance	Preliminary flow field	Final results
Realizable k-ε	Pressure	0.3	0.3
	Density	0.5	0.7
	Body Forces	0.5	0.7
	Momentum	0.5	0.8
	Turbulent Kinetic Energy	0.6	0.9
	Turbulent Dissipation Rate	0.6	0.9
	Turbulent Viscosity	0.7	1
	Energy	0.8	1

Table 4-19 Solution controls

4.3.3.4.2. Convergence controls

Solution reached convergence if the following criteria are all satisfied:

- Residuals magnitude is at least in the range of 1E-03;
- Area-weighed-averaged static pressure at domain inlets reached stable value;
- Net mass flow rate outlet-inlets is below 1E-07 kg/s;

4.3.4. Duct A + damper

In this section a damper is introduced in the duct A to obtain the negative static pressure required for the correct furnace operation. The lowering of this device physically creates a localized pressure drop, which mitigates the suction force upstream in the furnace chamber.

4.3.4.1. Domain Overview and Geometry Definition

The following section shows the domain. The geometry is essentially the same of duct A except for the damper, which consists of a wall that obstructs the fluid flow.

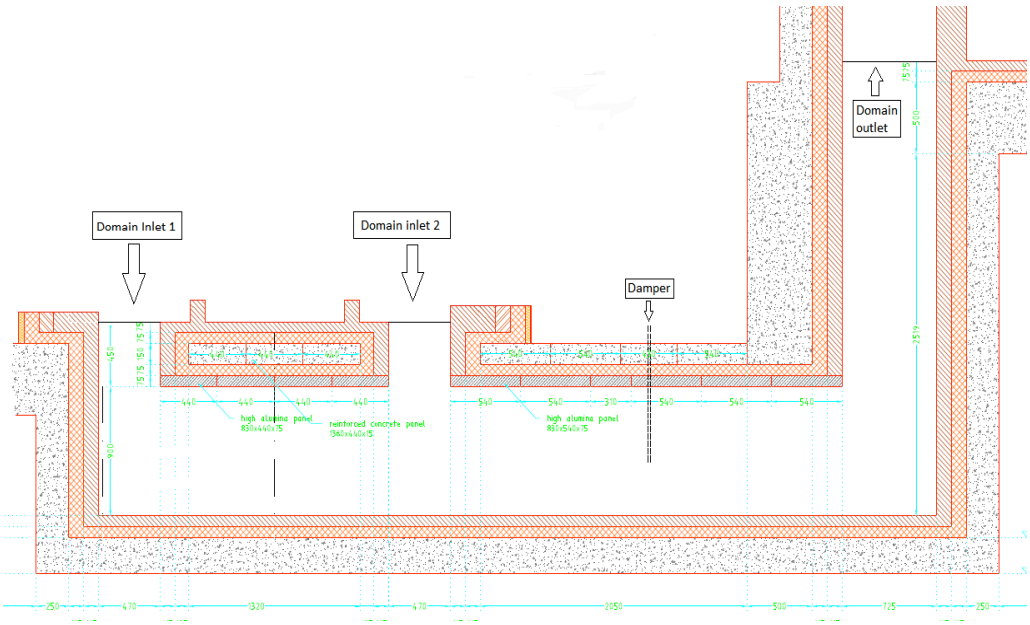

Section 4-5 Longitudinal section, duct A + damper. Courtesy of DCHP

Thanks to the symmetry with respect to the longitudinal axis, only one half of the whole part is considered.

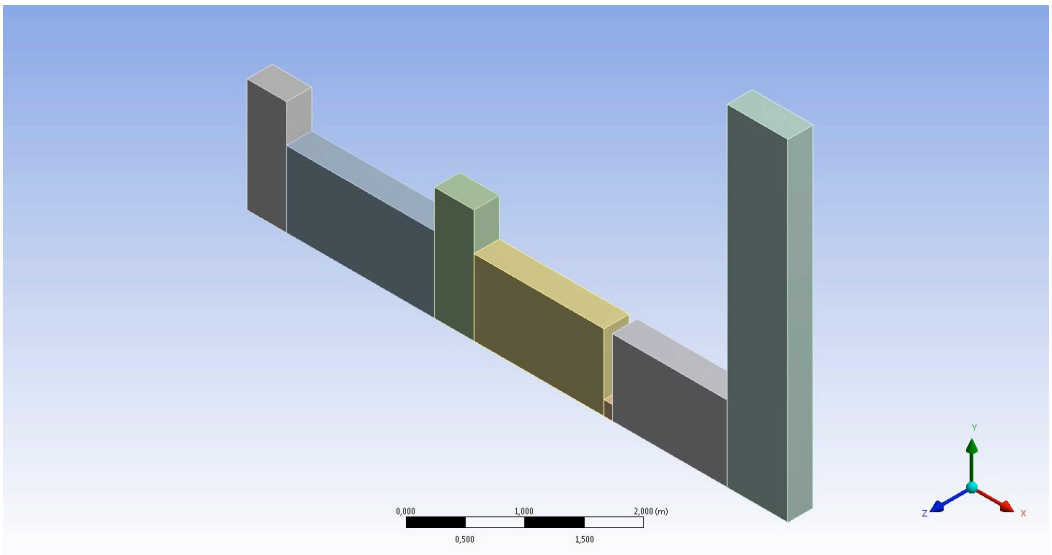

Figure 4-29 Duct A + damper. Global view

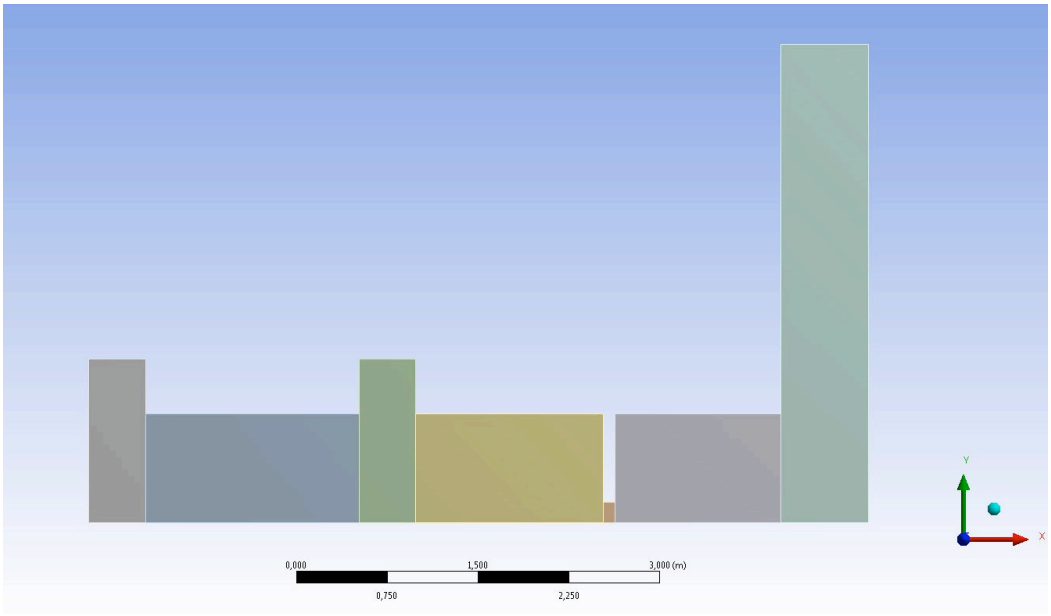

Figure 4-30 Duct A + damper. Side view

4.3.4.2. Mesh generation

The domain is still breakable into several parallelepipeds, hence multi-block technique can be employed for grid generation. The presence of the damper does not determine any substantial decrease of elements quality. However inflations are finer to take account of the narrow channel under the damper, where fluid flow is expected to accelerate.

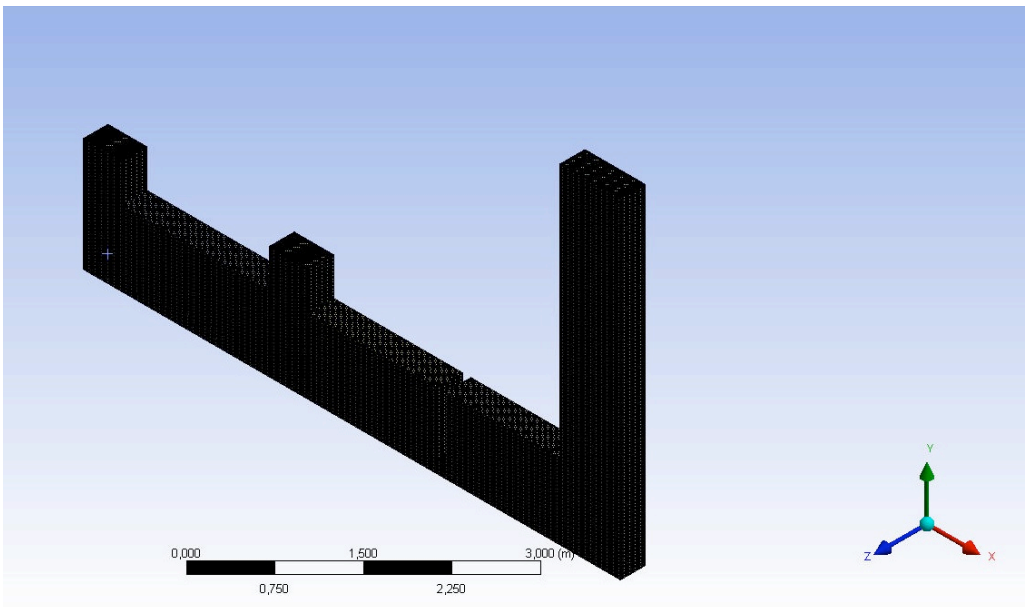

Figure 4-31 Duct A + damper. Mesh

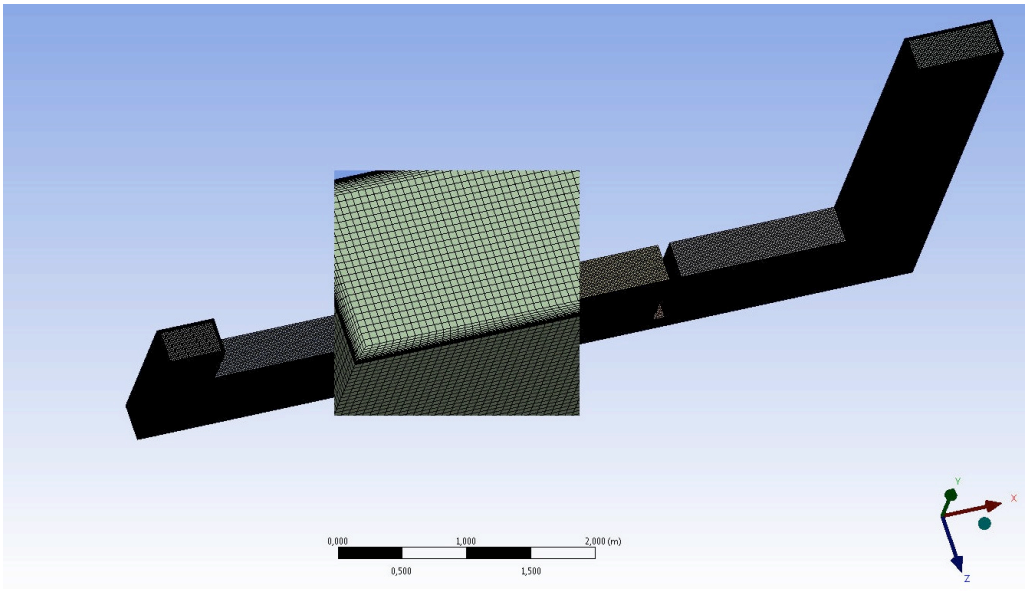

Figure 4-32 Duct A + damper. Mesh, detail of inlet 2

4.3.4.3. Model Settings

In this section general settings of the model are presented.

4.3.4.3.1. Solver

The solver general settings reported in the table are the same of the previous case:

Solver	Dimension	Time	Velocity formulation	Gradient option	Pressure-Velocity coupling
Pressure-based	3D	Steady	Absolute	Least Squares Cell Based	SIMPLE

Table 4-20 Solver settings for duct A + damper

4.3.4.3.2. Turbulence approach

Realizable k-ε is the turbulence model employed in this section.

Near-Wall treatment: Enhanced Wall Treatment is adopted.

4.3.4.3.3. Physical properties

Exhaust gas from burners is the working fluid. Physical properties do not vary in this section with respect to the previous case:

	ρ [kg/m^3]	Cp [J/kg/K]	k [W/m/K]	μ [kg/m/s]	MM [kg/kmol]	T [K]
Flue gas	Incompressible ideal gas	1186.37	0.0242	3.263 e-05	27.68	948

Table 4-21 Working fluid properties

4.3.4.3.4. Boundary conditions

- *Boundary conditions at domain openings are:*

  - Domain inlet 1: mass flow rate;
  - Domain inlet 2: mass flow rate;
  - Domain outlet: outlet static pressure;

	Domain inlet 1	Domain inlet 2	Domain outlet
Mass flow rate [kg/s]	0.296	0.296	------
Static Pressure Case 1 [Pa]	------	------	-494
Static Pressure Case 2 [Pa]	------	------	-422

Table 4-22 Boundary conditions at domain openings

- *Boundary conditions at the walls are:*

  - No-slip;
  - Adiabatic walls;

- *Boundary condition at the symmetry planes:*

  - Symmetry;

- *Turbulence and hydraulic diameter:*

Stream turbulence intensity and hydraulic diameter have been chosen as boundary conditions for the two inlets and the outlet.

	Stream turbulence intensity [%]	Hydraulic diameter [mm]
Inlet 1	1	527.1
Inlet 2	1	527.1
Outlet (backflow quantities)	1	46

Table 4-23 Boundary conditions for turbulence

4.3.4.4. Numerical Settings

Numerical settings are reported in this section.

4.3.4.4.1. Numerical Strategy

Discretization scheme: First order upwind scheme is adopted for the first iterative steps. It is then switched to second order upwind.

	Equation of balance	Numerical Method
Preliminary flow field	Pressure	Standard
	Momentum	First Order Upwind
	Turbulence parameters	First Order Upwind
	Energy	First Order Upwind
Final results	Pressure	Second Order Upwind
	Momentum	Second Order Upwind
	Turbulence parameters	Second Order Upwind
	Energy	Second Order Upwind

Table 4-24 Numerical scheme settings

Under-relaxation factors: In the table values for preliminary calculation and for developed fluid flow are shown.

	Equation of balance	Realizable k-ε
Preliminary flow field	Pressure	0.3
	Density	0.5
	Body Forces	0.5
	Momentum	0.5
	Turbulent Kinetic Energy	0.6
	Turbulent Dissipation Rate	0.6
	Turbulent Viscosity	0.7
	Energy	0.8

Final results	Pressure	0.3
	Density	0.8
	Body Forces	0.8
	Momentum	0.7
	Turbulent Kinetic Energy	0.9
	Turbulent Dissipation Rate	0.9
	Turbulent Viscosity	1
	Energy	1

Table 4-25 Solution controls

4.3.4.4.2. Convergence controls

Solution reached convergence if the following criteria are all satisfied:

- Residuals magnitude is at least in the range of 1E-05. For continuity equation residual order of magnitude is1E-03;
- Area-weighed-averaged static pressure at domain inlets reached stable value;
- Net mass flow rate outlet-inlets is below 1E-07 kg/s;

Chapter 5 **Post-processing**

In this chapter are reported and discussed simulation results for each domain presented in the previous sections.

5.2 Ejector-stack

5.2.2 Grid independence study

Three different grids with different element size but fixed inflation height at boundaries are analyzed: a coarse, a medium-size and a fine one. Realizable k-ε is the model employed to determine the static pressure at secondary flow. Significant results are shown in the table.

Number of elements	Outlet static pressure [Pa]	Fumes inlet static pressure [Pa]	Δ [%]
1,100,352	0	-734.1	33.3
2,315,881	0	-550.3	0.3
3,404,633	0	-551.5	-----

Table 5-1 Grid independence. Monitored point and percentage difference

Assumed the finer grid as reference, the medium size grid result is practically equal to the first, while the coarse one estimates a totally different pressure.
To establish what is the best grid for calculation other comparisons are required. Thus velocity values are sampled in 40 different points along the x axis on the symmetry plane:

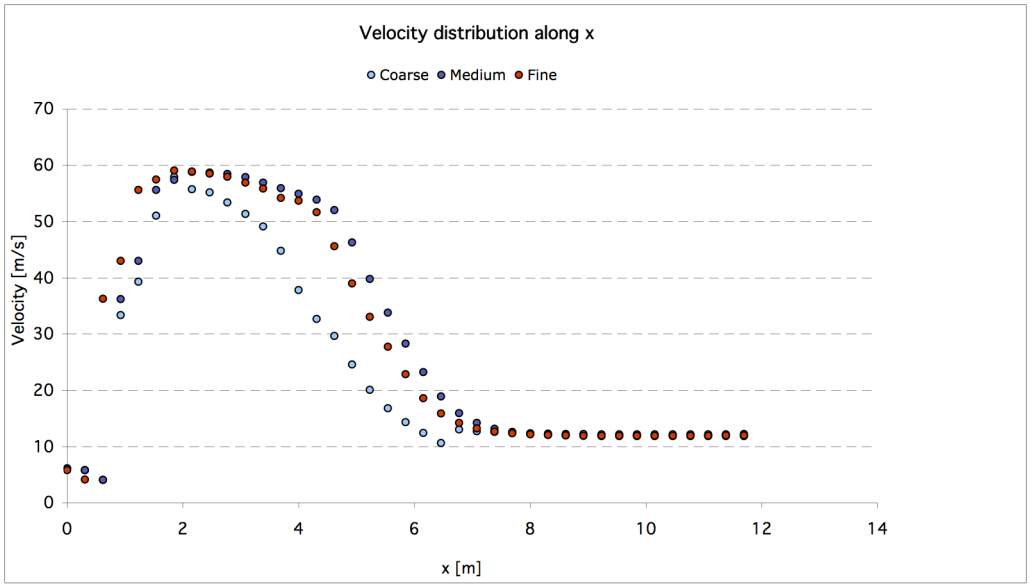

Figure 5-1 Axial velocity comparison between coarse, medium and fine grids. Values are sampled in 40 point along the x-axis on the simmetry plane.

In the suction and in the mixing zone is evident the higher discrepancy between the coarse and the other two grids, which on the other hand show a more similar trend.
Wall shear stress mean section values are then calculated in 5 different planes along the device. Even if a few samples are taken, big discrepancies with the other two grids are evident in the case of coarse mesh. The medium-size and the fine one are generally in good agreement.

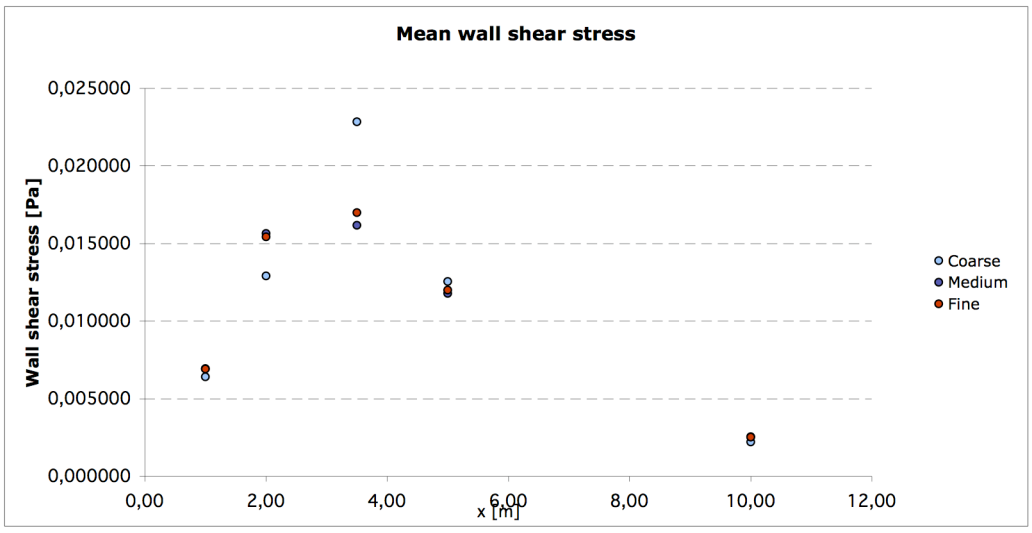

Figure 5-2 Mean wall shear stress comparison between grids on 5 different section planes.

Considering the results presented above, the usage of the medium size grid is justifiable. It guarantees accurate predictions at a reasonable computational cost. A finer mesh would produce the same results but with more computational expense, a coarser would produce a unreliable solution.

5.2.3 Results

Realizable k-ε and SST k-ω are employed to obtain the static pressure at ejector's fume flow inlet, being these two the most promising models, according to the literature review presented. The first is adequate for a wide range of generic problems, while the second gives well predictions in presence of swirling flows, reattachment and detachments and recirculation.
Results are reported in the following table:

	Turbulence models	
	k-ε Realizable	**k-ω SST**
Outlet pressure [Pa]	0	0
Result [Pa]	-550.3	-478.3
Δ Results [%]	15	----
Measured inlet [Pa]	- 480	- 480
Δ Result - Measured [%]	16.7	1.7

Table 5-2 Ejector-stack simulation results

The accuracy of the pressure measurement is 0.5 mbar.
It is noticeable that SST k-ω provides a value close to the measured data, while Realizable k-ε gives a slightly different result. The reasons of this discrepancy resides, as explained above, in the mathematical treatment of the turbulence. Anyway it is useful to investigate the development of some physical quantities along the device. As for the grid independence study, an axial velocity over 40 points is useful to have an idea of where there are significant differences between the two models.

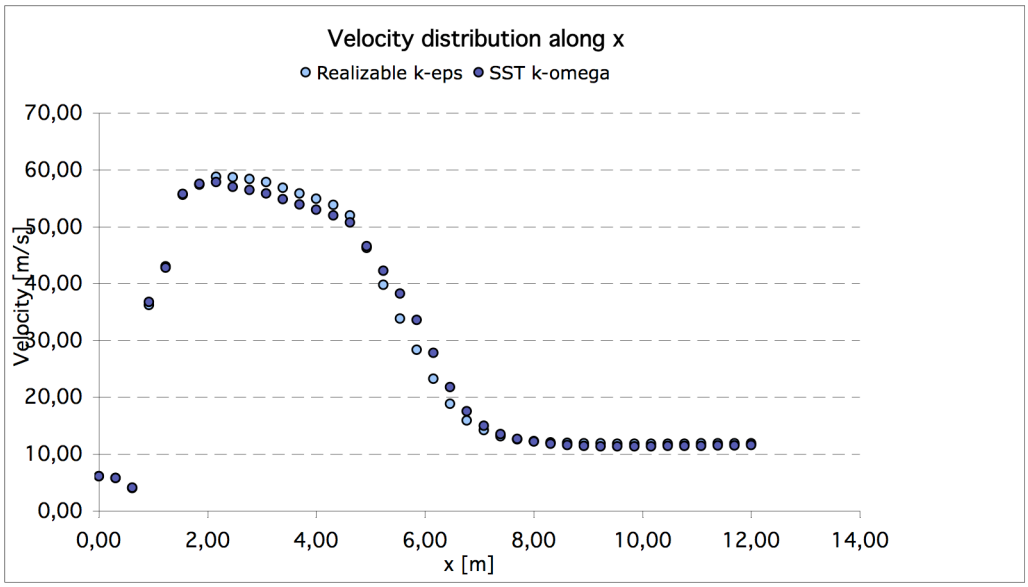

Figure 5-3 Axial velocity comparison over 40 points along the x-axis on the simmetry plane.

Axial velocity predictions are slightly different in the suction chamber, in the primary pipe and in the mixing section, while tend to the same values once the streams are mixed and the pressure field is stabilized.
A mean wall shear stress comparison on different section planes is again proposed for the analyzed cases:

	x [m]	SST [Pa]	Realizable [Pa]	Δ [%]
Suction1-plane	1,00	0,007605	0,006929	9,77
Suction2-plane	2,00	0,017928	0,015637	14,65
Diff-plane	5,00	0,005846	0,011777	50,36
Mixing-plane	3,50	0,010322	0,016164	36,14
Stack-plane	10,00	0,003470	0,002532	37,05

Table 5-3 Mean wall shear stress at sections

It is useful now to consider a series of velocity profiles along the ejector diameter (y axis), in order to quantify the local variation of the velocity in the two cases.
Starting from the suction chamber, moving to different locations on the x axis with the transverse coordinate fixed (z=0), the following figures represent the punctual velocities distributions along the y axis.

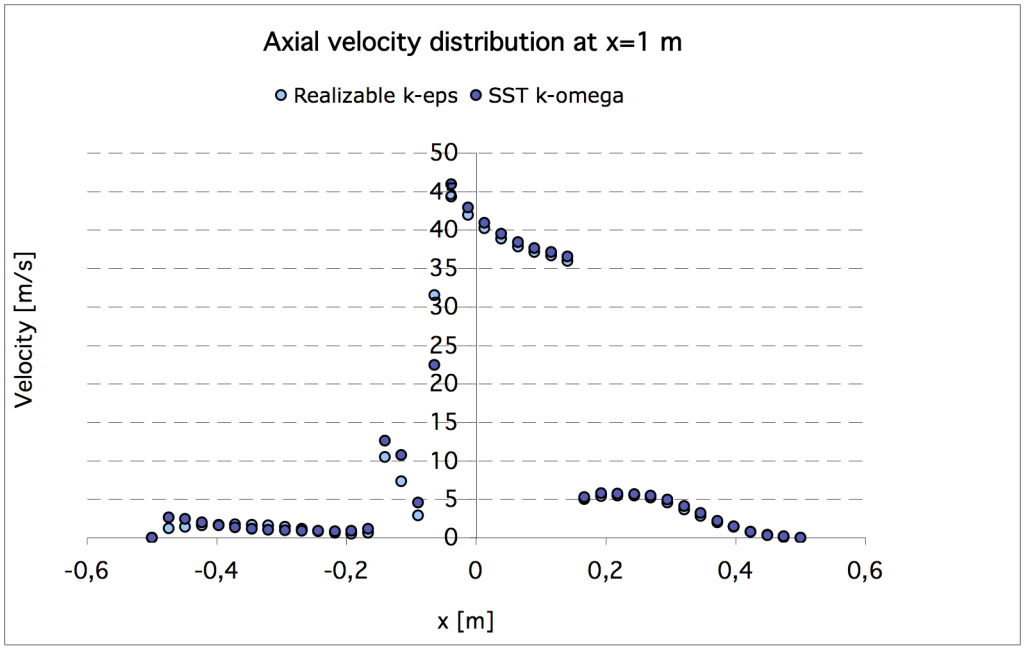

Figure 5-4 Axial velocity distribution in the suction chamber

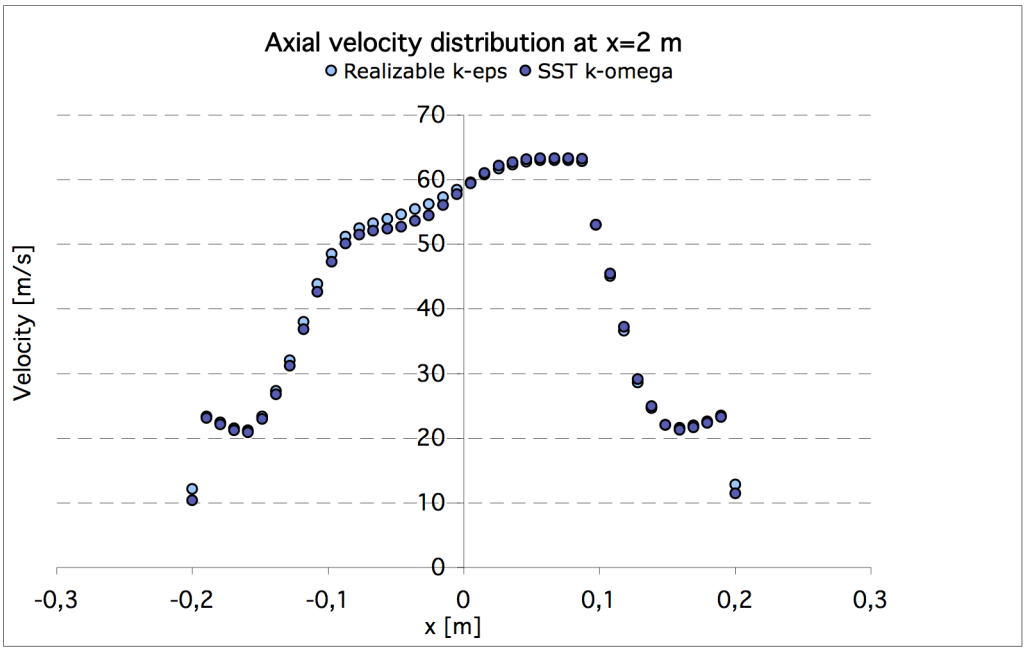

Figure 5-5 Axial velocity distribution near at the mixing section inlet

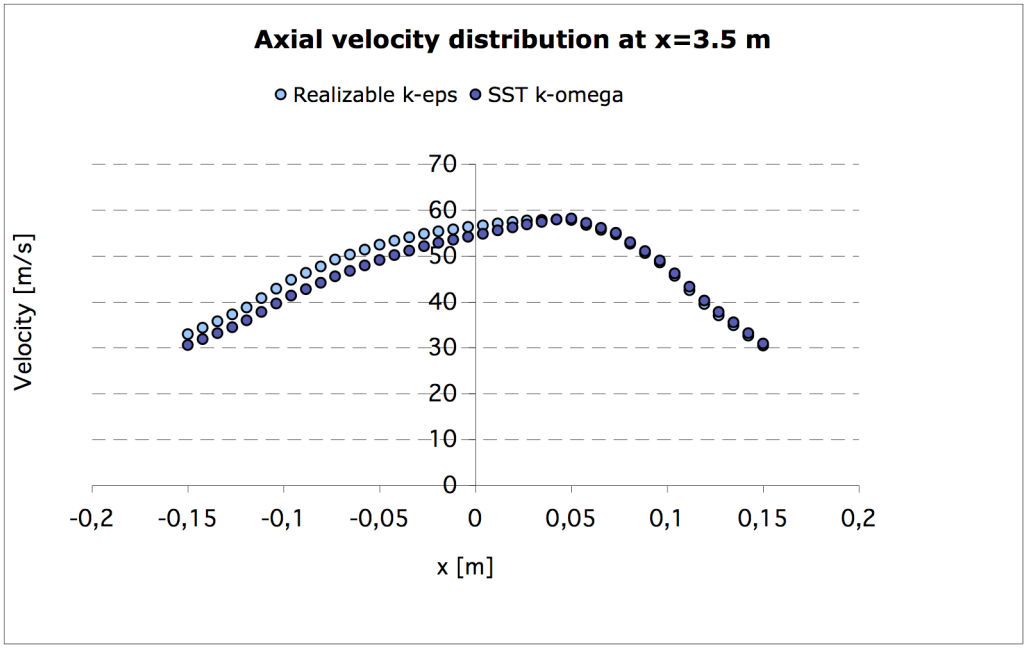

Figure 5-6 Axial velocity distribution in the mixing section inlet

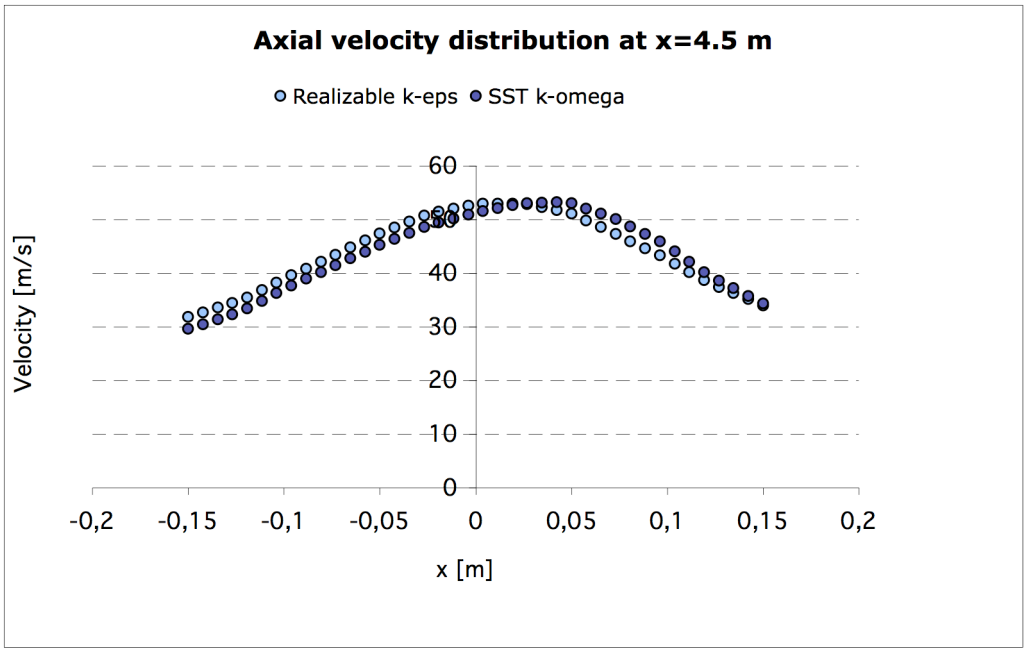

Figure 5-7 Axial velocity distribution near the mixing section outlet

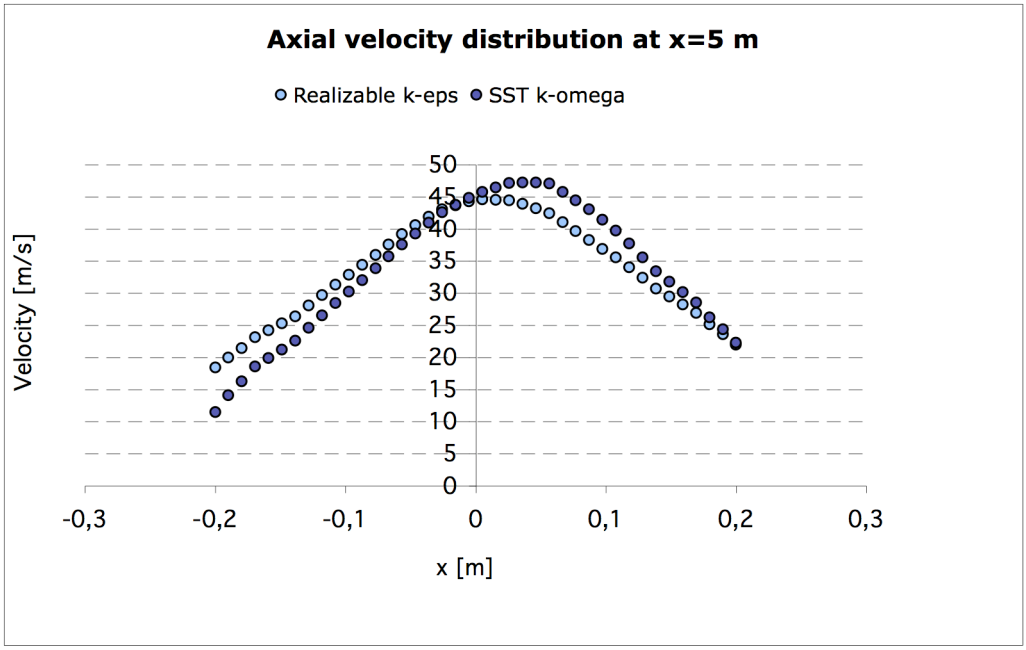

Figure 5-8 Axial velocity distribution in the diffuser

These last plots presented above show that the two velocity fields are not symmetric with respect to the x axis, and their discrepancy increases with the coordinate x. This can be distinguished better looking at the contours added later.

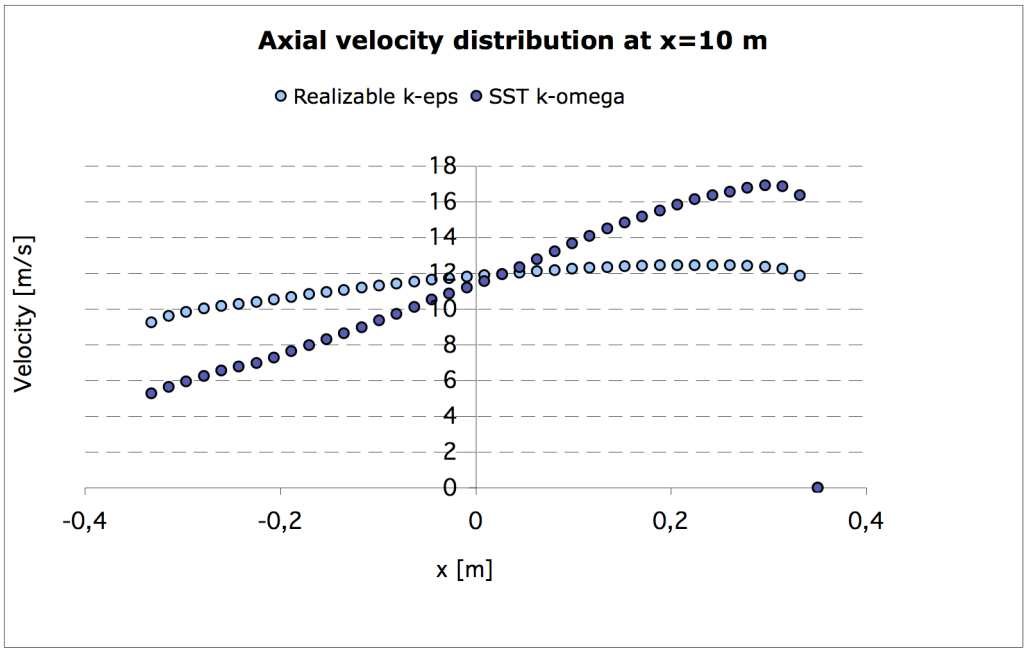

Figure 5-9 Axial velocity distribution near the stack entrance, where high recirculation is provided by the SST model.

The velocity distribution at x=10 m show the strong flow recirculation captured with SST k-ω, while k-ε Realizable predicts a more uniform pattern.
The following images are helpful for the visualization of this phenomenon, which could be explained as a physical consequence of the 90° bend of the primary pipe. The air stream is heavily influenced by the inertia forces developed along the bend, which determine an asymmetric distribution of the velocity at the nozzle. This effect propagates along the mixing chamber and the diffuser, where the pressure increases. The volume of fluid at lower velocity is then entrained, and recirculation occurs.

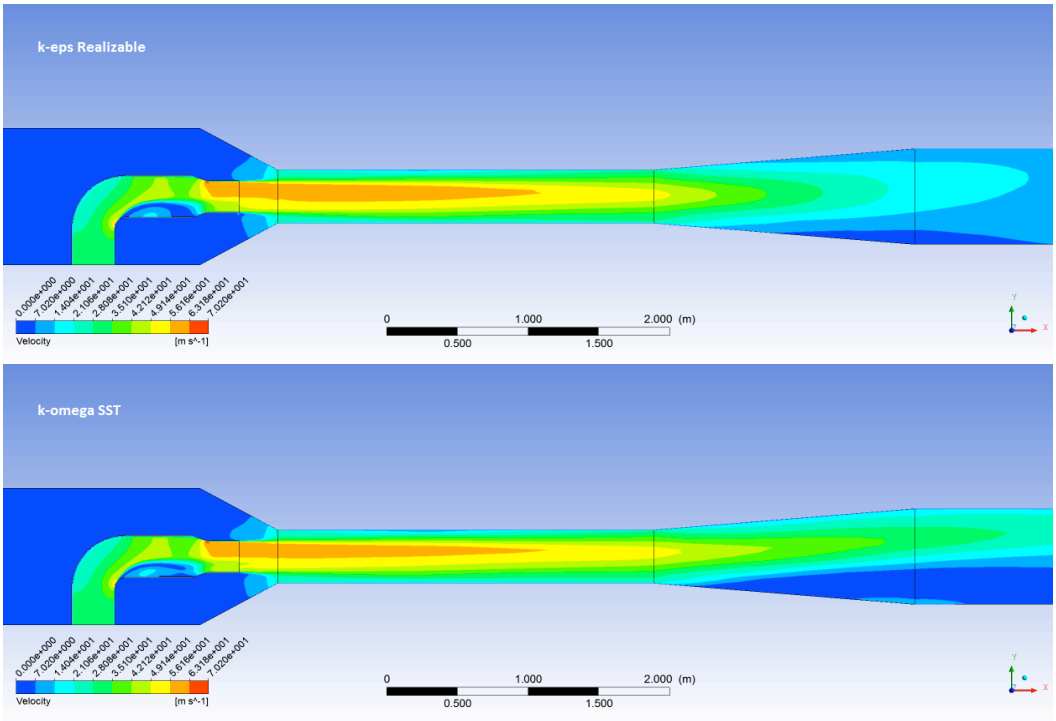

Figure 5-10 Velocity contours. Details of ejector components

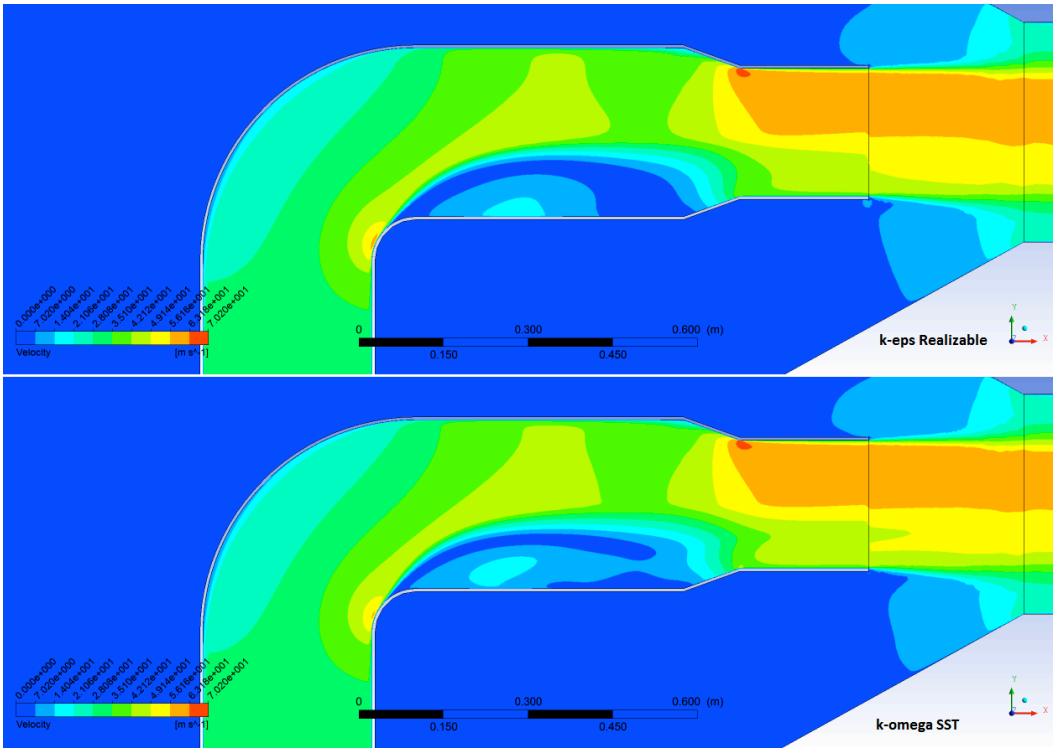

Figure 5-11 Velocity contours. Details of primary flow

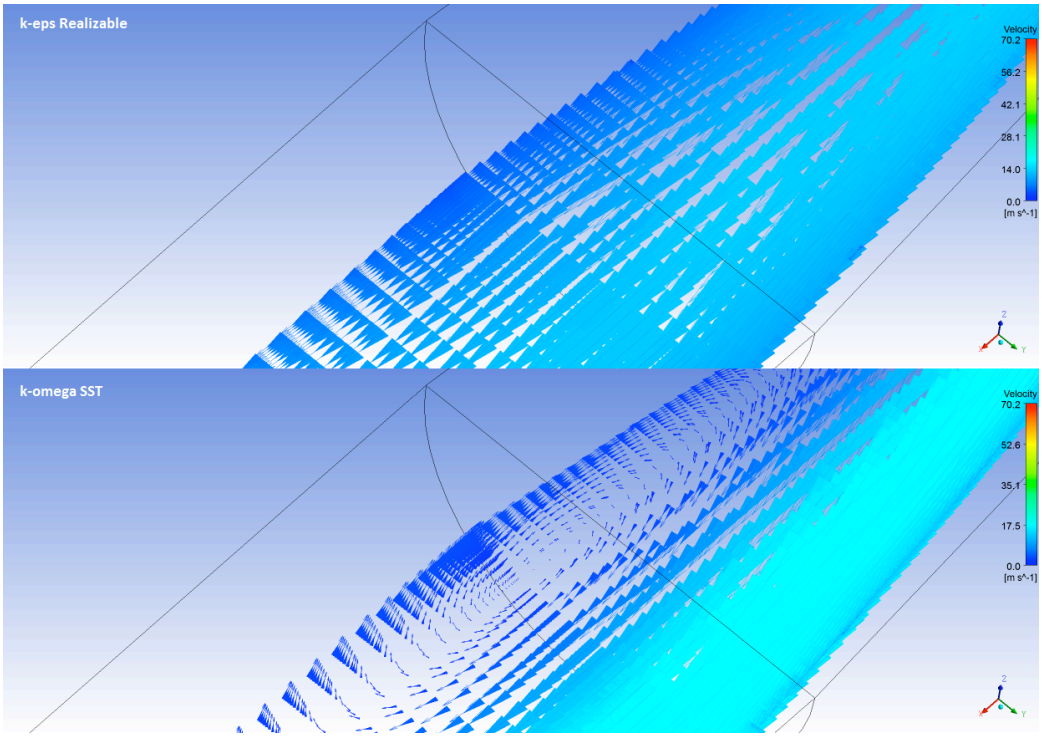

Figure 5-12 Velocity vector field. Details of diffuser-stack recirculation

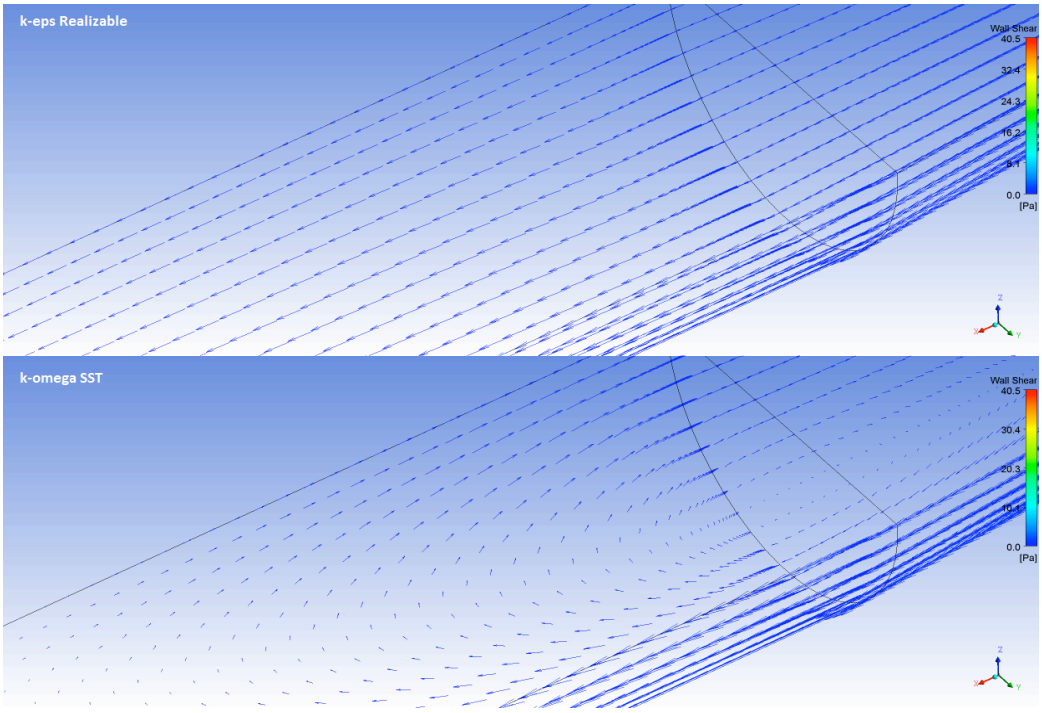

Figure 5-13 Wall shear vector field. Details of diffuser-stack recirculation

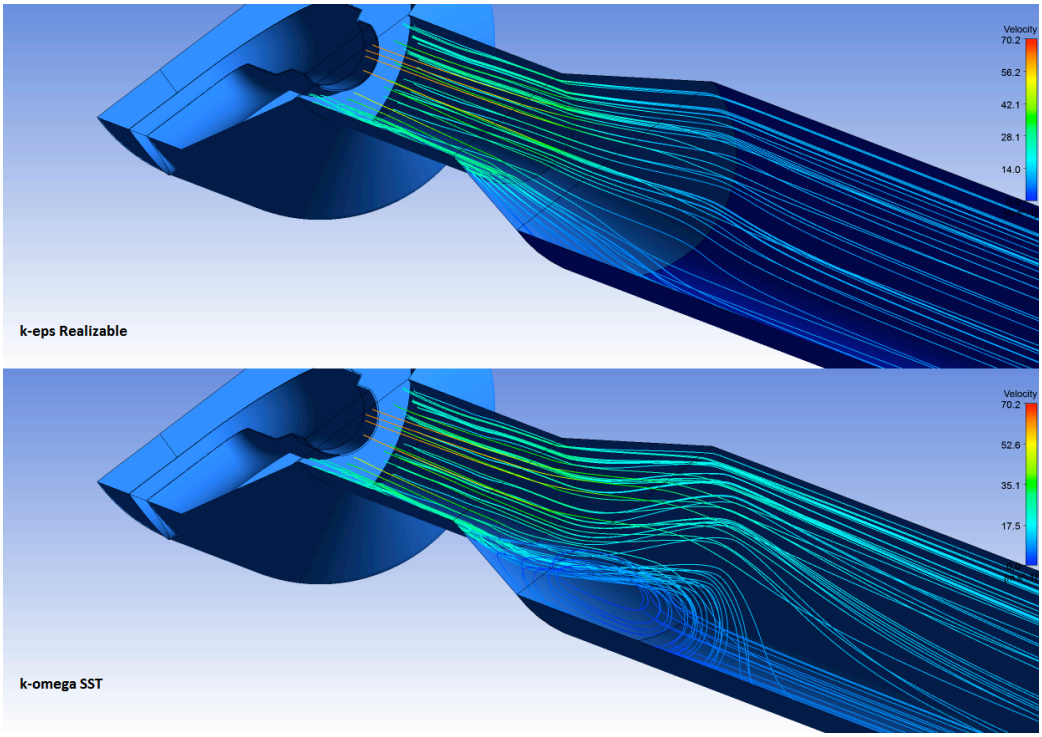

Figure 5-14 Particles streamlines. Details of diffuser-stack recirculation

It is interesting to represent how do velocity and static pressure vary along the z coordinate (in the transversal direction) according to the turbulence model.

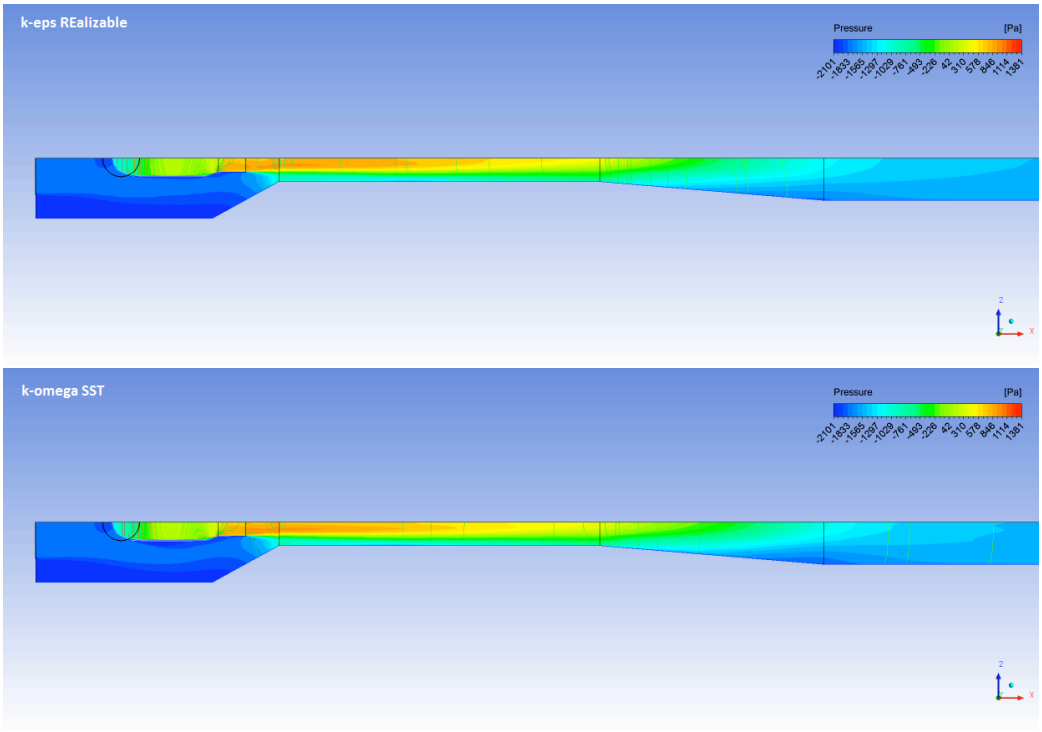

Figure 5-15 Velocity contour. Transverse view (xz plane)

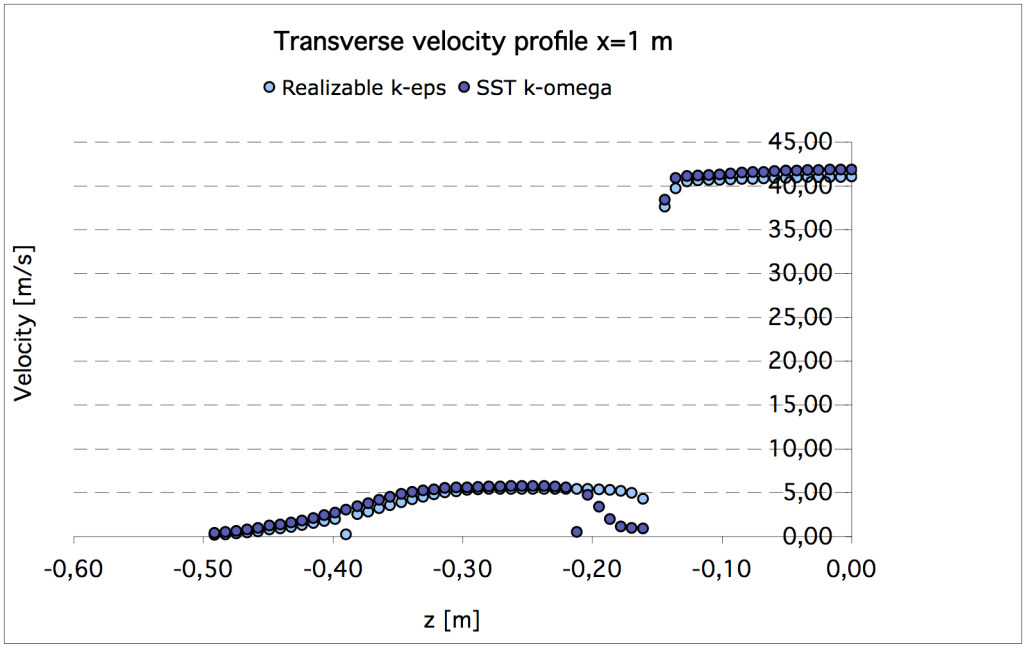

Figure 5-16 Tranverse velocity distribution in the suction chamber. Upper points represent the primary stream, which is separated from the secondary

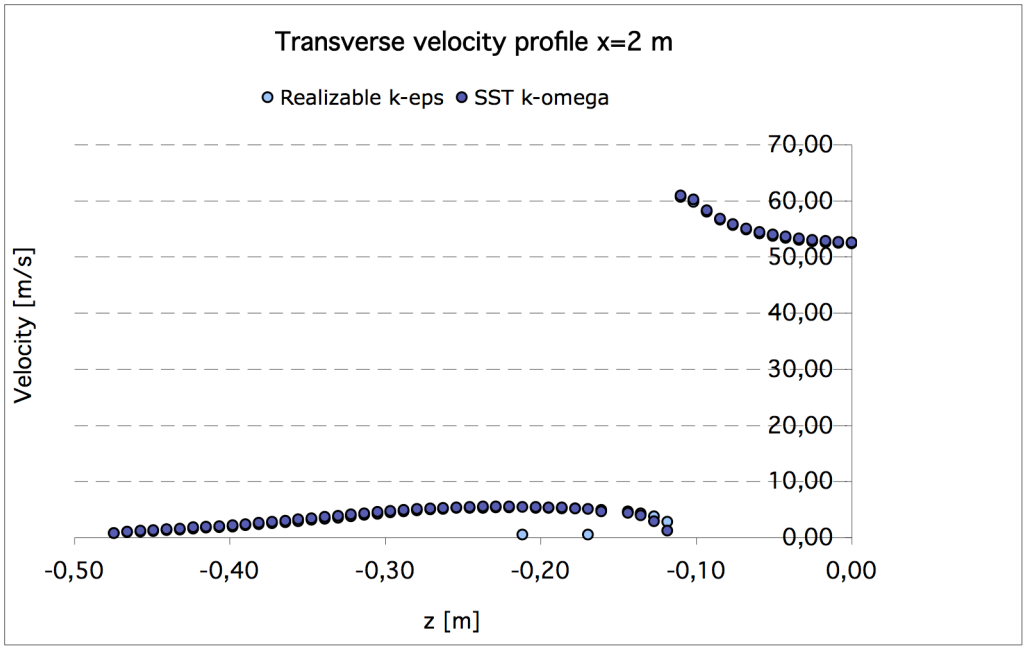

Figure 5-17 Tranverse velocity distribution just before the mixing chamber inlet. Upper points represent the primary stream, which progressively accelerates the secondary

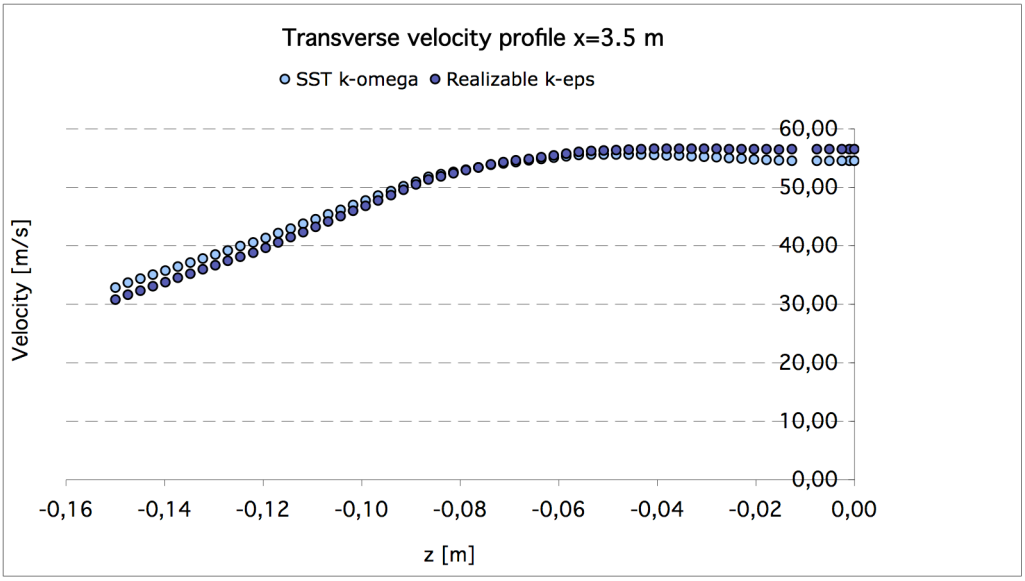

Figure 5-18 Tranverse velocity distribution in the mixing section

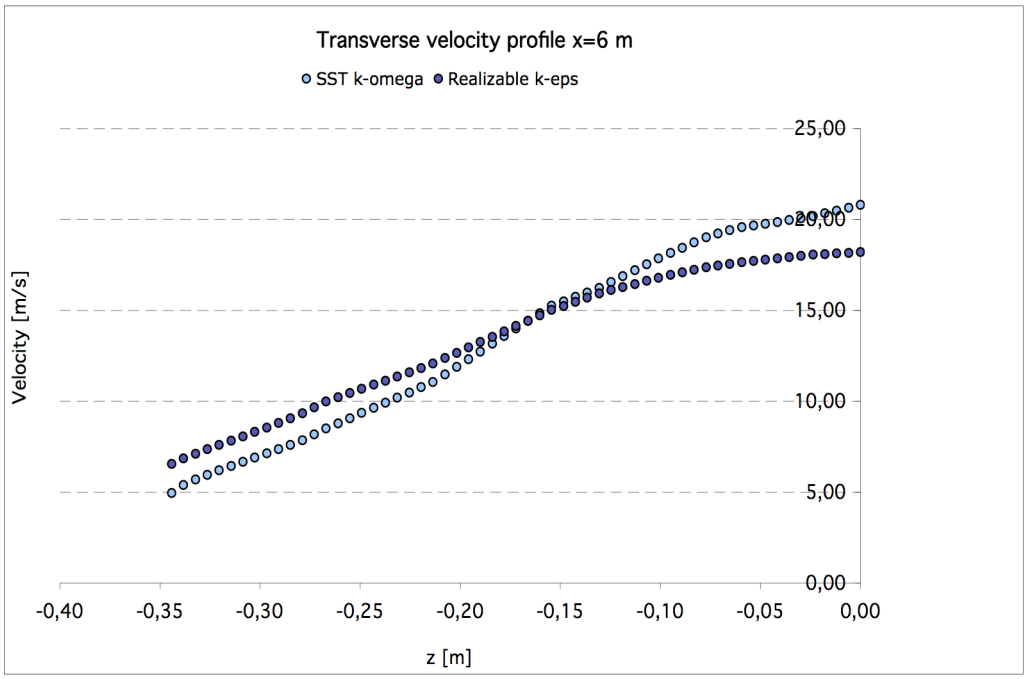

Figure 5-19 Tranverse velocity distribution at the stack inlet, where strong recirculation occurs

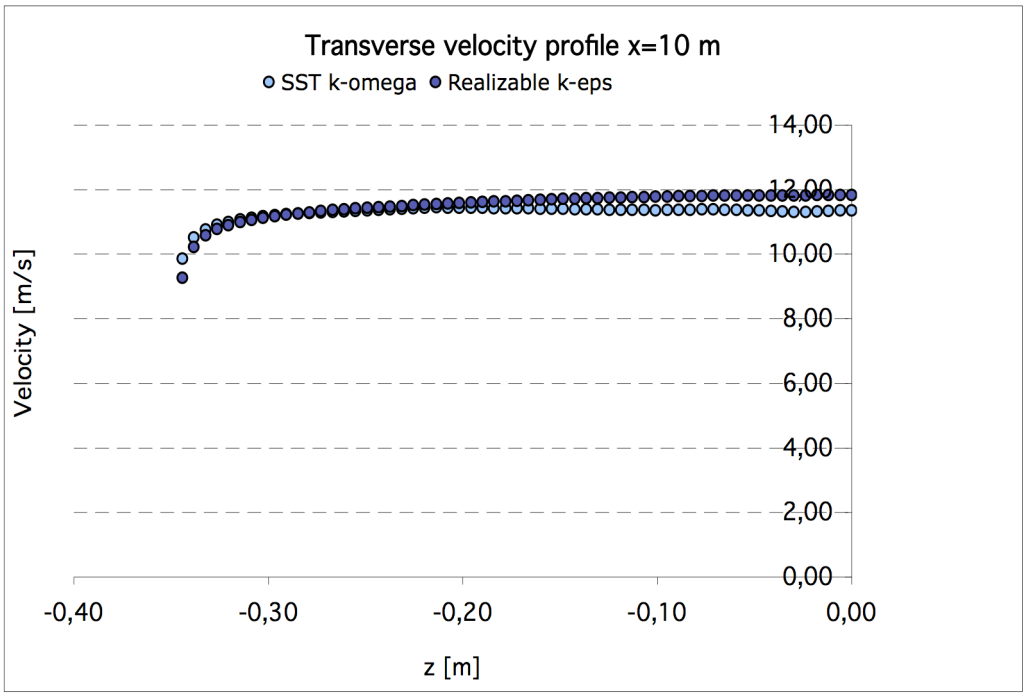

Figure 5-20 Tranverse velocity distribution in the stack inlet, where recirculation is smoothed

The static pressure field, shown in the next picture, is related to the velocity distribution. At the nozzle exit the shape of pressure contours vary significantly in the two cases. This probably depends on the different velocity pattern predicted in the primary flow and the viscosity dissipation related to it.

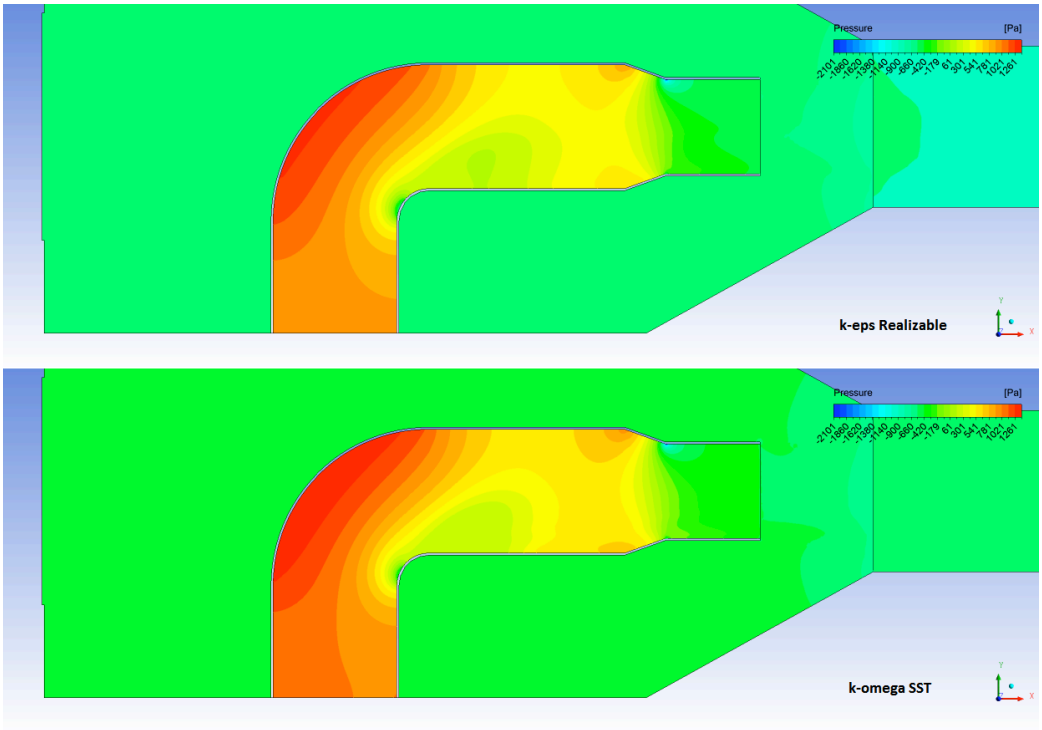

Figure 5-21 Tranverse pressure distribution in the suction chamber

Hereinafter is shown the static pressure distribution variation with the x coordinate along the z axis:

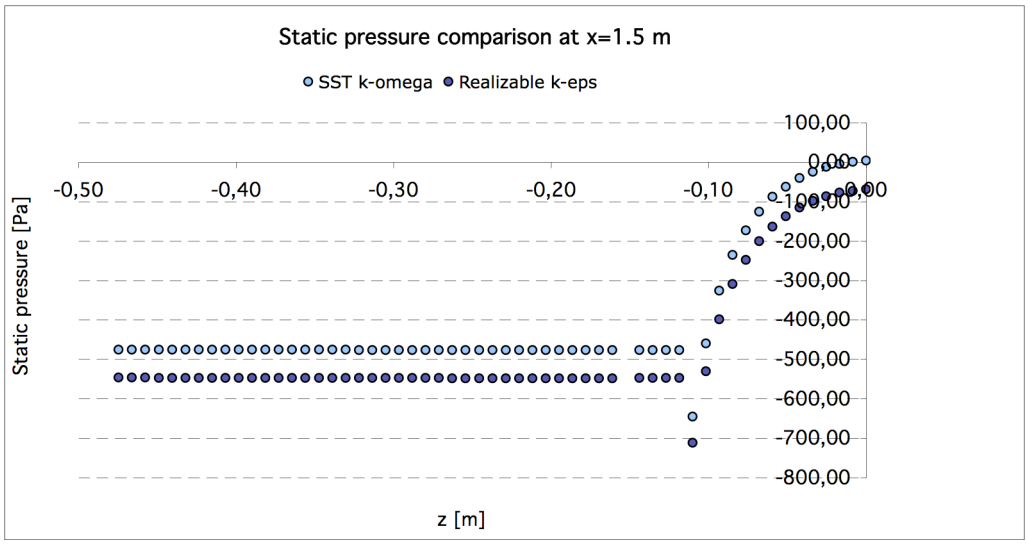

Figure 5-22 Tranverse pressure distribution in the suction chamber

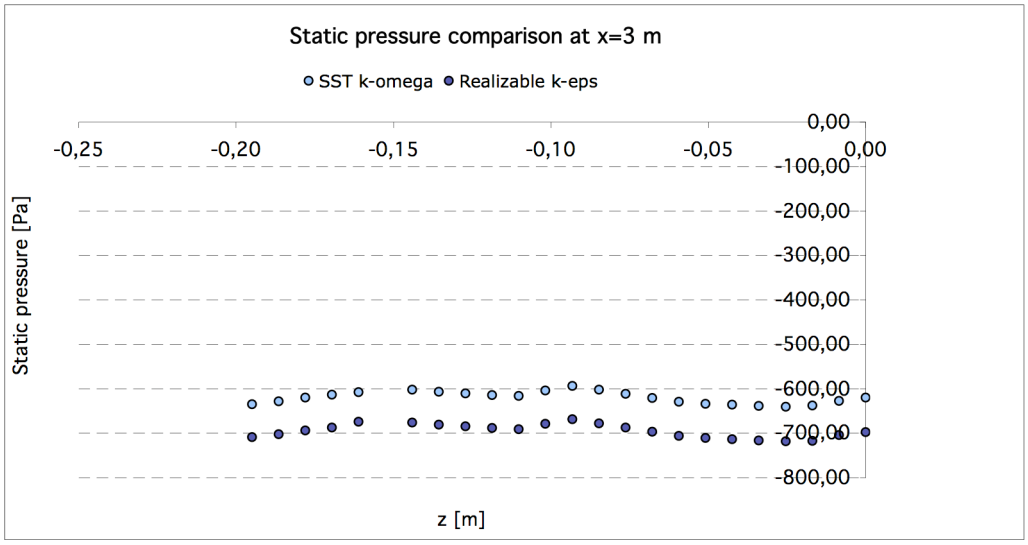

Figure 5-23 Tranverse pressure distribution in the mixing chamber

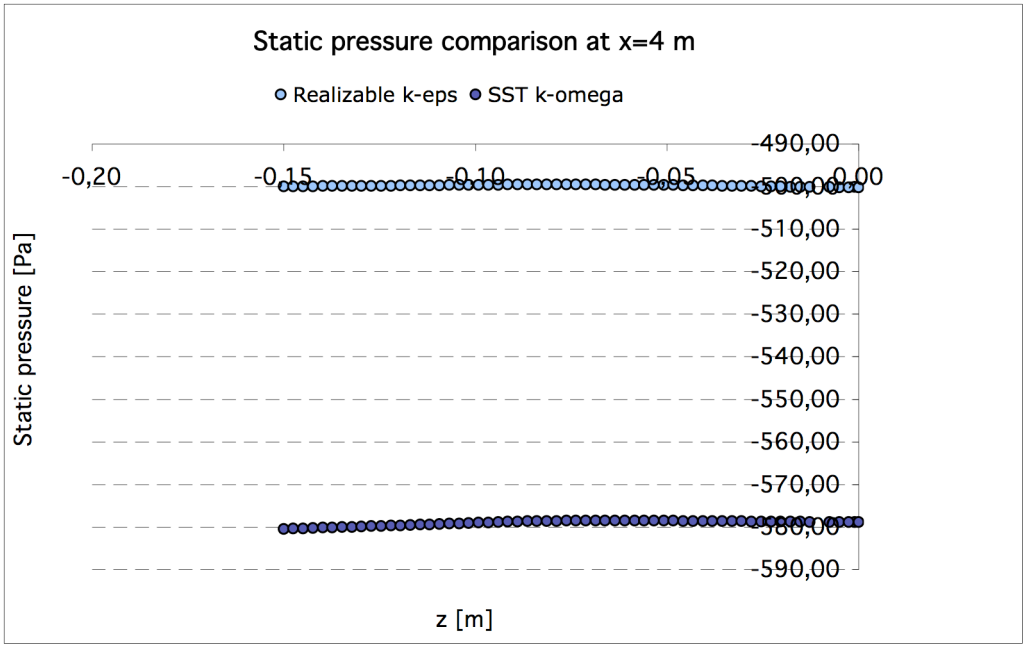

Figure 5-24 Tranverse pressure distribution near the mixing chamber exit

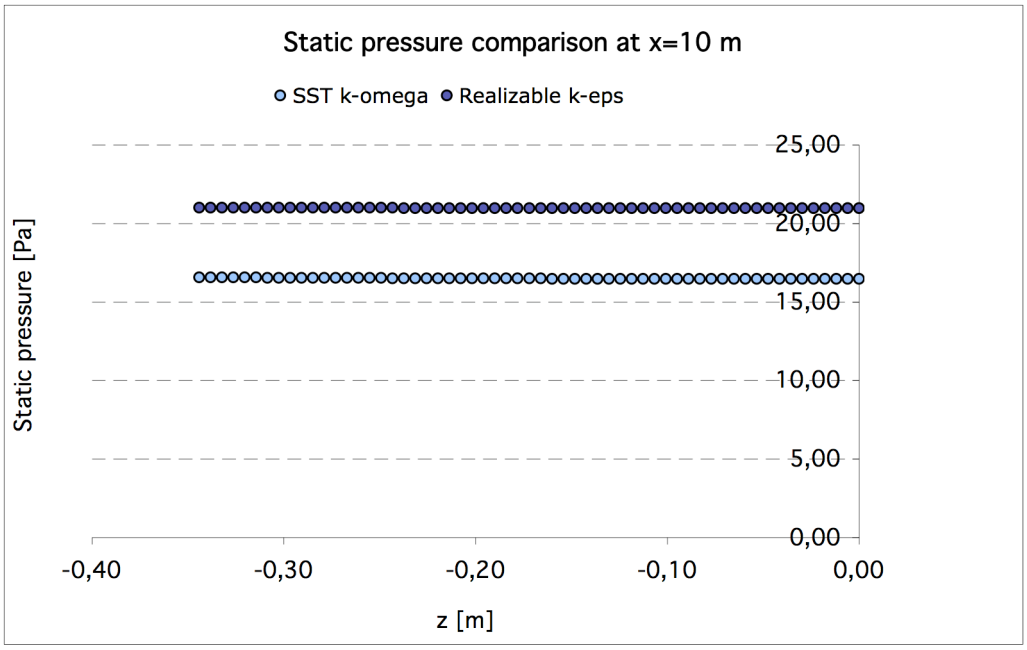

Figure 5-25 Tranverse pressure distribution in the stack after recirculation smoothed

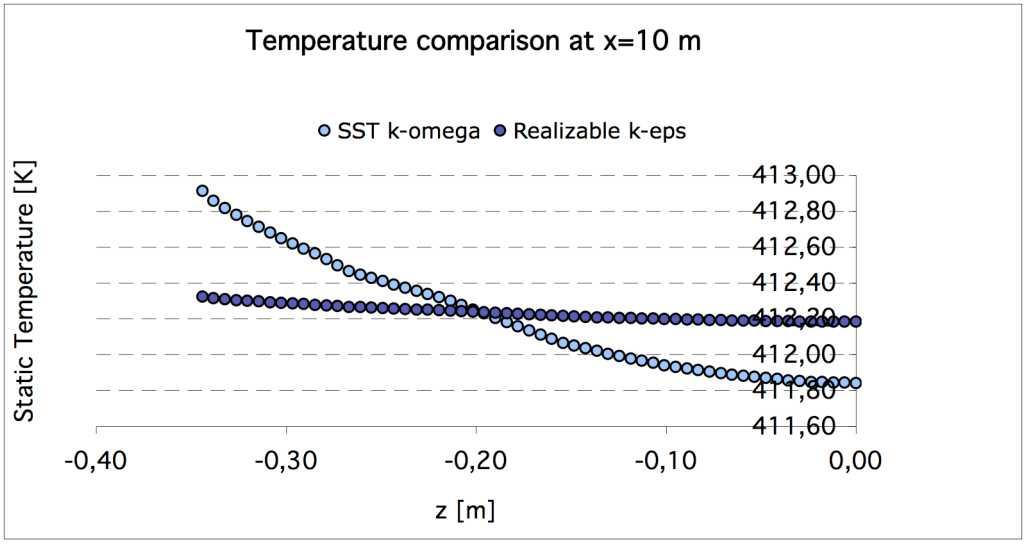

Figure 5-26 Tranverse temperature distribution in the stack after recirculation smoothed

Other recirculation flow phenomena are visible near the secondary flow inlet, where there is a sudden transition from square sectioned duct to the suction chamber.

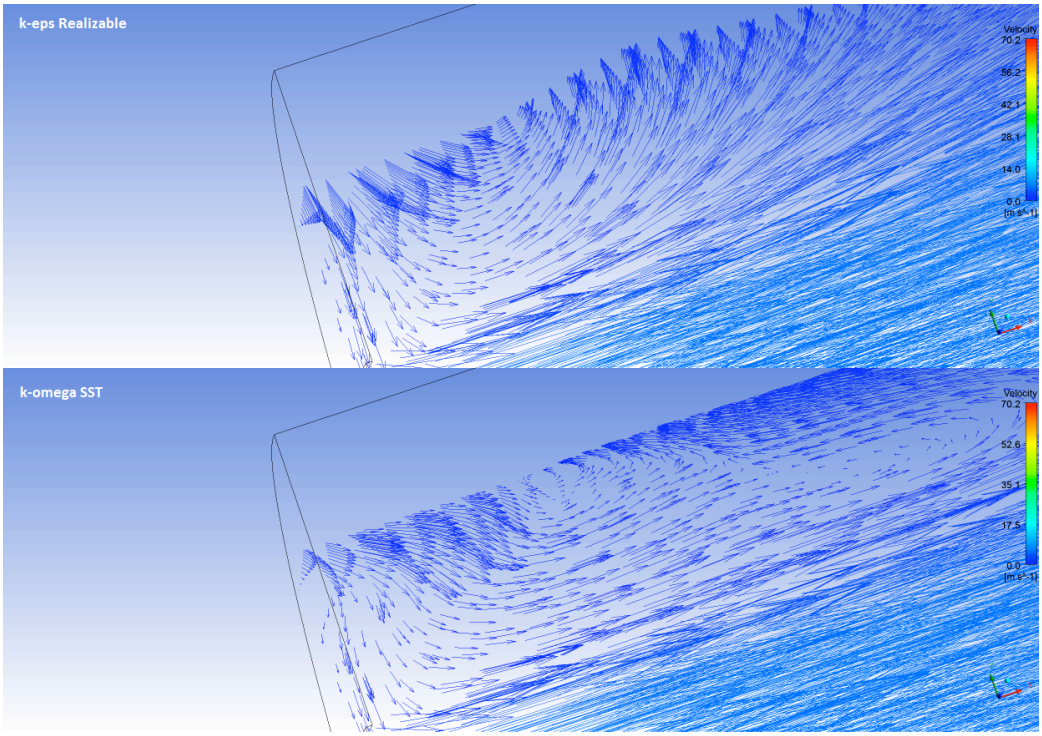

Figure 5-27 Fluid flow recirculation near the fumes inlet, caused by the sudden transition between square duct and suction chamber

5.3 Dryer + duct B

5.3.4 Grid independence study

Three grids with progressive increase of the refinement level are analyzed. The inflation height and growth rate are kept constant in order to assure the same spatial discretization perpendicularly to the wall. Significant results are reported in the table.

Number of elements	Outlet Pressure [Pa]	Inlet Pressure [Pa]	Δ [%]
2,825,298	-560.0	-503.9	0.22
3,427,971	-560.0	-502.8	0.03
4,189,928	-560.0	-503.0	----

Table 5-4 Grid independence. Monitored point and percentage difference

The finer grid is taken as reference. It is evident that both the coarse and the medium size meshes generate very close static pressure values at domain inlet.
The matching evaluation of other quantities is however necessary. As for the ejector-stack, velocity values are sampled along the domain on two rakes. The first intersects the pre-heater and counts 30 points, the second crosses duct B and counts 20 points. Results are visible in the following figure.

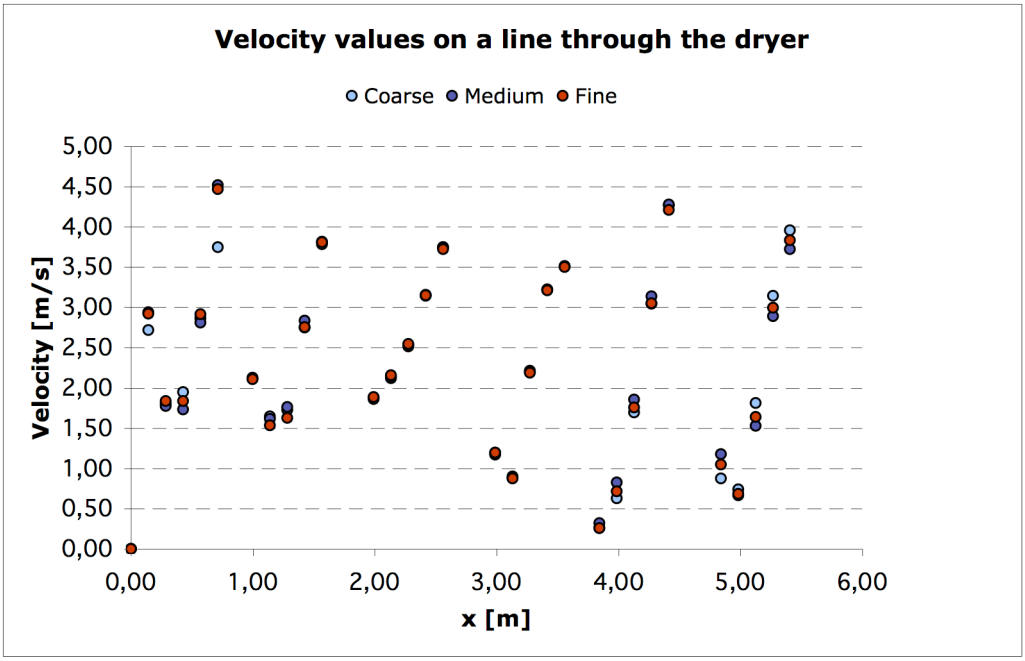

Figure 5-28 Velocity comparison between coarse, medium and fine grids. Values are sampled in a rake of 30 points in the dryer.

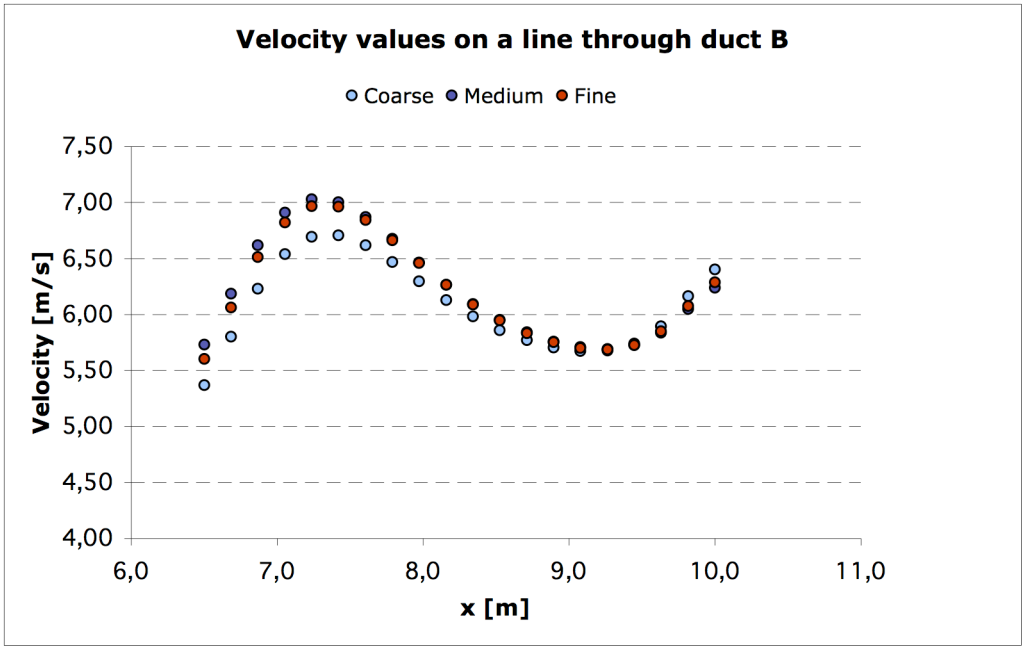

Figure 5-29 Velocity comparison between coarse, medium and fine grids. Values are sampled in a rake of 20 points in the duct B.

Thanks to the maze path shape of the pre-heater the samples reported in the first figure look like a random distribution, hence the comparison is limited to single points, while in the second figure a certain trend in inferable. Even if the coarse grid produces slightly different results, with respect to the finer meshes, the entity of the discrepancy consist of tenths of velocity unity. Furthermore, in the figure above the coarse reproduces similarly the velocity trend along the duct B.
In the sequent image the mean wall shear stress matching in different sections along the domain is shown.

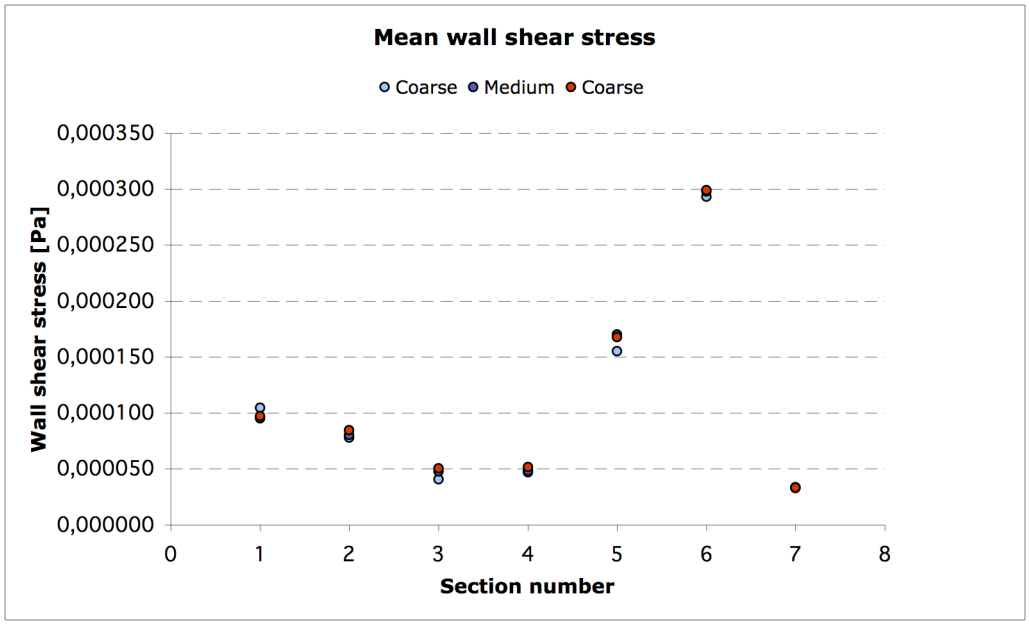

Figure 5-30 Mean wall shear stress comparison between coarse, medium and fine grids. Values are sampled in 7 different sections along the domain

Eventually it is useful to quantify the discrepancy of the velocity field is compared in the height direction (along the y axis) on three different rakes, each of 20 points. The first is located in duct B, the second and the third in the dryer.

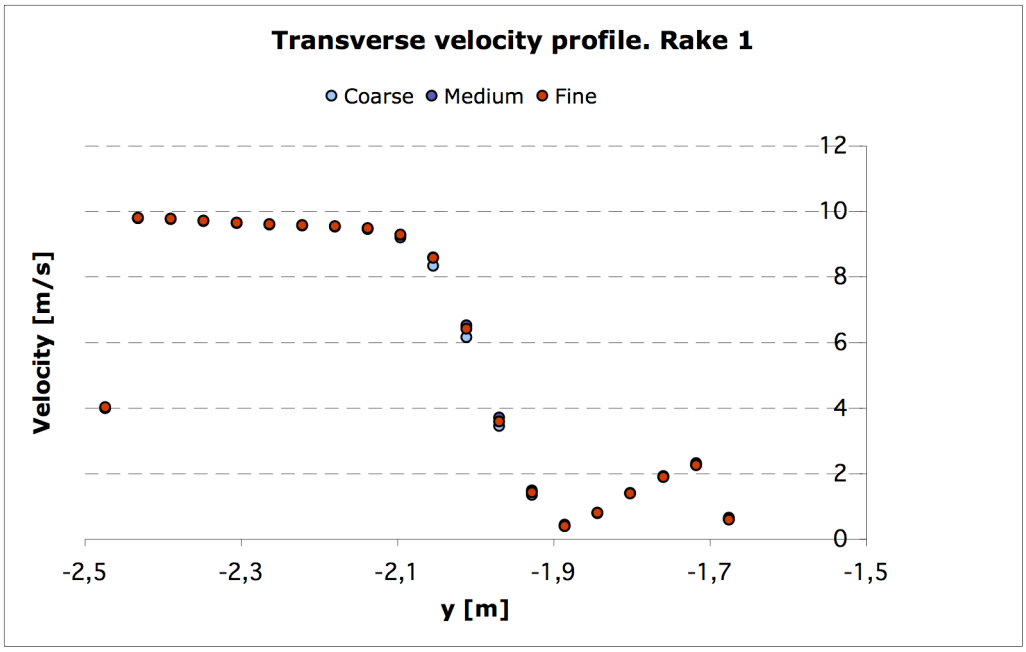

Figure 5-31 Transverse velocity comparison between coarse, medium and fine grids. Rake 1 is situated in the duct b.

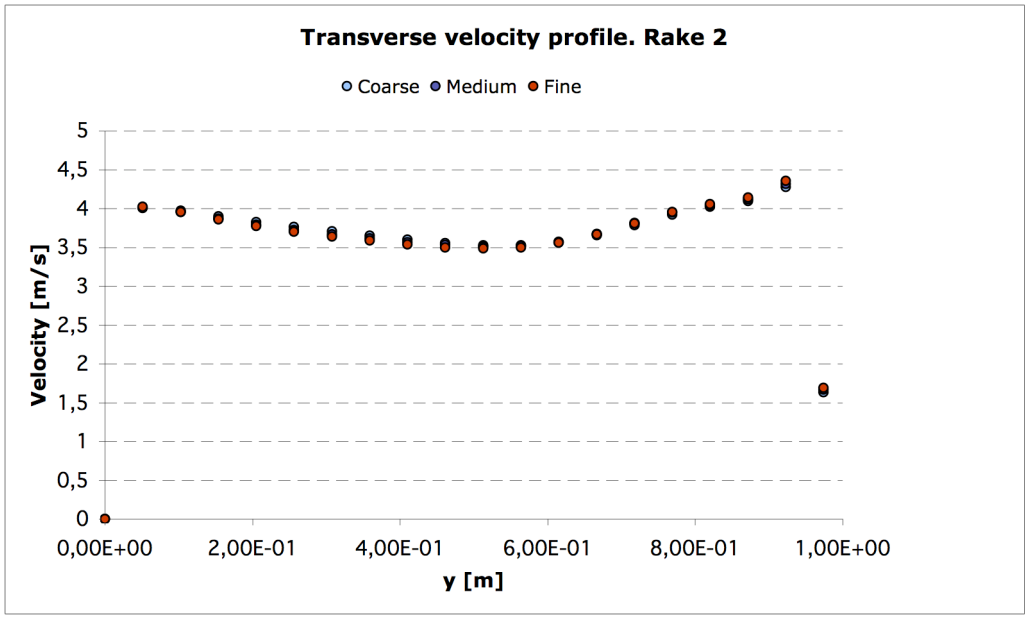

Figure 5-32 Transverse velocity comparison between coarse, medium and fine grids. Rake 2 is situated in the dryer.

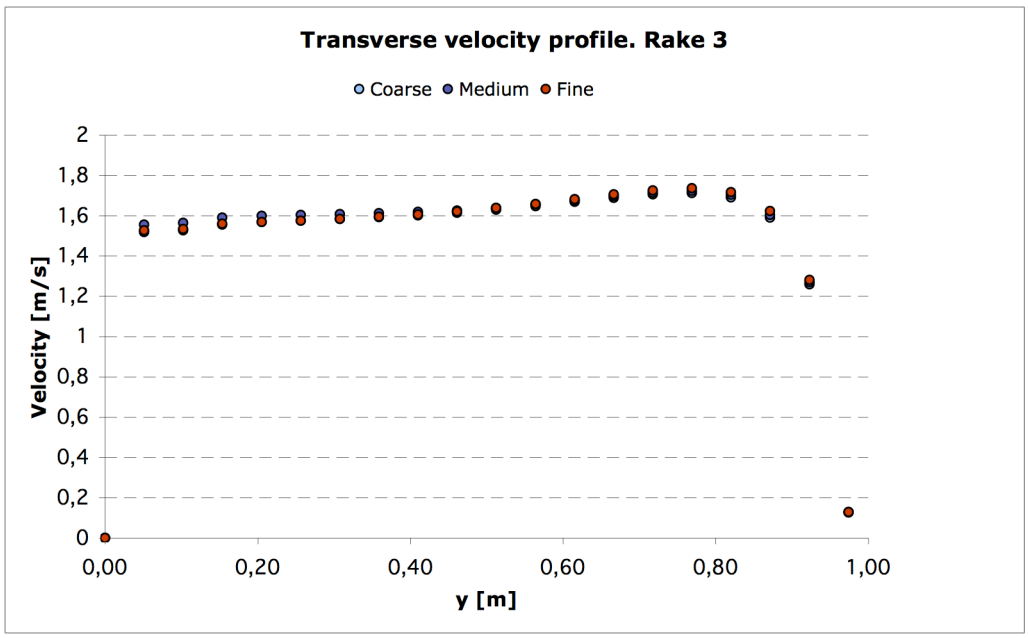

Figure 5-33 Transverse velocity comparison between coarse, medium and fine grids. Rake 3 is situated in the dryer.

The considerations about the presented data permit to judge the medium size grid as the most indicated for further investigations. It shows gives enough accurate result at acceptable computational expense.

5.3.5 Results

Realizable k-ε and Reynolds Stress model performance is compared in the determination of the static pressure at the pre-heater inlet. Two pressure values at domain outlet are set, each one correspondent to the ejector's secondary flow inlet result obtained with a different turbulence model, Realizable k-ε and SST k-ω respectively. The secondary goal of this investigation is to understand if RSM high computational cost is worthwhile in the examined case.

	Case 1		Case 2	
	Realizable	**RSM**	**Realizable**	**RSM**
Outlet pressure [Pa]	-550.3	-550.3	-478.3	-478.3
Inlet Pressure [Pa]	-493.9	-496.2	-421.9	-424.2
Δ Inlet [%]	0.47		0.55	
Pressure drop [Pa]	-56.4	-54.1	-56.4	-54.1

Table 5-5 Simulation results for dryer + duct B. Static pressure

The little discrepancy between the two models predictions indicates that the simpler Realizable is a valid choice, with respect to RSM, considering the computational effort required for this last one. The following images represent velocity profiles caught transversally to the stream main motion direction, in different sections along the domains. This is aimed to demonstrate the totally different distributions provided by the models in question. Vorticity profiles are furnished as a further quantitative tool for the evaluation of the models discrepancies.

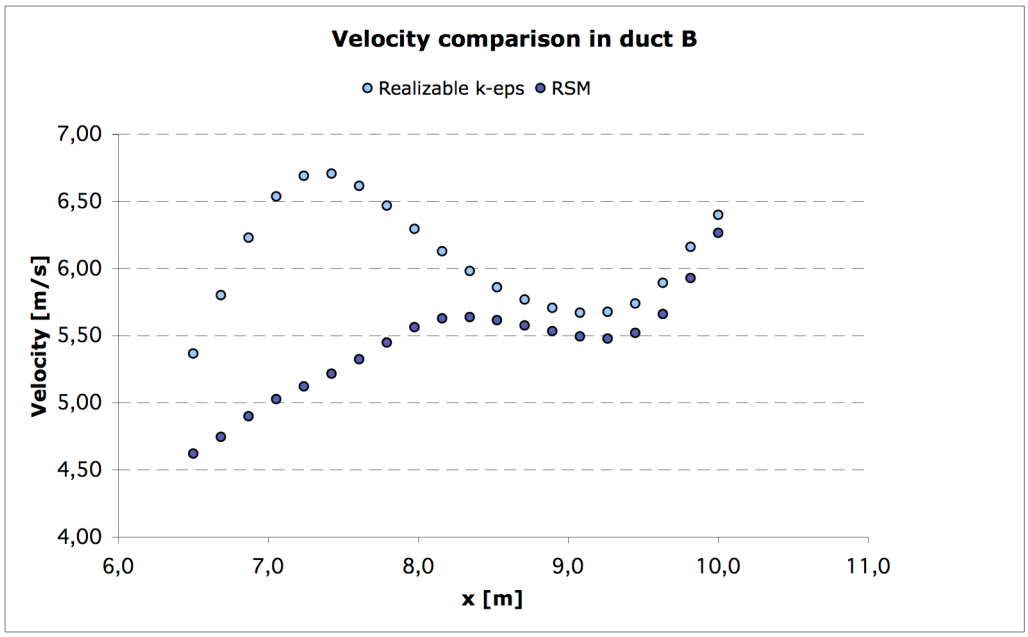

Figure 5-34 Axial velocity profile comparison in duct B

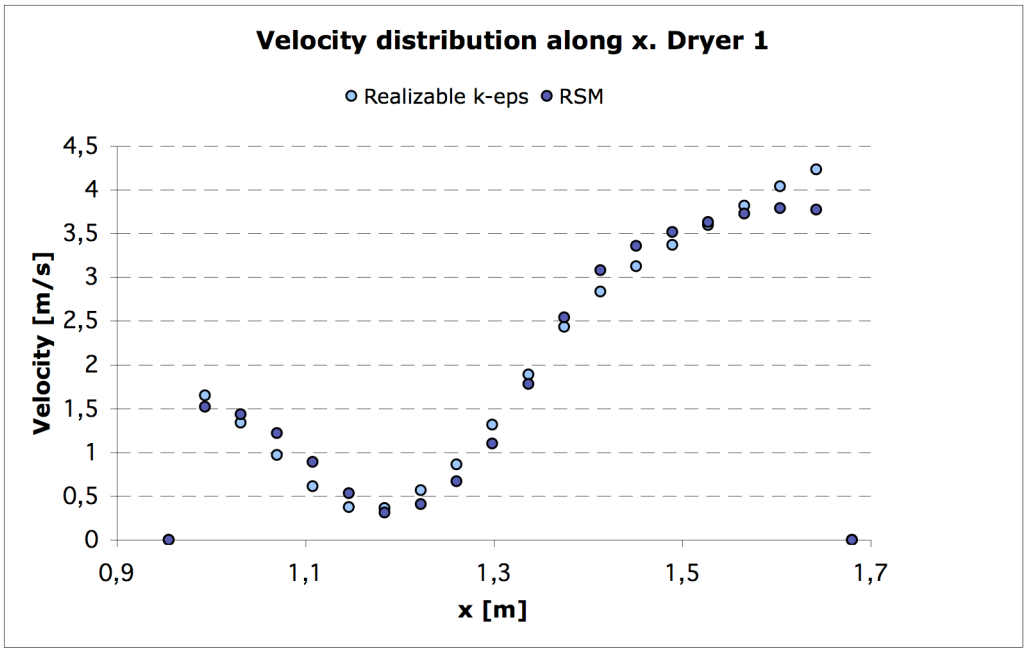

Figure 5-35 Longitudinal velocity profile in dryer, section 1

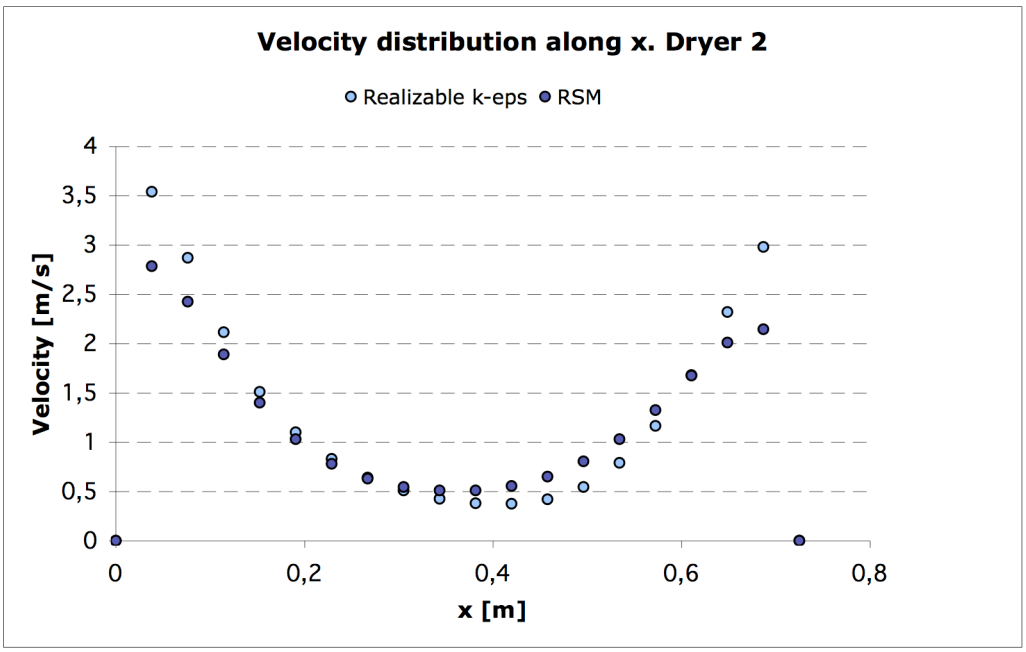

Figure 5-36 Longitudinal velocity profile in dryer, section 2

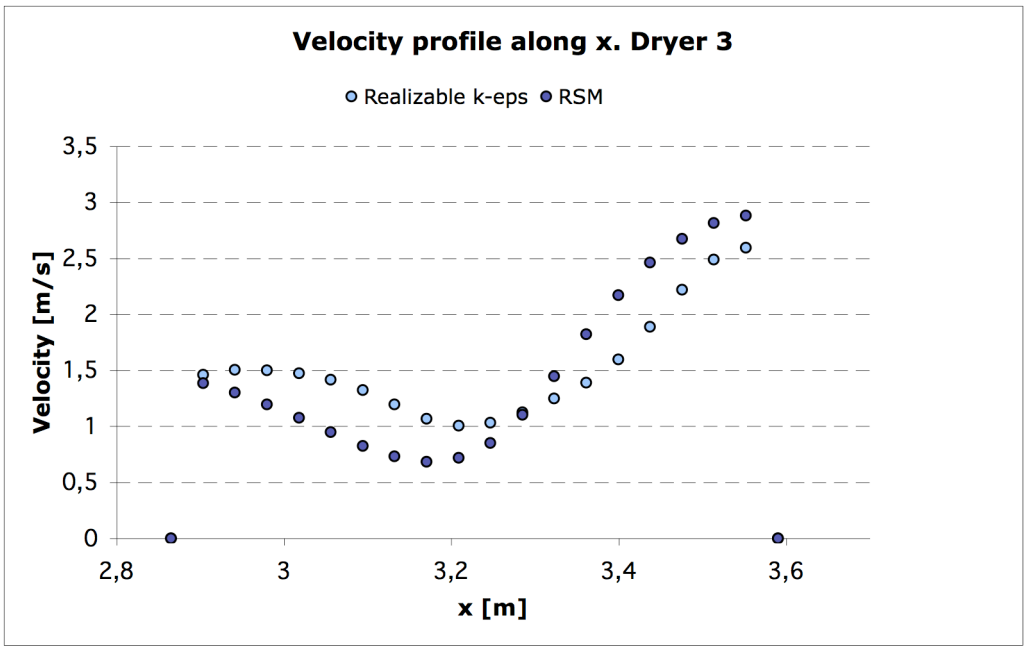

Figure 5-37 Longitudinal velocity profile in dryer, section 3

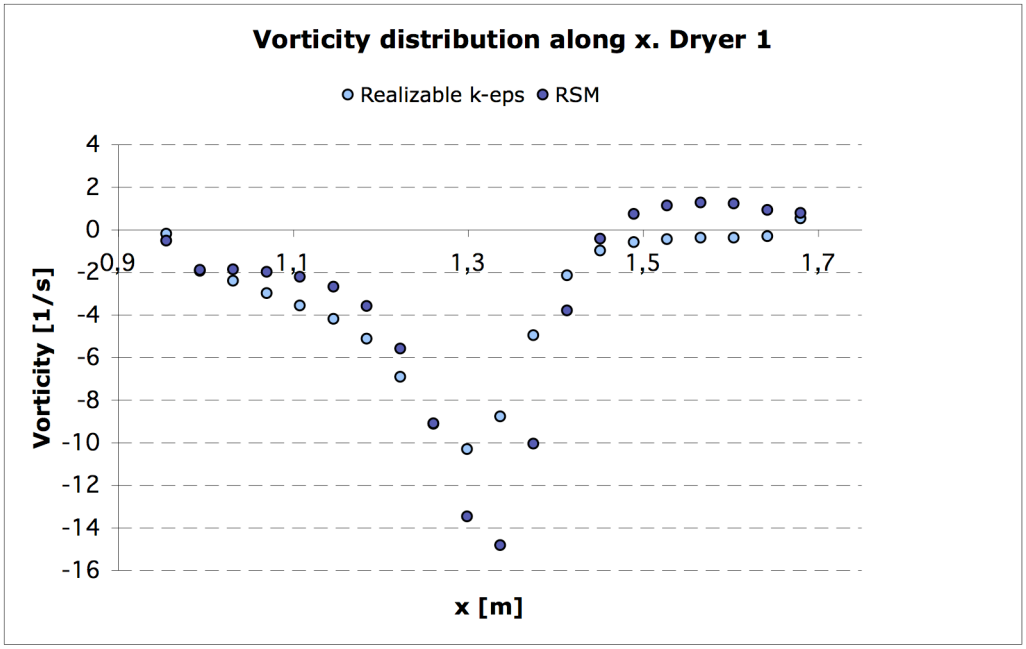

Figure 5-38 Longitudinal vorticity profile in dryer, section 1

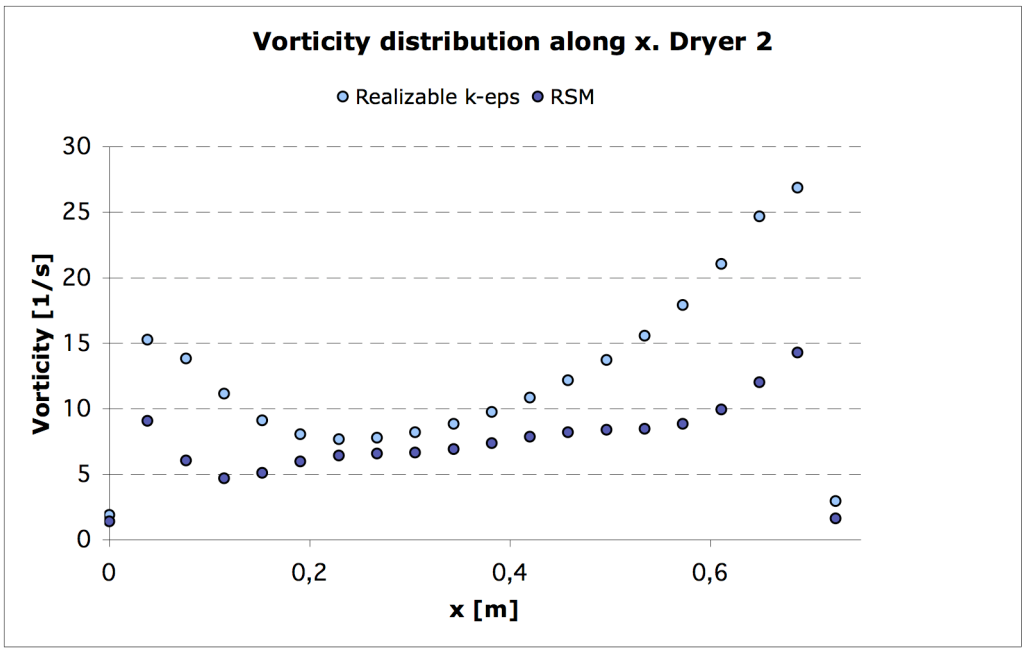

Figure 5-39 Longitudinal vorticity profile in dryer, section 2

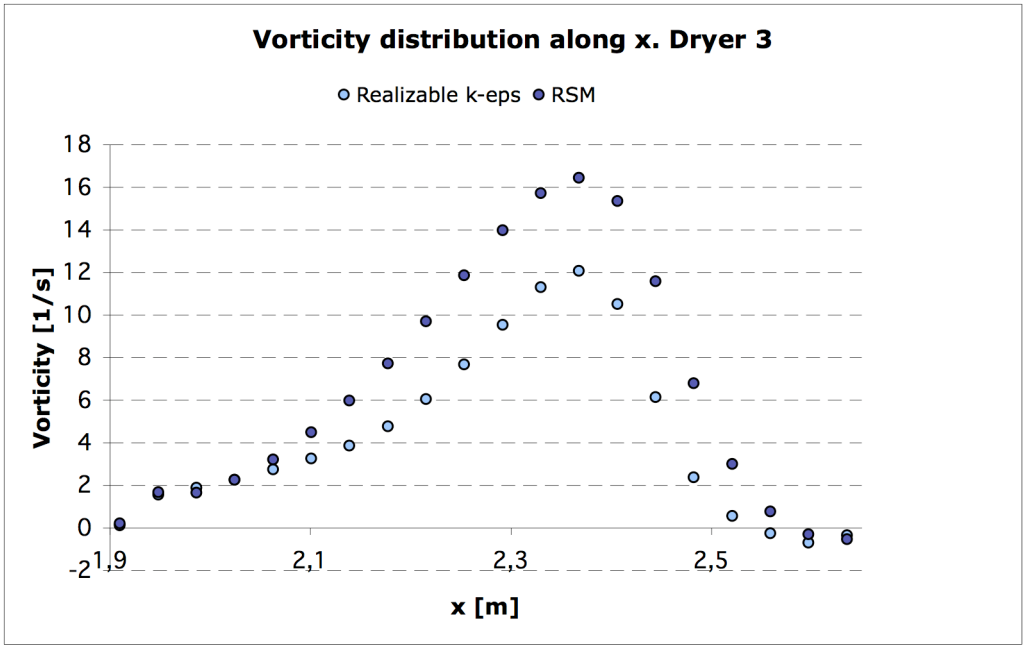

Figure 5-40 Longitudinal vorticity profile in dryer, section 3

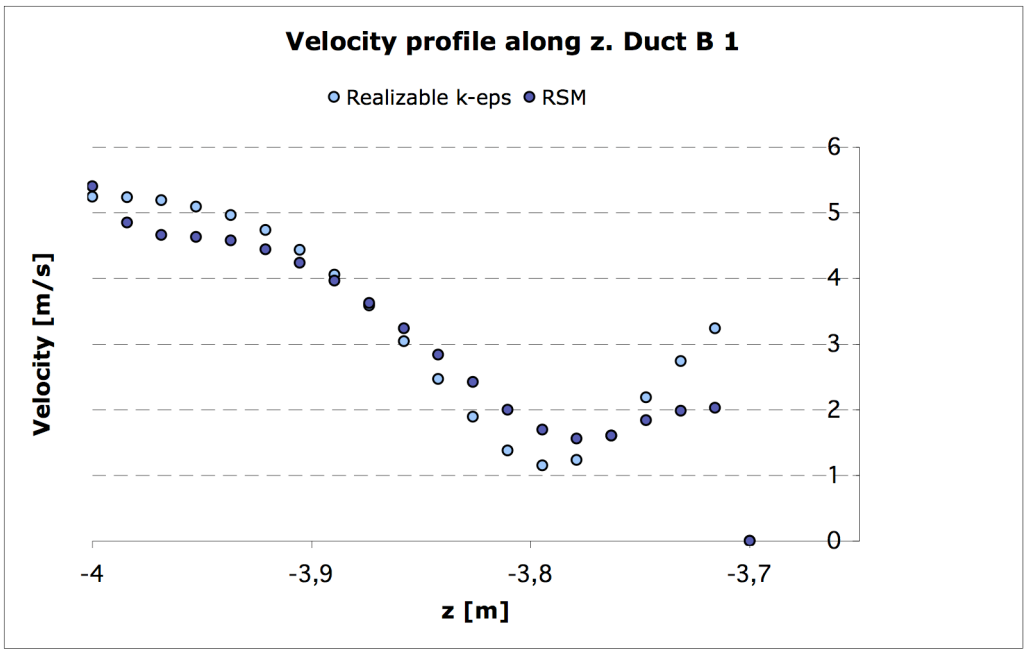

Figure 5-41 Transverse velocity profile in duct B, section 1

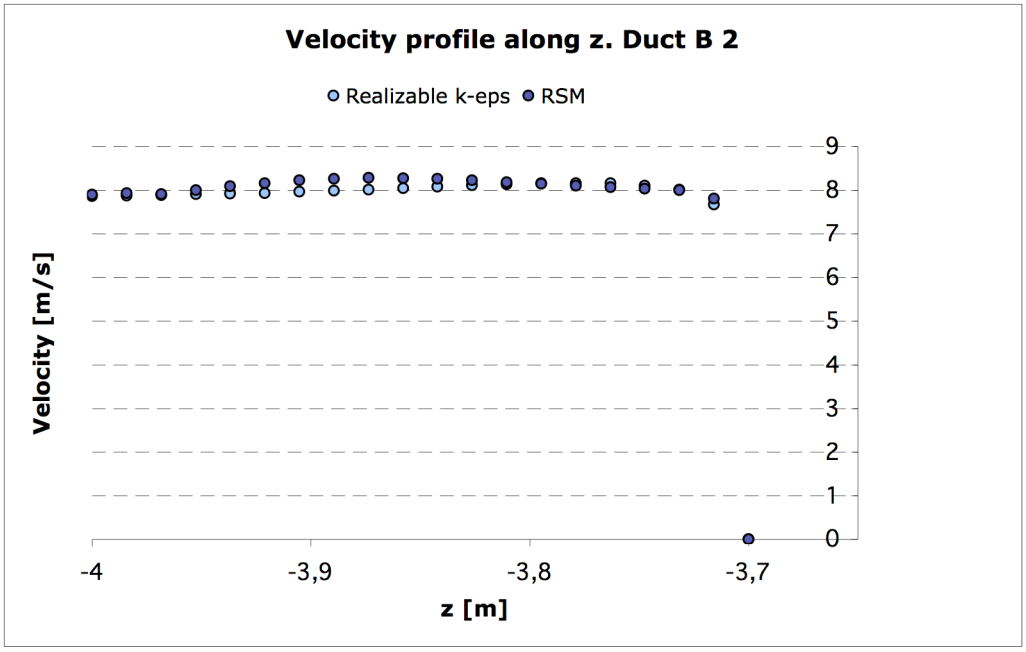

Figure 5-42 Transverse velocity profile in duct B, section 2

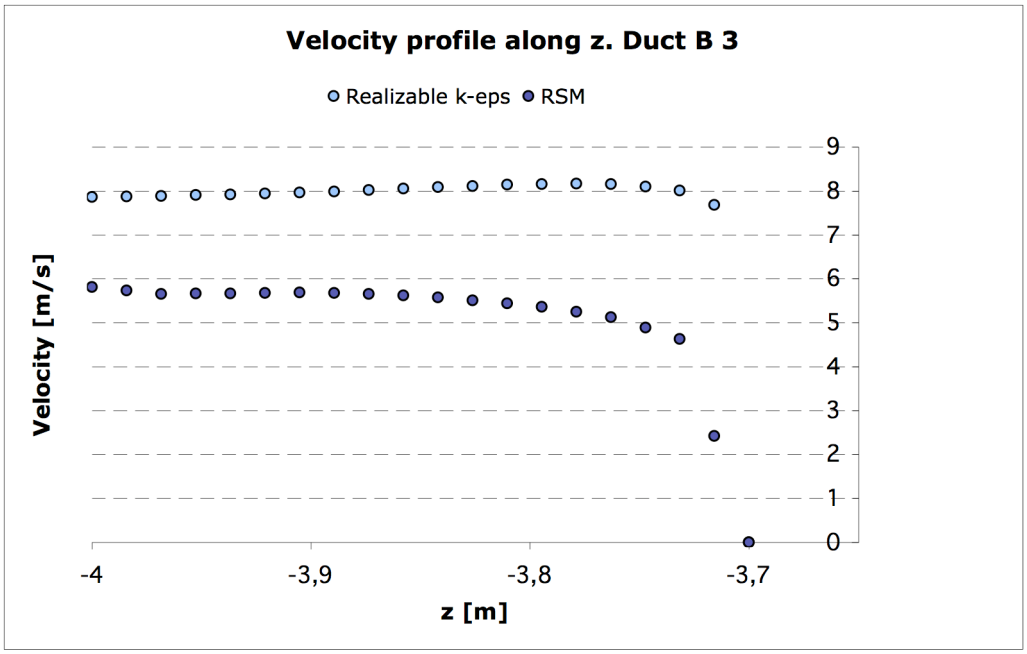

Figure 5-43 Transverse velocity profile in duct B, section 3

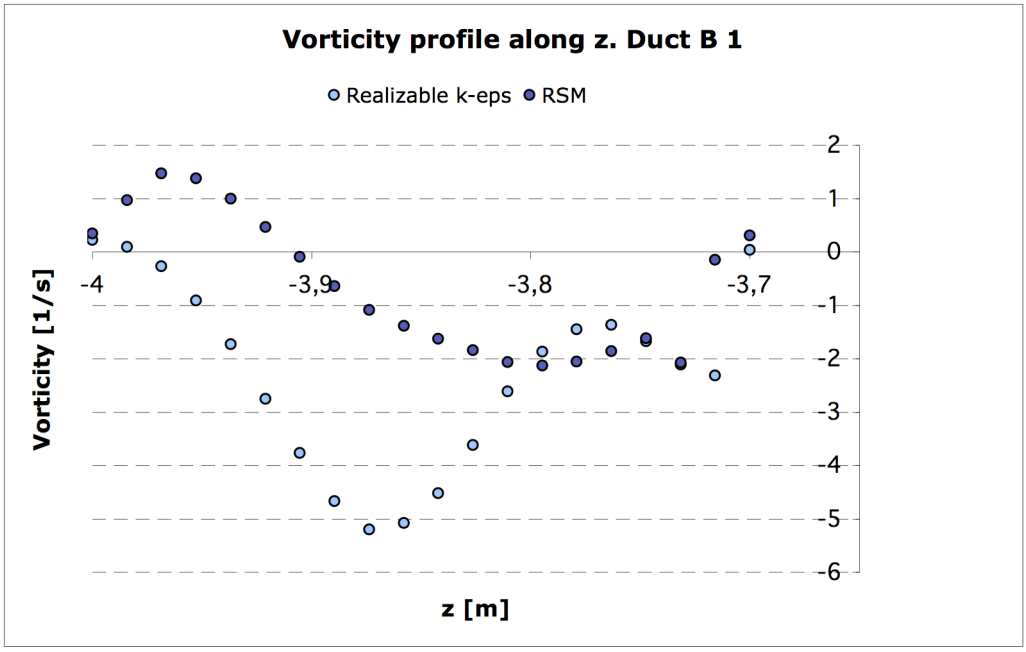

Figure 5-44 Transverse vorticity profile in duct B, section 1

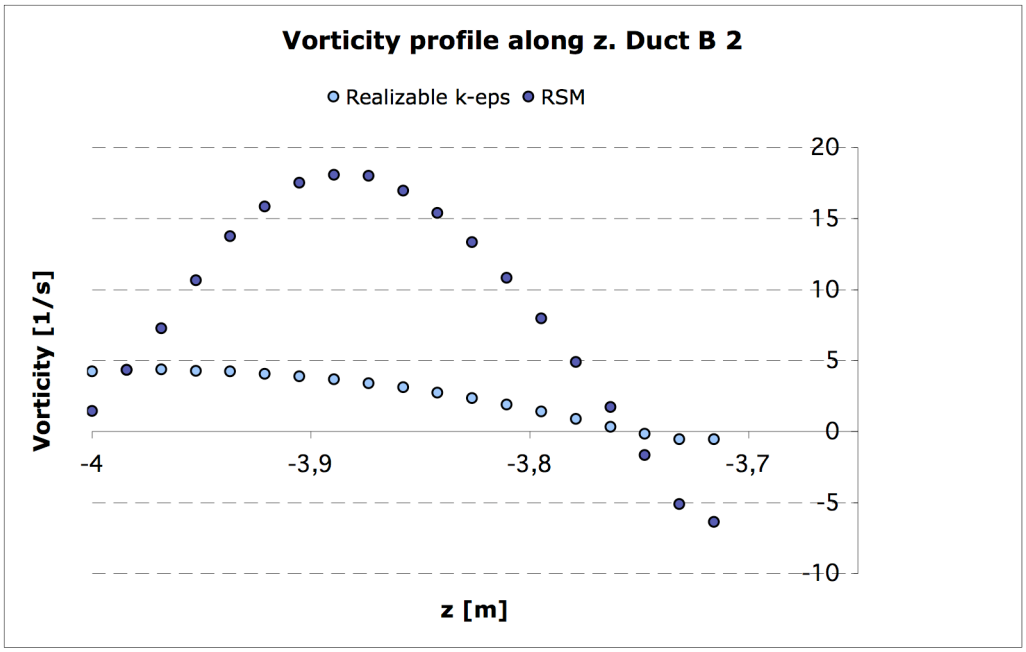

Figure 5-45 Transverse vorticity profile in duct B, section 2

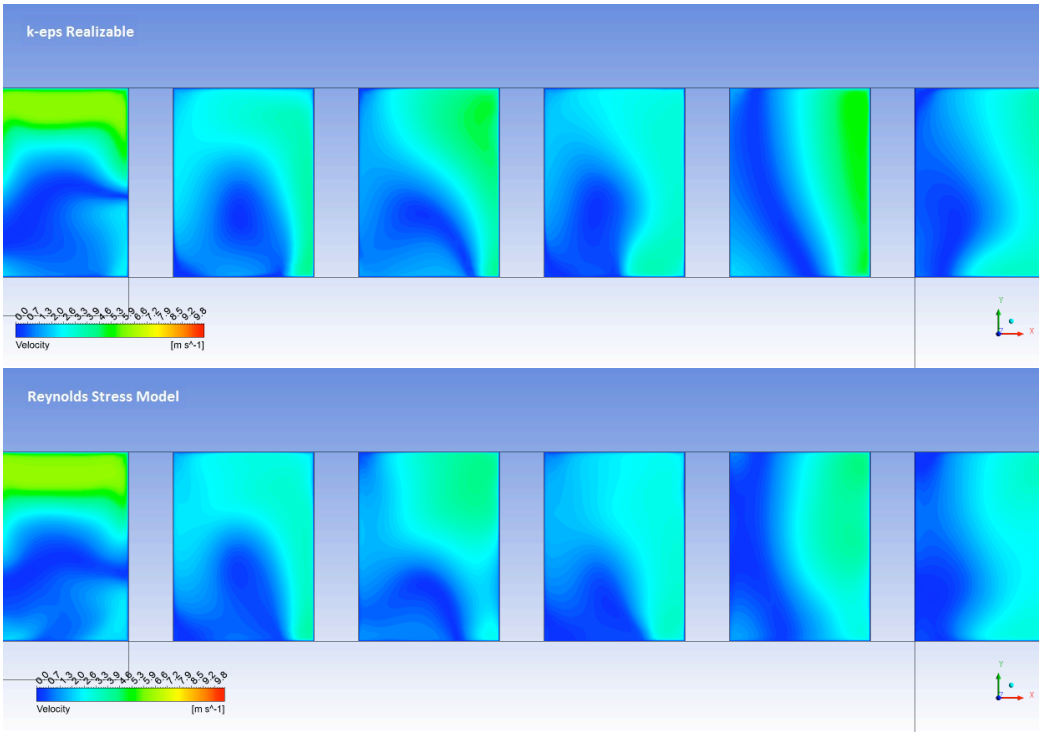

Figure 5-46 Velocity contours. Dryer longitudinal section

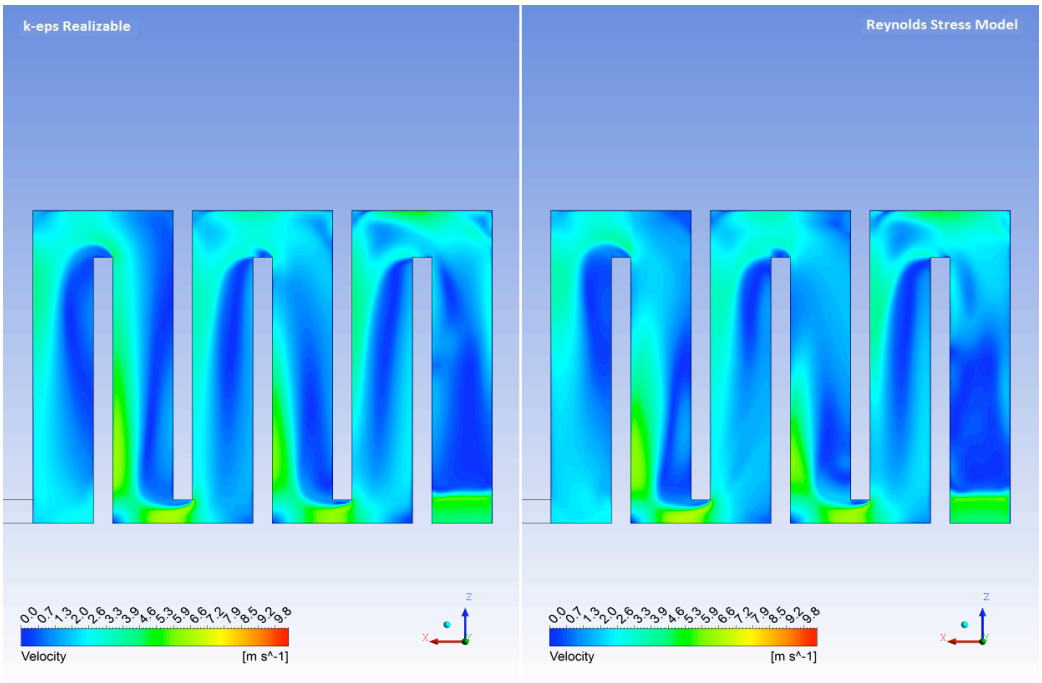

Figure 5-47 Velocity contours. Dryer top section

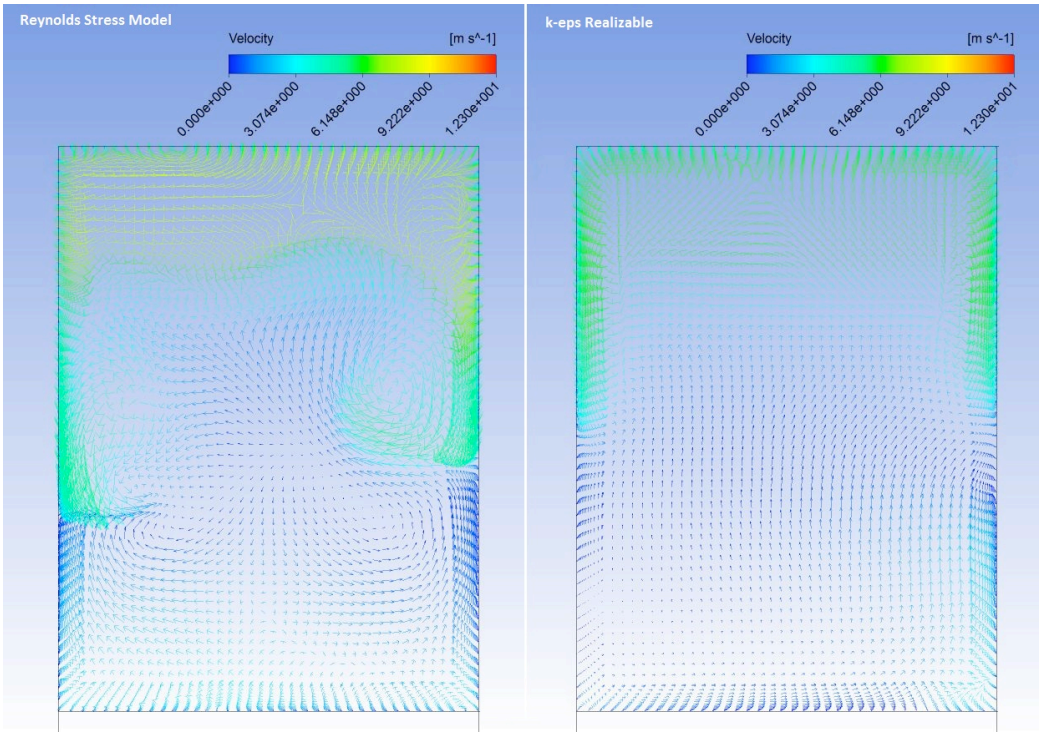

Figure 5-48 Velocity vectors. Dryer transverse section

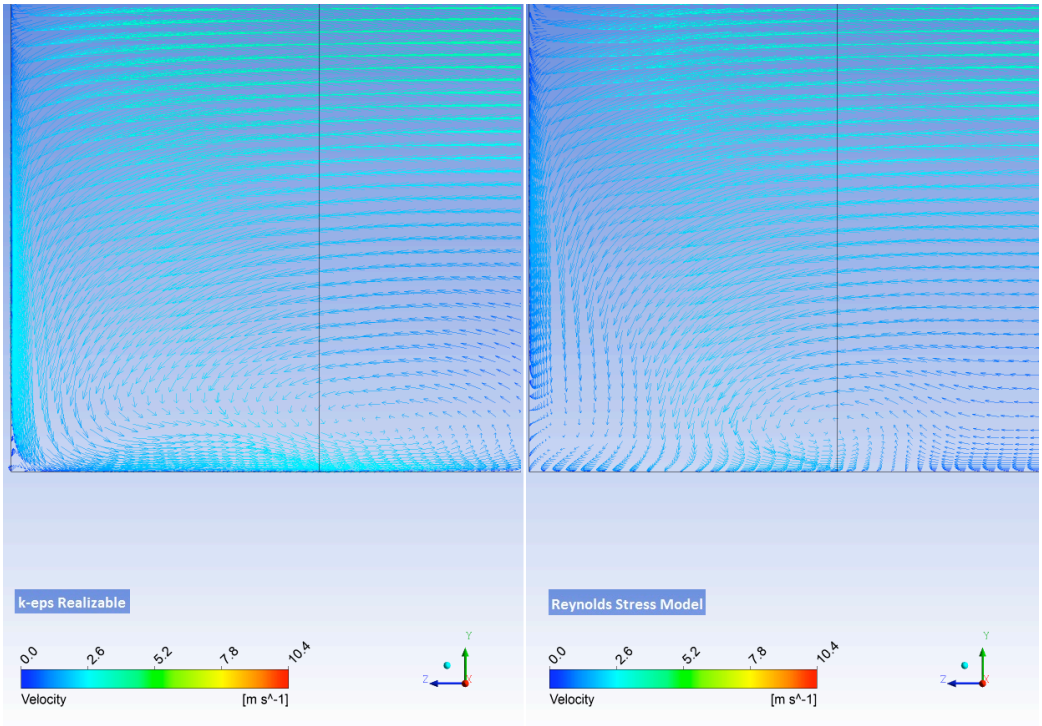

Figure 5-49 Dryer transverse section. Detail of velocity distribution in the corner

The previous image shows a velocity vector field in a corner totally different from the ones reported in the literature review, where it was visible a pair of counter-rotating vortexes for each corner of the duct cross section. This is due to the short length of the straight parts between two 90° consecutive elbows: the stream has not enough time to reach the stabilized condition. As noticeable in Figure 3-19, there are a lot of recirculation zones, and the stream accelerates in presence of the straight elbows. In duct B recirculation phenomena occur after each elbow, due to the presence of inertia forces which accelerate the stream near the outer wall:

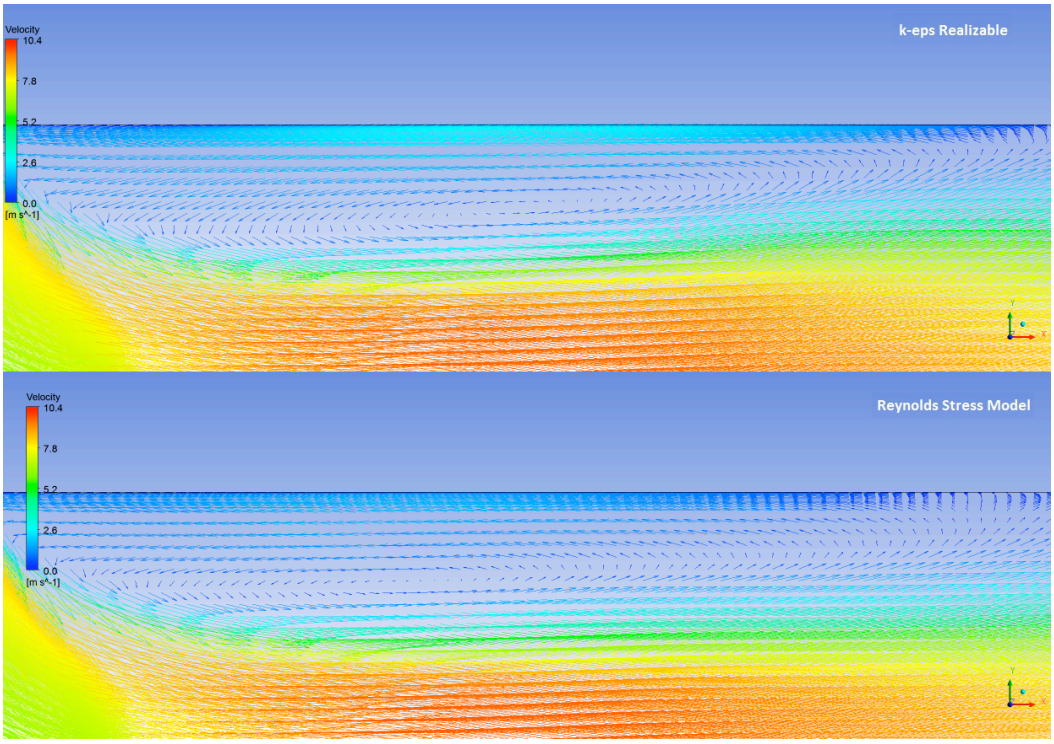

Figure 5-50 Duct B longitudinal section. Detail of velocity vector downstream the first 90° elbow

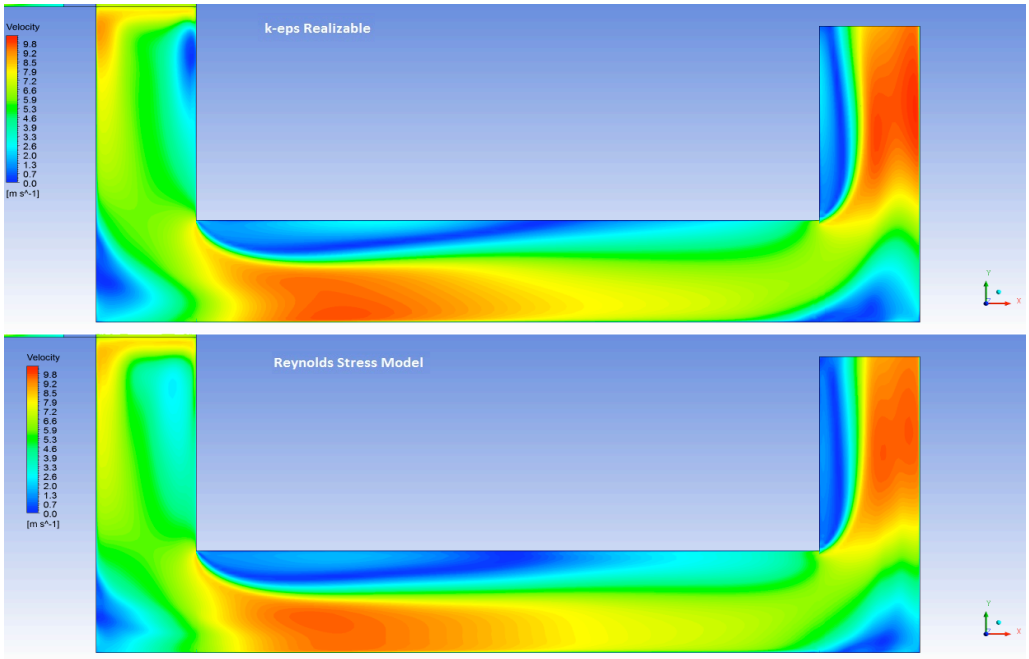

Figure 5-51 Duct B longitudinal section. Detail of velocity contour downstream the first 90° elbow

Hereinafter streamline patterns are proposed as instrument to investigate fluid motion.

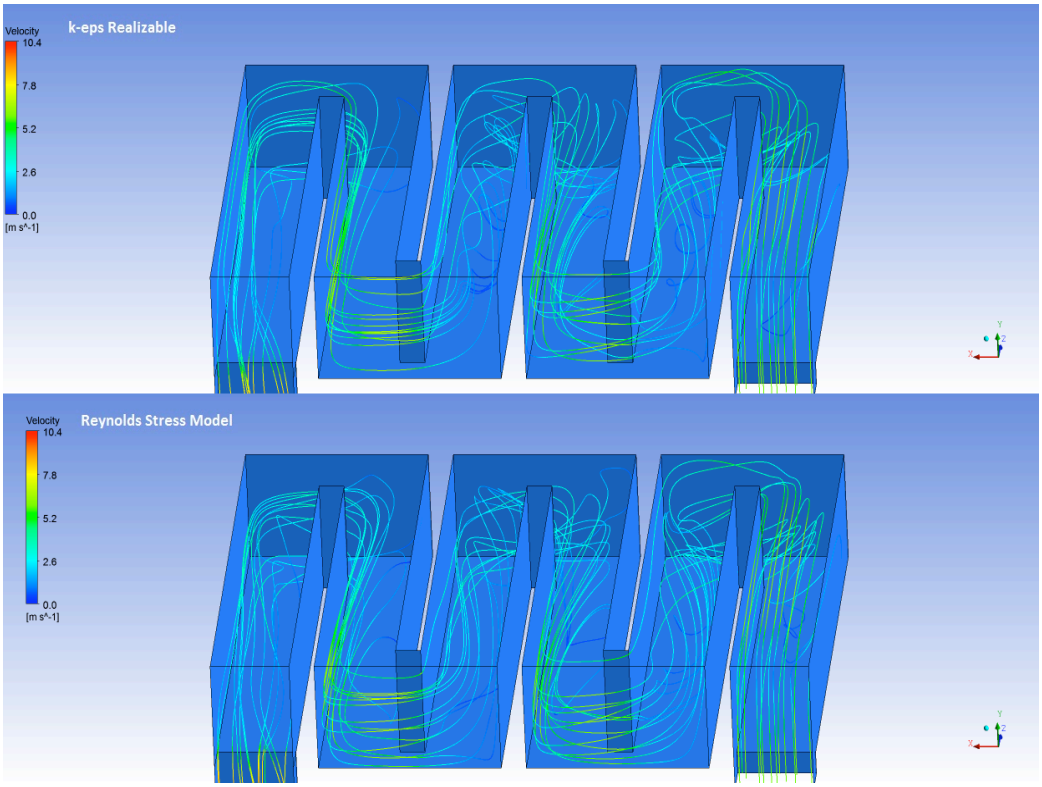

Figure 5-52 Dryer streamline pattern

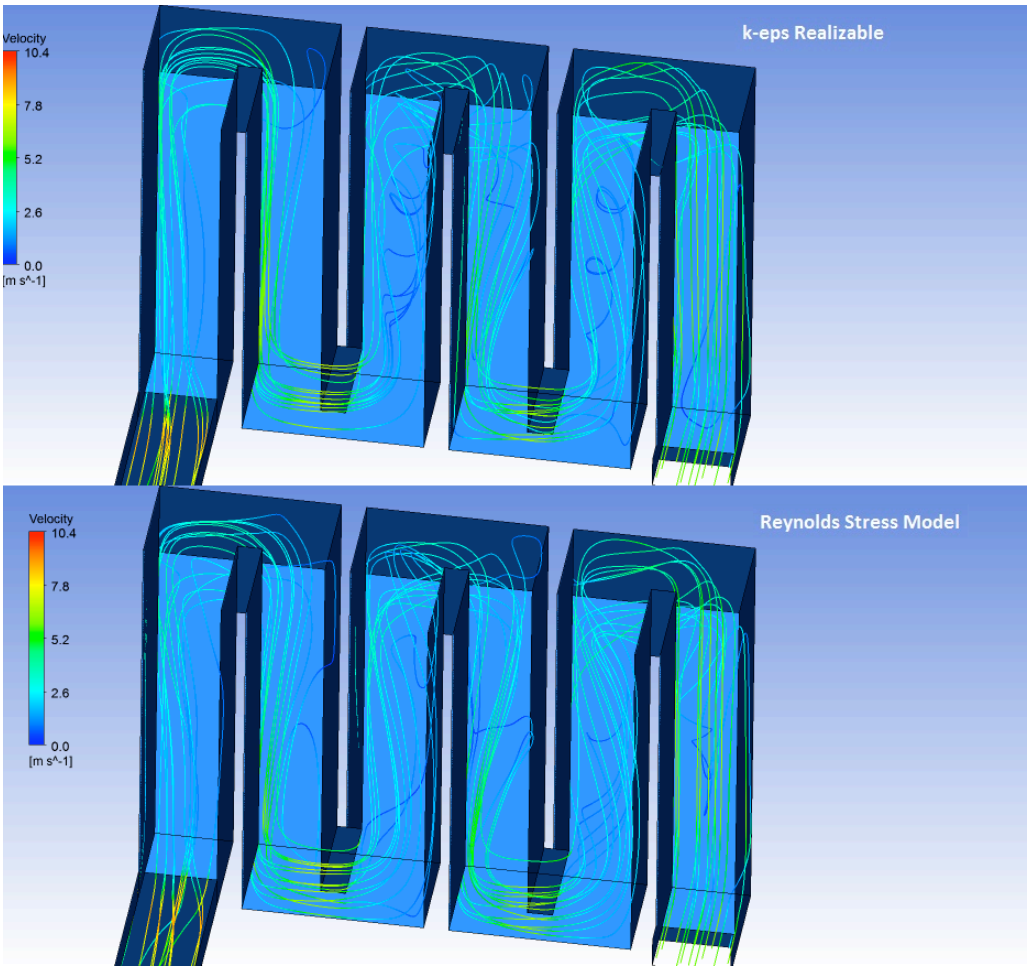

Figure 5-53 Dryer streamline pattern

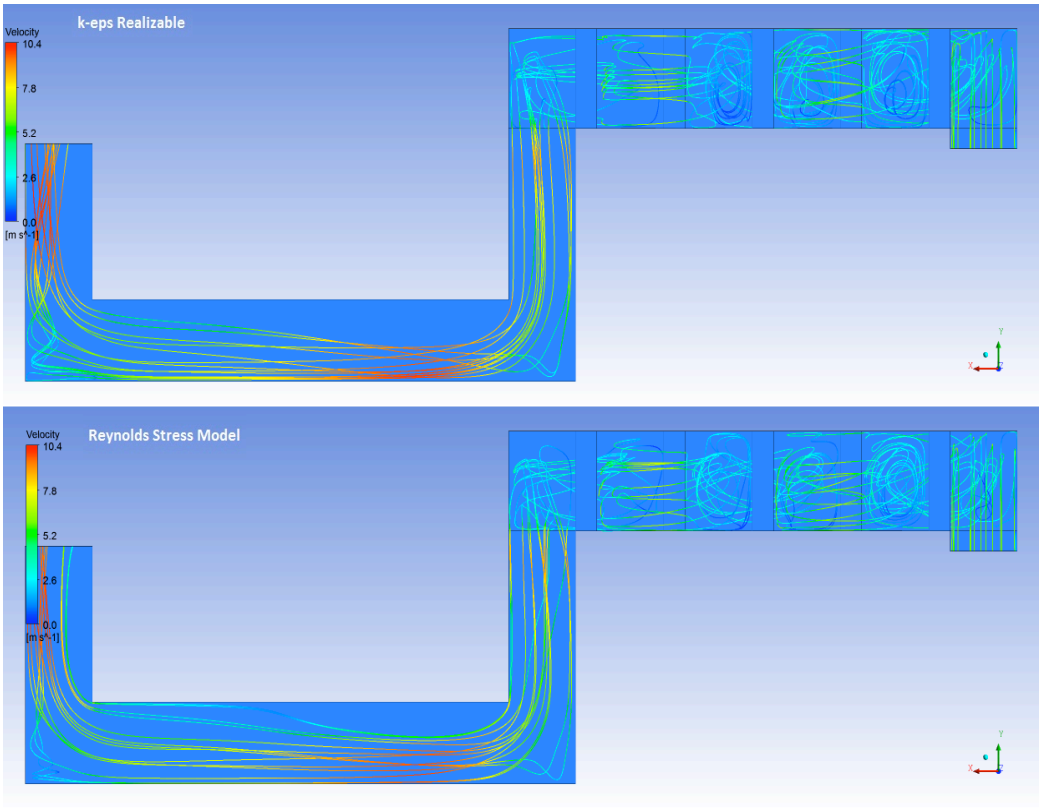

Figure 5-54 Dryer streamline pattern. Lateral view

The results presented above confirmed that the two models give similar global quantities, as for the static pressure and the mean wall shear stress in sections, but totally different local quantities, like velocity and vorticity distributions. RSM is well known for his unstable behaviour with several problems, in this case no turbulence ratio divergence occurred. The usage of one model or the other is related to the final goal of the investigation and level of detail desired.

Eventually, for the sake of completeness, is reported a static pressure contour comparison between Realizable k-ε and RSM at the symmetry plane.

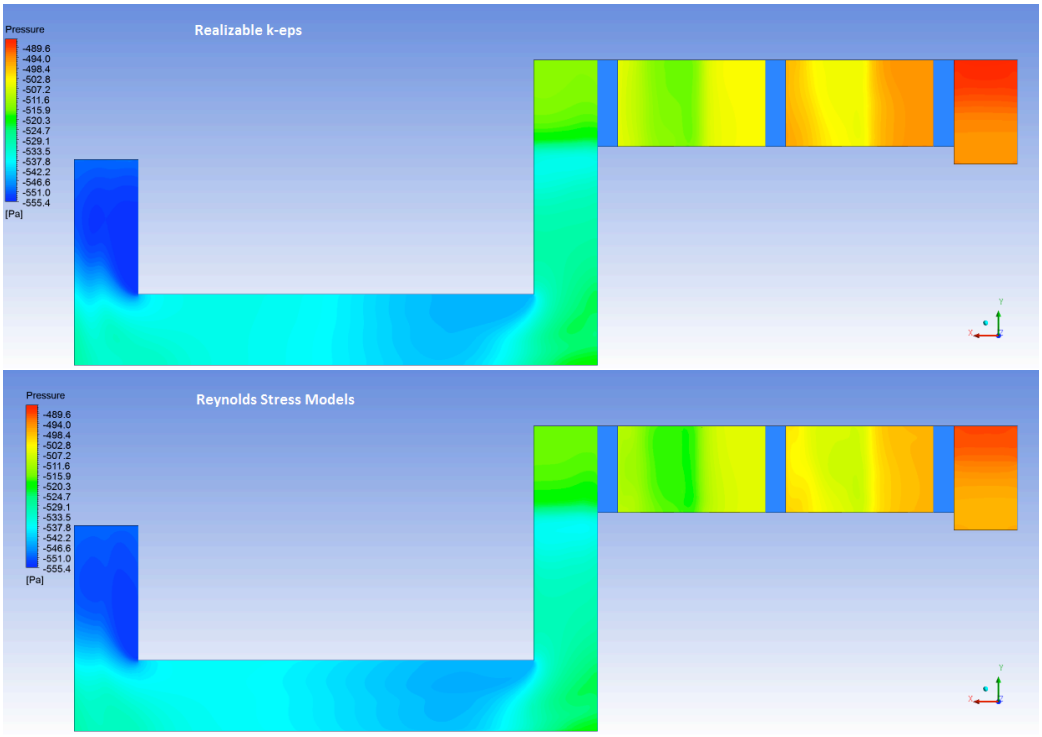

Figure 5-55 Static pressure contour comparison at simmetry plane

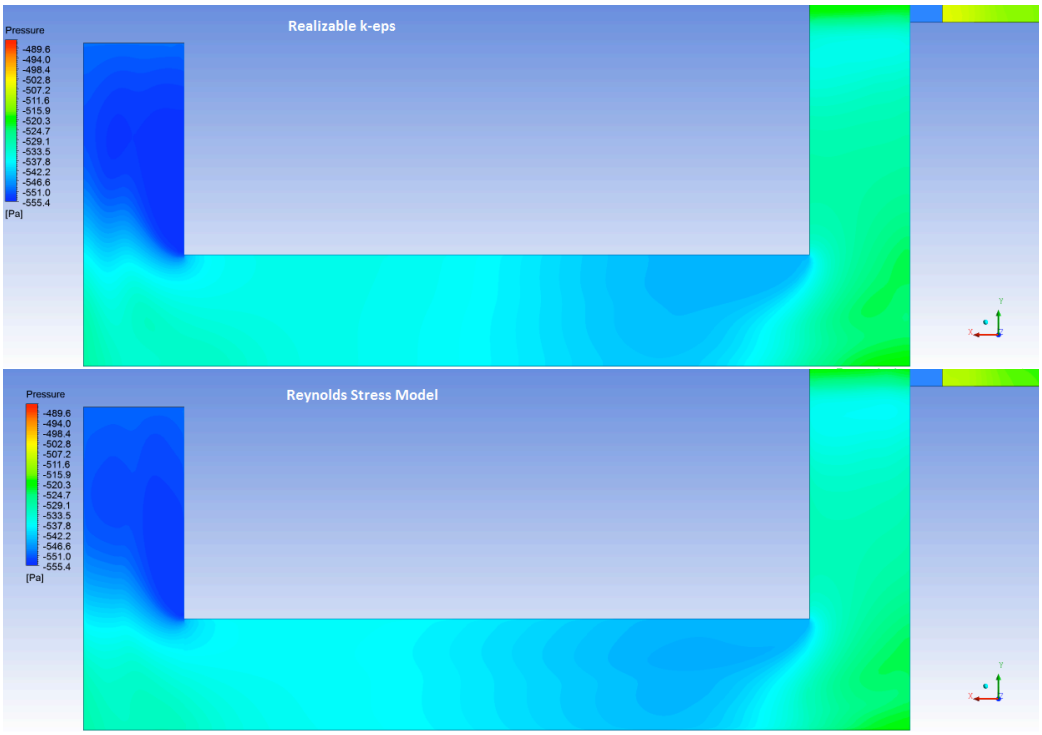

Figure 5-56 Static pressure contour. Detail of duct B

5.3 Duct A

In this section duct A without damper analyzed.

5.3.6 Grid independence study

As for the previous sections, grid independence is performed to understand which grid is the best choice, in terms of computational resources, for the development of calculations. Static pressure at the inlets is the main quantity of interest.
Results obtained through Realizable k-ε model are exposed in the table:

Number of elements	Outlet pressure [Pa]	Inlet 1 pressure [Pa]	Inlet 2 pressure [Pa]	Δ results inlet 1 [%]	Δ results inlet 2 [%]
515,820	-423	-398.4	-404.9	0.05	0.07
1,278,000	-423	-398.3	-404.6	0.025	0
2,445,250	-423	-398.2	-404.6	----	----

Table 5-6 Grid independence results. Static pressure at inlets

It is shown that values are almost coincident in all the three sections. Mean wall shear stress values calculated for three different sections are reported in the following picture:

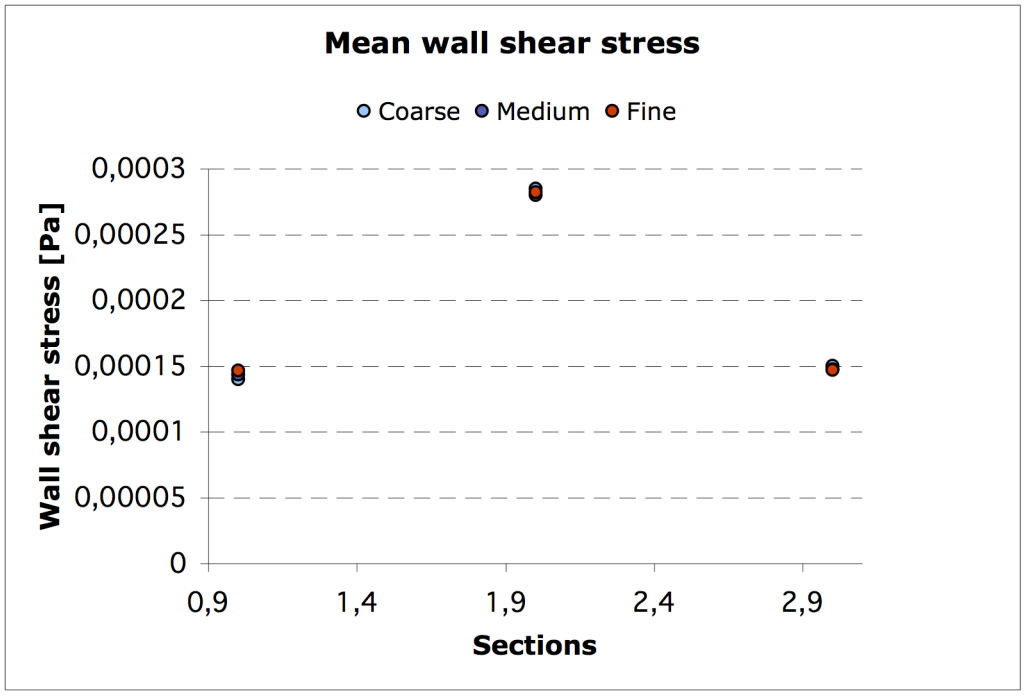

Figure 5-57 Grid independence study. Mean wall shear stresses for duct A

A velocity comparison is required for further investigations. Hence 40 punctual values are sampled along a line parallel to the x-axis, fixed y and z coordinate:

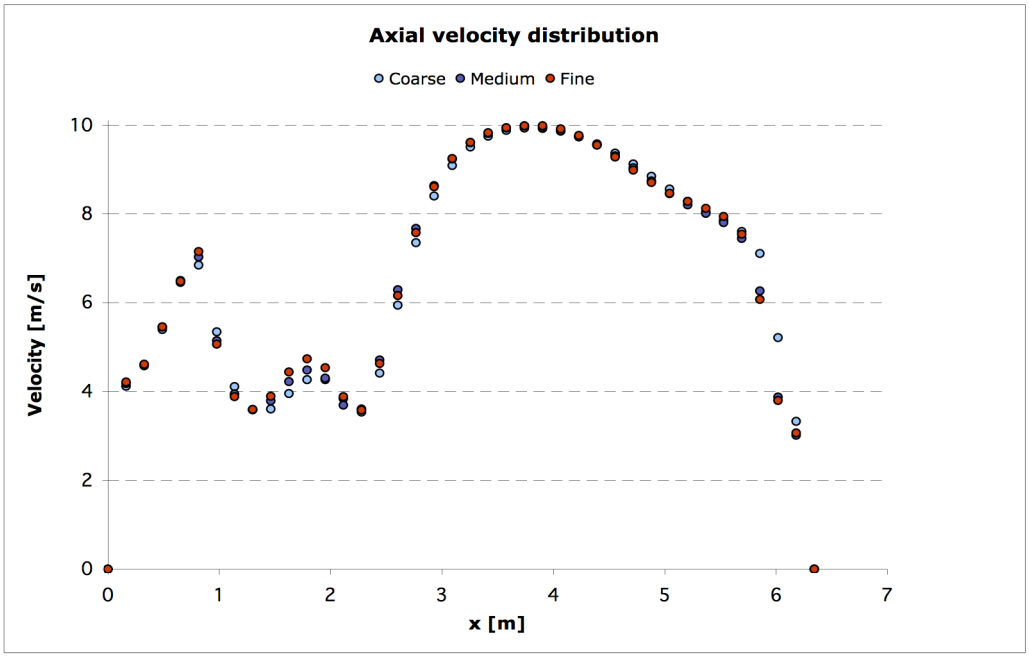

Figure 5-58 Grid independence study. Axial velocity distribution on a rake of 40 points

It is shown that all the three grids have the same trend, but the coarse generates slightly different values in the left side of the device, which corresponds to the two flow inlets. Another velocity distribution comparison along the y direction (channel height), fixed z coordinates, is performed moving in the x direction. Results are shown in the following pictures.

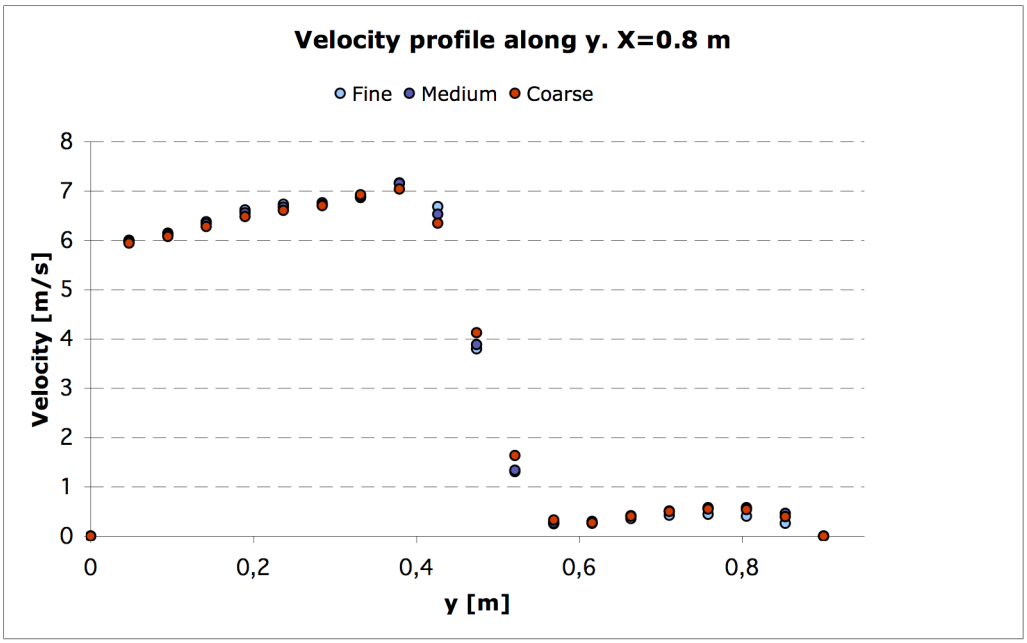

Figure 5-59 Velocity profile comparison in the height direction y

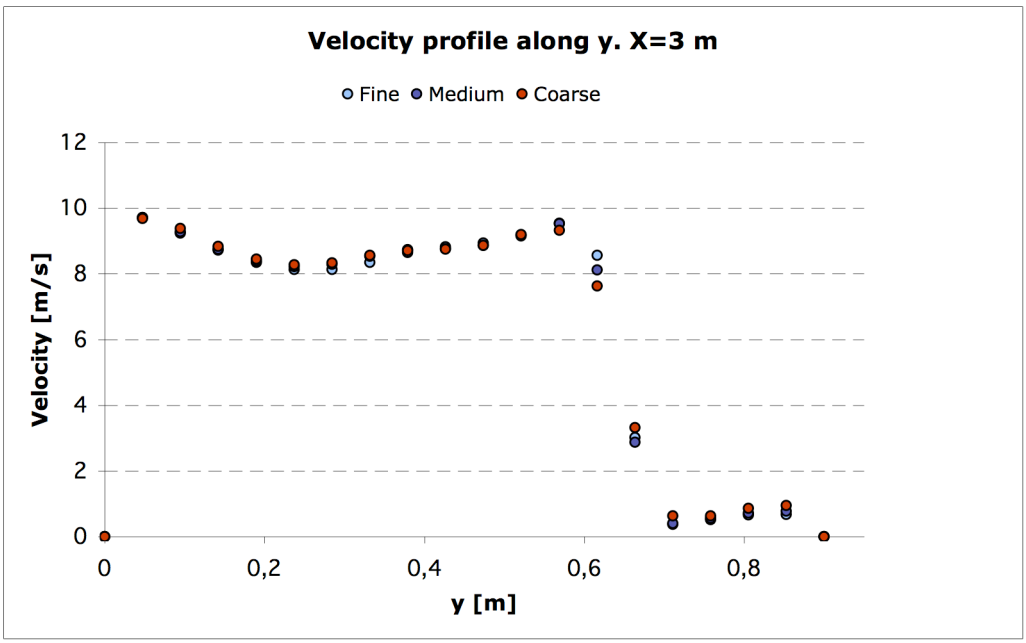

Figure 5-60 Velocity profile comparison in the height direction y

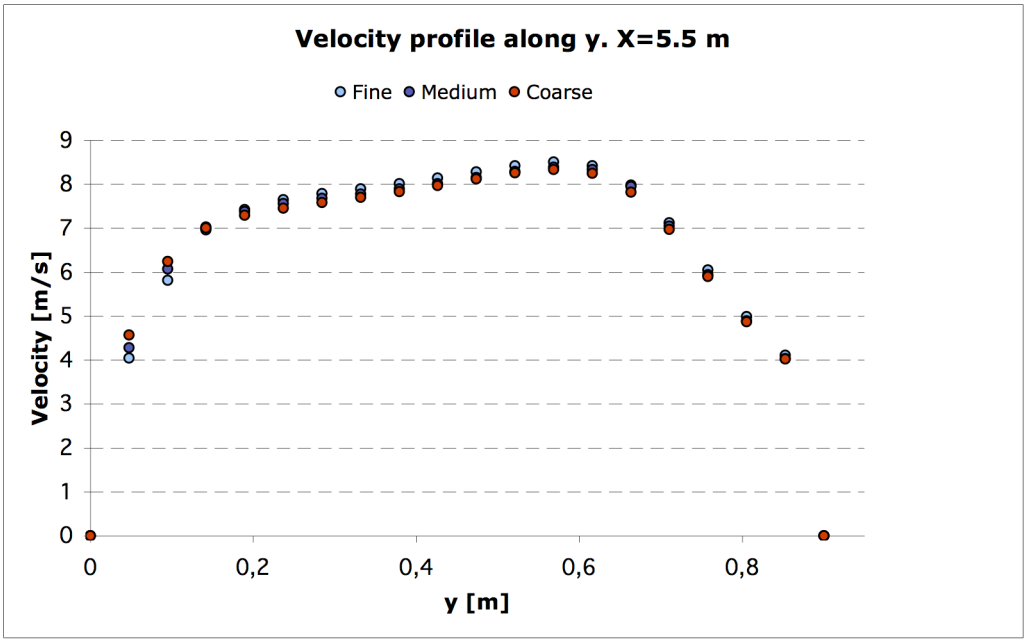

Figure 5-61 Velocity profile comparison in the height direction y

The last velocity profile comparison is performed along the x direction, in the rising part of the duct, at a height y = 3,5 m with z fixed:

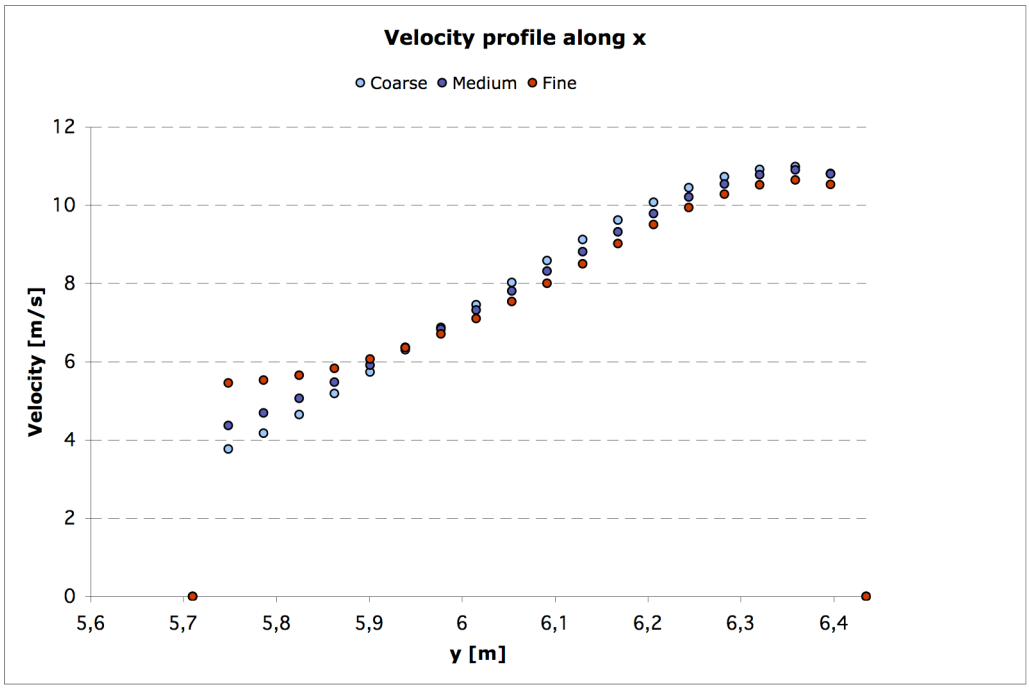

Figure 5-62 Velocity profile comparison in the longitudinal direction x

The velocity distributions presented above show that globally all the three grids produce the same results, but the coarse has more local discrepancies than the medium size, with respect of the fine. Hence the medium grid is adopted for further investigations.

5.3.7 Results

Realizable k-ε is the only model adopted for the calculation, since RSM here cannot converge to a stable solution. Two cases are analyzed for duct A. In the first the domain outlet pressure derives from the usage of Realizable model in the analysis of the ejector-stack, while in the second it comes from the k-ω SST model. Simulation results are reported in the table:

	Pressure [Pa]	
	Case 1	**Case 2**
Inlet 1	-469.5	-397.2
Inlet 2	-475.9	-403.6
Outlet	-494	-422
Pressure drop	-24.5	-24.8

Table 5-7 Simulation results for duct A

The investigated quantities reported in the grid convergence section are here integrated with velocity profile distributions and fluid flow visualizations.

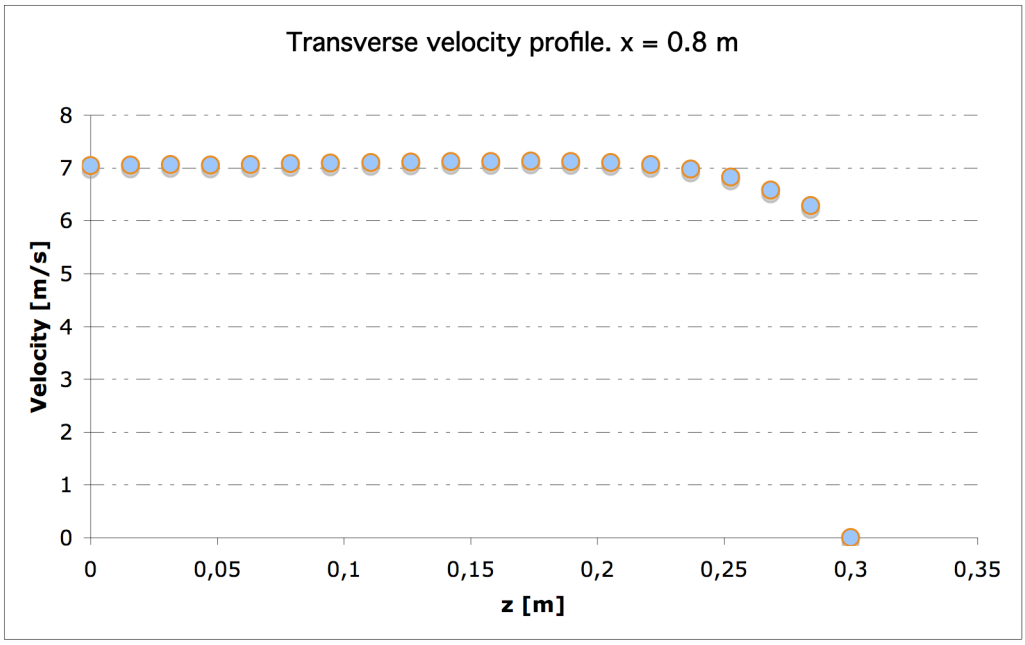

Figure 5-63 Velocity profile in the depth (z axis) direction

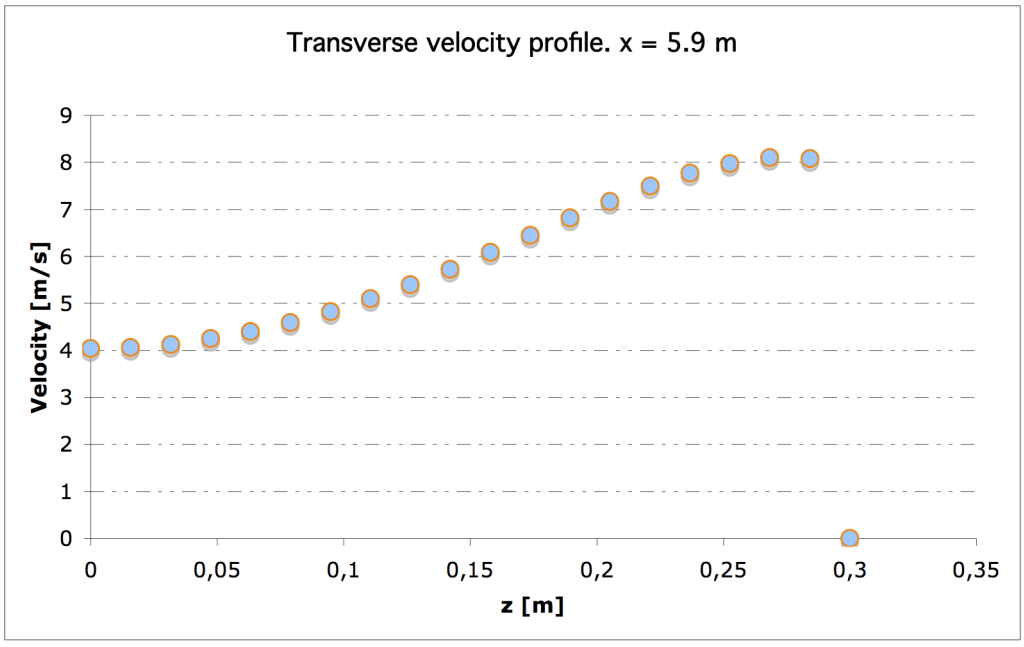

Figure 5-64 Velocity profile in the depth (z axis) direction

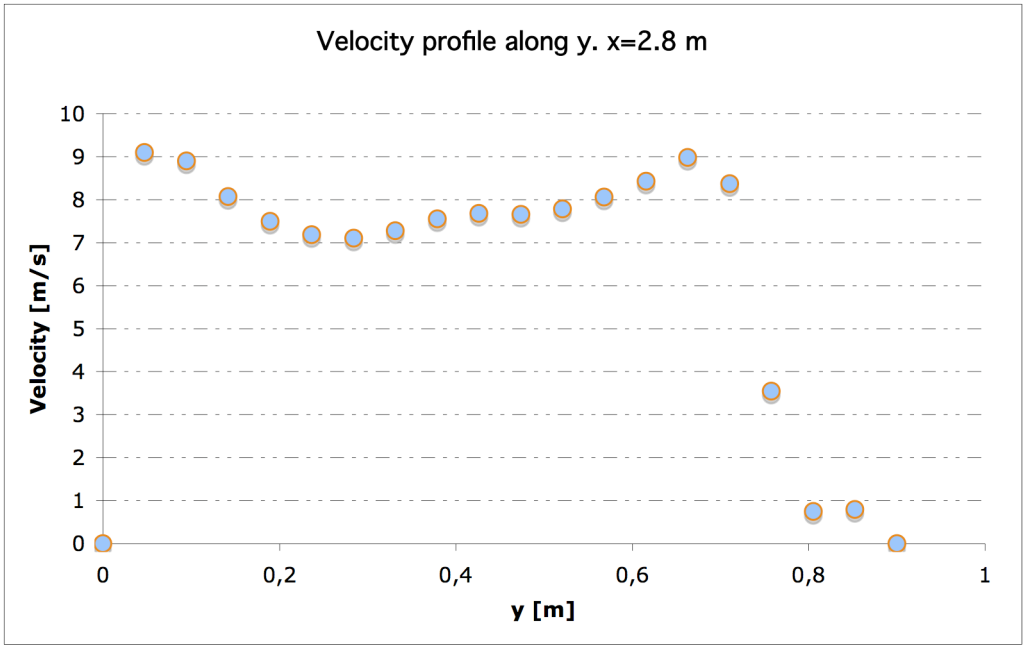

Figure 5-65 Velocity profile in the height (y axis) direction

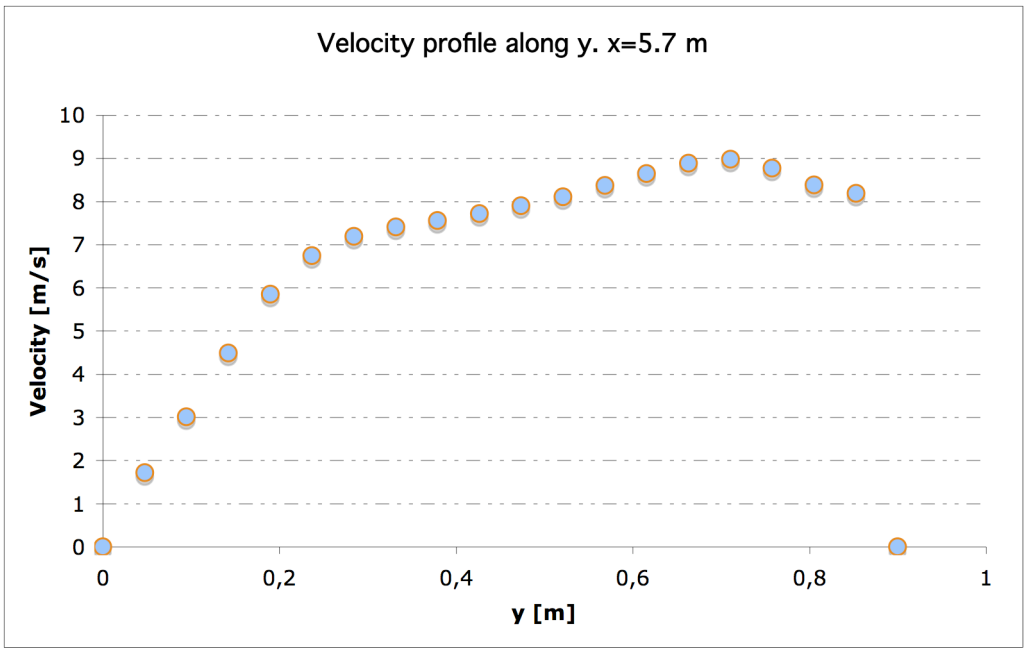

Figure 5-66 Velocity profile in the height (y axis) direction

In the following pictures velocity contours and vectors are reported. These permit to visualize the flow characteristics in the device. Noticeable are the recirculation

phenomena immediately after the two inlets, in the right corner and at the inner wall of the rising duct.

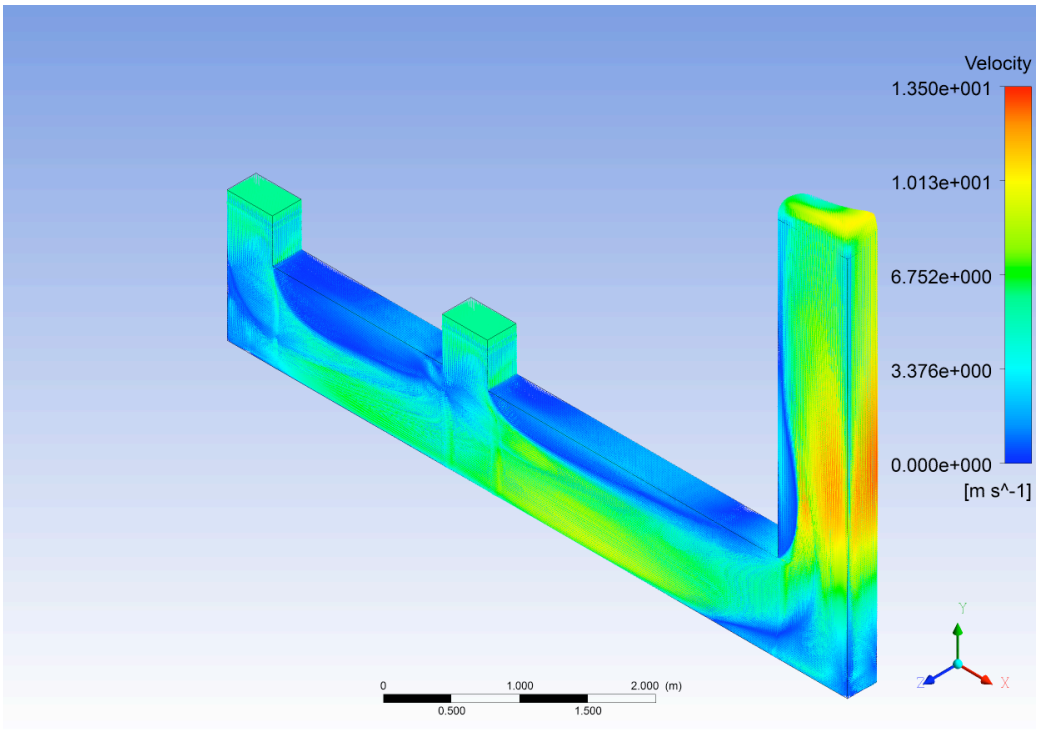

Figure 5-67 Velocity vectors. Global view

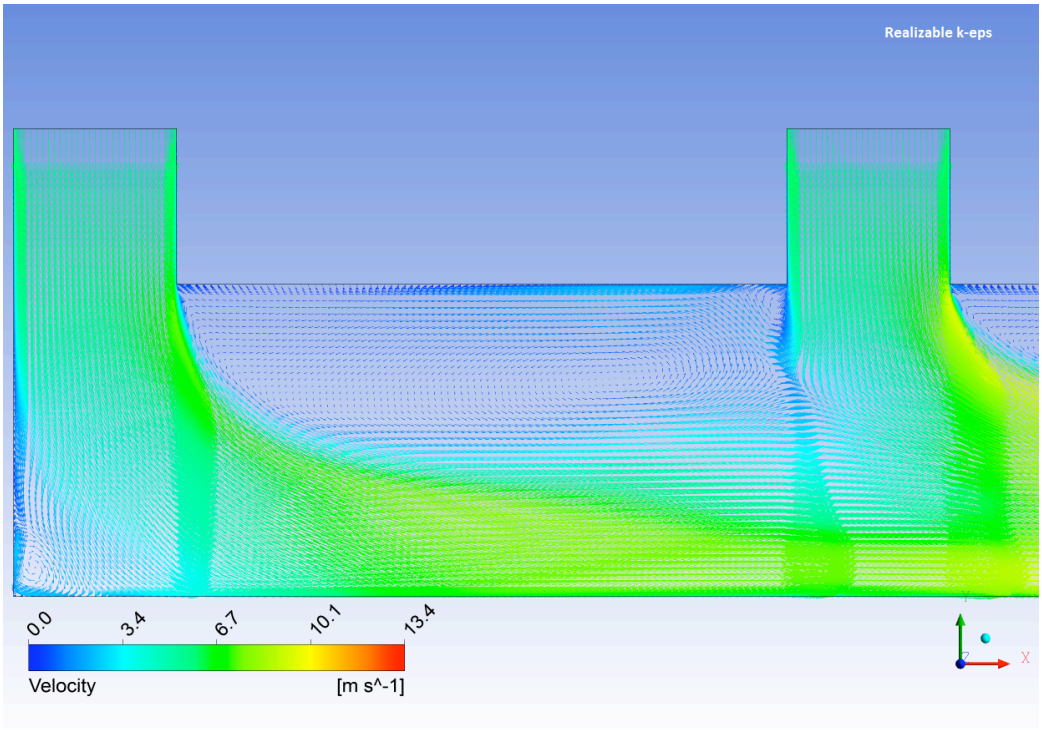

Figure 5-68 Velocity vectors. Detail of the section between the two inlets.

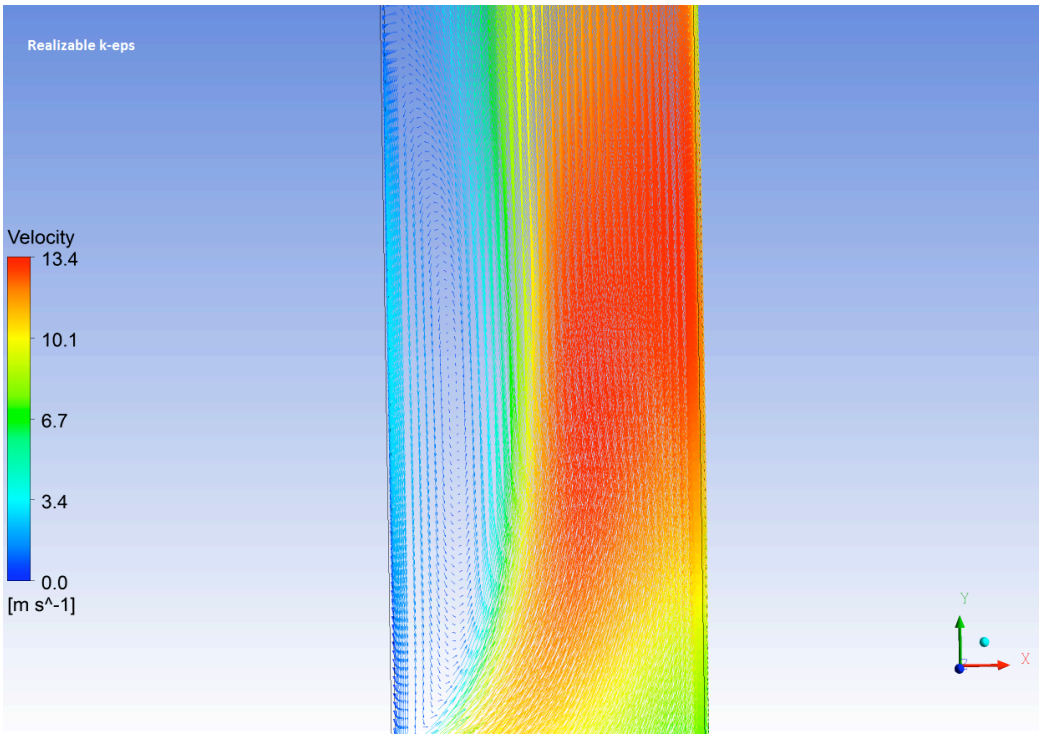

Figure 5-69 Velocity vector. Detail of recirculation in the rising duct

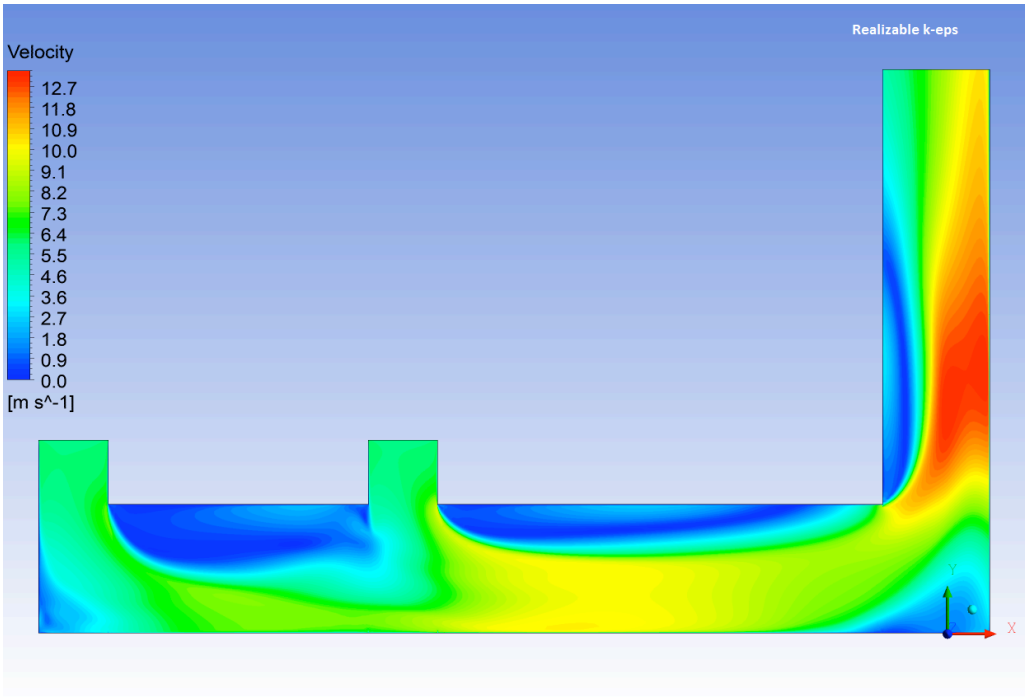

Figure 5-70 Velocity contour. Side view

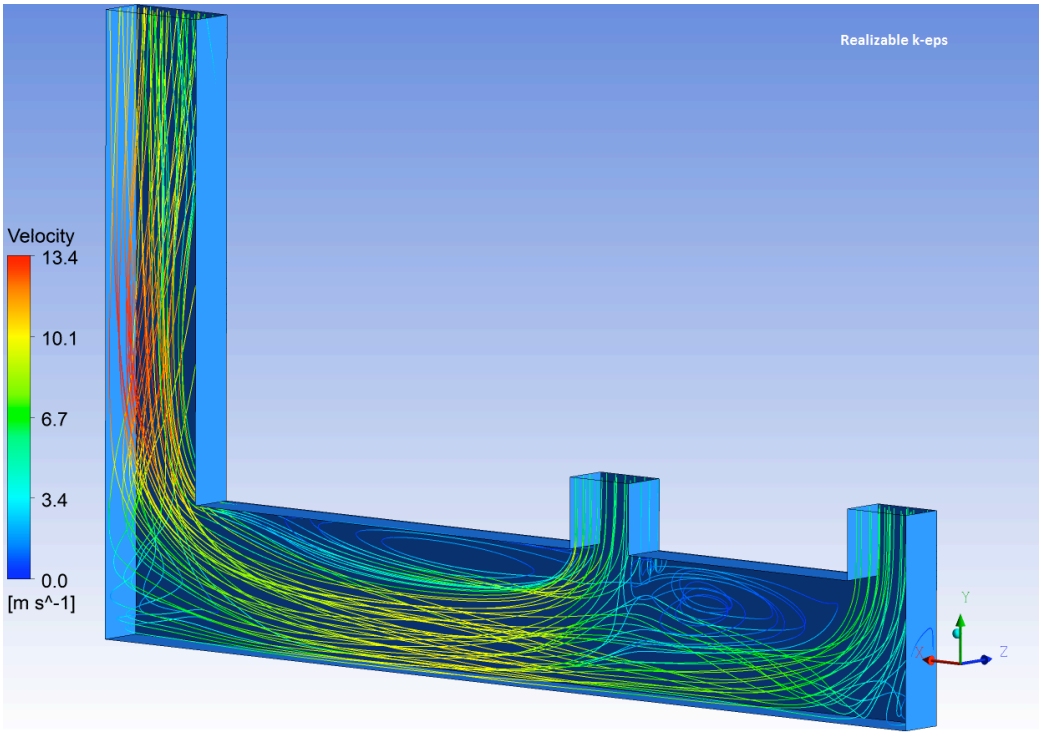

Figure 5-71 Streamlines. Strong recirculation after inlets is evident

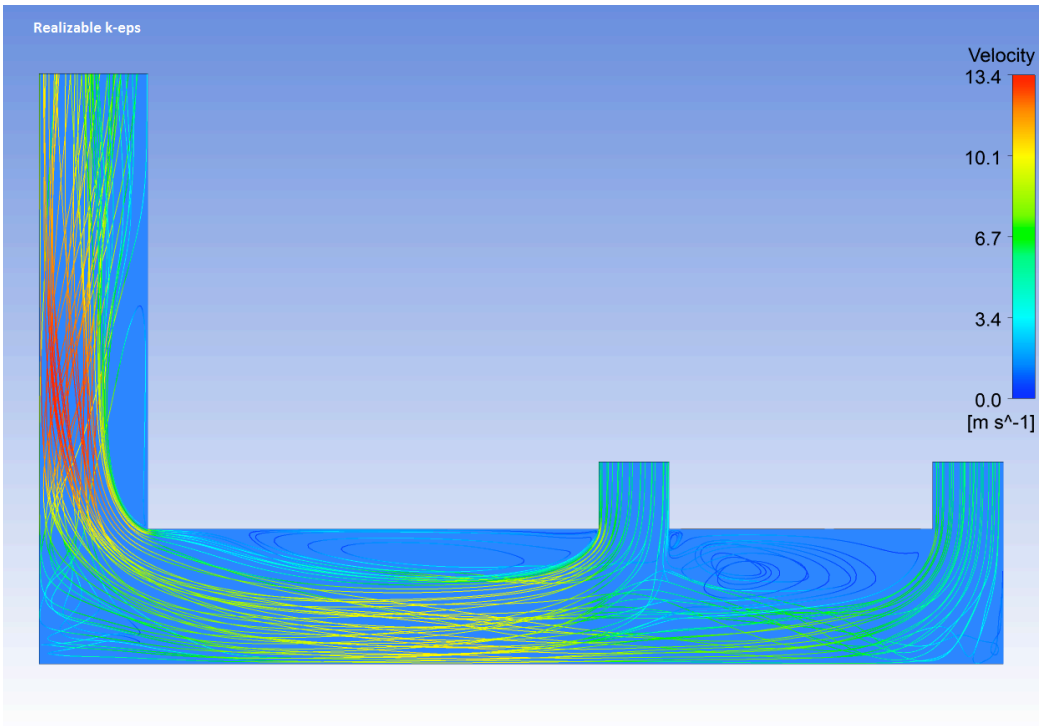

Figure 5-72 Streamlines. Lateral view

Finally a static pressure contour is showed for the case 1, with outlet pressure value equal to -424 Pa. The other for case 2 is not reported because is similar to the first, pressure values are simply translated upward.

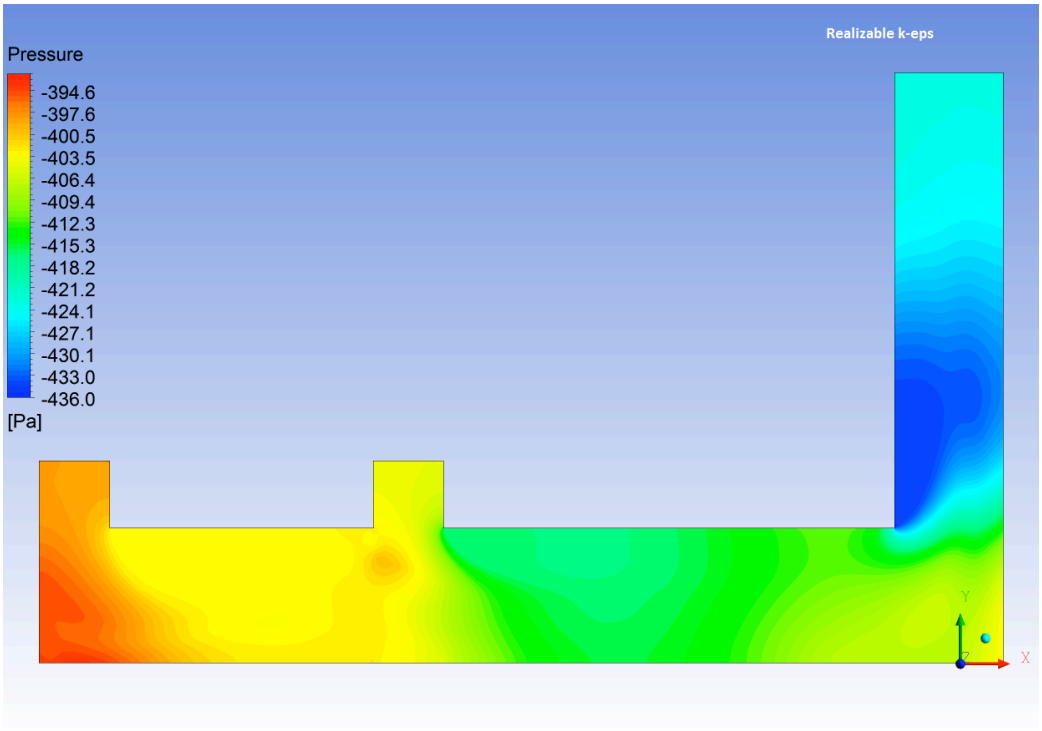

Figure 5-73 Static pressure contour. Side view

5.4 Duct A + damper

In this section the damper is lowered in the duct A in order to obtain the desired pressure value upstream in the furnace chamber. It is located at x = 4.25 m far from the domain origin.

5.4.1 Grid independence study

Three meshes with progressive refinement level are involved in this phase: a coarse, a medium size and a coarse grid. As for the previous section, static pressure at inlets is the main goal. Results obtained through Realizable k-ε model are reported in the table:

Number of elements	Outlet pressure [Pa]	Inlet 1 pressure [Pa]	Inlet 2 pressure [Pa]	Δ results inlet 1 [%]	Δ results inlet 2 [%]
2,166,175	-423	-41.7	-47.9	0.5	0.4
3,465,000	-423	-42.5	-48.6	1.5	1.1
4,199,250	-423	-41.9	-48.1	----	----

Table 5-8 Grid independence results. Static pressure at inlets for duct A

Values calculated for coarse and fine mesh are really close, while medium size differs of a few tenths of Pascal. Mean wall shear stress is evaluated for 4 different sections along the device. Results are reported in the figure below.

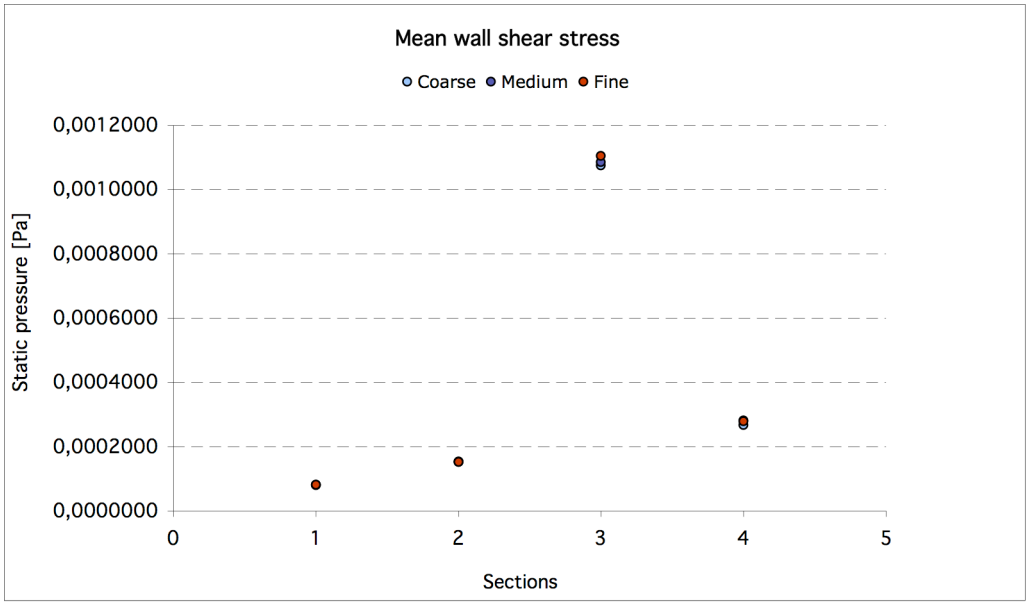

Figure 5-74 Grid independence study. Mean wall shear stress for different sections of duct A + damper

It is noticeable that results do not differ significantly for the three grids. A punctual velocity comparison on a line parallel to the x-axis, fixed x and y coordinates, is performed to quantify the discrepancy between the meshes:

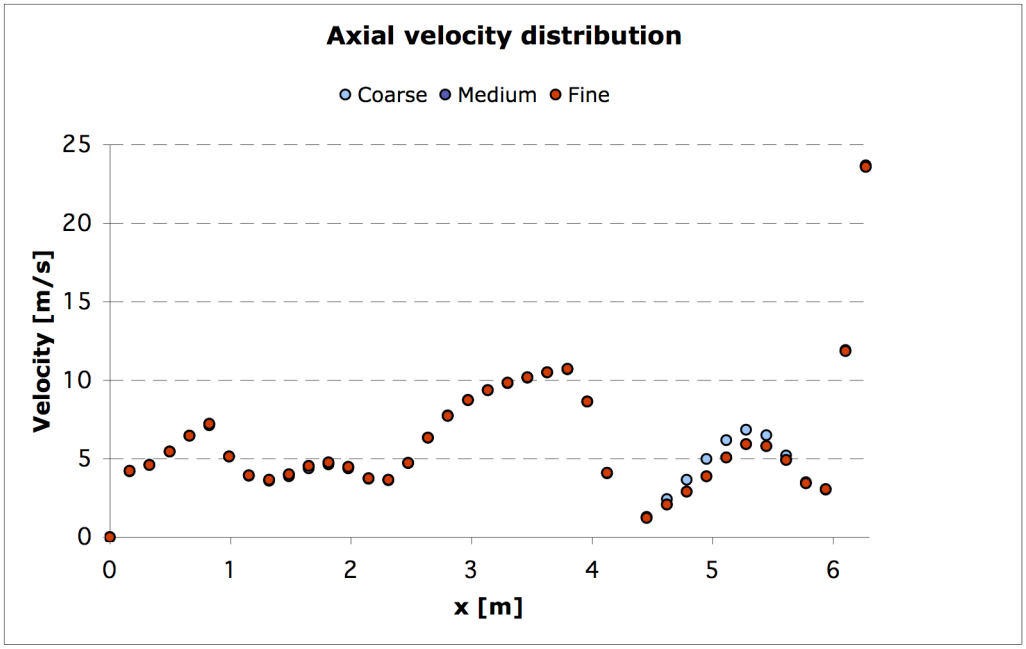

Figure 5-75. Axial velocity comparison along a line of 40 points. Damper is located at x = 4.25 m, it is visible the velocity reduction around that distance, because the line crosses this device

The coarse mesh differs slightly, with respect to the others, in the region immediately after the damper, where the stream expands progressively and its velocity magnitude is high. More profiles in the depth (z) and height (y) directions are presented in the following pictures.

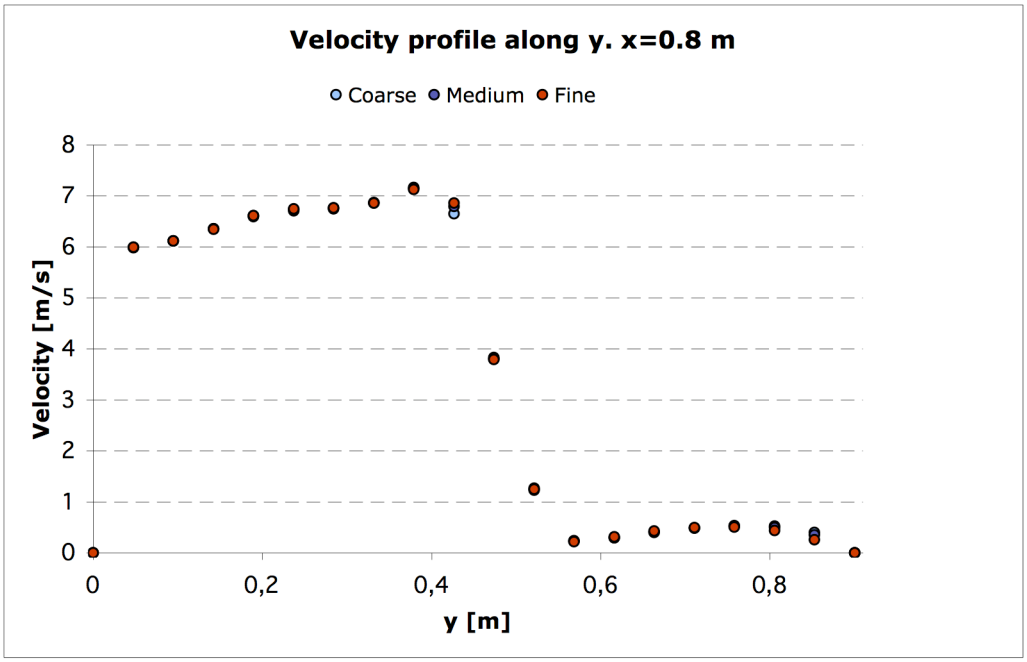

Figure 5-76. Transverse velocity profile in the height direction

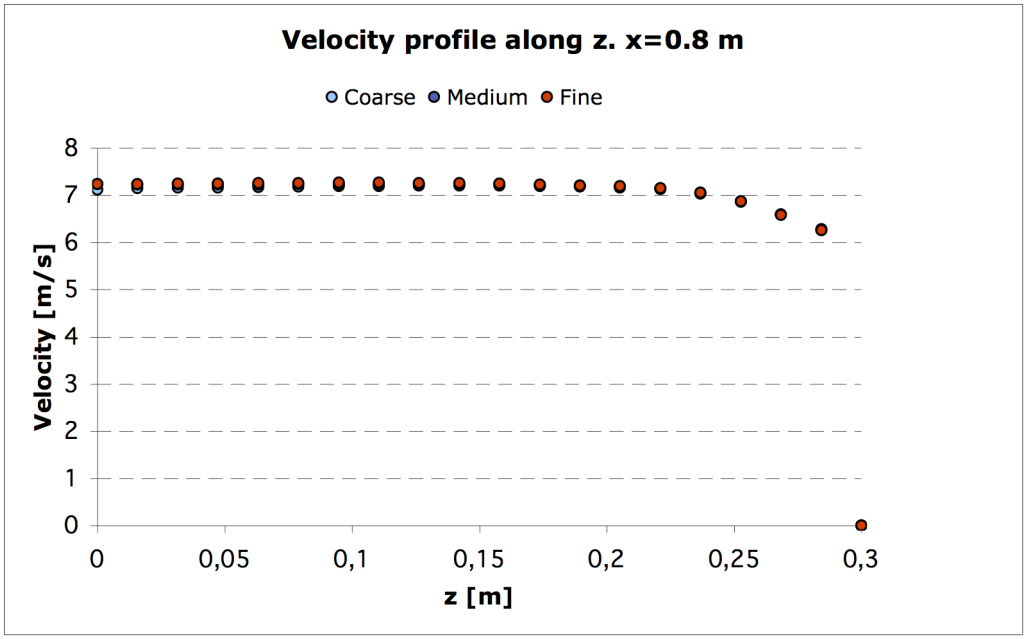

Figure 5-77. Transverse velocity profile in the depth direction

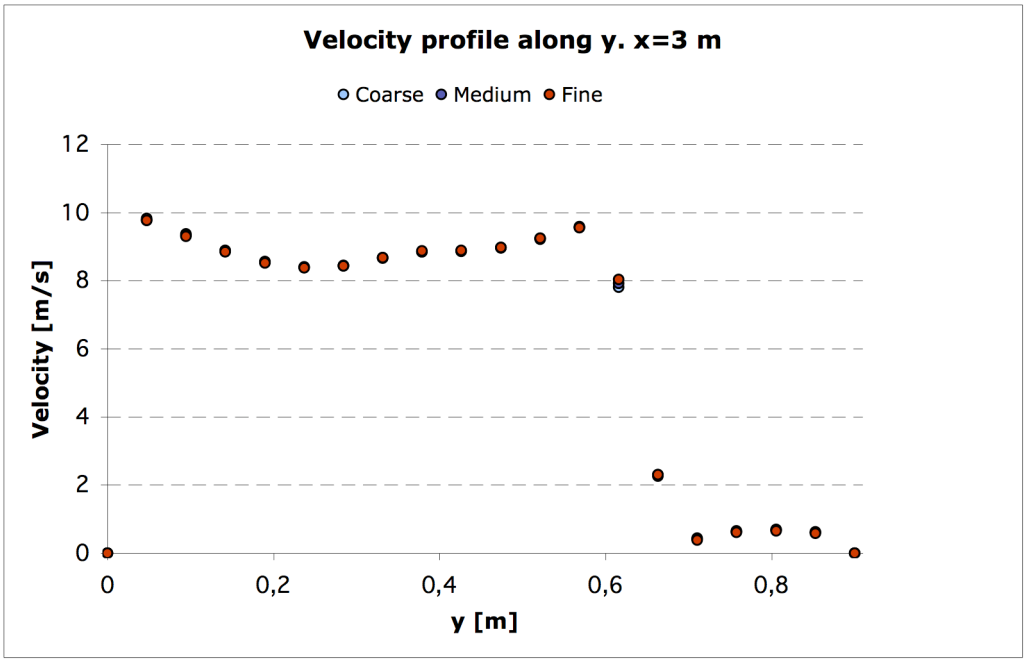

Figure 5-78. Transverse velocity profile in the height direction

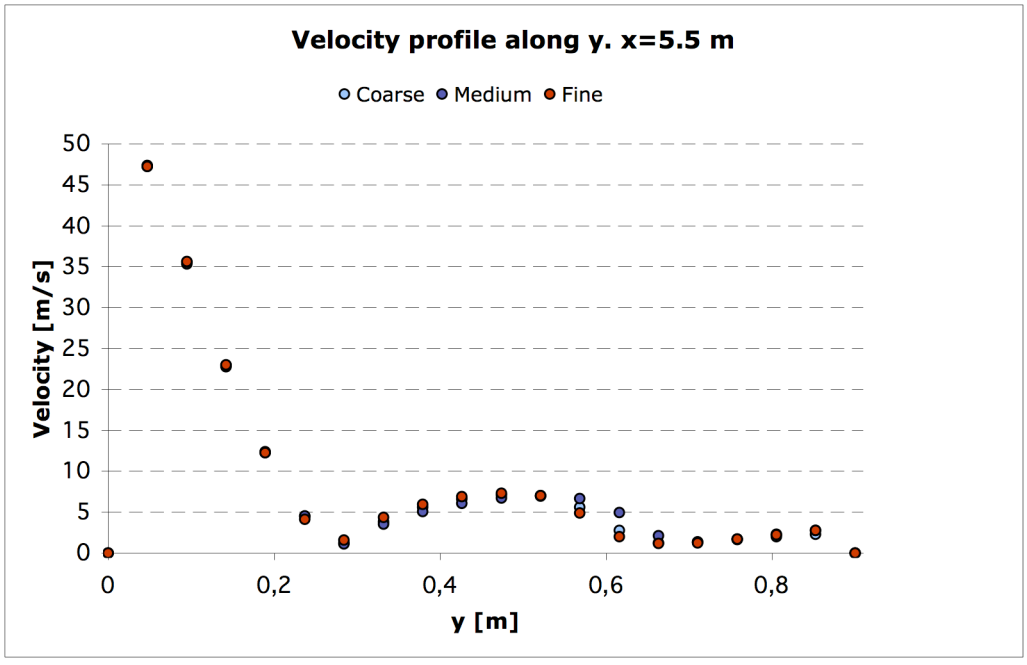

Figure 5-79. Transverse velocity profile in the height direction

The figures presented above show that neither globally nor locally there are significant discrepancies between the three meshes for the quantities analyzed. Hence the coarse mesh is chosen for further calculations, since it offers a good quality solution with an acceptable CPU expense.

5.4.2 Results

The aim of the investigation in this chapter is to determine the damper lowering level that guarantees a static pressure value in the range between -0.5 and -65 Pa at the domain inlets. DCHP tutor's experience states that this range of values is compatible with the on-design galvanizing plant operation condition. Case 1 and 2 referred to the ejector-stack output determine here a different damper lowering, measured from the roof of the duct.

Number of elements	Outlet pressure [Pa]	Inlet 1 pressure [Pa]	Inlet 2 pressure [Pa]	Lowering level [mm]	Pressure drop [Pa]
Case 1	-422	-41.7	-47.9	730	380.3
Case 2	-494	-57.7	-64.0	740	436.3

Table 5-9 Duct A + damper results. Static pressure at inlets

Additional velocity profiles complete the comparison between duct A without damper:

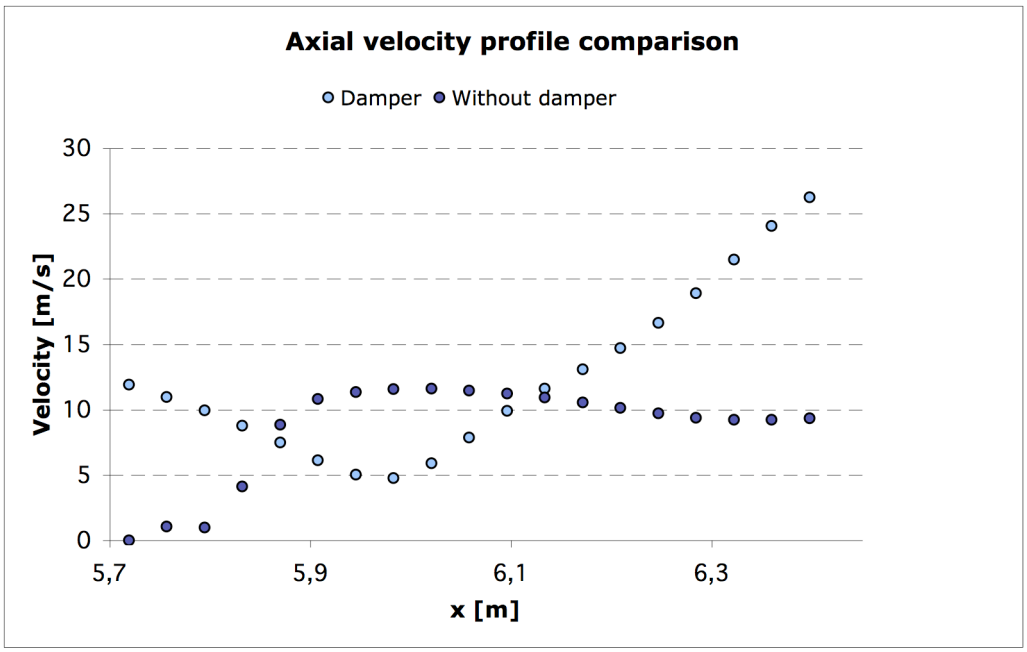

Figure 5-80 Axial velocity comparison in the region downstream the damper

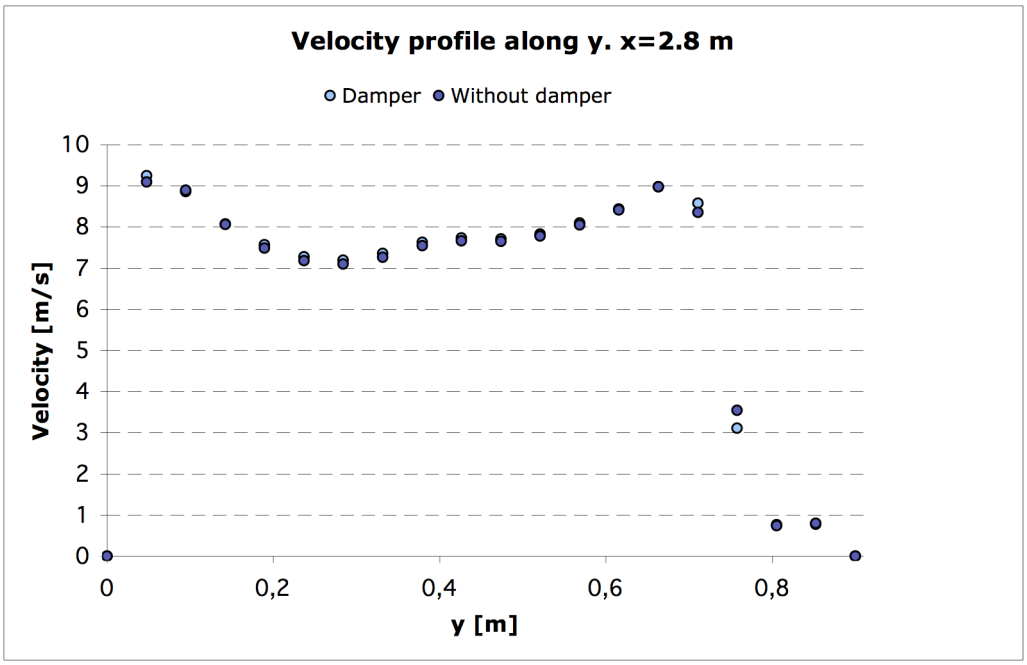

Figure 5-81 Transverse velocity comparison in the region upstream the damper

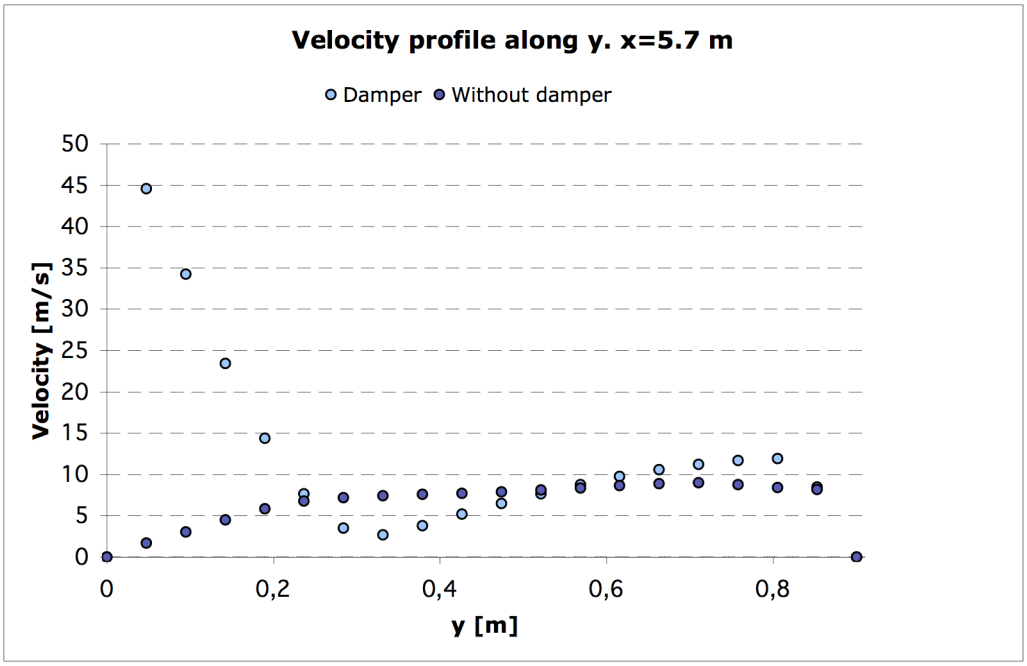

Figure 5-82 Transverse velocity comparison in the region downstream the damper

The presence of the damper causes a big perturbation of the velocity field in the device, with respect to the duct A. The strong acceleration of the fluid flow near the floor downstream the obstacle and the high recirculation in the upper region near the channel roof are visible in the following pictures.

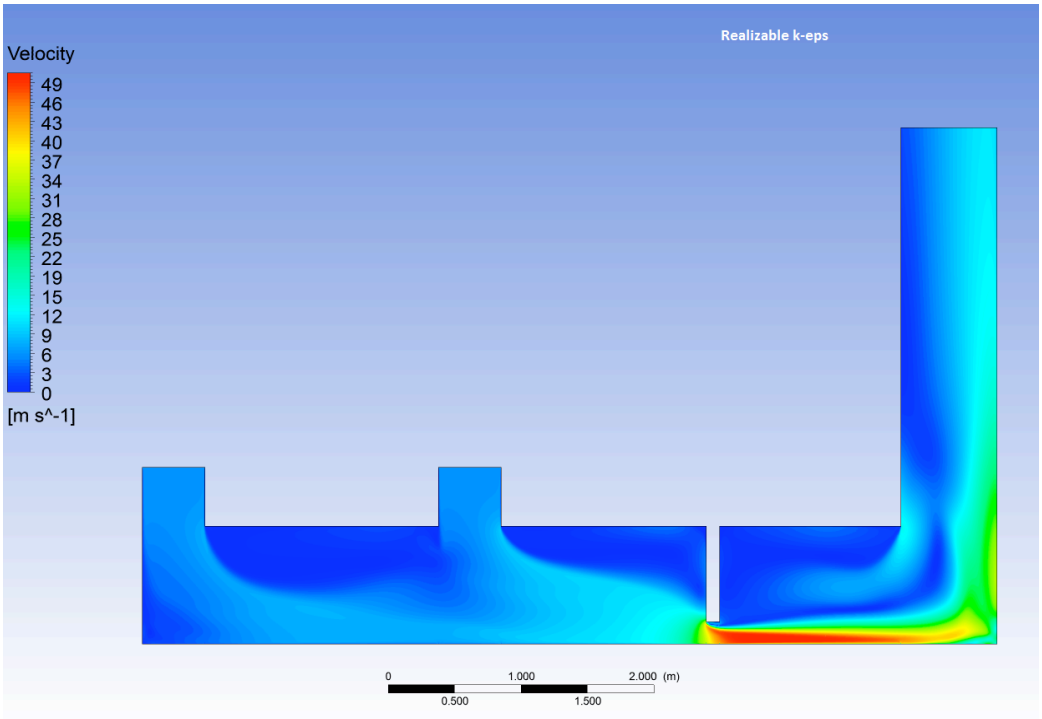

Figure 5-83 Velocity contour. Duct A + damper

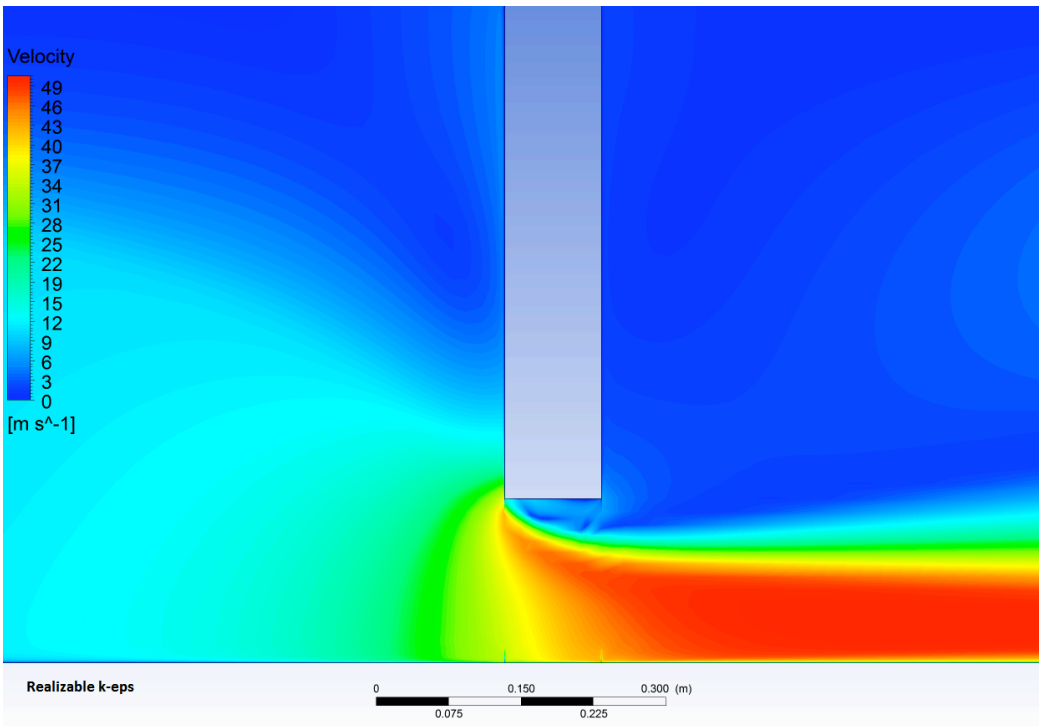

Figure 5-84 Velocity contour. Detail of the damper tip region

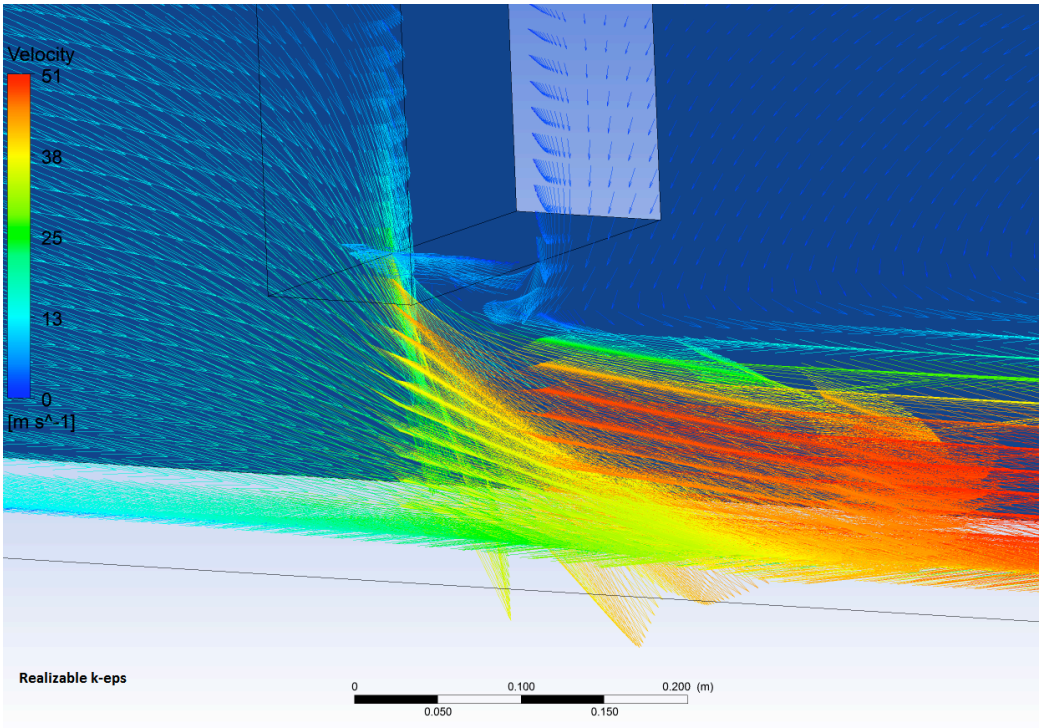

Figure 5-85 Velocity vector, detail of the region immediately after the damper. The stream accelerates near the floor, while recirculates in the upper part.

Streamlines are here extremely useful to visualize all the abovementioned phenomena:

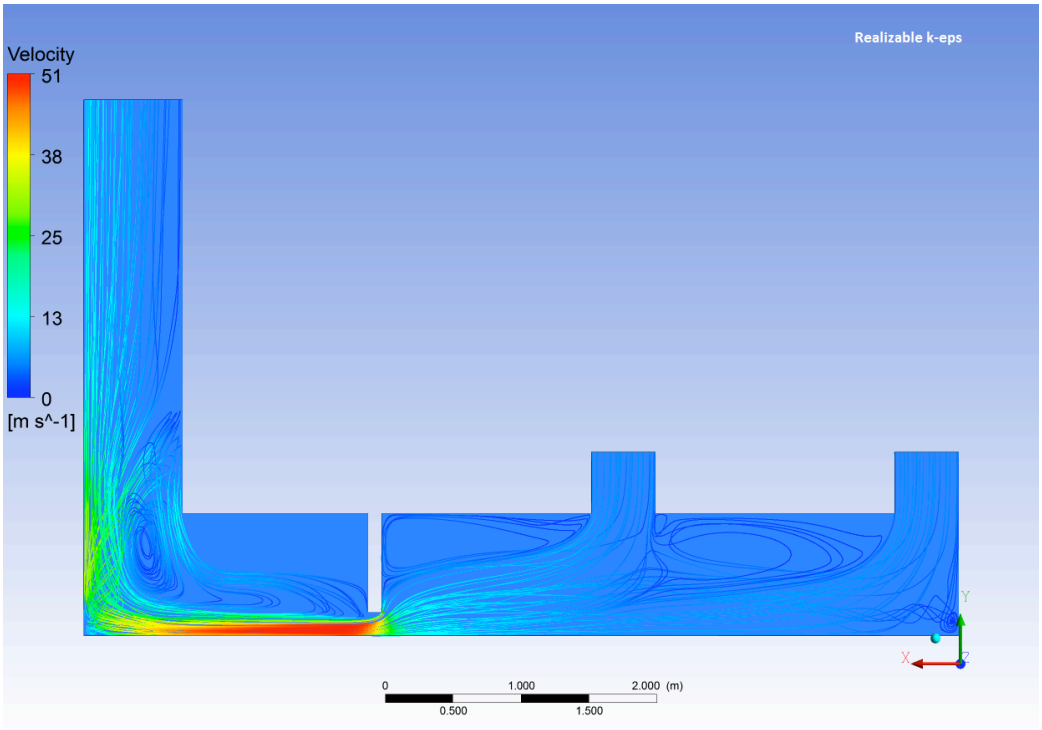

Figure 5-86 Streamlines. Global view

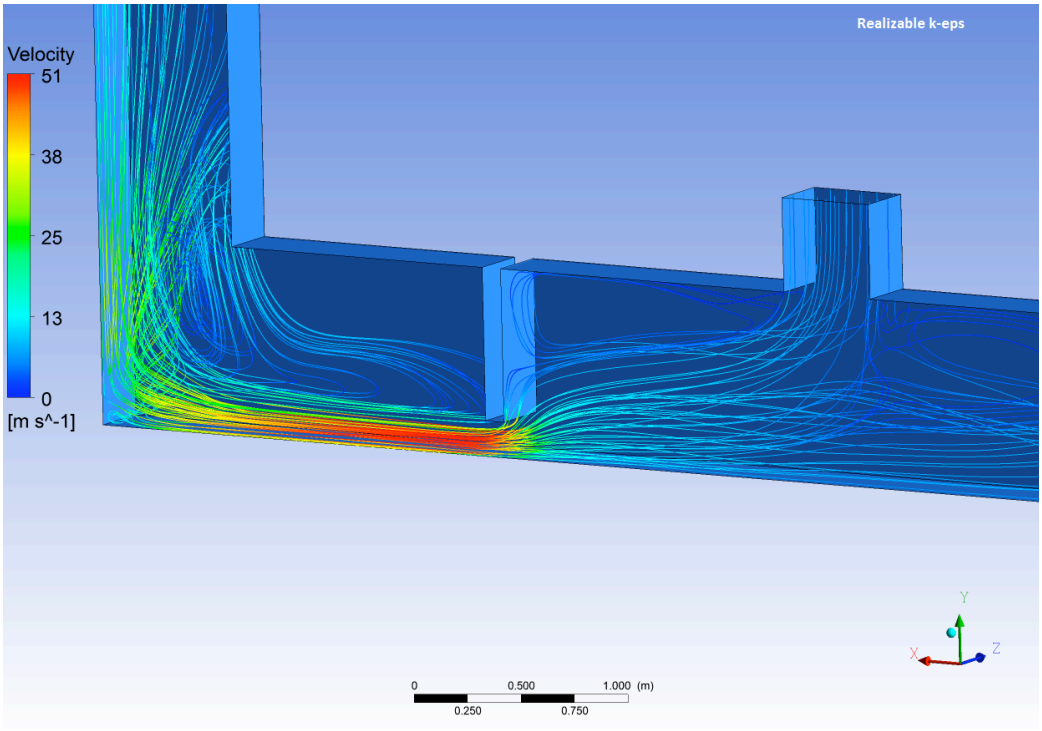

Figure 5-87 Streamlines. Detail of the damper surrounding region

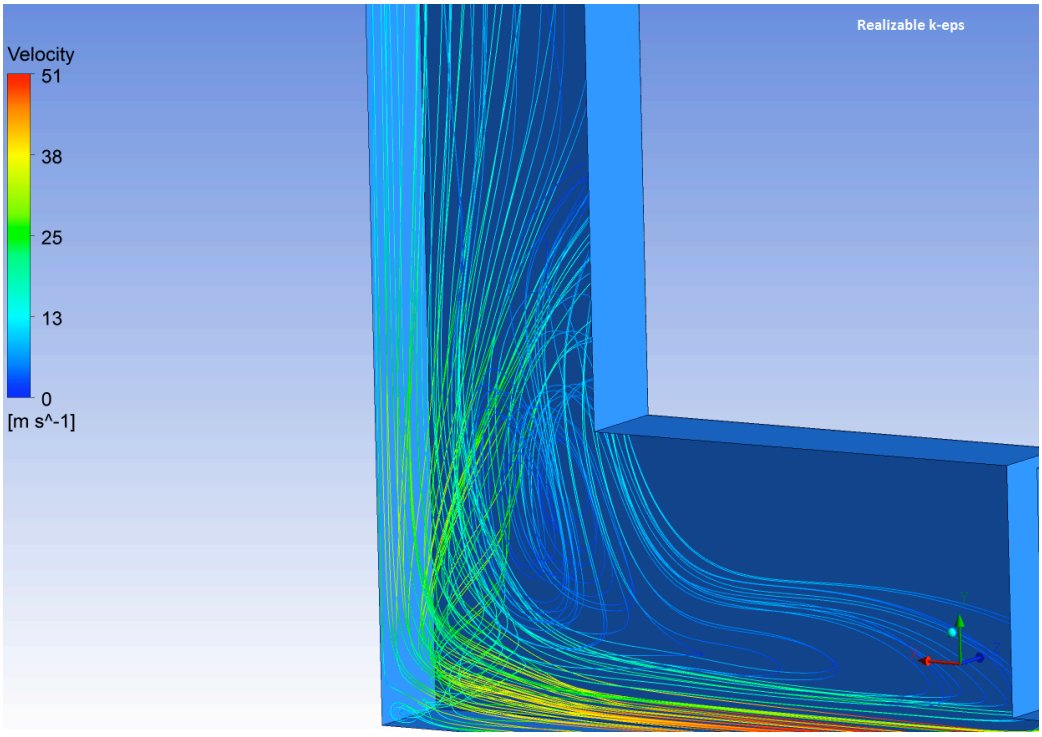

Figure 5-88 Streamlines. Detail of the damper downstream region

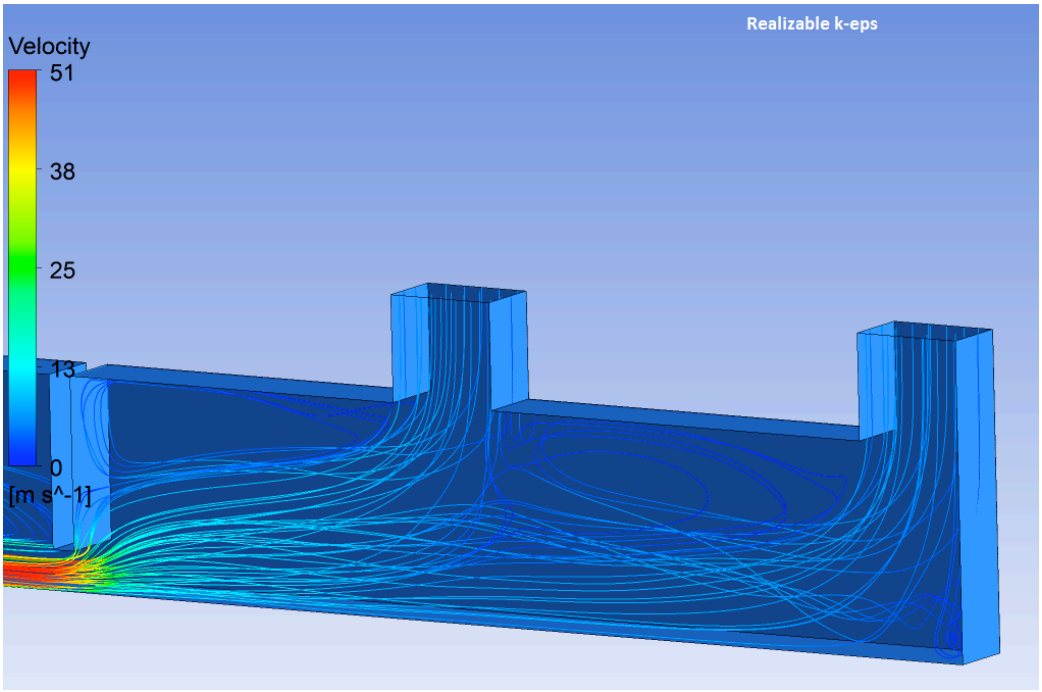

Figure 5-89 Streamlines. Detail of the damper upstream region

Finally a pressure contour is reported for the case 1 (outlet pressure = -422 Pa) to visualize how field develops in presence of a localized pressure drop:

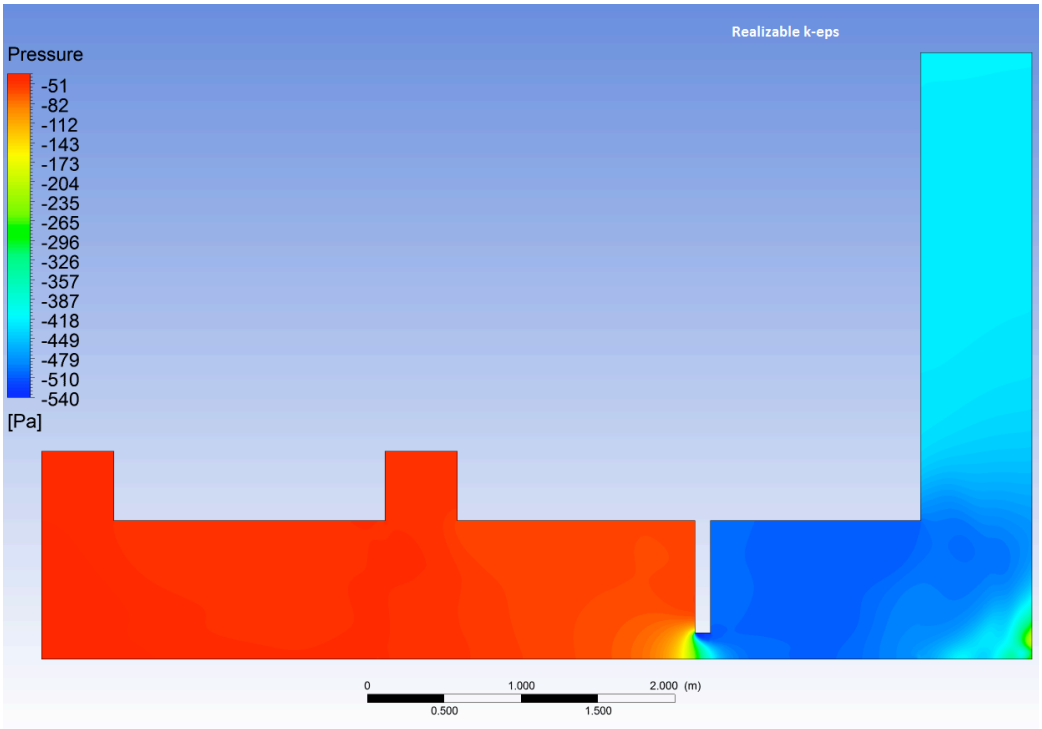

Figure 5-90 Static pressure contour. Global view

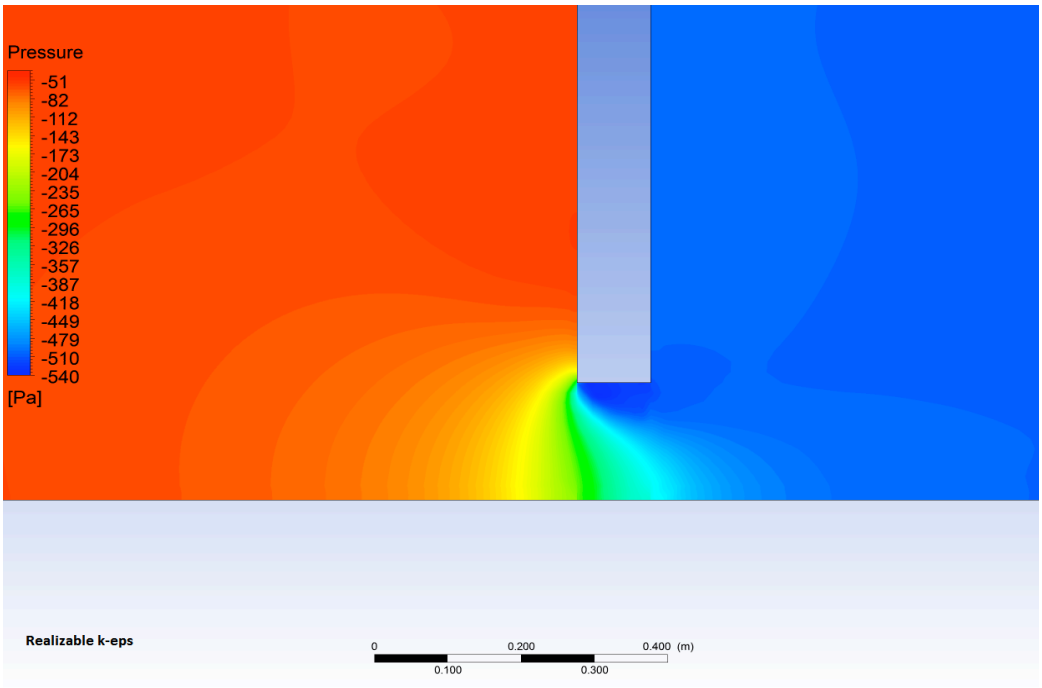

Figure 5-91 Static pressure contour. Detail of the damper region

After several attempts it was found out that the required static pressure at inlet is obtained for a short range of damper levels. In case 1 (p_{outlet} = -422 Pa) the lowering value of 740 mm gives a pressure near -90 Pa, while a slightly positive pressure is obtained for 720 mm. In the real plant this difference is negligible, because the burners work with discontinuity and the burner is moved manually, hence the furnace will operate some moments in a slight positive pressure, other moments in a slight negative value. It is only important to notice that CFD predicts the damper closure of the most part of the duct to achieve the required operation condition. This is what exactly happens in the reality.

Chapter 6 **Conclusions**

In the present dissertation the exhaust system of a galvanization plant, whose burners were converted from traditional to BFG power source, was analyzed. As a consequence of the low LHV (approx. 1000 kcal/Nm^3), fumes volumetric rate produced was increased considerably, with respect to the traditional source. Therefore the analysis of the pressure drops along the duct through CFD became necessary, in order to verify if the retrofitted facility could discharge the highest flow rate forecasted by DCHP estimation. Provided a fixed suction force at the stack through a subsonic ejector, the first objective of this analysis was the calculation of the static pressure at the domain inlet. The second consisted in the determination of the localized pressure drop, obtained through a damper, which assured the on-design operation condition of the furnace.
In the first chapter BFG was presented as an eco-friendly fuel, although its combustion was shown to be not simple; the concept of energy density and the objectives of this work were introduced. In the second chapter was reported a literary review about the main topics encountered during the plant analysis: the ejector, which generates the suction force that moves fumes, and square ducts. Particular care was given to the state of art of their CFD modelling. The third chapter introduced the main aspects concerning with numerical simulations: turbulence models and boundary conditions. The protocol developed (as part of the Q^3 approach) to guide the CFD process and to achieve quality results was introduced as the frame of this study. In chapter 4 all the aspects regarding the pre-processing were exposed. Section by section, each part resulting from the decomposition of the plant was modelled, the computational grid was generated, the solver numerical settings and all the working hypothesis were explained in detail. Grid independence studies and simulation results were reported in detail with the support of contours, vector fields and streamlines representations in chapter 5. Comparison between models, according to the notions learned by the literature research, were performed whether feasible. “Ejector-stack” was investigated through Realizable k-ε and SST k-ω. Both the models gave reasonable static pressures at secondary flow inlets, even if the local quantities such as velocity and pressure profiles inside the domain resulted totally different, as already explained in chapter 2. Subsequently the other domains were analyzed according to these two results. “Dryer + duct B” was investigated through Realizable k-ε and Reynolds Stress Model (RSM). It was found out that the first could predict a comparable static pressure at inlet, with respect to the second, but total different local quantities such as velocity and vorticity distributions. For “Duct A” and “Duct A + damper” only Realizable k-ε was applicable, because in both cases RSM solution diverged. Velocity and pressure fields were compared without and in presence of the damper to show the significant differences.

The total pressure loss calculated along the domain with Realizable are reported in the next table:

k-ε Realizable	Pressure drop [Pa]	
	Case 1	**Case 2**
Duct B + pre-heater	-56.4	-56.4
Duct A	-24.5	-24.8
Total	-80.9	-90.2

Table 6-1 Total pressure drop along the parts, no damper

k-ε Realizable	Pressure drop [Pa]	
	Case 1	**Case 2**
Duct B + pre-heater	-56.4	-56.4
Duct A + damper	-380.3	-436.3
Total	-436.7	-492.7
Damper lower [mm]	730	740

Table 6-2 Total pressure drop along the parts, with damper

It has to be noticed that RSM results in the dryer section were not considered in the calculation above, because the static pressure obtained differed only of a few tenths of Pascal, with respect to Realizable. The predicted damper lowering in the two cases is practically the same, considering the size of the device. As explained at the end of section 5.4.2, the examined is simply a mean working condition, while in real situations burners function discontinuously. The damper position is adjusted manually during the furnace start, but practically no regulation follows the burners activity schedule. Hence in some situations the pressure in the combustion chamber will be in slightly positive, in other it will be the opposite.

An interesting future development of this study consists in the removal of the incompressibility hypothesis and the evaluation of its effects on results, considering a ideal gas as working fluid. It has to be noticed that it would increase exponentially the time required to obtain solution convergence, because of the mesh size involved. Another simpler improvement can be the assumption of a temperature profile in the square ducts, which accounts the effect of the heat exchange on the density. Previous calculations were performed on single duct, but were not reported in this work.

References

[1] R. Remus, M.A. Aguado Monsonet, S. Roudier, L. Delgrado Rancho, Best Available Techniques (BAT) Reference Document for Iron and Steel Production, ed. 2013, p. 318;
[2] R. Remus, M.A. Aguado Monsonet, S. Roudier, L. Delgrado Rancho, Best Available Techniques (BAT) Reference Document for Iron and Steel Production, ed. 2013, p. 48;
[3] K. Sumeru, H. Nasution, F.N. Ani, "A review on two-phase ejector as an expansion device in vapor compression refrigeration cycle", Renewable and Sustainable Energy Reviews 16, p. 4927-4937 (2012);

[4] Y. Zhu, P. Jiang, "Experimental and numerical investigation of the effect of shock wave characteristics on the ejector performance", International Journal of refrigeration 40, p. 31-42 (2014);
[5] S. Varga, A.C. Oliveira, X. Ma, S.A. Omer, W. Zhang, S.B. Riffat, "Experimental and numerical analysis of a variable area ratio stream ejector", International Journal of Refrigeration 34, p. 1668-1675 (2001);
[6] J.T. Munday, D.F. Bagster, "A new ejector theory applied to steam jet refrigeration", Ind. Chem. Process. Des. Dev. 16, p. 442-449 (1977);
[7] V. Lijo, H.D. Kim, S. Matsuo, T.Setoguchi, "A study of the supersoni ejector-diffuser system with an inlet orifice", Aerospace Science and Technology 23, p. 321-329 (2012);
[8] X. Chen, S. Omer, M. Worall, S. Riffat, "Recent developments in ejector refrigeration technologies", Renewable and Sustainable Energy Reviews 19, p. 629-651 (2013);
[9] H.E Gonzales Bravo et al., "State of art of simple and hybrid jet compression refrigeration systems and the working fluid influence", Internationa Journal of Refrigeration 35, p. 386-396 (2012);
[10] S. Alimohammadi, T. Persoons, Da.B. Murray, M.S. Tehrani, B. Farhanieh, J. Koehler, "A validated Numerical-experimental design Methodology for a Movable Supersonic Ejector Compressor for Waste heat Recovery", Journal of Thermal Science and Engineering Apllications 6, 2013
[11] R. Yapici, C.C. Yetisen, "Experimental Study on ejector refrigeration system powered by low grade heat", Energy Conversion and Management 48, p.1560-1568 (2007);
[12] I.W. Eames, S. Aphornratana, D.W. Sun, "The jet-pump cycle. A low cost Refrigerator option powered by waste heat", Heat Recovery Systems & CHP Vol. 15 (8), p. 711-721 (1995);
[13] A. J. Meyer, T.M. Harms,R.T. Dobson, "Steam jet ejector cooling powered by waste or solar heat", Renewable energy 34, p. 297-306 (2009);

[14] S. Sanaye, B. Niroomand, "Vertical ground coupled steam ejector heat pump; thermal-economic modelling and optimization", Int. J. of Refrigeration 34, p. 1562-1576 (2011);
[15] I. Sarbu, C. Sebarchievici, "Review of solar refrigeration and cooling systems", Energy and Buildings 67, p. 286-297 (2013);
[16] J.M. Abdulateef, K. Sopian, M.A. Alghoul, M.Y. Sulaiman, "Review on solar-driven ejector refrigeration technologies", Renewable and Sustainable Energy Reviews 13, p. 1338-1349 (2009);
[17] K. Chunnanond, S. Aphornratana, "Ejectors: applications in refrigeration technology", Renewable & Sustainable energy Reviews 8, p.129-155 (2004);
[18] D.S. Kim, C.A. Infante Ferreira, "Solar refrigeration options – a state-of-the-art review", Int. Journal of Refrigeration 21, p. 3-15 (2008);
[19] Da-Wen Sun, ""Comparative study of the performance of an ejector refrigeration cycle operating with various refrigerants", Energy Conversion & Management 40, p. 873-884 (1999);
[20] S. Aphornratana, I.W. Eames, "A small capacity steam-ejector refrigerator: experimental investigation of a system using ejector with movable primary nozzle", International Journal of Refrigeration 20 (5), p. 352-358 (1997);
[21] F. Marsano, L. Magistri, A.F. Massardo, "Ejector performance influence on a solid oxide fuel cell anodic recirculation system", Journal of Power Sources 129, p. 216-228 (2004)
[22] M. L. Ferrari, M. Pascenti, A.F. Massardo, "Ejector Model for High Temperature Fuel Cell Hybrid Systems: Experimental Validation at Steady-State and Dynamic Conditions", Journal of Fuel Cell Science Technology 5(4) (2008)
[23] M. L. Ferrari, M. Pascenti ,L. Magistri, A.F. Massardo, "MGT/HTFC Hybrid System Emulator Test Rig: Experimental Investigation on the Anodic Recirculation System", Journal of Fuel Cell Science and Technology 8 (2) (2010);
[24] F.J. Gardner, M.J. Day, N.P. Brandon, M.N. Pashley, M.Cassidy, "SOFC technology development at Rolls Royce", Journal of Power Sources 86, p. 122-129 (2000);
[25] B. Kim, D.H. Kim, J. Lee, S. W. Kang, H. C. Lim, "The operation or a 125 kW molten carbonate fuel cell system", Renewable Energy 42, p. 145-151 (2012);
[26] D. Marra, B. Bosio, "Process analysis of 1MW MCFC plant", international Journal of Hydrogen energy 32, p.809-818 (2007);
[27] M. L. Ferrari, A.F. Massardo, " Cathode-anode side interaction in SOFC hybrid systems", Applied Energy 105, p. 369-379 (2013);
[28] L. Vincenzo, N.M. Pagh, K.S. Knudsen, "Ejector design andperformance evaluation for recirculation of anode gas in a micro combined heat and power systems based on solid oxide fuel cell ", Applied Thermal Engineering 54, p. 26-34 (2013);
[29] Y. Wang, K.S. Chen, J. Mishler, S.C. Cho, X.C. Adroher, "A review of polymer electrolyte membrane fuel cells: Technology, applications and needs on fundamental research", Applied Energy 88, p. 981-1007 (2011);
[30] Y. Zhu, y. Li, "New theoretical model for convergent nozzle ejector in the proton exchange membrane fuel cell system" Journal of Power Sources 191, p.510-519 (2009);
[31] T. Van Nguyen, M.W. Knobbe, " A liquid water management strategy for PEM fuel cell stacks ", Journal of Power Sources 114 (1), p. 70-79 (2003);

[32] J. He, J. Ahn, S. Choe, "Analysis and control of a fuel delivery system considering a two-phase anode model of the polymer electrolyte membrane fuel cell stack", Journal of Power Sources 196, p. 4655-4670 (2011);

[33] J. He, S. Choe, C. Hong, "Analysis and control of a hybrid fuel delivery system for a polymer electrolyte membrane fuel cell", Journal of Power Sources 185, p. 973-984 (2008);
[34] J.H. Keenan, E.P. Neumann, "A simple air ejector", ASME Journal of Applied Mechanics 64, p. 75-82 (1942);
[35] J.H. Keenan, E.P. Neumann, F. Lustwerk, "An investigation of ejector design by analysis and experiment", ASME journal of Applied Mechanics 72, p. 299-309 (1950);
[36] I.W. Eames, S. Aphornratana, H. Haider, "A theoretical and experimental study of a small scale steam jet refrigerator", International Journal of Refrigeration 18 (6), p. 378-386 (1995);
[37] D.A. Pounds, J.M. Dong, P. Cheng, H.B. Ma, "Experimental investigation and theoretical analysis of an ejector refrigeration system", International Journal of Thermal Sciences 67, p. 200-209 (2013);
[38] B.J. Huang, J.M. Chang, C.P. Wang, V.A. Petrenko, "A 1-D analysis of ejector performance", International Journal of Refrigeration 22, p. 354-364 (1999);
[39] W. Chen, M. Liu, D. Chong, J. Yan, A.B. Little, Y. Bartosiewicz, "A 1-D model to predict ejector performance at critical and sub-critical operational regimes", International Journal of Refrigeration 36, p. 1750-1761 (2013);
[40] J.M. Cardemil, S. Colle, "A general model for evaluation of vapour ejectors performance for application in refrigeration", Energy conversion and management 64, p. 79-86 (2012);
[41] S. He, Y. Li, R.Z. Wang, " Progress of mathematical modelling on ejectors", Renewable and Sustainable Energy Reviews 13, p. 1760-1780 (2009);
[42] J. Dong, D.A. Pounds, P. Cheng, H.B. Ma, "Experimental investigation and theoretical analysis of an ejector refrigeration system", International Journal of Thermal Sciences 67, p.200-209 (2012);
[43] T. Sriveerakul, S. Aphornratana, K. Chunnanond, "Performance prediction of steam ejector using computational fluid dynamics: Part 1. Validation of the CFD results", International Journal of Thermal Sciences 46, p.812-822 (2007);
[44] N. Sharifi, M. Boroomand, "An investigation of thermo-compressor design by analysis and experiment: Part 1. Validation of the numerical method", Energy Conversion and Management 69, p.217-227 (2013);
[45] V.V. Chandra, M.R. Ahmed, "Experimental and computational studies on a steam jet refrigeration system with constant area and variable area ejectors", Energy Conversion and Management 79, p.377-386 (2014);
[46] Y. Bartosiewicz, Z. Aidoun, P. Desevaux, Y. Mercadier, "Numerical and experimental investigations on supersonic ejectors", International Journal of Heat and Fluid Flow26, p. 56-70 (2005);
[47] M. Ji, T. Utomo, J. Woo, Y. Lee, H. Jeong, H. Chung, "CFD investigation on the flow structure inside thermo vapor compressor", Energy 35, p. 2694-2702 (2012);

[48] J. Kolar, V. Dvorak, "Verification of k-omega SST turbulence model for supersonic internal flows", World Academy of Science, Engineering and Technology 57 (2001);
[49] Y. Bartosiewicz, A. Hemidi, F. Henry, S. Leclaire, J. Seynhaeve, "CFD analysis of a supersonic air ejector. Part 1: Experimental validation of single-phase and two-phase operation", Applied Thermal engineering 29, p.1523-1531 (2009);
[50] A. Hemidi, F. Henry, S. Leclaire, J. Seynhaeve, Y. Bartosiewicz, "CFD analysis of a supersonic air ejector. Part 2: Relation between global operation and local flow features", Applied Thermal Engineering 29, p.2990-2998 (2009);
[51] T. Sriveerakul, S. Aphornratana, K. Chunnanond, "Performance prediction of steam ejector using computational fluid dynamics: Part 2. Flow structure of a steam ejector influenced by operating pressures and geometries", International Journal of Thermal Sciences 46, p. 823-833 (2007);
[52] A. Bouhanguel, P. Desevaux, E. Gavignet, "Flow visualization in supersonic ejectors using laser tomography techniques", International Journal of Refrigeration 34, p.1633-1640 (2011);
[53] P. Desevaux, "A method for visualizing the mixing zone between two co-axial flows in an air ejector", Optics and Lasers in Engineering 35, p.317-323 (2001);
[54] Y. Zhu, P. Jiang, "Experimental and numerical investigation of the effect of shock wave characteristics on the ejector performance", International Journal of Refrigeration 40, p. 31-42 (2014);
[55] J. Gagan, K. Smierciew, D. Butrymowicz, J. Karwacki, "Comparative study of turbulence models in application to gas ejectors", International Journal of Thermal Sciences 78, p. 9-15 (2014);
[56] W. Sobieski, "Performance of an air-air ejector: an attempt at numerical modelling", Task Quarterly 3, p. 449-457 (2003);
[57] X. Lang, X. Long, X. Yao, "Numerical investigation on the mixing process in a steam ejector with different nozzle structures", International Journal of Thermal Sciences 56, p. 95-106 (2012);
[58] Z. Aidoun, Y. Bartosiewcz, Y. Mercadier, "Numerical assessment of ejector operation for refrigeration applications based on CFD", Applied Thermal Engineering 26, p. 604-612 (2006);
[59] Y. Allouche, C. Bouden, S. Varga, " A CFD analysis of the flow structure inside a steam ejector to identify the suitable experimental operating conditions for a solar-driven refrigeration system", International Journal of Refrigeration (article in press) (2013);
[60] N. Ruangtrakoon, T. Thongtip, S. Aphornratana, T. Sriveerakul, "CFD simulation the effect of primary nozzle geometries for a steam ejector in refrigeration cycle", International Journal of Thermal Sciences 63, p. 133-145 (2013);
[61] S.B. Riffat, G. Gan, S. Smith, "Computational fluid dynamics applied to ejector heat pumps", Applied Thermal Engineering 16(4), p. 291-297 (1996);
[62] S. Varga, A.C. Oliveira, B. Diaconu, "Numerical Assessment of steam ejector efficiencies using CFD", International Journal of Refrigeration 32, p.1203-1211 (2009);
[63] M. Yazdani, A.A. Alahyari, T.D. Radcliff, "Numerical modelling of two-phase supersonic ejectors for work-recovery applications", International Journal of Heat and Mass Transfer 55, p. 5744-5753 (2012);

[64] S. Varga, A.C. Oliveira, X. Ma, S.A. Omer, W. Zhang, S.B. Riffat, "Experimental and numerical analysis of a variable area ratio steam ejector", International Journal of refrigeration 34, p. 1668-1675 (2011);
[65] G. Besagni, "An integrated thermodynamic/CFD approach to ejector modeling", (Master Thesis) Politecnico di Milano (2012);
[66] G.A. Rivas, E.C. Garcia, M. Assato, "Forced turbulent heat convection in a square duct with non-uniform wall temperature", International Communications in Heat and Mass Transfer 38, p. 844-851 (2011);
[67] C.M. Winkler, S.L. Rani, S.P. Vanka, "A numerical study of particle wall-deposition in a turbulent square duct flow", Powder Technology 170, p. 12-25 (2006);
[68] J. Nikuradse, "Untersuhung uber die Geschwindigkeitsverteilung in turbulenten Stromungen", Diss. Goettingen, VDI-forschungsheft 281 (1926);
[69] F.B. Gessner, A.F. Emery, "A Reynolds stress model for turbulent corner floes – part 1: Development of the model", Journal Fluids Engineering 98, p. 261-268 (1976);
[70] F.B. Gessner, J.K. Po, "A Reynolds stress model for turbulent corner flows – part 2: Comparison between theory and experiment" , Journal Fluids Engineering 98, p. 269-277 (1976);
[71] A. Nakayama, W.L. Chow, D. Sharma, "Calculation of fully development turbulent flows in ducts of arbitrary cross-section", Journal of Fluid Mechanics 128, p. 199-217 (1983);
[72] A.O. Demuren, "Calculation of Turbulence-Driven Secondary Motion in Ducts With Arbitrary Cross Section", NASA Technical Memorandum 102142 ICOMP-89-16;
[73] M Hirota, H. Fujita, H. Yokosawa, H. Nakai, H. Itoh, "Turbulent heat transfer in a square duct", International Journal of Heat and Fluid Flow 18, p. 170-180 (1997);
[74] A. Melling, J.H. Whitelaw, "Turbulent flow in a rectangular duct", Journal of Fluid Mechanics 78, p. 289-315 (1976);
[75] N. Maeda, M. Hirota, h. Fujita, "Turbulent flow in a rectangular duct with a smooth-to-rough step change in surface roughness", Energy 30, p. 129-148 (2005);
[76] J. Bredberg, S. Peng, L. Davidson, "An improved k-w turbulence model applied to recirculating flows", International Journal of Heat and Fluid Flow 23, p. 731-743 (2002);
[77] Y. Moryossef, Y. Levy, "Unconditionally positive implicit procedure for two-equation turbulence models: Application to k-w turbulence models", Journal of Computational Physics 220, p. 88-108 (2006);
[78] S. Nisizima, "A Numerical Study of Turbulent Square-Duct Flow Using an Anisotropic k-eps Model", Theoretical and Computational Fluid Dynamics 2(1), p. 61-71 (1990);
[79] C.G. Speziale, "On nonlinear K-I and K-epsilon models of turbulence", Journal of Fluid Mechanics 178, p. 459-475 (1987);
[80] R. Rubinstein, J.M. Barton, "Nonlinear Reynolds stress models and the renormalization group", Physics of Fluids A 2, 1472 (1990);
[81] M. Zhang, C.W. Li, Y. Shen, "A 3D non –linear k-eps turbulent model for prediction of flow and mass transport in channel with vegetation", Applied Mathematical Modelling 34, p. 2012-1031 (20102);

[82] S. Nia, H. Kuorosh, "2DV Nonlinear k-ε Turbulence Modelling of Stratified Flows", Journal of the Persian Gulf (Marine Science) 3(10), p. 7-16 (2012);
[83] G. Xiyao, L. Jintao, W. Yulin, Y. Junlian, "A nonlinear k-ε turbulence model applicable to high pressure gradient and large curvature flow", Mathematical Problems in Engineering, Volume 2014, Article ID 405202 (2014);
[84] K. Suga, K. Abe, "Nonlinear eddy viscosity modelling for turbulence and heat transfer near wall and shear-free boundaries", International Journal of heat and Fluid Flow 21, p. 37-48 (2000);
[85] K.B. Lee, H.C. Jang, "A numerical prediction on the turbulent flow in closely spaced bare rod arrays by a nonlinear k-ε model", Nuclear Engineering anfd Design 172, p. 351-357 (1997);
[86] T.B. Gatski, t. Jongen, "Nonlinear eddy viscosity and algebraic stress models for solving complex turbulent flows", Progress in Aerospace Sciences 36, p. 655-682 (2000);
[87] Ville Hämäläinen, "Implementing an explicit algebraic Reynolds stress model into the three-dimensional finflo flow solver", Thesis Work, Laboratory of aerodynamics, Helsinki University of Technology, Espoo (2001);
[88] G.A.R. Rivas, E.C. Garcia, M. Assato, "Turbulent flow simulation in a square-duct using non linear and Reynolds stress model", Anais do 14° encontro de iniciação cientifica e pòs-graduação do ITA-XIV ENCITA (2008);
[89] Jung-Chul Shin, "Experiments on the Turbulent Shear Flow in a Turn-Around Duct (I) – The Mean Flow Characteristics", KSME Journal 8(4), p. 444-459 (1994);
[90] Jung-Chul Shin, "Experiments on the Turbulent Shear Flow in a Turn-Around Duct (II) – The Structure of Turbulence", KSME Journal 8(4), p. 460-474 (1994);
[91] Ping-Ho Tsai, "Turbulent flow in a curved streamwise corner", Master of Science Thesis in Mechanical Engineering at University of Iowa (1985);
[92] P.P. Modi, S. Jayanti, "Pressure losses and flow maldistribution in ducts with sharp bends", Chemical Engineering Research and Design 82 (A3), p. 321-331 (2004);
[93] K. Yakinthos, Z. Vlahostergios, a. Goulas, "Modelling the flow in a 90° rectangular duct using one Reynolds-stress and two eddy-viscosity models", International Journal of Heat and Fluid Flow 29, p. 35-47 (2008);
[94] C.G. Speziale, S. Thangam, N. Hur, "Numerical Study of turbulent secondary flows in curved ducts", NASA Contractor Report 181830, ICASE report No. 89-25 (1989)
[95] H.K. Versteeg and W. Malalasekera. An introduction to computational fluid dynamics. The finite volume method (Second edition), Pearson Education, 2007;
[96] A. Balabel, W.A. El-Askary, "On the performance of linear and nonlinear k-ε turbulence models in various jet flow applications", European Journal of Mechanics B/Fluids 30, p. 325-340 (2011);
[97] T.S. Park, H.J. Sung, "A nonlinear low-Reynolds-number k-ε model for turbulent separated and reattaching flows-I. Flow field computations", Int. J. Heat Mass Transfer 38 (14), p. 2657-2666 (1995);
[98] Ansys Fluent User Guide;

[99] E. Colombo, F. Inzoli, R. Mereu, "A methodology for qualifying industrial CFD: The Q^3 approach and the role of a protocol", Computer & Fluids, p. 56-66 (2012);
[100] G. Besagni, "An integrated thermodynamic/CFD approach to ejector modelling", Thesis (Master), Politecnico di Milano (2012);
[101] Ghani Zigh and Jorge Solis (U.S. NRC). Computational Fluid Dynamics Best Practice Guidelines for Dry Cask Applications. Final Report, March 2013
[102] http://www.CFD-ONLINE.com/
[103] http://www.**computationalfluiddynamics**.com.au/
[104] http://www.linkedin.com/groups/Computational-Fluid-Dynamics-134907
[105] http://www.innovative-cfd.com/
[106] http://www.grc.nasa.gov/
[107] Ansys FLUENT, Ansys FLUENT 14.5 – Theory Guide, Ansys FLUENT, 2012;
[108] http://www.engineering toolbox.com/surface-roughness.html